



Virginia Commonwealth University  
**VCU Scholars Compass**

---

Theses and Dissertations

Graduate School

---

2011

## Designed Synthesis of Halogenated Borazine-Linked Polymers and Their Applications in Gas Storage and Separation

Thomas Reich  
*Virginia Commonwealth University*

Follow this and additional works at: <https://scholarscompass.vcu.edu/etd>

 Part of the [Chemistry Commons](#)

© The Author

---

Downloaded from

<https://scholarscompass.vcu.edu/etd/282>

This Dissertation is brought to you for free and open access by the Graduate School at VCU Scholars Compass. It has been accepted for inclusion in Theses and Dissertations by an authorized administrator of VCU Scholars Compass. For more information, please contact [libcompass@vcu.edu](mailto:libcompass@vcu.edu).

**© COPYRIGHT BY**

**Thomas E. Reich**

**2011**

**All Rights Reserved**

**DESIGNED SYNTHESIS OF HALOGENATED BORAZINE-LINKED POLYMERS AND  
THEIR APPLICATIONS IN GAS STORAGE AND SEPARATION**

A dissertation submitted in partial fulfillment of the requirements for the degree of Doctor of Philosophy at Virginia Commonwealth University.

by

**Thomas Eugene Reich**

Bachelor of Science

James Madison University, 2003

Director: Hani M. El-Kaderi,

Assistant Professor, Department of Chemistry

Virginia Commonwealth University

Richmond, Virginia

December 2011

## **Acknowledgement**

I would like to acknowledge the support and guidance of Professor Dr. Hani M. El-Kaderi whose ideas and talents helped to make this work possible. I would also like to acknowledge my committee members Professor Dr. Scott Gronert, Professor Dr. Everett E. Carpenter, and Professor Dr. Purusottam Jena for their input in pursuit of a doctorate. I am very thankful to the members of the El-Kaderi Group who have been a pleasure to work beside. I would also like to thank the Department of Chemistry at Virginia Commonwealth University for giving me the chance to pursue a doctorate as well as for the financial support early in my career. I would also like to acknowledge the selflessness of the many donors who have allowed me to focus my efforts on research more than I ever thought I could have. I would especially like to thank my family for all their love and care. My parents, Richard and Sherry (1952-2006) Reich, have been, and continue to be, a true inspiration for what a good person can be. My brother, Jeremy Reich, serves as an excellent example of what hard work can do for a lifelong goal. I would certainly like to thank my wonderful wife Jessica as well. I could not imagine a better person with whom to share life's exciting experiences. She is my other half and my better half. Without her by my side, I would not be close to the man that I am today. Most assuredly, I would like to thank F. S. H. for the love, compassion, and guidance that knows no bounds. You are the best.



## Table of Contents

List of Tables.....	vi
List of Figures.....	viii
List of Abbreviations .....	xvi
Abstract.....	xvii
Chapter 1—Introduction	
1.1 Global Energy Concerns.....	1
1.2 Hydrogen and Methane Energy.....	3
1.3 Purification of Hydrogen and Methane Fuels.....	4
1.4 The Use of Hydrogen in Automotive Applications.....	6
1.5 The Storage of Hydrogen by High Pressure and Liquid Systems.....	9
1.6 The Storage of Hydrogen by Chemisorption and Physisorption .....	11
1.6.1 Chemisorption.....	14
1.6.2 Physisorption.....	14
1.7 Borazine .....	19
1.8 Dissertation Problem .....	23
Chapter 2—Reticular Chemistry and the Design of Porous Polymers	
2.1 Introduction.....	25
2.2 Design of Borazine-Linked Polymers.....	27
Chapter 3—Synthesis of Halogenated Borazine-Linked Polymers	

3.1 Introduction.....	49
3.2 Synthesis of Halogenated Borazine-Linked Polymers .....	50
3.3 Characterization of Halogenated Borazine-Linked Polymers.....	55
Chapter 4—Porosity Measurements and Hydrogen, Carbon Dioxide, and Methane Gas Storage Capabilities of Halogenated Borazine-Linked Polymers	
4.1 Introduction.....	89
4.2 Nitrogen Sorption of Halogenated Borazine-Linked Polymers.....	97
4.3 Hydrogen, Carbon Dioxide, and Methane Sorption of Halogen-Decorated Borazine-Linked Polymers.....	116
Chapter 5—Experimental and Theoretical Calculations for the Isothermic Heat of Adsorption of Hydrogen, Carbon Dioxide, and Methane with Halogenated Borazine-Linked Polymers	
5.1 Introduction.....	124
5.2 Experimental Isothermic Heat of Adsorption of Hydrogen, Carbon Dioxide, and Methane with Halogenated Borazine-Linked Polymers .....	128
5.3 Theoretical Calculations for the Isothermic Heat of Adsorption of Hydrogen, Carbon Dioxide, and Methane with Halogenated Borazine-Linked Polymers .....	133
Chapter 6—Gas Separation and Selectivity Capabilities for Benzimidazole-Linked Polymers and Halogenated Borazine-Linked Polymers	
6.1 Introduction.....	139
6.2 IAST Calculations for Benzimidazole-Linked Polymers .....	144

6.3 Detailed Methodology for the Calculation of Selectivity by the Ideal Adsorbed Solution Theory .....	172
6.4 IAST Calculations for Halogenated Borazine-Linked Polymers .....	180
Chapter 7—Concluding Remarks .....	191
List of References .....	196
Vita .....	240

## List of Tables

Table 1: Typical Composition of Natural Gas .....	5
Table 2: Nomenclature of Borazine-Linked Polymers .....	28
Table 3: Theoretical Textural Properties of BLPs .....	34
Table 4: Fractional Atomic Coordinates for the Eclipsed Conformation of BLP-1(Br)...	35
Table 5: Fractional Atomic Coordinates for the Staggered Conformation of BLP-1(Br) .....	36
Table 6: Fractional Atomic Coordinates for the Eclipsed Conformation of BLP-1(Cl)...	37
Table 7: Fractional Atomic Coordinates for the Staggered Conformation of BLP-1(Cl) .....	38
Table 8: Fractional Atomic Coordinates for the Eclipsed Conformation of BLP-2(Br)...	39
Table 9: Fractional Atomic Coordinates for the Staggered Conformation of BLP-2(Br) .....	40
Table 10: Fractional Atomic Coordinates for the Eclipsed Conformation of BLP-2(Cl) .....	41
Table 11: Fractional Atomic Coordinates for the Staggered Conformation of BLP-2(Cl) .....	42
Table 12: Fractional Atomic Coordinates for the Eclipsed Conformation of BLP-10(Br) .....	43

Table 13: Fractional Atomic Coordinates for the Staggered Conformation of BLP-10(Br)	44
Table 14: Fractional Atomic Coordinates for the Eclipsed Conformation of BLP-10(Cl)	45
Table 15: Fractional Atomic Coordinates for the Staggered Conformation of BLP-10(Cl)	46
Table 16: Fractional Atomic Coordinates for the Boracite Conformation of BLP-12(Cl)	47
Table 17: Fractional Atomic Coordinates for the Carbon Nitride Conformation of BLP-12(Cl)	48
Table 18: Porous Textural Properties of BLPs	99
Table 19: H <sub>2</sub> , CO <sub>2</sub> , and CH <sub>4</sub> Gas Sorption Uptakes of BLPs	119
Table 20: Virial Fitting Coefficients of BLPs	129
Table 21: Zero-coverage Isosteric Heats of Adsorption, Q <sub>st</sub> , of H <sub>2</sub> , CO <sub>2</sub> , and CH <sub>4</sub> for BLPs	130
Table 22: Theoretically Calculated Binding Affinities of H <sub>2</sub> , CO <sub>2</sub> , and CH <sub>4</sub> with Chlorinated Borazine and the Respective Experimental Values.	135
Table 23: Data Points for CO <sub>2</sub> and CH <sub>4</sub> isotherms at 273 K for BLP-10(Cl)	179
Table 24: Langmuir-Freundlich Fitting Coefficients for BLP-10(Cl)	179

## List of Figures

Figure 1: Cross-section of a typical PEMFC.....	8
Figure 2: Schematic representation of the formation of the boroxine rings and triazine rings .....	18
Figure 3: Pore wall polarization effect on diatomic hydrogen .....	21
Figure 4: Boroxine, triazine, and borazine building blocks .....	22
Figure 5: Design Representation of Selected Geometries .....	26
Figure 6: Structural Geometries of the Aryl Amine Borazine-Linked Polymer Building Units.....	27
Figure 7: Model Structures of Eclipsed BLP-1(Cl) and BLP-10(Cl) and Their Respective Staggered Models .....	29
Figure 8: The Six Halide-Decorated Pore of BLP-1(X) and the Three Halide-Decorated Pore of BLP-2(X) .....	31
Figure 9: Boracite (left) and Carbon Nitride (right) Topologies for BLP-12(Cl) .....	32
Figure 10: Catalytic Dehydrocoupling of Amine-Borane Adducts.....	49
Figure 11: Synthetic Strategies for the Formation of BLPs.....	50
Figure 12: Scanning Electron Microscopy Images of BLPs.....	58
Figure 13: FT-IR Spectrum of p-Phenylenediamine .....	60
Figure 14: FT-IR Spectrum of Benzidine .....	61
Figure 15: FT-IR Spectrum of 1,3,5-tris-(4-aminophenyl)benzene .....	62

Figure 16: FT-IR Spectrum of tetra-(4-aminophenyl)methane.....	63
Figure 17: FT-IR Spectrum of BLP-1(Br).....	64
Figure 18: FT-IR Spectrum of BLP-1(Br) with Its Starting Material.....	65
Figure 19: FT-IR Spectrum of BLP-1(Cl) .....	66
Figure 20: FT-IR Spectrum of BLP-1(Cl) with Its Starting Material .....	67
Figure 21: FT-IR Spectrum of BLP-2(Br).....	68
Figure 22: FT-IR Spectrum of BLP-2(Br) with Its Starting Material.....	69
Figure 23: FT-IR Spectrum of BLP-2(Cl) .....	70
Figure 24: FT-IR Spectrum of BLP-2(Cl) with Its Starting Material .....	71
Figure 25: FT-IR Spectrum of BLP-10(Br).....	72
Figure 26: FT-IR Spectrum of BLP-10(Br) with Its Starting Material.....	73
Figure 27: FT-IR Spectrum of BLP-10(Cl) .....	74
Figure 28: FT-IR Spectrum of BLP-10(Cl) with Its Starting Material .....	75
Figure 29: FT-IR Spectrum of BLP-12(Cl) .....	76
Figure 30: FT-IR Spectrum of BLP-12(Cl) with Its Starting Material .....	77
Figure 31: Solid-State $^{11}\text{B}$ NMR Spectrum of BLP-1(Cl).....	79
Figure 32: Solid-State $^{11}\text{B}$ NMR Spectrum of BLP-1(Cl).....	79
Figure 33: Solid-State $^{11}\text{B}$ NMR Spectrum of BLP-1(Cl).....	80
Figure 34: Solid-State $^{11}\text{B}$ NMR Spectrum of BLP-10(Cl).....	81
Figure 35: Solid-State $^{13}\text{C}$ NMR Spectrum of BLP-1(Cl) .....	82
Figure 36: Solid-State $^{13}\text{C}$ NMR Spectrum of BLP-10(Cl) .....	83
Figure 37: TGA for an Activated Sample of BLP-1(Br) .....	85
Figure 38: TGA for an Activated Sample of BLP-1(Cl) .....	86

Figure 39: TGA for an Activated Sample of BLP-2(Br) .....	86
Figure 40: TGA for an Activated Sample of BLP-2(Cl) .....	87
Figure 41: TGA for an Activated Sample of BLP-10(Br) .....	87
Figure 42: TGA for an Activated Sample of BLP-10(Cl) .....	88
Figure 43: TGA for an Activated Sample of BLP-12(Cl) .....	88
Figure 44: Schematic Representation for a Quantachrome Autosorb 1-C Low Pressure Sorption Instrument .....	91
Figure 45: Brunauer, Deming, Deming, and Teller Isotherm Curves .....	93
Figure 46: Nitrogen Uptake Isotherms for Chlorine-Lined BLPs .....	98
Figure 47: Nitrogen Uptake Isotherms for Bromine-Lined BLPs .....	99
Figure 48: Pore Size Distribution for BLP-1(Br) .....	101
Figure 49: Pore Size Distribution for BLP-1(Cl) .....	102
Figure 50: Pore Size Distribution for BLP-2(Br) .....	102
Figure 51: Pore Size Distribution for BLP-2(Cl) .....	103
Figure 52: Pore Size Distribution for BLP-10(Br) .....	103
Figure 53: Pore Size Distribution for BLP-10(Cl) .....	104
Figure 54: Pore Size Distribution for BLP-12(Cl) .....	104
Figure 55: NLDFT Calculated Isotherm for BLP-1(Br) .....	105
Figure 56: Langmuir Plot for BLP-1(Br) .....	106
Figure 57: Multipoint BET Plot for BLP-1(Br) .....	106
Figure 58: NLDFT Calculated Isotherm for BLP-1(Cl) .....	107
Figure 59: Langmuir Plot for BLP-1(Cl) .....	107
Figure 60: Multipoint BET Plot for BLP-1(Cl) .....	108



Figure 61: NLDFT Calculated Isotherm for BLP-2(Br).....	108
Figure 62: Langmuir Plot for BLP-2(Br) .....	109
Figure 63: Multipoint BET Plot for BLP-2(Br).....	109
Figure 64: NLDFT Calculated Isotherm for BLP-2(Cl) .....	110
Figure 65: Langmuir Plot for BLP-2(Cl) .....	110
Figure 66: Multipoint BET Plot for BLP-2(Cl).....	111
Figure 67: NLDFT Calculated Isotherm for BLP-10(Br).....	111
Figure 68: Langmuir Plot for BLP-10(Br) .....	112
Figure 69: Multipoint BET Plot for BLP-10(Br).....	112
Figure 70: NLDFT Calculated Isotherm for BLP-10(Cl) .....	113
Figure 71: Langmuir Plot for BLP-10(Cl) .....	113
Figure 72: Multipoint BET Plot for BLP-10(Cl).....	114
Figure 73: NLDFT Calculated Isotherm for BLP-12(Cl) .....	114
Figure 74: Langmuir Plot for BLP-12(Cl) .....	115
Figure 75: Multipoint BET Plot for BLP-12(Cl).....	115
Figure 76: Hydrogen Isotherms for BLPs at 77 K.....	116
Figure 77: Hydrogen Isotherms for BLPs at 87 K.....	117
Figure 78: Carbon Dioxide Isotherms for BLPs at 273 K.....	117
Figure 79: Carbon Dioxide Isotherms for BLPs at 298 K.....	118
Figure 80: Methane Isotherms for BLPs at 273 K.....	118
Figure 81: Methane Isotherms for BLPs at 298 K.....	119
Figure 82: Electron Density of a Monomeric Chlorinated Borazine .....	123
Figure 83: Hydrogen Isosteric Heat of Adsorption Curves of BLPs.....	131

Figure 84: Carbon Dioxide Isothermic Heat of Adsorption Curves of BLPs.....	132
Figure 85: Methane Isothermic Heat of Adsorption Curves of BLPs .....	132
Figure 86: Optimized Geometries of H <sub>2</sub> , CO <sub>2</sub> , and CH <sub>4</sub> Adsorbed on Chlorinated Borazine Calculated at the M06/6-311+G* Level of Theory .....	136
Figure 87: Optimized Geometries of H <sub>2</sub> , CO <sub>2</sub> , and CH <sub>4</sub> Adsorbed on Chlorinated Borazine Calculated at the SVWN/6-311+G* Level of Theory.....	137
Figure 88: Optimized Geometries of H <sub>2</sub> and CH <sub>4</sub> Adsorbed on Chlorinated Borazine Calculated at the B3LYP/6-311+G* Level of Theory .....	138
Figure 89: Example IAST Graph of Selectivity versus Pressure at Different Molar Ratios .....	143
Figure 90: Selected Benzimidazole-Linked Polymers used in IAST studies.....	145
Figure 91: BILP-2 CO <sub>2</sub> /CH <sub>4</sub> Selectivity versus Pressure at 273 K.....	149
Figure 92: BILP-2 CO <sub>2</sub> /CH <sub>4</sub> Selectivity versus Molar Ratio of CH <sub>4</sub> at 273 K .....	149
Figure 93: BILP-2 CO <sub>2</sub> /CH <sub>4</sub> Selectivity versus Pressure at 298 K.....	150
Figure 94: BILP-2 CO <sub>2</sub> /CH <sub>4</sub> Selectivity versus Molar Ratio of CH <sub>4</sub> at 298 K .....	150
Figure 95: BILP-2 CO <sub>2</sub> /N <sub>2</sub> Selectivity versus Pressure at 273 K .....	151
Figure 96: BILP-2 CO <sub>2</sub> /N <sub>2</sub> Selectivity versus Molar Ratio of N <sub>2</sub> at 273 K.....	151
Figure 97: BILP-2 CO <sub>2</sub> /N <sub>2</sub> Selectivity versus Pressure at 298 K .....	152
Figure 98: BILP-2 CO <sub>2</sub> /N <sub>2</sub> Selectivity versus Molar Ratio of N <sub>2</sub> at 298 K.....	152
Figure 99: BILP-2 CO <sub>2</sub> /H <sub>2</sub> Selectivity versus Pressure at 273 K .....	153
Figure 100: BILP-2 CO <sub>2</sub> /H <sub>2</sub> Selectivity versus Molar Ratio of H <sub>2</sub> at 273 K.....	153
Figure 101: BILP-2 CO <sub>2</sub> /H <sub>2</sub> Selectivity versus Pressure at 298 K .....	154
Figure 102: BILP-2 CO <sub>2</sub> /H <sub>2</sub> Selectivity versus Molar Ratio of H <sub>2</sub> at 298 K.....	154

Figure 103: BILP-3 CO <sub>2</sub> /CH <sub>4</sub> Selectivity versus Pressure at 273 K.....	155
Figure 104: BILP-3 CO <sub>2</sub> /CH <sub>4</sub> Selectivity versus Molar Ratio of CH <sub>4</sub> at 273 K .....	155
Figure 105: BILP-3 CO <sub>2</sub> /CH <sub>4</sub> Selectivity versus Pressure at 298 K.....	156
Figure 106: BILP-3 CO <sub>2</sub> /CH <sub>4</sub> Selectivity versus Molar Ratio of CH <sub>4</sub> at 298 K .....	156
Figure 107: BILP-3 CO <sub>2</sub> /N <sub>2</sub> Selectivity versus Pressure at 273 K .....	157
Figure 108: BILP-3 CO <sub>2</sub> /N <sub>2</sub> Selectivity versus Molar Ratio of N <sub>2</sub> at 273 K.....	157
Figure 109: BILP-3 CO <sub>2</sub> /N <sub>2</sub> Selectivity versus Pressure at 298 K .....	158
Figure 110: BILP-3 CO <sub>2</sub> /N <sub>2</sub> Selectivity versus Molar Ratio of N <sub>2</sub> at 298 K.....	158
Figure 111: BILP-3 CO <sub>2</sub> /H <sub>2</sub> Selectivity versus Pressure at 273 K .....	159
Figure 112: BILP-3 CO <sub>2</sub> /H <sub>2</sub> Selectivity versus Molar Ratio of H <sub>2</sub> at 273 K.....	159
Figure 113: BILP-3 CO <sub>2</sub> /H <sub>2</sub> Selectivity versus Pressure at 298 K .....	160
Figure 114: BILP-3 CO <sub>2</sub> /H <sub>2</sub> Selectivity versus Molar Ratio of H <sub>2</sub> at 298 K.....	160
Figure 115: BILP-6 CO <sub>2</sub> /CH <sub>4</sub> Selectivity versus Pressure at 273 K.....	161
Figure 116: BILP-6 CO <sub>2</sub> /CH <sub>4</sub> Selectivity versus Molar Ratio of CH <sub>4</sub> at 273 K .....	161
Figure 117: BILP-6 CO <sub>2</sub> /CH <sub>4</sub> Selectivity versus Pressure at 298 K.....	162
Figure 118: BILP-6 CO <sub>2</sub> /CH <sub>4</sub> Selectivity versus Molar Ratio of CH <sub>4</sub> at 298 K .....	162
Figure 119: BILP-6 CO <sub>2</sub> /N <sub>2</sub> Selectivity versus Pressure at 273 K .....	163
Figure 120: BILP-6 CO <sub>2</sub> /N <sub>2</sub> Selectivity versus Molar Ratio of N <sub>2</sub> at 273 K.....	163
Figure 121: BILP-6 CO <sub>2</sub> /N <sub>2</sub> Selectivity versus Pressure at 298 K .....	164
Figure 122: BILP-6 CO <sub>2</sub> /N <sub>2</sub> Selectivity versus Molar Ratio of N <sub>2</sub> at 298 K.....	164
Figure 123: BILP-6 CO <sub>2</sub> /H <sub>2</sub> Selectivity versus Pressure at 273 K .....	165
Figure 124: BILP-6 CO <sub>2</sub> /H <sub>2</sub> Selectivity versus Molar Ratio of H <sub>2</sub> at 273 K.....	165
Figure 125: BILP-6 CO <sub>2</sub> /H <sub>2</sub> Selectivity versus Pressure at 298 K .....	166

Figure 126: BILP-6 CO <sub>2</sub> /H <sub>2</sub> Selectivity versus Molar Ratio of H <sub>2</sub> at 298 K.....	166
Figure 127: BILP-7 CO <sub>2</sub> /CH <sub>4</sub> Selectivity versus Pressure at 273 K.....	167
Figure 128: BILP-7 CO <sub>2</sub> /CH <sub>4</sub> Selectivity versus Molar Ratio of CH <sub>4</sub> at 273 K .....	167
Figure 129: BILP-7 CO <sub>2</sub> /CH <sub>4</sub> Selectivity versus Pressure at 298 K.....	168
Figure 130: BILP-7 CO <sub>2</sub> /CH <sub>4</sub> Selectivity versus Molar Ratio of CH <sub>4</sub> at 298 K .....	168
Figure 131: BILP-7 CO <sub>2</sub> /N <sub>2</sub> Selectivity versus Pressure at 273 K .....	169
Figure 132: BILP-7 CO <sub>2</sub> /N <sub>2</sub> Selectivity versus Molar Ratio of N <sub>2</sub> at 273 K.....	169
Figure 133: BILP-7 CO <sub>2</sub> /N <sub>2</sub> Selectivity versus Pressure at 298 K .....	170
Figure 134: BILP-7 CO <sub>2</sub> /N <sub>2</sub> Selectivity versus Molar Ratio of N <sub>2</sub> at 298 K.....	170
Figure 135: BILP-7 CO <sub>2</sub> /H <sub>2</sub> Selectivity versus Pressure at 273 K .....	171
Figure 136: BILP-7 CO <sub>2</sub> /H <sub>2</sub> Selectivity versus Molar Ratio of H <sub>2</sub> at 273 K.....	171
Figure 137: BILP-7 CO <sub>2</sub> /H <sub>2</sub> Selectivity versus Pressure at 298 K .....	172
Figure 138: BILP-7 CO <sub>2</sub> /H <sub>2</sub> Selectivity versus Molar Ratio of H <sub>2</sub> at 298 K.....	172
Figure 139: CO <sub>2</sub> /N <sub>2</sub> Selectivity for BLP-10(Cl) at 298 K by Pressure .....	182
Figure 140: CO <sub>2</sub> /N <sub>2</sub> Selectivity for BLP-10(Cl) at 298 K by Molar Ratio .....	182
Figure 141: CO <sub>2</sub> /CH <sub>4</sub> Selectivity for BLP-10(Cl) at 273 K by Pressure.....	183
Figure 142: CO <sub>2</sub> /CH <sub>4</sub> Selectivity for BLP-10(Cl) at 273 K by Molar Ratio.....	183
Figure 143: CO <sub>2</sub> /CH <sub>4</sub> Selectivity for BLP-1(Br) at 273 K by Pressure.....	186
Figure 144: CO <sub>2</sub> /CH <sub>4</sub> Selectivity for BLP-1(Br) at 273 K by Molar Ratio.....	186
Figure 145: CO <sub>2</sub> /CH <sub>4</sub> Selectivity for BLP-1(Cl) at 273 K by Pressure.....	187
Figure 146: CO <sub>2</sub> /CH <sub>4</sub> Selectivity for BLP-1(Cl) at 273 K by Molar Ratio.....	187
Figure 147: CO <sub>2</sub> /CH <sub>4</sub> Selectivity for BLP-2(Br) at 273 K by Pressure.....	188
Figure 148: CO <sub>2</sub> /CH <sub>4</sub> Selectivity for BLP-2(Br) at 273 K by Molar Ratio.....	188

Figure 149: CO <sub>2</sub> /CH <sub>4</sub> Selectivity for BLP-2(Cl) at 273 K by Pressure.....	189
Figure 150: CO <sub>2</sub> /CH <sub>4</sub> Selectivity for BLP-2(Cl) at 273 K by Molar Ratio.....	189
Figure 151: CO <sub>2</sub> /CH <sub>4</sub> Selectivity for BLP-10(Br) at 273 K by Pressure .....	190
Figure 152: CO <sub>2</sub> /CH <sub>4</sub> Selectivity for BLP-10(Br) at 273 K by Molar Ratio .....	190
Figure 153: CO <sub>2</sub> /CH <sub>4</sub> Selectivity for BLP-12(Cl) at 273 K by Pressure.....	191
Figure 154: CO <sub>2</sub> /CH <sub>4</sub> Selectivity for BLP-12(Cl) at 273 K by Molar Ratio.....	191

## List of Abbreviations

BILP .....	Benzimidazole-Linked Polymer
BLP .....	Borazine-Linked Polymer
COF .....	Covalent Organic Framework
DCM .....	Dichloromethane
DFT .....	Density Functional Theory
IAST .....	Ideal Adsorbed Solution Theory
IR .....	Infrared Spectroscopy
LDA .....	Local Density Approximation
MOF .....	Metal Organic Framework
NLDFT .....	Non-Local Density Functional Theory
NMR .....	Nuclear Magnetic Resonance Spectroscopy
PAW .....	Projector Augmented Wave
SEM .....	Scanning Electron Microscopy (Microscope)
VASP .....	Vienna <i>ab initio</i> Simulation Package
XRD .....	X-Ray Diffraction

## Abstract

### **DESIGNED SYNTHESIS OF HALOGENATED BORAZINE-LINKED POLYMERS AND THEIR APPLICATIONS IN GAS STORAGE AND SEPARATION**

By Thomas Eugene Reich, Ph.D.

A dissertation submitted in partial fulfillment of the requirements for the degree of Doctor of Philosophy at Virginia Commonwealth University.

Virginia Commonwealth University, 2011

Director: Hani M. El-Kaderi, Assistant Professor, Department of Chemistry

The synthesis of highly porous organic polymers with predefined porosity has attracted considerable attention due to their potential in a wide range of applications. Of particular interest in porous organic polymers is their potential use in automotive applications as well as separation processes whereby advancements could result in a reduction in carbon dioxide emissions and the production of natural gas in a more economically friendly manner. Along these pursuits, seven borazine-linked polymers (BLPs) have been synthesized through the introduction of *p*-phenylenediamine, 1,3,5-tris-(4-aminophenyl)benzene, benzidine, or tetra-(4-aminophenyl)methane with boron tribromide or boron trichloride followed by the thermolysis reaction of the resulting *in situ* adduct. All resulting polymers exist as amorphous polymers whose chemical connectivity was confirmed through FT-IR, solid state  $^{11}\text{B}$  and  $^{13}\text{C}$  NMR, and elemental analysis while thermogravimetric analysis reveals moderate thermal stabilities up to

about 200°C. To assess their textural properties, all BLPs were subjected to nitrogen sorption experiments at 77 K. In all cases, the polymers possess high surface areas with chlorinated BLPs exhibiting higher values than their brominated analogues (1174-1569 m<sup>2</sup>/g versus 503-849 m<sup>2</sup>/g, respectively). Gas storage capabilities of BLPs for hydrogen, carbon dioxide, and methane were investigated as well. BLPs possess good hydrogen uptakes (0.68-1.75 wt% at 77 K) and zero-coverage isosteric heat of adsorption,  $Q_{st}$ , (7.06-7.65 kJ/mol) as calculated by the virial method. The uptakes and heats of adsorption for carbon dioxide (51-141 mg/g at 273 K with  $Q_{st}$ : 22.2-31.7 kJ/mol) are also attractive. BLPs do not, however, appear to exhibit significant methane storage capabilities (1.9-15.2 mg/g at 273 K with  $Q_{st}$ : 17.1-21.7 kJ/mol). In light of such a difference in storage between carbon dioxide and methane, CO<sub>2</sub>/CH<sub>4</sub> selectivity was calculated for each polymer according to the ideal adsorbed solution theory (IAST). Three of the polymers, BLP-1(Br), BLP-2(Br), and BLP-10(Cl), possess excellent selectivity capabilities over 20 even at low pressures for all molar ratios. Additionally, these selectivity values increase further with increasing pressure. Selectivity was also investigated for benzimidazole-linked polymers. In such systems, the CO<sub>2</sub>/N<sub>2</sub> selectivity values reach 73 at low pressure and exhibit an increasing trend with increasing pressure.



## **CHAPTER 1**

### **Introduction**

#### **1.1 Global Energy Concerns**

For millennia, humankind has been dependent on energy for the sustenance of life as well as the advancement of the quality of life. Humans have consumed the plants that use the sun's energy or consumed the animals that consume the plants that use the sun's energy. Humans have burned wood for warmth and cooking. Over time, humankind's methods of energy production have matured. Of particular importance are electricity and how the world has advanced its capabilities in harnessing this electricity, whether it is from the burning of coal and oil or the use of nuclear energy sources among others. Throughout human history, humankind has continued to expand and develop new energy sources. However, the current global status and trends jeopardize the energy sector.

The global energy use has increased extensively over the past few decades of which there are a number of causes. Firstly, the world population is ever increasing. Owing to the fact that energy use is at the cornerstone of life even on the basic level of food consumption, an increase in world population also increases energy consumption regardless of how a particular person chooses (or is forced) to live. An increase in population in the Americas or in Europe or in Asia or in Australia or in Africa, regardless of whether they are rich or poor, results in the same general effect: an increase in

energy consumption. The world's current population has nearly doubled over the last 40 years. The United Nations has set forth a number of projections for the near and distant future for the world's population.<sup>1</sup> These projections are highlighted by three basic trends. On the low end, the population will slow from its current pace and maximize around eight billion people—an increase of only another billion from today's numbers. The population will then slowly but steadily decrease by about 2 billion people over the following 50 years. On the high end, the population will continue to rise, perhaps at not quite as quick as the current pace, where it will double to 14 billion over the next 80 years. In the middle of these projections is a slowing and saturating rate up to about 9.5 billion people. At which point, there is slight drop in population although at not nearly the pace of the low end projection. These three trends represent a wide berth for the future world population. Nevertheless, among the many significant factors that the United Nations found that will influence the future world population is how we handle the energy crisis.

Newfound demand from developing countries represents a second cause for an increase in global energy consumption. Energy is becoming more readily available to parts of the world that could not take advantage of advanced energetic capabilities. As a result, a number of these sectors are experiencing an energy renaissance much like what the developed world has already experienced in generations past. A large population that has never consumed energy beyond their basic needs for food is being introduced to, say, a car or the light bulb which represent much larger energy demands. As a result, the total energy consumption from developing countries has increased significantly of late.

An increase in the per-capita use from already developed countries represents a third cause for an increase in global energy consumption. The burgeoning market of handheld devices as well as an increase in the sophistication and widespread use of computer-based electronics certainly contributes to this effect. In addition to the energy consumption required to run these devices in the first place, energy is used to manufacture these devices before they are even turned on. To compound upon these demands, energy is also consumed to make the tools used to make these devices, and energy is consumed to make the factory that makes these tools.

With this ever-increasing world population, newfound demand from developing countries, and increase in per-capita use from already established locales, energy production continues to receive great interest. At the forefront of many discussions is the realization of alternative fuel sources away from energy standards such as oil and coal. Naturally occurring coal and oil is finite in quantity, and the rate of the world's consumption of these commodities grossly exceeds its rate of replenishment. At present, oil usage represents about a third of the world's total. Although this percentage share of total energy usage is reducing, the aforementioned increase in overall demands results in a net increase in oil usage on a barrel per unit time basis. Additionally, energy from coal has shown a steady rise in both percentage share and overall consumption. As such, discovery and optimization of alternative fuel sources is an imperative challenge. Ideally, these alternative energy sources would be renewable and cost effective while lessening the impact on the environment as well as lessening the demand on the consumable energy standards.

## **1.2 Hydrogen and Methane Energy**

One such alternative that has received great interest is hydrogen, which is abundant in complex and is consumed through oxidation cleanly to produce water as the only byproduct.<sup>2-7</sup> In fuel cell technology, the combination of hydrogen and oxygen in the presence of a catalyst produces electricity and water. While the water is released as a byproduct, the electricity is used to power an electric traction motor, which ultimately can supply power to a drive train. Additionally, dihydrogen can be mixed with dioxygen and burned in an internal combustion engine to produce motion.

Methane, which is about 80% of natural gas, is also an attractive fuel source alternative. Methane gas can be used to drive a gas turbine or can be burned to heat water for use by a steam turbine. A key advantage of the use of methane as a fuel source is that upon combustion it exhibits a much smaller carbon footprint than what is found with gasoline. Natural gas is produced through two mechanisms: biogenic and thermogenic.<sup>8</sup> In biogenic production, methane is generated through microscopic organisms known as methanogens. Methanogens are archaea similar to bacteria and produce methane as a natural byproduct of their metabolic processes in anoxic environments.<sup>9</sup> They are commonly found in wetlands as well as the digestive tract of many mammals including humans. In thermogenic production, natural gas is produced deep under the earth's surface from organic material that has collected and been subjected to high temperatures and pressures for long periods of time. Over time, this gas condenses into pockets that can be reached by drill from the surface.

### **1.3 Purification of Hydrogen and Methane Fuels**

Although hydrogen and methane represent attractive alternative fuel sources, purification must be performed on both before either can be used as an efficient energy

source. Hydrogen can be produced from a number of different methods. One of the most economically friendly manners of hydrogen production is through the reaction of methane with steam in the presence of a catalyst at elevated temperatures.<sup>10</sup> Carbon dioxide is also formed as a byproduct. Methane, on the other hand, is harvested from natural gas itself; nevertheless, many impurities to methane are present in natural gas as is shown in Table 1.<sup>8</sup> In most cases, the composition of methane is closer to 90% while the larger hydrocarbons are closer to 0% although variations still exist. Most other impurities are removed without significant difficulties; however, the presence of carbon dioxide poses as a significant obstacle for methane purification.

**Table 1.** Typical Composition of Natural Gas

	Percent	Notes
Methane	70-90%	
Larger Hydrocarbons	0-20%	Ethane, Propane, Butane
Carbon Dioxide	0-8%	
Oxygen	0-0.2%	
Nitrogen	0-5%	
Hydrogen Sulfide	0-5%	
Rare gases	trace	Ar, He, Ne, Xe

Whether the intended fuel source is methane or hydrogen, the removal of carbon dioxide is important for the sake of efficient energy production. Carbon dioxide does not burn like methane nor does it oxidize in fuel cells like hydrogen can. The existence of

carbon dioxide within these energy sources decreases the energy density of the system creating a more economically unfriendly effect.

The production of carbon dioxide also poses a significant unwanted effect from an environmental standpoint. Earth's climate has seen a cyclic pattern of rising and falling in temperature that lasts about 100,000 years.<sup>11</sup> The greenhouse effect whereby some sunlight reflected by the earth up into the atmosphere can be redirected back to the earth's surface is a natural cause of this cyclic behavior. Carbon dioxide contributes to this natural greenhouse effect. Although carbon dioxide is not the only contributing gas (water vapor, methane, nitrous oxide, and chlorofluorocarbons being others),<sup>12-14</sup> a direct comparison has been made to illustrate that the 100,000-year cyclic temperature fluctuations are nearly directly proportional to the concentration of carbon dioxide in the atmosphere. As a result, increasing these carbon dioxide concentrations should result in an increase in worldwide temperature that potentially exceeds beyond this natural cycle.

Gas selectivity continues to garner great attention among the scientific community. Of particular interest is in the selective adsorption and separation of CO<sub>2</sub> from N<sub>2</sub>, CH<sub>4</sub>, and H<sub>2</sub>. More specifically, carbon dioxide exists as an impurity in flue gases (gases that exit to the atmosphere via an exhaust port such as smoke stacks from power plants or even household fireplaces) as well as in natural gas as was mentioned beforehand. Advancements in this area can result in a reduction in atmospheric greenhouse gases as well as the production of high purity natural gas in a more economically friendly manner.<sup>15-17</sup>

#### **1.4 The Use of Hydrogen in Automotive Applications**

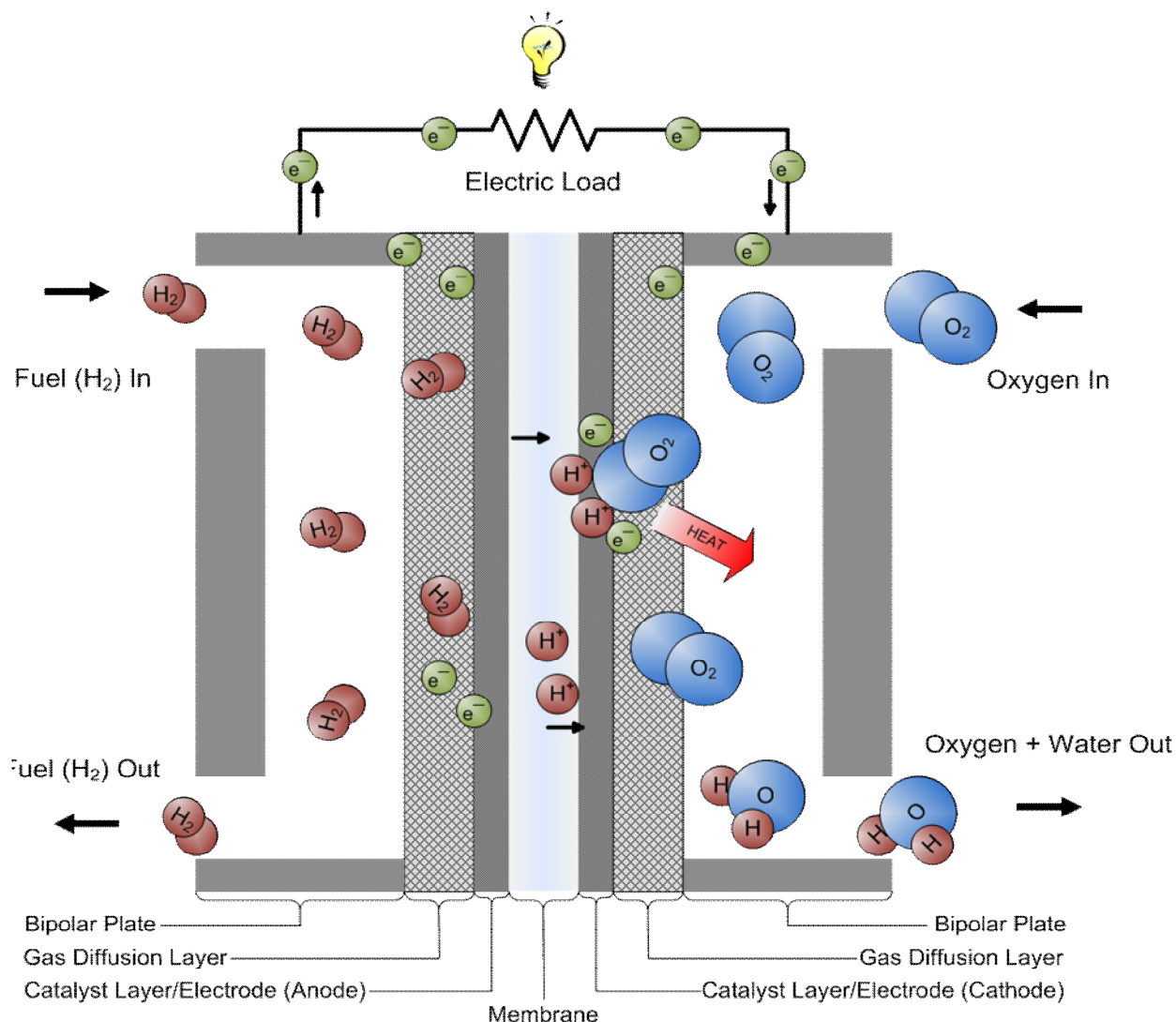
The use of a hydrogen energy source in the automobile industry has received a particularly large amount of interest. According to a study by the European Union as reported by the European Commission's HyWays project, the widespread use of hydrogen in automobiles alone could reduce road transport oil consumption by 40% by the year 2050. Such a savings represents a reduction in oil consumption of over 50 million barrels of oil each day in the year 2050 by even conservative projections.

The use of hydrogen in automotive applications revolves around the concept of the fuel cell. Although a fuel cell in the general sense does not need to employ hydrogen as its fuel source (methane and methanol being others), hydrogen is certainly the most common source. Within the fuel cell, hydrogen combines with oxygen to form water and electricity. This electricity is harnessed for later use while the water is emitted as a byproduct. With exceptionally high efficiencies, this technology converts chemical energy inherent in the dihydrogen and dioxygen bonds into electrical energy which makes it attractive for everyday use.<sup>18-22</sup> As evidenced by the myriad of manufacturers that have produced hydrogen-based vehicles—BMW, Toyota, and Chevrolet to name a few—the technology that is required to propel an automobile at sufficient speeds for safe roadway driving has been developed already. However, improvements within this field are sought to improve the efficiencies of fuel cells further and help to reduce mainstream concerns over current technological developments in fuel cells, namely their cost, durability, and reliability.

Among these attractive approaches is the pursuit of high-efficiency proton-exchange membrane fuel cells (PEMFC).<sup>23-27</sup> Within this type of fuel cell (Figure 1) a polymer

electrolyte membrane (PEM) separates the hydrogen and oxygen while simultaneously umpiring the proton transfer process between the anode and the cathode.

**Figure 1.** Cross-section of a typical PEMFC.



Highly fluorinated material remain the most studied of PEMs; however, these systems suffer from high costs, low working temperatures, and flooding of the electrodes.<sup>28-34</sup> Such low working temperatures are undesirable as elevated temperatures are typically needed to reduce the sensitivity of platinum to carbon monoxide as well as encouraging faster kinetic reaction speeds and the management of



the flooding of the electron through water displacement. Overall, PEMs need to strike the most appropriate balance among attractive properties to enhance fuel cell efficiency: high proton conduction, good mechanical, chemical, and thermal strength, and low gas permeability.

### **1.5 The Storage of Hydrogen by High Pressure and Liquid Systems**

Despite the need for improvements in the generation of electricity from a hydrogen fuel source as well as in the production of hydrogen itself, a major stumbling block still exists before the realization of a hydrogen economy can be achieved: the storage of hydrogen. Continuing in the context of the automobile industry, the current range of the already-produced hydrogen-fueled cars is typically limited to a couple hundred miles. This distance is inadequate when compared to the current standards of gasoline-powered automobiles and expectations of today's consumers at a range of nearly double that amount. Additionally, the current methods of storing hydrogen employed in such vehicles are highly energetically unfavorable and results in a contradictory situation in which this alternative fuel designed to reduce the demand on other sources actually increases it in indirect ways. In addition to its energetic shortcoming, the storage of dihydrogen without the aid of a media is typically unsafe and spatially inefficient as is discussed below.

The United States Department of Energy has set performance targets for the storage of enough hydrogen to overcome these limitations at 5.5 wt% H<sub>2</sub> and 40 g H<sub>2</sub>/L by 2015<sup>35-36</sup> and has also set ultimate performance targets at 7.5 wt% H<sub>2</sub> and 70 g H<sub>2</sub>/L. Additionally, these targets, according to the Department of Energy, must be clearly surpassed for the realization of efficient hydrogen use in automobiles. Of important

note is that systems must meet these levels under ambient temperatures which are in contrast to the standard for publishing hydrogen uptake numbers done under cryogenic conditions and most commonly at 77 K.

A common practice for storing hydrogen in current hydrogen-fueled cars is employing high pressures (200 bar). As mentioned before, this technique does not generate a high enough energy density to propel an automobile for a range approaching today's standards and expectations. Even at such high pressures, the individual dihydrogen molecules are still too far away from each other. Additionally, storing an adequate supply of dihydrogen in its gaseous state at such high pressures creates a system in which the automobile has become essentially a "moving bomb". A rupture or puncture of sufficient size of the storage chamber would result in a pressure explosion capable of disfiguring and dispersing shrapnel at the risk of causing significant bodily injury or even death not to mention significant property damage. In addition to causing a pressure explosion, such a rupture would result in the rapid release of a very flammable gas. Exposure to a flame or a spark—say by metal scrapping on the surface of a roadway as is frequently seen in automobile accidents—would ignite the hydrogen and create an even larger explosion.

To make matters worse, the volume required to store enough hydrogen at this high of a pressure to propel an automobile a sufficient range would require a storage tank roughly half the size of today's automobiles. Attempts to mitigate the size of the tank by increasing the size of the vehicle itself would add unnecessary weight to the vehicle's chassis. This added weight would in turn require more energy for propulsion, thus requiring a still larger tank and defeating the purpose of increasing the automobile's size

to accommodate the tank in the first place. This catch-22 nature is similar in thought to the concept of why birds do not grow to be as large as non-airborne species such as mammals. A larger bird would require a larger wingspan to fly. A larger wingspan would require larger muscles to push them. Larger muscles would require larger organs to supply energy for the muscles. And larger organs would require a still larger bird. Similarly, increasing the size of the automobile to diminish the percentage of space used by the storage tank would require a still larger storage tank to keep the range at a sufficient level.

Another method for the storing of dihydrogen onboard an automobile is through its liquid state. Storing dihydrogen in its liquid state is energetically unfavorable. Dihydrogen liquefies at 20 K, and the amount of energy required to chill the fuel would significantly hinder the efficiency of the output energy. Keeping the storage tank at 20 K would also require the development of a new system and potentially a significant input of energy as well. As a result, chilling to and storing dihydrogen at its liquid state at 20 K would require energy demands contradictory to the purpose of vitalizing an alternative energy source.

### **1.6 The Storage of Hydrogen by Chemisorption and Physisorption**

Despite the energetic and safety-based shortcomings of storing hydrogen at high pressures or in its liquid state, other methods of hydrogen storage have emerged. Among these methods are through the chemisorption or physisorption of hydrogen. Both methods are designed to help improve upon both the gravimetric and volumetric storage of hydrogen to reach the targets set forth by the U. S. Department of Energy.

In chemisorption, hydrogen is stored within a molecular storage media and held in place via chemical bonds. In the case of ammonia-borane,  $\text{H}_3\text{NBH}_3$ , which has attracted considerable attention,<sup>37-39</sup> hydrogen represents about 19 wt% of the total molecule. Although this number greatly exceeds the Department of Energy's 2015 and ultimate targets, a number of disadvantages plague the chemisorption method of storage as will be discussed later in section 1.6.1. As a result improved chemisorption systems are being investigated to overcome these obstacles.

In physisorption, hydrogen is stored within a porous storage media and held in place via the electrostatic interaction between the dihydrogen molecules and the walls of the media itself. This electrostatic interaction is much weaker than a chemical bond; however, such an occurrence is not necessarily an undesirable condition. For example, this weaker interaction allows for the facile regeneration of the storage media in a fashion similar to pumping gas into the fuel tank of an internal combustion engine automobile. Further information on the advantages and disadvantages of physisorption hydrogen storage will be discussed later in section 1.6.2.

Oftentimes, the scientific community will raise the question of within a system, particularly ones that utilize porous media, whether the storage of hydrogen is of the chemisorption or physisorption variety. Although seemingly trivial at first glance, the worth of the question is certainly with merit. At the root of the question is the distance between the dihydrogen molecules and the storage media. In physisorption, this distance can vary greatly but is typically on the order of a few angstroms; in chemisorption this distance is the bond distance between two atoms—a hydrogen atom and an atom in the storage media. Nevertheless, the concepts of an electrostatic

interaction and a chemical bond share a similarity. Despite what is implied by introductory chemistry courses to aid in the simplification of a complex concept, a chemical bond is not a line attached to the cores of two atoms. Instead, it is two atoms whose cores share a certain level of proximity to each other, and electrons surround them with varying degrees of movement about each core (i.e. the gradient in electron density for ionic versus covalent bonds). At its essence, physisorption is very similar whereby the attractive forces of an electron cloud to a positively charged core bring the systems closer together until the repulsive forces of the system are equal and opposite. The main differences between these systems at an atomic level are the sharing of electrons in the storage media-dihydrogen molecule system and the spatial distance between atomic cores, but the fundamental similarity of the proton-electron interaction in both systems is not trivial.

The concept of the isosteric heat of adsorption aids in distinguishing between these two types of storage although it is not the only aid. Heat of adsorption, which will be discussed at greater length in a later chapter, assesses the affinity that an incident gas has for the storage media. For chemisorption, this heat of adsorption is much higher than what is found for current generation physisorption. Additionally, a plot of heat of adsorption versus gas uptake in a chemisorption system would reveal a significant drop. This drop represents the point at which all of the binding sites to the storage media have been exhausted. Any remaining affinity would be the result of a weak interaction between the now-saturated media and the incident gas. For physisorption, however, any drop of heat of adsorption in the graphical plot is typically smooth and less significant in slope.

### 1.6.1 Chemisorption

Current investigations into hydrogen storage by chemisorption including systems with chemical hydrides<sup>40-51</sup> or metal hydrides<sup>52</sup> have not been able to match the Department of Energy targets under the requisite conditions. Firstly, harvesting the entirety of the chemically-bound hydrogen can be exceedingly difficult. This challenge makes the effective hydrogen storage much less. For instance, in the ammonia-borane example where hydrogen represents 19 wt% of the material, such a high hydrogen storage value would demand that all six hydrogen atoms per molecule were harvested. For each hydrogen atom that is not able to be used, the uptake drops by over 3 wt%.

Secondly, the storage of hydrogen chemically encounters the problem of the irreversible nature of the storage. Any hydrogen that is removed from the storage media for fuel must be replaced for recurring use of the automobile's "gas tank". Any irreversibility in the system results in an accumulation of waste that diminishes or even forbids the possibility of long-term hydrogen storage. Consequently, removal of the spent chemical or metal hydrides would become a necessity, which carries a host of other problems such as the safe disposal or deactivation of the remaining storage media. Proceeding along such lines of research as increasing the waste and safety concerns would mitigate the overall goal of using hydrogen as an alternative energy source that is more environmentally friendly than many other forms of energy.

### 1.6.2 Physisorption

Hydrogen storage by physisorption, which typically employs porous materials such as coordination polymers,<sup>53-60</sup> porous carbon,<sup>61-62</sup> and organic polymers,<sup>63-69</sup> represents a promising method for the storage of hydrogen by creating a system in which the

dihydrogen molecules can weakly interact with the walls of the host material in addition to exhibiting other attractive potential applications such as in catalysis and conductivity.<sup>70-75</sup> This weak interaction allows for the confinement and release of dihydrogen under ambient conditions. The reversibility of this weak interaction allows for the storage and use of hydrogen to be more energetically favorable and under safer conditions than alternative hydrogen storage media. A downfall of this weak interaction remains that the storage of hydrogen under ambient conditions is limited in its capabilities. However, experimental and theoretical investigations into factors that affect hydrogen storage have already shown areas where improvements can be made.

Current investigations into the metal doping of porous structures like carbon nanotubes (CNTs),<sup>76-86</sup> fullerenes,<sup>87-88</sup> and metal organic frameworks<sup>89-92</sup> reveal that such systems exhibit a high capacity for dihydrogen both theoretically and experimentally. The prevailing concept behind such systems is that the large electronegativity of the structures parlay a positive charge on the metal. Subsequent introduction of dihydrogen molecules results in a polarization effect across either side of the molecule's single bond; in turn, this polarization can potentially impart a similar effect on other dihydrogen molecules albeit with theoretically diminishing returns as the distance from the metal is increased. Overall, this effect results in a greatly enhanced hydrogen storage capacity.<sup>76-85, 87-88</sup> Jena and co-workers at Virginia Commonwealth University performed computational studies on hydrogen storage in lithium and titanium-decorated fullerenes.<sup>87-88</sup> Their studies on the titanium systems revealed that only metal atoms bonded to the structure contributed positively to hydrogen storage while titanium clusters reduced the total surface area as well as the storage capacity. In

lithium-fullerene systems, metal clustering is avoided; however, aggregation from neighboring molecules could exist to reduce the overall hydrogen storage capacity. Steps to limit such interactions would then need to be employed. More recently, the use of atomic layer deposition (ALD), molecular organic chemical vapor deposition (MOCVD), solution infiltration, and lithium-reducible organic links have been investigated for the impact of metal doping on coordination polymers.<sup>93-99</sup> In many of the resulting materials, enhanced hydrogen storage was observed. Hupp and co-workers examined structures similar to metal organic frameworks wherein he replaced organic links with boron-rich carboranes.<sup>100</sup> The resulting polymers were observed to enhance the hydrogen storage. These findings in particular are relevant to this dissertation as the incorporation of boron-rich building units for the production of a new class of organic polymers to enhance gas storage will be discussed.

To aid in the discovery of more efficient methods of hydrogen storage, several theoretical and experimental studies relay the potential of amorphous or crystalline organic polymers.<sup>101-119</sup> Their reports indicate that there are a number of factors that contribute to gas uptake including high surface area, pore shape, and the aforementioned electronegativity. To ease the difficulty of designing organic polymers with the intent of tailoring the structural characteristics, Yaghi and co-workers developed the concept of reticular chemistry.<sup>120-130</sup> This science considers the shape of the building units to predict the topology, or polymeric structure, of the products. Development of a database for many different permutations of building units has been essential for the development of covalent organic frameworks (COFs). Although the aforementioned metal organic frameworks have yielded strong experimental and

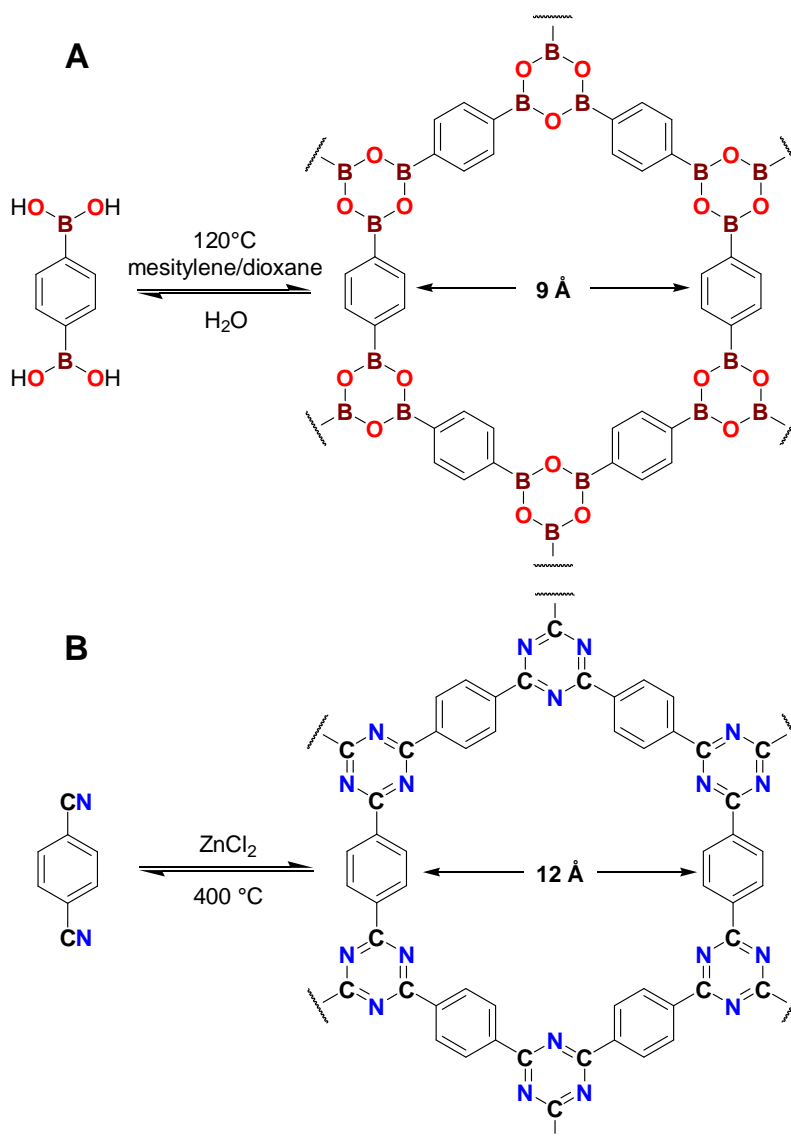


computational results, COFs have a number of advantages over their metallic counterparts. Among them are the presence of strong covalent bonds throughout the polymer and their incorporation of light weight atoms (C, H, N, B, and O) that contribute to an increase in the uptake/weight ratio.<sup>120-126, 131-132</sup> The hydrogen sorption of two- and three-dimensional COFs has been studied as an emerging field from both an experimental and theoretical standpoint.<sup>105-109</sup> The work of Goddard and co-workers has shown particularly strong agreement by using first-principles-based grand canonical Monte-Carlo simulations.<sup>105</sup> Their predicted hydrogen adsorption of 3.3 wt% at 50 bar and 77 K for COF-5 agrees well with the experiment value of 3.4 wt%. Interestingly, Goddard's work also predicted that COF-105 and COF-108 are expected to have a reversible excess hydrogen uptake of 10.0 wt% at 77 K, which would make them the best known hydrogen storage media at 77 K to date. Additional computation studies<sup>133-140</sup> investigating the effect of decorating COFs with metal ions indicate that the dopant adheres to the walls of COFs and avoids the diminishing effect agglomeration has on hydrogen storage. In such a case, the hydrogen storage capacities and hydrogen adsorption energies improve significantly.<sup>101</sup> These many experimental and computational studies show that covalent organic frameworks overshadow metal organic frameworks as a media for hydrogen storage.<sup>141-142</sup>

Of important note regarding factors that affect hydrogen storage is the surface area of the material. All other factors being equal, a system of greater surface area provides more planar space with which the hydrogen can interact and increases the overall hydrogen uptake. Nevertheless, increasing the surface area of the material rarely keeps all other factors equal. Oftentimes, increasing the surface area also results in an

increase in pore size. Pore size has an inverse relationship with hydrogen storage capacity whereby an increase in pore size typically results in a decrease in storage capability. In fact, pore size can have a significant impact on hydrogen storage as is exemplified by activated carbons and zeolite-templated systems which, despite their low surface areas, have high hydrogen uptakes due to their ultrafine pores typically less than 1 nm in size.<sup>62, 143</sup>

**Figure 2.** Schematic representation of the formation of the boroxine rings<sup>122</sup> (A) and triazine rings<sup>124</sup> (B).



Covalent-organic frameworks, which are constructed by condensation reactions that yield covalent B-O bonds (Figure 2), can be tailored to possess exceptional porosities, very low densities, and pore metrics that span the micro- and meso-porous ranges.<sup>120-123, 125-126</sup> Additionally, trimerization reactions in ionothermal zinc chloride conditions have yielded organic polymers with triazine linkers (Figure 2) that exhibit high surface area.<sup>124</sup> In the case of covalent-organic frameworks, the reversible nature of the boroxine forming bond results in its organization into a crystalline system. In the absence of reversible bond formation processes or sufficient kinetic control over key formation steps, covalent polymers lack long range ordering and tend to be amorphous as in the case of polymers of intrinsic microporosity (PIMs), conjugated microporous polymers (CMPs), and porous organic frameworks (POFs).<sup>144-147</sup> Nevertheless, crystallinity is not a prerequisite for exhibiting significant gas uptake and selectivity properties, and the library of porous polymers expands with other systems that have shown enhanced gas uptake and selectivity including zeolitic imidazolate frameworks (ZIFs), zeolitic tetrazolate frameworks (ZTFs), metal organic frameworks (MOFs), and benzimidazole-linked polymers (BILPs).<sup>148-156</sup> Additionally the potential for this library is dramatic in size as a variety of attractive building blocks only adds to the potential for new systems.<sup>157-162</sup>

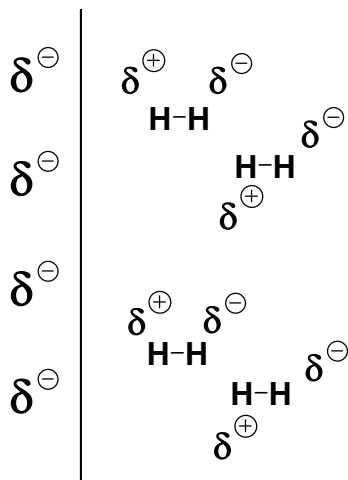
## **1.7 Borazine**

Despite an ever-expanding library of porous polymers each with their own capabilities in gas storage and selectivity, a significant drawback for many of these types of polymers is the lack of functionalization of the pores. Pore functionalization can have a significant impact on the electronegativity of the pores as well as spatial effects

resulting in a net positive or negative change in hydrogen storage.<sup>163</sup> As previously stated, the size of the pores of the polymer has a significant effect on its gas storage capabilities. Projecting large functional groups like alkyl chains can reduce the pore size. Pore size can also be controlled by the size of a single atom. Functionalization by a large bromine atom would shrink the size of the pore more than if the functionalization was carried out by a chlorine atom. Nevertheless, careful consideration must be taken to ensure that any pore shrinkage does not occur to the point of sealing off the system. Creating an effective wall within the pore would shield any input gas and drop its uptake significantly. In regards to the effect that electronegativity plays on gas uptake, the incorporation of polarizable building blocks into porous architectures has shown enhanced gas uptake as well.<sup>163</sup> The differences in electronegativity of the building block and the resulting electron density gradient contributes to a polarizing effect on the gas itself conceptually similar to what was demonstrated by the metal doping of carbon nanotubes, fullerenes, and metal organic frameworks mentioned previously. In the case of hydrogen, a dipole moment within the diatomic molecule will be created whereby a partially positive charge will form on the hydrogen atom closest to the wall of the polymer and a partially negative charge will form on the hydrogen atom furthest from the wall. This polarity can in turn function to polarize an additional dihydrogen molecule itself (Figure 3). The strength of the polarizability of one hydrogen molecule to another is expected to decrease as the distance from the polymer surface is increased as was found for metal-dopant systems; nevertheless, a trickle-down effect which increases the overall gas uptake is expected to result. It should be noted that any beneficial effect on gas uptake from a polarizable building unit requires that the gas is polarizable itself.

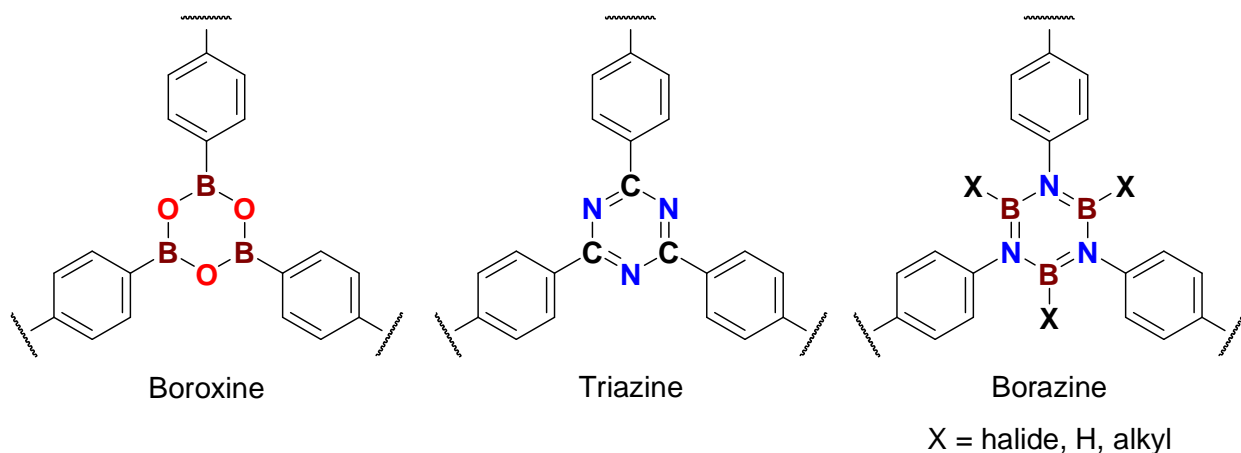
This class includes both hydrogen and carbon dioxide. However, methane, which is also of interest for gas storage applications, is not expected to be significantly polarizable and therefore would not benefit from a polarizable building unit.

**Figure 3.** Pore wall polarization effect on diatomic hydrogen.



In regards to the ever-expanding library of organic porous polymers, the lack of suitable sites of extension into the pores of many of these polymers, including boroxine and triazine-based polymers (Figure 4), forbids simple pore functionalization. The bi-coordinated oxygen atoms of boroxine prevent the presence of an additionally bonded atom that projects into the pores of COFs, and the  $sp^2$ -hybridized nitrogen atoms in triazines result in a similar limitation. As such, changing the electronic or spatial nature of the polymer in addition to its gas storage characteristics requires an entirely new model design and denies the flexibility of simple pore modification by either pre- or post-synthesis methods. Borazine rings (Figure 4), however, allow for the appropriate sites of extension.

**Figure 4.** Boroxine, triazine, and borazine building blocks.



Borazine rings are isostructural to the boroxine units found in COFs and the triazine units found in CTFs. Coordination of the extended framework through the nitrogen atoms of borazines leaves boron atoms free to bond to another atom that would project into the pores of the polymer. Changing the pore-decorating atom would be as simple as changing the atom bonded to the boron in the starting material without the need for redesigning the entire polymer and results in many polymer possibilities with just a small demand on polymer design. Additionally, post-synthesis modification can be possible if the bonding between the boron atom and the projecting atom possesses suitable reactivity characteristics.

Monomeric species containing borazine rings have been previously synthesized through diverse procedures.<sup>164-187</sup> Inclusion of borazine within a polymeric system has also been previously reported and has been mainly used for the fabrication of boron nitride-based ceramics, polyborazylenes, or organic optoelectronics.<sup>188-194</sup> Additionally, polyborazylenes have been investigated for their suitability in the regeneration of ammonia-borane fuel,<sup>195-200</sup> but such methods remain underdeveloped and, at present,

require significant improvements in their cyclic process to enhance their automotive applicability in addition to their economical and environmental friendliness.

### **1.8 Dissertation Problem**

A significant need exists for improvements in gas storage and separation for energy-based applications. This need is heightened by the increase in worldwide energy consumption. At present, the requisite targets set forth by the U.S. Department of Energy for storage capabilities remain unmet under ambient temperature. Heightened purification techniques would also be highly beneficial as they could enhance the energy density of alternative fuel sources and make the use of such methods more cost effective. Additionally, the employment of borazine rings within organic porous polymers for the purpose of gas storage and separation has been previously undeveloped. The main objectives of this dissertation are to develop porous media incorporated with halogenated borazine rings capable of storing small gases (hydrogen, methane, and carbon dioxide) and exhibiting the ability to separate gas mixture systems. With these considerations in mind, we set out to design, synthesize, and characterize a library of polymers utilizing aromatic systems in conjunction with the six-member cyclic structure borazine. As such, these polymers have been dubbed borazine-linked polymers (BLPs). Polymers were synthesized through the introduction of aryl amines with boron trichloride or boron tribromide under ideally facile conditions. Amine selection will be dictated based on topological and chemical design desires. The successful formulation of new polymers as well as their thermal stability will be determined through spectral and analytical methods. Gas sorption capabilities will be investigated through gas sorption experiments, and textural properties will also be

assessed through these experiments. To assess each polymer's capabilities as a gas separation media, computational calculations will be performed based on pure component data to predict their performance in gas mixtures. Advancements along these lines could enhance the scientific community's understanding of the effects that contribute to efficient gas storage and separation, and in our opinion research in this area represents an important step for the development of a viable hydrogen economy as well as yield significant benefits in the storage and separation of other gases.



## Chapter 2

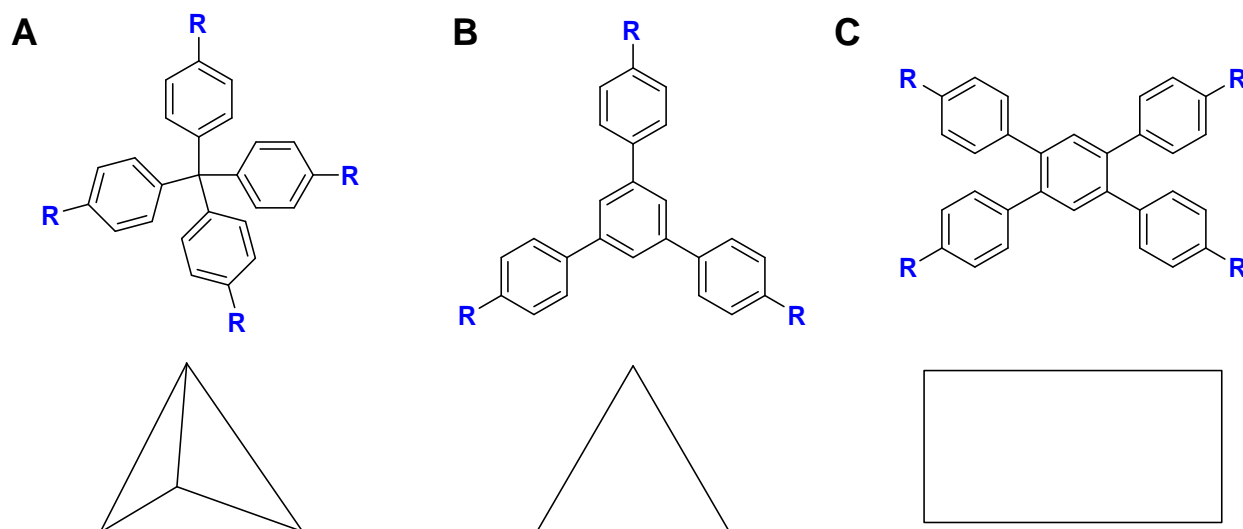
### Reticular Chemistry and the Design of Porous Polymers

#### 2.1 Introduction

Within the realm of porous polymers exist many different groups. Among them are the highly crystalline metal organic frameworks (MOFs). Following synthesis of most of this class of porous polymers, crystals of sufficiently large enough size are formed so that they might be examined via single-crystal x-ray diffraction (XRD) to assess the exact ordering of the network. Within the realm of purely covalent organic polymers, however, single crystals of large enough size for XRD examination rarely form; oftentimes, they are in fact microcrystalline. As a result, knowing information about a polymer's potential order within the crystalline matrix before XRD examination can greatly aid in the assessment of a successful synthesis. To aid along these lines, the concept of reticular chemistry was developed.

Reticular chemistry, developed by Yaghi and coworkers, describes the shape of how a porous network might be formed. This concept suggests that the way in which a polymer forms can be predicted based on the geometric structure of the building blocks used in the synthesis as well as its degree of coordinated extension. As such, the polymeric formation resulting from the combination of a tetrahedral and a triangular building unit (Figure 5, A with B) would be different than what would be expected from combining building units of triangular and rectangular geometries (Figure 5, B with C).

**Figure 5.** Design Representation of Selected Geometries: (A) tetrahedral, (B) triangular, and (C) rectangular.



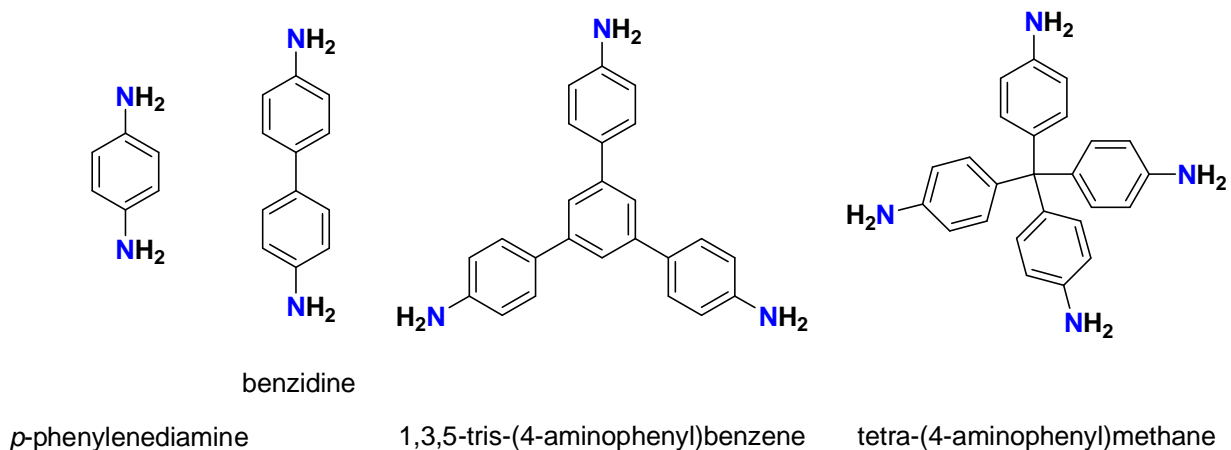
The resulting formations, often called topologies, are the result of the minimization of energy within the network. For many combinations of geometries, multiple topologies could be energetically favorable. As a result, it is often appropriate to consider the formation or packing of two or more different types of topologies. Once these polymers are formed, they typically adopt a single consistent topology throughout the polymer if the matrix is of sufficient crystallinity and order; therefore, understanding XRD patterns from the theoretically possible topologies can help characterize the material from experimental XRD patterns. Molecular modeling can produce other pieces of important information such as theoretically optimum surface area and pore sizes.

Yaghi and coworkers analyzed the resulting topologies for a number of different combinations.<sup>201-205</sup> Additionally, to allow for researchers to more easily access the great number of topological possibilities, they created the Reticular Chemistry Structure Resource.<sup>206</sup> This database can be accessed free of charge via the worldwide web.

## 2.2 Design of Borazine-Linked Polymers

This dissertation entails the design, synthesis, and characterization of halogenated borazine-linked polymers (BLPs). The synthesis, characterization, sorption properties, and separation capabilities will be relayed in later chapters; however, their design aspects will be discussed here. Each of these polymers shares a number of similarities. Firstly, they all incorporate a borazine ring. With respect to reticular chemistry, borazine rings are of a triangular geometry and extend out to the rest of the polymers through their nitrogen atoms. Although the third valency of the boron atoms could certainly serve as sites of extension, polymers designed and synthesized as such were not examined within the confines of this research. As such, only borazine derived through the nitrogen atoms will be discussed. A second similarity between the borazine-linked polymers within this research is that they are all composed of aryl building units. The geometries of these four aryl building units that were used to create BLPs are illustrated in Figure 6.

**Figure 6.** Structural Geometries of the Aryl Amine Borazine-Linked Polymer Building Units.



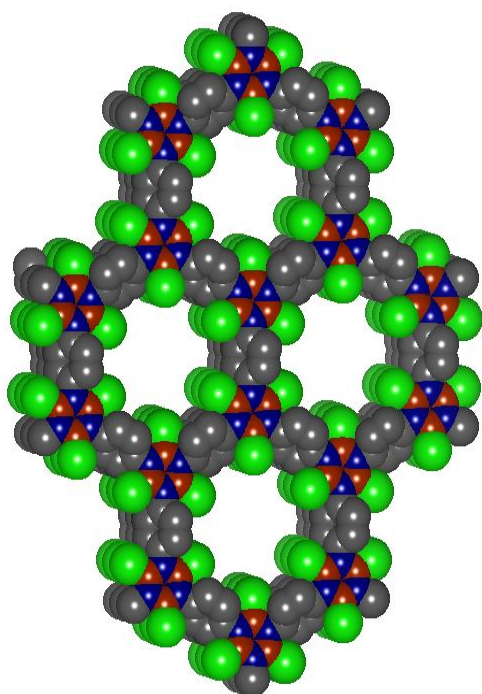
The names associated with these polymers are determined by the amine used in Figure 6 in conjunction with the halide atom attached to the boron source. More specifically, BLPs are given the moniker: BLP-#(X), where # represents a running counted number based on the timing of its discovery and successful synthesis, and X represents the chemical symbol of the halide attached to the borazine boron atom, Cl or Br. Extrapolation of this naming concept for each of the seven BLPs discussed within this research is shown in Table 2.

**Table 2.** Nomenclature of Borazine-Linked Polymers.

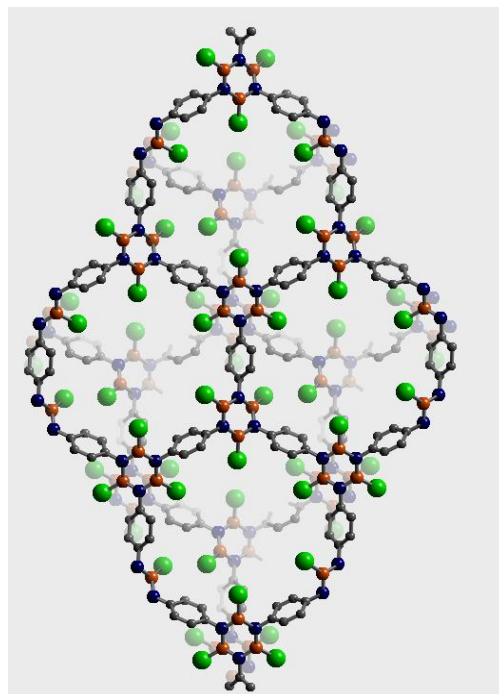
Amine	Boron Source	
	Boron Trichloride	Boron Tribromide
<i>p</i> -Phenylenediamine	BLP-1(Cl)	BLP-1(Br)
1,3,5-tris-(4-aminophenyl)benzene	BLP-2(Cl)	BLP-2(Br)
Benzidine	BLP-10(Cl)	BLP-10(Br)
tetra-(4-aminophenyl)methane	BLP-12(Cl)	

As will be discussed later, all seven polymers exist as amorphous material thus forbidding their characterization by powder XRD methods. Nevertheless, the expected porosity of each of the polymers can be considered with the understanding that such exercises would describe ordering that is of a short-range basis only. In the cases of the six polymers derived from *p*-phenylenediamine, 1,3,4-tris-(4-aminophenyl)benzene, and benzidine, polymer design examines the solid-state packing of two-dimensional sheets. In the case of BLP-12(Cl) which is derived from tetra-(4-aminophenyl)methane, the tetrahedral shape of the amine building unit prohibits the formation of two-dimensional sheets and exists optimally as what is referred to as a three-dimensional net.

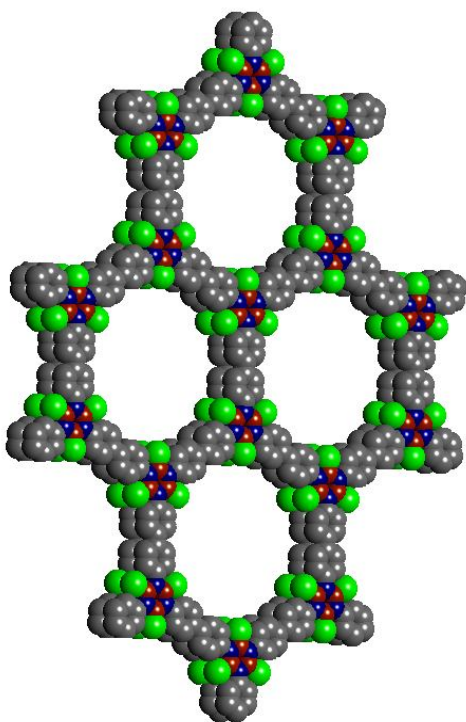
**Figure 7.** Model Structures of Eclipsed BLP-1(Cl) (A) and BLP-10(Cl) (C) and Their Respective Staggered Models, (B) and (D). Atomic colors represent: Cl (green), B (red), N (blue), and C (gray). Hydrogen is omitted for clarity.



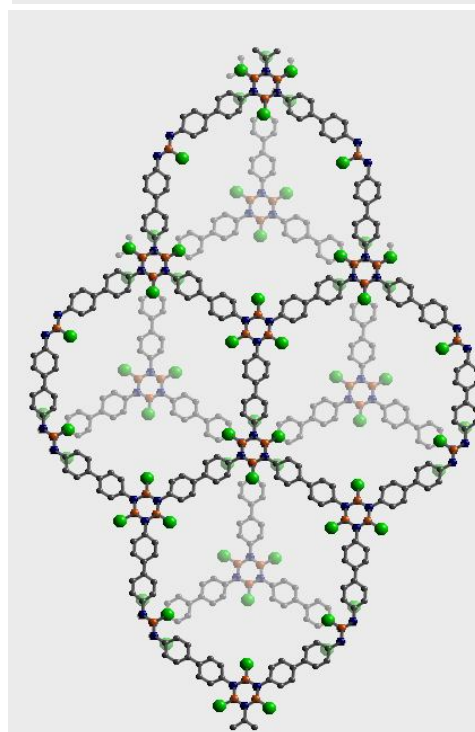
A



B



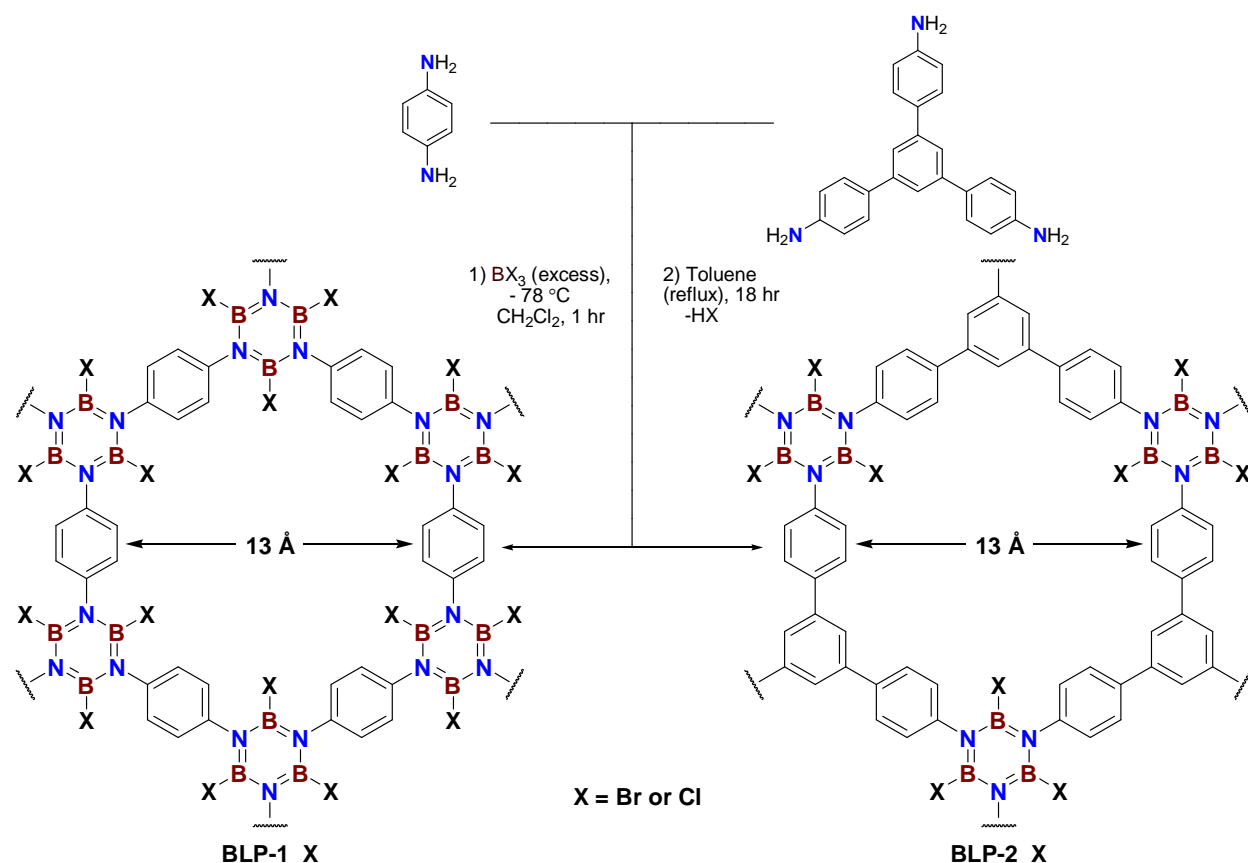
C



D

For both types of BLP-1 (Cl and Br) and both types of BLP-10, the packing of the two-dimensional sheets is expected to adopt an eclipsed conformation as in the case of boron nitride or a staggered conformation as observed for graphite and COF-1<sup>122, 207</sup> (Figure 7). In the case of both types of BLP-2, the packing of the two-dimensional sheets is expected to adopt a similar conformation of a derivative form of the eclipsed boron nitride topology or the staggered graphite topology as it is. The need for a derivative form of the eclipsed topology results from the differences in symmetry between the linear *p*-phenylenediamine/benzidine and the triangular 1,3,5-tris-(4-aminophenyl)benzene. The staggered graphite topology allows for this change in symmetry without the need to alter the space group of the crystal matrix. Nevertheless, the structural similarity between BLP-1(X) and BLP-2(X) are significant. From a theoretical standpoint, the structures differ in the “replacement” of half of the borazine rings in BLP-1(X) with benzene rings in BLP-2(X). As a result, each standard pore is decorated by only half as many halide atoms—six in the case of BLP-1(X) and three for BLP-2(X) (Figure 8).

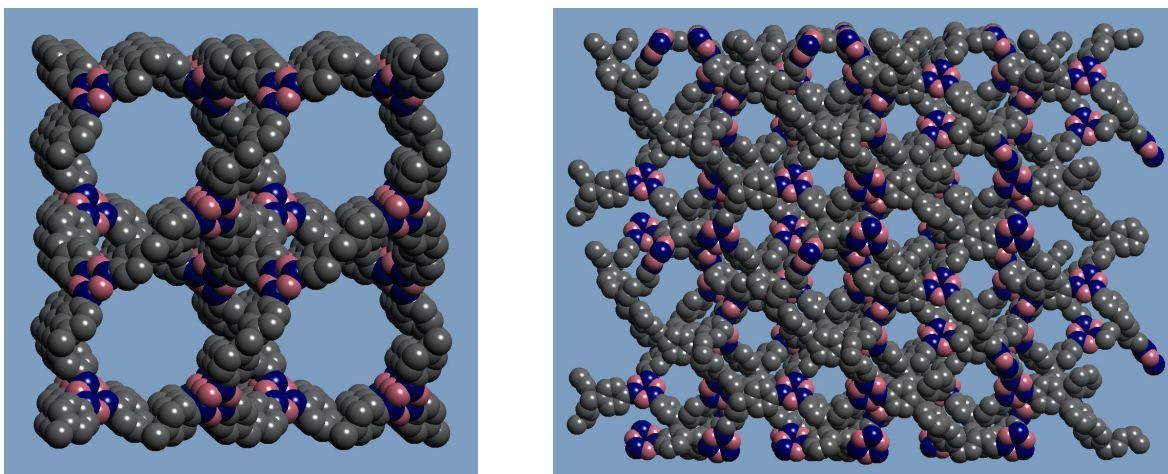
**Figure 8.** The Six Halide-Decorated Pore of BLP-1(X) (left) and the Three Halide-Decorated Pore of BLP-2(X) (right). Theoretical pore sizes are labeled.



All seven polymers were constructed and their energies minimized using *Materials Studio Visualizer* software,<sup>208</sup> their unit cell coordinates were then extracted by the *CrystalMaker for Windows* software<sup>209</sup> from on the *Materials Studio* models. BLP-1(Cl), BLP-1(Br), BLP-10(Cl), and BLP-10(Br) were modeled using boron nitride (**bnn**,  $\text{P6}/\text{mmm}$ ) or graphite (**gra**,  $\text{P6}_3/\text{mmc}$ ) topologies. Vertex positions were obtained from the Reticular Chemistry Structure Resource. The vertices were replaced by a borazine ( $\text{B}_3\text{N}_3$ ) ring with the nitrogen atoms pointing along the means of extension. The midpoint of each extension was replaced by benzene or biphenyl for BLP-1s and BLP-10s, respectively. BLP-2(Br) and BLP-2(Cl) models were constructed by a derivative

form of boron nitride using the space group  $P-6m2$  or graphite (**gra**,  $P6_3/mmc$ ) as it is. BLP-12(Cl) models were constructed using boracite (**bor**,  $P-43m$ ) and carbon nitride (**ctn**,  $I-43d$ ) topologies. Of important note is that the models for boracite and carbon nitride (Figure 9) are remarkably different from a visual standpoint than for the eclipsed and staggered conformations seen in the other six BLPs.

**Figure 9.** Boracite (left) and Carbon Nitride (right) Topologies for BLP-12(Cl). Atomic colors represent: B (pink), N (blue), and C (gray). Note that the chlorine and hydrogen atoms are not shown for clarity.



Through collaboration with Prof. Purusottam Jena, a better theoretical approximation for the solid state packing was gained for BLP-1(Cl) and BLP-10(Cl). The geometry of each model was optimized using the Vienna *ab initio* simulation package (VASP) and projector augmented wave (PAW) methods, and calculations were carried out using local density approximation (LDA) based on the density functional theory (DFT). High precision calculations with a cutoff energy of 400 eV for the plane-wave basis were used. The Brillouin zone integration was carried out using the special



Monkhorst-Pack sampling. There are 48 and 96 atoms in the eclipsed and staggered conformations of BLP-1(Cl), respectively, and 78 and 156 atoms in the eclipsed and staggered conformations of BLP-10(Cl), respectively. We have used  $3 \times 3 \times 15$ ,  $2 \times 2 \times 6$ ,  $1 \times 1 \times 7$ , and  $2 \times 2 \times 7$  k-points mesh in the Brillouin zone for the above structures. The total energies were converged to below 0.1 meV. Gaussian smearing was applied for relaxing the geometry. The optimization was considered to be converged when the total force on the atoms was less than 5 meV/Å. All four potential structures remain as layered hexagonal structures when the starting structure was taken to be planar. However, when the structure for each of these configurations was slightly distorted, the optimization led to distortion of the planar system (more specifically deviations of the benzene rings from planar) giving rise to structures with P1 symmetry. These distortions of the benzene rings led to a net energy gain for each of the structures and were the result of the minimization of the interactions between benzene and the large neighboring halide atoms.

From the molecular models obtained for all seven polymers, theoretical surface areas and pore sizes were calculated and are shown in Table 3. These surface areas, called Connolly surface areas, are derived by theoretically rolling a spherical ball about the accessible surface of the polymer to calculate the coverage. The larger the radius of this ball, the lower the apparent surface area becomes since the larger ball cannot access as many sites. In this case, a Connolly radius of 1.82 Å was used. It should be noted that the theoretical surface areas for BLP-1s, BLP-2s, and BLP-10s assume that the two-dimensional sheets stack uniformly in accordance with their respective topologies. Deviation from this stacking to any degree (as can be the case for

amorphous material) could result in the exposure of these sheets on the surface. As such, the experimental surface area could be higher than the theoretical values calculated from the molecular models. Unit cell coordinates for all atoms and topologies are shown in Tables 4-17.

**Table 3.** Theoretical Textural Properties of BLPs.

Polymer	Topology	Connolly Surface Area (m <sup>2</sup> g <sup>-1</sup> )	Theoretical Pore Size (nm)
BLP-1(Cl)	Eclipsed	1291	1.3
	Staggered	2252	0.6
BLP-1(Br)	Eclipsed	937	1.2
	Staggered	1644	0.6
BLP-2(Cl)	Eclipsed	1540	1.2
	Staggered	2659	0.6
BLP-2(Br)	Eclipsed	1230	1.2
	Staggered	2086	0.6
BLP-10(Cl)	Eclipsed	1661	2.1
	Staggered	3318	1.2
BLP-10(Br)	Eclipsed	1292	2.1
	Staggered	2509	1.2
BLP-12(Cl)	Boracite	3759	1.3
	Carbon Nitride	3949	1.0

**Table 4.** Fractional Atomic Coordinates for the Eclipsed Conformation of BLP-1(Br).

<b>BLP-1(Br)</b>			
Boron Nitride			
<i>P6/mmm</i>			
$a = b = 16.6630 \text{ \AA} ; c = 3.6529 \text{ \AA}$ $\alpha = \beta = 90^\circ ; \gamma = 120^\circ$			
Atom	<i>x</i>	<i>y</i>	<i>z</i>
B1	0.2807	0.5615	0.0000
Br1	0.7857	0.2142	0.0000
C1	0.4077	0.4572	0.0000
C2	0.4449	0.5551	0.0000
H1	0.4074	0.0685	0.0000
N1	0.7806	0.3903	0.0000

**Table 5.** Fractional Atomic Coordinates for the Staggered Conformation of BLP-1(Br).

<b>BLP-1(Br)</b>			
Graphite			
<i>P</i> 6 <sub>3</sub> / <i>mmc</i>			
$a = b = 15.7095 \text{ \AA} ; c = 6.8546 \text{ \AA}$ $\alpha = \beta = 90^\circ ; \gamma = 120^\circ$			
Atom	<i>x</i>	<i>y</i>	<i>z</i>
B1	0.3893	0.6107	0.2500
B2	0.1118	0.0559	0.2500
Br1	0.4633	0.5367	0.2500
Br2	0.1298	0.2595	0.7500
C1	0.1126	0.2252	0.2500
C2	0.2207	0.4414	0.2500
C3	0.2153	0.2820	0.2500
C4	0.2666	0.3846	0.2500
H1	0.5720	0.6550	0.2500
H2	0.7690	0.7560	0.2500
N1	0.0576	0.1153	0.2500
N2	0.2756	0.5512	0.2500

**Table 6.** Fractional Atomic Coordinates for the Eclipsed Conformation of BLP-1(Cl).

<b>BLP-1(Cl)</b>			
Boron Nitride			
<i>P6/mmm</i>			
$a = b = 16.4547 \text{ \AA} ; c = 3.5878 \text{ \AA}$ $\alpha = \beta = 90^\circ ; \gamma = 120^\circ$			
Atom	<i>x</i>	<i>y</i>	<i>z</i>
B1	0.2806	0.5612	0.0000
C1	0.4057	0.4555	0.0000
C2	0.4451	0.5549	0.0000
Cl1	0.7806	0.2194	0.0000
H1	0.4055	0.0706	0.0000
N1	0.7807	0.3903	0.0000

**Table 7.** Fractional Atomic Coordinates for the Staggered Conformation of BLP-1(Cl).

<b>BLP-1(Cl)</b>			
Graphite			
<i>P6<sub>3</sub>/mmc</i>			
$a = b = 16.5011 \text{ \AA} ; c = 6.8643 \text{ \AA}$			
$\alpha = \beta = 90^\circ ; \gamma = 120^\circ$			
Atom	<i>x</i>	<i>y</i>	<i>z</i>
B1	0.3838	0.6162	0.2500
B2	0.1007	0.0504	0.2500
C1	0.1092	0.2183	0.2500
C2	0.2234	0.4467	0.2500
C3	0.2098	0.2819	0.2500
C4	0.2609	0.3836	0.2500
Cl1	0.4423	0.5577	0.2500
Cl2	0.1097	0.2195	0.7500
H1	0.5951	0.6675	0.2500
H2	0.7398	0.7405	0.2500
N1	0.0538	0.1076	0.2500
N2	0.2796	0.5591	0.2500

**Table 8.** Fractional Atomic Coordinates for the Eclipsed Conformation of BLP-2(Br).

<b>BLP-2(Br)</b>			
Boron Nitride Derivative			
P-6m2			
a = b = 15.7273 Å ; c = 3.6481 Å $\alpha = \beta = 90^\circ$ ; $\gamma = 120^\circ$			
Atom	x	y	z
B1	0.4407	0.7204	0.0000
Br1	0.5783	0.7891	0.0000
C1	0.5654	0.2827	0.0000
C2	0.6145	0.2290	0.0000
C3	0.5532	0.5927	0.0000
C4	0.6054	0.5423	0.0000
C5	0.5590	0.4410	0.0000
C6	0.4481	0.5519	0.0000
H1	0.4120	0.3157	0.0000
H2	0.3365	0.3901	0.0000
H3	0.7558	0.5116	0.0000
N1	0.3901	0.6099	0.0000

**Table 9.** Fractional Atomic Coordinates for the Staggered Conformation of BLP-2(Br).

<b>BLP-2(Br)</b>			
Graphite			
<i>P6<sub>3</sub>/mmc</i>			
$a = b = 15.5929 \text{ \AA} ; c = 7.1543 \text{ \AA}$			
$\alpha = \beta = 90^\circ ; \gamma = 120^\circ$			
Atom	<i>x</i>	<i>y</i>	<i>z</i>
B1	0.3836	0.6164	0.2500
Br1	0.4469	0.5530	0.2500
C1	0.0525	0.1050	0.2500
C2	0.1083	0.2166	0.2500
C3	0.2206	0.4412	0.2500
C4	0.1018	0.0509	0.2500
C5	0.2108	0.2716	0.2500
C6	0.2614	0.3753	0.2500
H1	0.0895	0.1791	0.7500
H2	0.6113	0.6666	0.2500
H3	0.7628	0.7434	0.2500
N1	0.2787	0.5575	0.2500



**Table 10.** Fractional Atomic Coordinates for the Eclipsed Conformation of BLP-2(Cl).

<b>BLP-2(Cl)</b>			
Boron Nitride Derivative			
P-6 $m$ 2			
$a = b = 15.5253 \text{ \AA} ; c = 3.6681 \text{ \AA}$ $\alpha = \beta = 90^\circ ; \gamma = 120^\circ$			
Atom	$x$	$y$	$z$
B1	0.4411	0.7206	0.0000
C1	0.5647	0.2824	0.0000
C2	0.6143	0.2286	0.0000
C3	0.5539	0.5946	0.0000
C4	0.6067	0.5441	0.0000
C5	0.5587	0.4413	0.0000
C6	0.4478	0.5522	0.0000
Cl1	0.5708	0.7854	0.0000
H1	0.4085	0.3131	0.0000
H2	0.3331	0.3898	0.0000
H3	0.7564	0.5129	0.0000
N1	0.3900	0.6100	0.0000

**Table 11.** Fractional Atomic Coordinates for the Staggered Conformation of BLP-2(Cl).

<b>BLP-2(Cl)</b>			
Graphite			
<i>P6<sub>3</sub>/mmc</i>			
$a = b = 15.5267 \text{ \AA} ; c = 7.1876 \text{ \AA}$			
$\alpha = \beta = 90^\circ ; \gamma = 120^\circ$			
Atom	<i>x</i>	<i>y</i>	<i>z</i>
B1	0.3835	0.6165	0.2500
C1	0.0528	0.1056	0.2500
C2	0.1089	0.2179	0.2500
C3	0.2211	0.4422	0.2500
C4	0.1026	0.0513	0.2500
C5	0.2124	0.2730	0.2500
C6	0.2635	0.3774	0.2500
Cl1	0.4426	0.5574	0.2500
H1	0.0902	0.1804	0.7500
H2	0.6057	0.6627	0.2500
H3	0.7615	0.7412	0.2500
N1	0.2790	0.5580	0.2500

**Table 12.** Fractional Atomic Coordinates for the Eclipsed Conformation of BLP-10(Br).

<b>BLP-10(Br)</b>			
Boron Nitride			
<i>P6/mmm</i>			
$a = b = 24.2265 \text{ \AA} ; c = 3.6143 \text{ \AA}$ $\alpha = \beta = 90^\circ ; \gamma = 120^\circ$			
Atom	<i>x</i>	<i>y</i>	<i>z</i>
B1	0.2972	0.5945	0.0000
Br1	0.4968	0.7484	0.0000
C1	0.8196	0.4098	0.0000
C2	0.8610	0.3827	0.0000
C3	0.9281	0.4158	0.0000
C4	0.9638	0.4819	0.0000
H1	0.8504	0.3359	0.0000
H2	0.9510	0.3874	0.0000
N1	0.7447	0.3724	0.0000

**Table 13.** Fractional Atomic Coordinates for the Staggered Conformation of BLP-10(Br).

<b>BLP-10(Br)</b>			
Graphite			
<i>P6<sub>3</sub>/mmc</i>			
$a = b = 24.0402 \text{ \AA} ; c = 6.7035 \text{ \AA}$			
$\alpha = \beta = 90^\circ ; \gamma = 120^\circ$			
Atom	<i>x</i>	<i>y</i>	<i>z</i>
B1	0.9638	0.9276	0.2500
B2	0.3695	0.7390	0.2500
Br1	0.5847	0.4153	0.7500
Br2	0.9176	0.8352	0.2500
C1	0.1448	0.9507	0.2500
C2	0.1485	0.8515	0.2500
C3	0.1847	0.8153	0.2500
C4	0.2568	0.7432	0.2500
C5	0.1788	0.9176	0.2500
C6	0.1543	0.7492	0.2500
C7	0.1883	0.7161	0.2500
C8	0.0764	0.9236	0.2500
H1	0.1806	0.9973	0.2500
H2	0.2301	0.9460	0.2500
H3	0.1030	0.7208	0.2500
H4	0.1523	0.6693	0.2500
N1	0.0390	0.9610	0.2500
N2	0.2942	0.7058	0.2500

**Table 14.** Fractional Atomic Coordinates for the Eclipsed Conformation of BLP-10(Cl).

<b>BLP-10(Cl)</b>			
Boron Nitride			
<i>P6/mmm</i>			
$a = b = 24.0391 \text{ \AA} ; c = 3.5633 \text{ \AA}$ $\alpha = \beta = 90^\circ ; \gamma = 120^\circ$			
Atom	<i>x</i>	<i>y</i>	<i>z</i>
B1	0.2973	0.5946	0.0000
C1	0.8192	0.4096	0.0000
C2	0.8601	0.3814	0.0000
C3	0.9276	0.4150	0.0000
C4	0.9635	0.4817	0.0000
Cl1	0.4894	0.7447	0.0000
H1	0.8475	0.3333	0.0000
H2	0.9506	0.3863	0.0000
N1	0.7445	0.3722	0.0000

**Table 15.** Fractional Atomic Coordinates for the Staggered Conformation of BLP-10(Cl).

<b>BLP-10(Cl)</b>			
Graphite			
<i>P6<sub>3</sub>/mmc</i>			
a = b = 24.0402 Å ; c = 6.7035 Å			
$\alpha = \beta = 90^\circ$ ; $\gamma = 120^\circ$			
Atom	x	y	z
B1	0.9639	0.9279	0.2500
B2	0.3694	0.7388	0.2500
C1	0.1452	0.9520	0.2500
C2	0.1483	0.8517	0.2500
C3	0.1849	0.8151	0.2500
C4	0.2570	0.7430	0.2500
C5	0.1792	0.9184	0.2500
C6	0.1540	0.7484	0.2500
C7	0.1879	0.7148	0.2500
C8	0.0762	0.9238	0.2500
Cl1	0.5886	0.4114	0.7500
Cl2	0.9218	0.8435	0.2500
H1	0.1807	0.9999	0.2500
H2	0.2309	0.9472	0.2500
H3	0.1023	0.7197	0.2500
H4	0.1524	0.6667	0.2500
N1	0.0389	0.9611	0.2500
N2	0.2944	0.7056	0.2500

**Table 16:** Fractional Atomic Coordinates for the Boracite Conformation of BLP-12(Cl).

<b>BLP-12(Cl)</b>			
Boracite			
<i>P</i> -43 <i>m</i>			
$a = b = c = 18.0042 \text{ \AA}$ $\alpha = \beta = \gamma = 90^\circ$			
Atom	<i>x</i>	<i>y</i>	<i>z</i>
B1	0.2162	0.8826	0.7838
C1	0.6845	0.8892	0.1108
C2	0.5000	0.0000	0.0000
C3	0.6483	0.8574	0.0479
C4	0.5854	0.8892	0.0163
C5	0.5538	0.9535	0.0465
Cl	0.7126	0.2874	0.8908
H1	0.0320	0.1371	0.5600
H2	0.6643	0.8059	0.0226
N1	0.1411	0.8589	0.7543

**Table 17:** Fractional Atomic Coordinates for the Carbon Nitride Conformation of BLP-12(Cl).

<b>BLP-12(Cl)</b>			
Carbon Nitride			
<i>I</i> -43d			
a = b = c = 27.1429 Å			
$\alpha = \beta = \gamma = 90^\circ$			
Atom	x	y	z
B1	0.1934	0.1648	0.2409
C1	0.3750	0.0000	0.2500
C2	0.3020	0.8758	0.2448
C3	0.2708	0.8806	0.2855
C4	0.3073	0.9608	0.3023
C5	0.3402	0.9560	0.2624
C6	0.2744	0.9230	0.3151
C7	0.3366	0.9123	0.2338
Cl1	0.1372	0.5702	0.0260
H1	0.4423	0.9267	0.2448
H2	0.2577	0.9269	0.3477
H3	0.3577	0.9068	0.2007
H4	0.2981	0.8441	0.2205
N1	0.2340	0.8435	0.2948



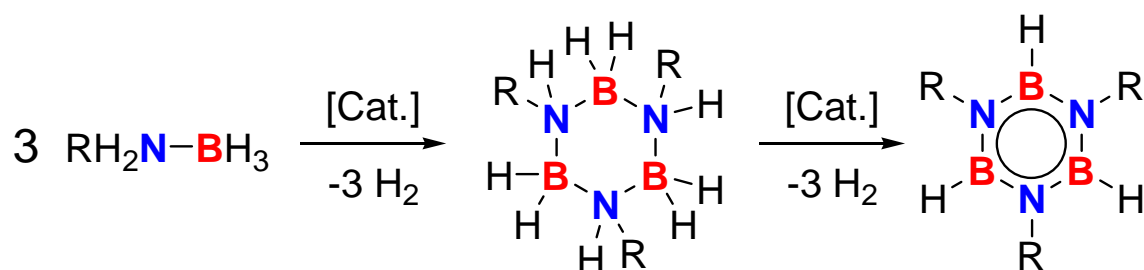
## Chapter 3

### Synthesis of Halogenated Borazine-Linked Polymers

#### 3.1 Introduction

As mentioned earlier in Chapter 1, borazine rings have been synthesized previously through a diverse range of procedures. Among the many methods is through the catalytic dehydrocoupling reaction of amine borane adducts exemplified by Manners and coworkers.<sup>170, 173</sup> Through their research, they showed that this dehydrocoupling could proceed through a variety of catalytic systems utilizing rhodium, palladium, titanium or iridium to name a few. According to Manners, the formation of borazine is expected to proceed through a double stepwise loss of hydrogen (Figure 10).

**Figure 10.** Catalytic Dehydrocoupling of Amine-Borane Adducts.



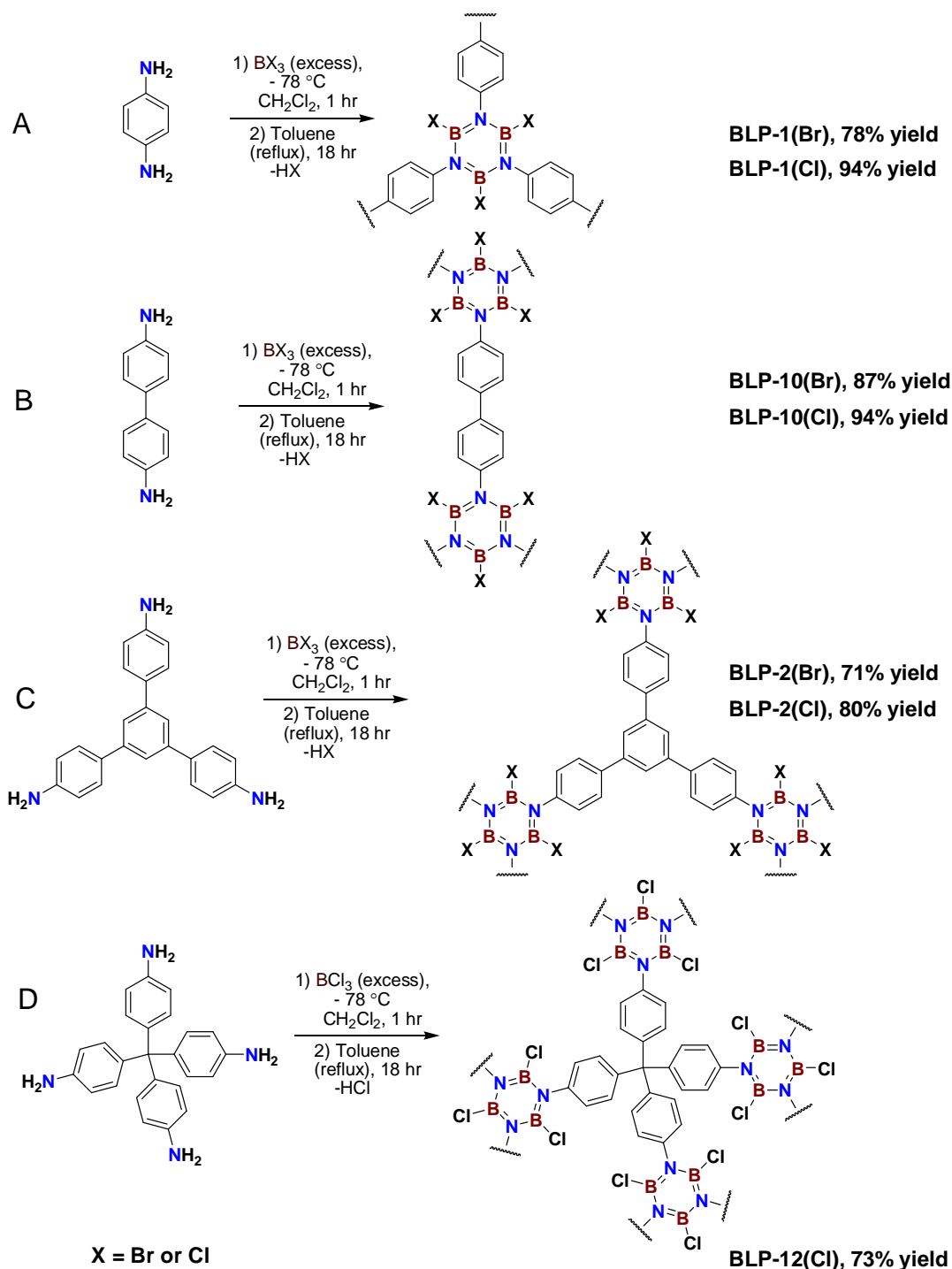
For the first step, one boron-based and one nitrogen-based hydrogen atom per adduct combine to yield a *borazane* ring whereby the six-membered ring is composed entirely of tetra-coordinated atoms. In the second step, a repetition of the dihydrogen

elimination from the *borazane* ring results in the formation of a *borazine* ring. For Manners' work, these reactions were performed at either 25°C or 45°C. More recently, however, the work of Karl Jackson and Hani El-Kaderi at Virginia Commonwealth University showed that the dehydrocoupling of amine-borane adducts can proceed catalyst-free with a sufficient increase in temperature (120°C) to afford highly porous BLPs up to about 2980 m<sup>2</sup>/g.<sup>210</sup>

### 3.2 Synthesis of Halogenated Borazine-Linked Polymers

Monomeric halogen-functionalized borazine molecules analogous to the polymeric BLPs have been prepared previously by the thermal decomposition of aryl amines-boron trihalides in aprotic solvents at elevated temperatures.<sup>211-213</sup> The synthetic strategies for the preparation of BLPs are summarized in Figure 11 and have been recently reported for four of the seven species in literature.<sup>214</sup> 1,3,5-tris-(4-aminophenyl)benzene and tetra-(4-aminophenyl)methane were synthesized according to previously reported procedures.<sup>215-217</sup> All other starting materials were obtained from Thermo Fisher Scientific Inc. and used without further purification. Dichloromethane and dichloroethane was distilled from calcium hydride, and toluene was distilled from sodium. All products were handled under a nitrogen atmosphere using glovebox and Schlenk line techniques. All yields reported represent un-optimized synthesis.

**Figure 11.** Synthetic Strategies for the Formation of BLPs. Reactions were performed through the thermolysis of *p*-phenylenediamine (A), benzidine (B), 1,3,5-tris-(4-aminophenyl)benzene (C), or tetra-(4-aminophenyl)methane (D) boron trihalide adducts.



**Preparation of BLP-1(Br).** *p*-Phenylenediamine (0.30 g, 2.77 mmol) was dissolved in 60 mL of dry dichloromethane under a nitrogen atmosphere and cooled to -78 °C. While stirring, 6.5 mL of 1M boron tribromide (6.5 mmol) in dichloromethane was added. After 30 minutes of stirring, all of the dichloromethane was removed under reduced pressure and replaced with 60 mL of dry toluene. The mixture was refluxed overnight and taken into a glovebox. The white solid was filtered over a medium glass frit and rinsed with dry dichloromethane. The product was soaked in dry dichloromethane for 24 hours at which point the solvent was decanted, and fresh, dry dichloromethane was replenished. Decantation and addition of fresh solvent was repeated once more. The solid was then activated at 80 °C under reduced pressure for 18 hours to afford **BLP-1(Br)** (0.62 g, 78%) as a white solid. Anal. Calcd. for  $C_{18}H_{12}B_6N_6Br_6$ : C, 25.24; H, 1.41; N, 9.81. Found: C, 27.65; H, 2.26; N, 9.97.

**Preparation of BLP-1(Cl).** In a similar fashion to BLP-1(Br), 0.30 g (2.77 mmol) of *p*-phenylenediamine was dissolved in 60 mL of dry dichloromethane under a nitrogen atmosphere and cooled to -78 °C. While stirring, 6.5 mL of 1M boron trichloride (6.5 mmol) in dichloromethane was added. After 30 minutes of stirring, all of the dichloromethane was removed under reduced pressure and replaced with 60 mL of dry toluene. The mixture was refluxed overnight and taken into a glovebox. The white solid was filtered over a medium glass frit and rinsed with dry dichloromethane. The product was soaked in dry dichloromethane for 24 hours at which point the solvent was decanted, and fresh, dry dichloromethane was replenished. Decantation and addition of fresh solvent was repeated once more. The solid was then activated at 80 °C under reduced pressure for 18 hours to afford **BLP-1(Cl)** (0.51 g, 94%) as a white solid. Anal.

Calcd. for  $C_{18}H_{12}B_6N_6Cl_6$ : C, 36.65; H, 2.05; N, 14.25. Found: C, 37.77; H, 2.87; N, 13.12.

**Preparation of BLP-2(Br).** In a similar fashion to BLP-1(Br), 0.30 g (0.85 mmol) of 1,3,5-tris-(4-aminophenyl)benzene was dissolved in 60 mL of dry dichloromethane under a nitrogen atmosphere and cooled to  $-78^{\circ}C$ . While stirring, 4.0 mL of 1M boron tribromide (4.0 mmol) in dichloromethane was added. After 30 minutes of stirring, all of the dichloromethane was removed under reduced pressure and replaced with 60 mL of dry toluene. The mixture was refluxed overnight and taken into a glovebox. The off-white solid was filtered over a medium glass frit and rinsed with dry dichloromethane. The product was soaked in dry dichloromethane for 24 hours at which point the solvent was decanted, and fresh, dry dichloromethane was replenished. Decantation and addition of fresh solvent was repeated once more. The solid was then activated at  $80^{\circ}C$  under reduced pressure for 18 hours to afford **BLP-2(Br)** (0.32 g, 71%) as an off-white solid. Anal. Calcd. for  $C_{24}H_{15}B_3N_3Br_3$ : C, 46.68; H, 2.45; N, 6.81. Found: C, 48.83; H, 2.95; N, 6.89.

**Preparation of BLP-2(Cl).** In a similar fashion to BLP-2(Br), 0.30 g (0.85 mmol) of 1,3,5-tris-(4-aminophenyl)benzene was dissolved in 60 mL of dry dichloromethane under a nitrogen atmosphere and cooled to  $-78^{\circ}C$ . While stirring, 4.0 mL of 1M boron trichloride (4.0 mmol) in dichloromethane was added. After 30 minutes of stirring, all of the dichloromethane was removed under reduced pressure and replaced with 60 mL of dry toluene. The mixture was refluxed overnight and taken into a glovebox. The off-white solid was filtered over a medium glass frit and rinsed with dry dichloromethane. The product was soaked in dry dichloromethane for 24 hours at which point the solvent

was decanted, and fresh, dry dichloromethane was replenished. Decantation and addition of fresh solvent was repeated once more. The solid was then activated at 80 °C under reduced pressure for 18 hours to afford **BLP-2(Cl)** (0.30 g, 80%) as an off-white solid. Anal. Calcd. for  $C_{24}H_{15}B_3N_3Cl_3$ : C, 59.53; H, 3.12; N, 8.68. Found: C, 58.90; H, 3.66; N, 8.49.

**Preparation of BLP-10(Br).** In a similar fashion to BLP-1(Br), 0.30 g (1.63 mmol) of benzidine was dissolved in 60 mL of dry dichloromethane under a nitrogen atmosphere and cooled to -78°C. While stirring, 5.0 mL of 1M boron trichloride (5.0 mmol) in dichloromethane was added. After 30 minutes of stirring, all of the dichloromethane was removed under reduced pressure and replaced with 60 mL of dry toluene. The mixture was refluxed overnight and taken into a glovebox. The white solid was filtered over a medium glass frit and rinsed with dry dichloromethane. The product was soaked in dry dichloromethane for 24 hours at which point the solvent was decanted, and fresh, dry dichloromethane was replenished. Decantation and addition of fresh solvent was repeated once more. The solid was then activated at 80 °C under reduced pressure for 18 hours to afford **BLP-10(Br)** (0.51 g, 87%) as a white solid. Anal. Calcd. for  $C_{36}H_{24}B_6N_6Br_6$ : C, 39.85; H, 2.23; N, 7.75. Found: C, 40.97; H, 2.66; N, 7.32.

**Preparation of BLP-10(Cl).** In a similar fashion to BLP-10(Br), 0.30 g (1.63 mmol) of benzidine was dissolved in 60 mL of dry dichloromethane under a nitrogen atmosphere and cooled to -78°C. While stirring, 5.0 mL of 1M boron trichloride (5.0 mmol) in dichloromethane was added. After 30 minutes of stirring, all of the dichloromethane was removed under reduced pressure and replaced with 60 mL of dry toluene. The mixture was refluxed overnight and taken into a glovebox. The white solid

was filtered over a medium glass frit and rinsed with dry dichloromethane. The product was soaked in dry dichloromethane for 24 hours at which point the solvent was decanted, and fresh, dry dichloromethane was replenished. Decantation and addition of fresh solvent was repeated once more. The solid was then activated at 80 °C under reduced pressure for 18 hours to afford **BLP-10(Cl)** (0.42 g, 94%) as a white solid. Anal. Calcd. for  $C_{36}H_{24}B_6N_6Cl_6$ : C, 52.84; H, 2.96; N, 10.27. Found: C, 52.92; H, 3.40; N, 10.37.

**Preparation of BLP-12(Cl).** In a similar fashion to BLP-10(Cl), 0.15 g (0.394 mmol) of tetra-(4-aminophenyl)methane was dissolved in 180 mL of dry dichloroethane under a nitrogen atmosphere. While stirring, 5.0 mL of 1M boron trichloride (5.0 mmol) in hexane was added. After 2 hours of stirring, all of the dichloroethane was removed under reduced pressure and replaced with 60 mL of dry toluene. The mixture was refluxed overnight and taken into a glovebox. The white solid was filtered over a medium glass frit and rinsed with dry dichloromethane. The product was soaked in dry dichloromethane for 24 hours at which point the solvent was decanted, and fresh, dry dichloromethane was replenished. Decantation and addition of fresh solvent was repeated once more. The solid was then activated at 80 °C under reduced pressure for 18 hours to afford **BLP-12(Cl)** (0.16 g, 73%) as a white solid. Anal. Calcd. for  $C_{75}H_{48}B_{12}N_{12}Cl_{12}$ : C, 53.86; H, 2.89; N, 10.05. Found: C, 51.52; H, 3.39; N, 9.20.

### 3.3 Characterization of Halogenated Borazine-Linked Polymers

The chemical composition and structural aspects of these polymers were investigated by spectral and analytical methods. SEM samples were prepared by dispersing the material onto a sticky carbon surface attached to a flat aluminum sample

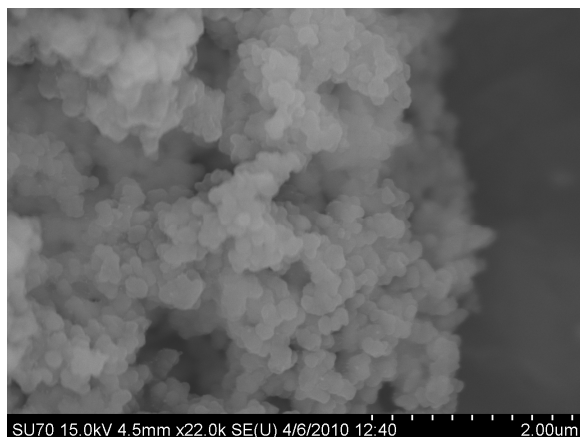
holder. The samples were then gold coated using an EMS (Electron Microscopy Sciences) 550x Sputter Coater at  $1 \times 10^{-1}$  mbar of pressure in a nitrogen atmosphere for 120 seconds while maintaining 20 mA of current. Samples were analyzed on a Zeiss EVO XVP Scanning Electron Microscope using the SEI detector with accelerating voltages ranging from 10 kV to 20 kV. FT-IR spectra were obtained as KBr pellets using a Nicolet Nexus 670 FT-IR spectrometer. Representative solid-state nuclear magnetic resonance (NMR) spectra were recorded at ambient temperature on a Bruker DSX-300 spectrometer using a Bruker magic angle spinning (MAS) probe with 4 mm (O.D.) 80  $\mu$ L volume zirconia rotors with Kel-F drive caps. Thermogravimetric analysis was obtained using a TA Instruments TGA Q5000 analyzer with 50  $\mu$ L platinum pans to assess the thermal stability of each borazine-linked polymer. Experiments were run at a ramp rate of 5 K/minute under a nitrogen atmosphere.

Unlike COFs, all BLPs are amorphous which precluded their investigation by XRD technique. Despite the structural similarity between the borazine building units in BLPs and the boroxine building units in COFs, the reactive nature of the boron-halide bonds might promote the formation of cross-linked and hyper-branched polymers. This kind of reactivity in addition to the more robust boron-nitrogen linkage might be the reasons behind the amorphous nature of all BLPs. Additionally, the large halide atoms might sterically preclude the close stacking of two-dimensional sheets typically found in crystalline COFs. This stacking aversion would result in more accessible sheets and explain why BLPs generally exhibit higher surface areas than their analogous COFs as will be detailed in Chapter 4. The scanning electron microscopy (SEM) images (Figure 12) showed that these polymers exist as irregular particles of about 200 to 500 nm in

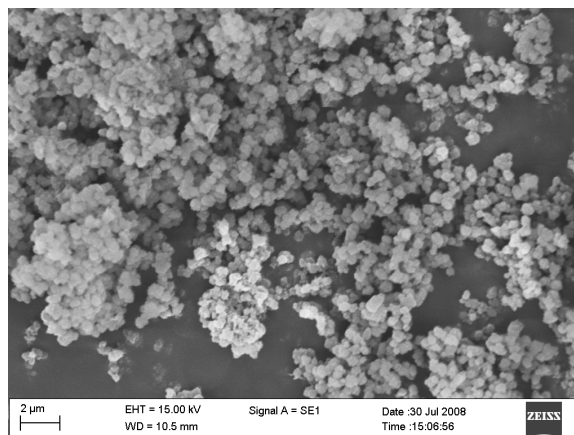


size. Within these images, the bright sections of the polymer are the result of charging effects from the gold coating whereby sections of gold which are inherently closer in proximity to the electron source within the instrument exhibit heightened intensities in brightness.

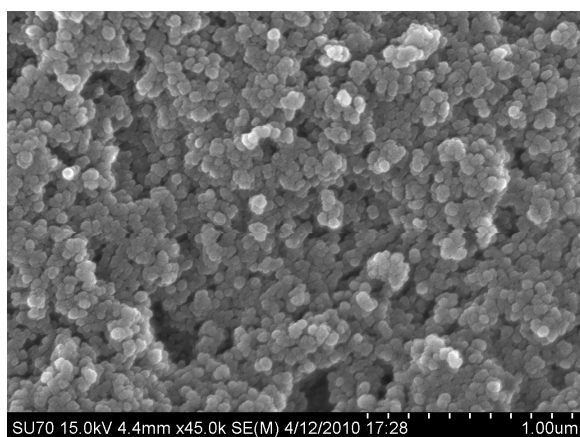
**Figure 12.** Scanning Electron Microscopy Images of BLPs.



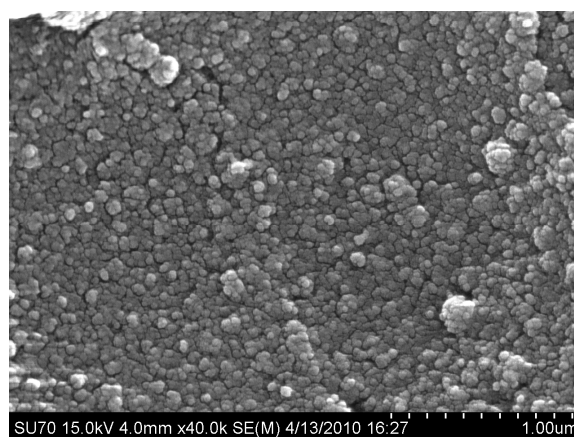
BLP-1(Br)



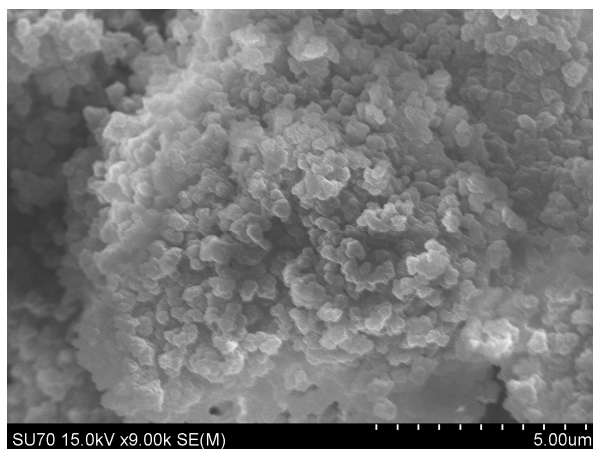
BLP-1(Cl)



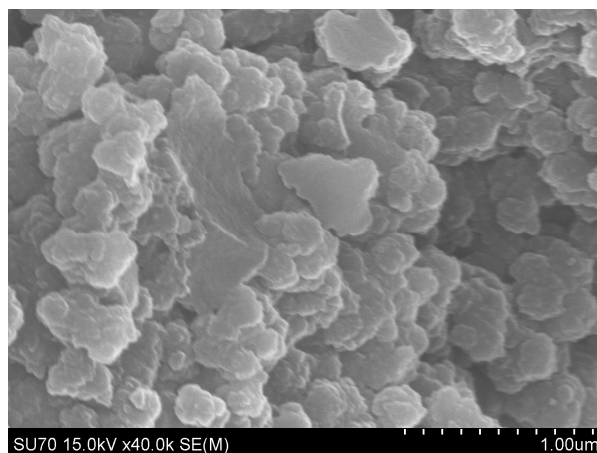
BLP-2(Br)



BLP-2(Cl)



BLP-10(Br)



BLP-10(Cl)



BLP-12(Cl)

To establish the chemical connectivity and geometry of the boron sites, we collected FT-IR spectra and carried out solid-state  $^{11}\text{B}$  multiple quantum magic angle spinning (MQMAS) NMR experiments. FT-IR spectra were collected for all amine starting material (Figures 13-16) and their respective BLPs (Figures 17, 19, 21, 23, 25, 27, and 29) in addition to comparative overlays (Figures 18, 20, 22, 24, 26, 28, and 30). FT-IR spectra show significant depletion of the stretching and bending bands of the amine protons around  $3420\text{ cm}^{-1}$  and  $1610\text{ cm}^{-1}$ , respectively, and the formation of new bands  $\sim 1400$  and  $1000\text{ cm}^{-1}$  which are characteristic of the  $\text{B}_3\text{N}_3$  ring.<sup>218-220</sup>

**Figure 13.** FT-IR Spectrum of *p*-Phenylenediamine.

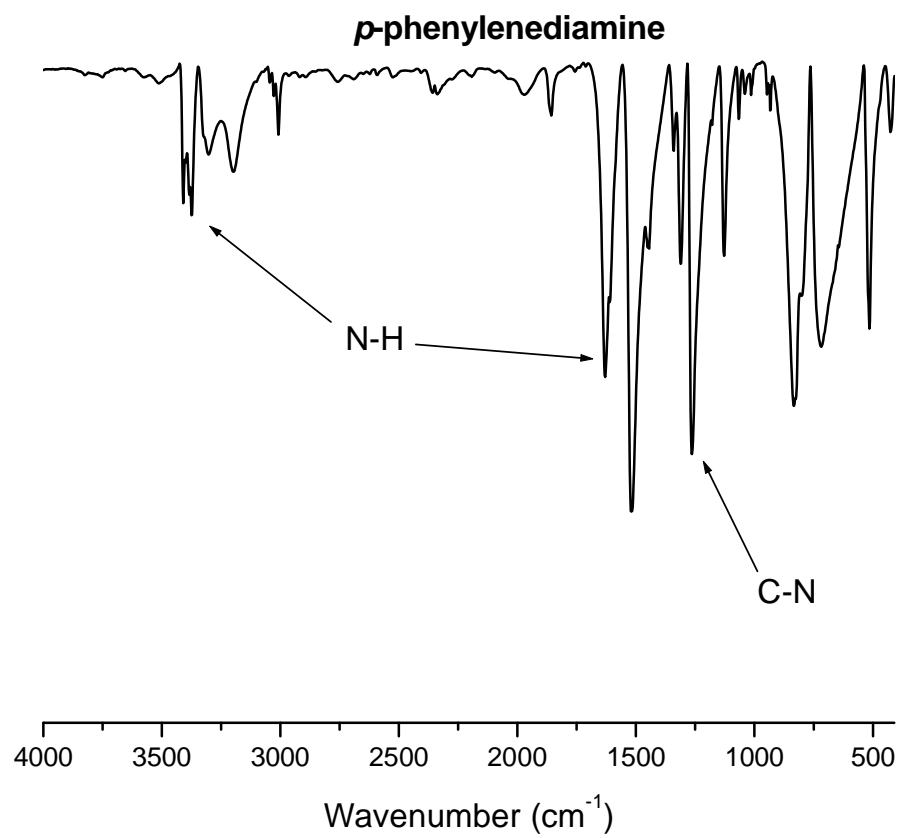


**Figure 14.** FT-IR Spectrum of Benzidine.

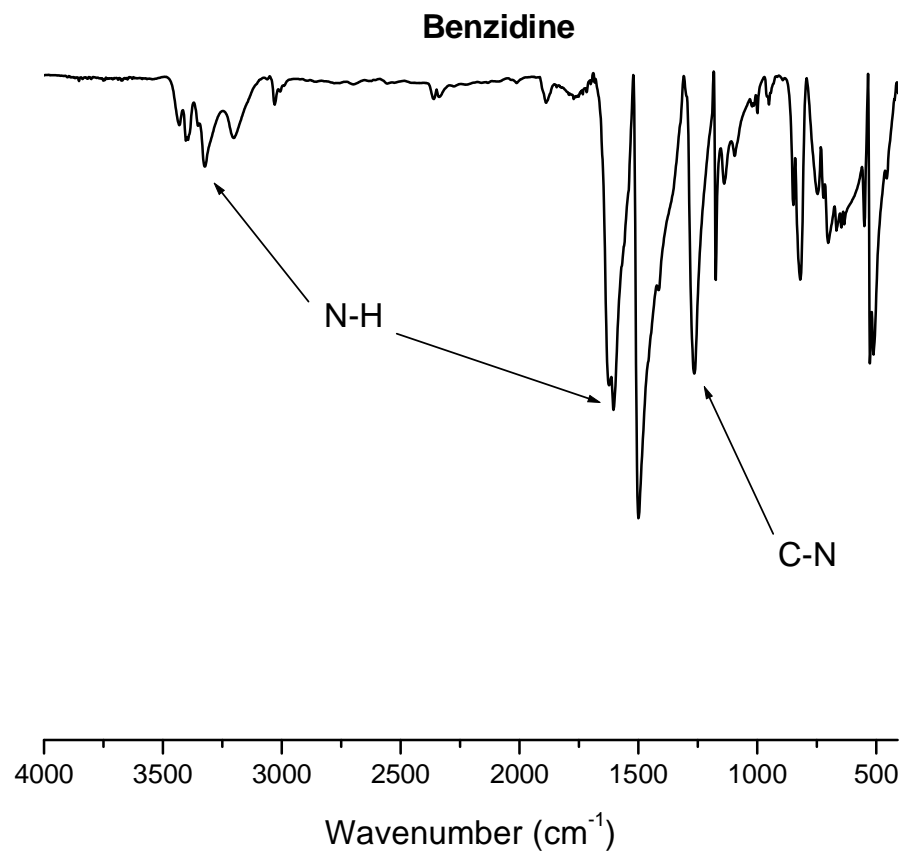


**Figure 15.** FT-IR Spectrum of 1,3,5-tris-(4-aminophenyl)benzene.

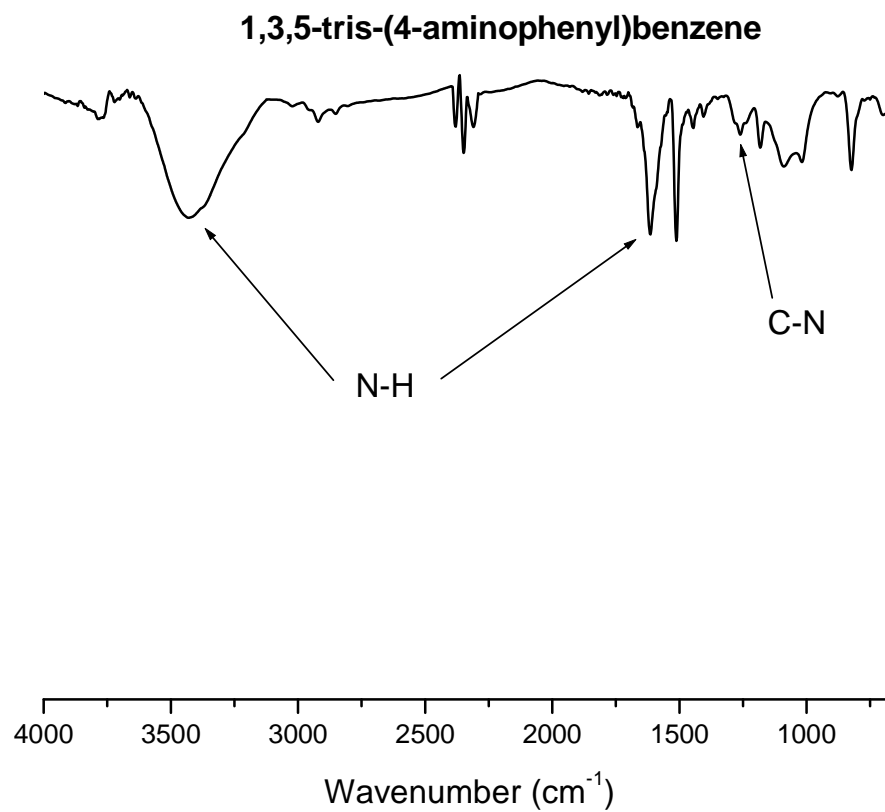


**Figure 16.** FT-IR Spectrum of tetra-(4-aminophenyl)methane.

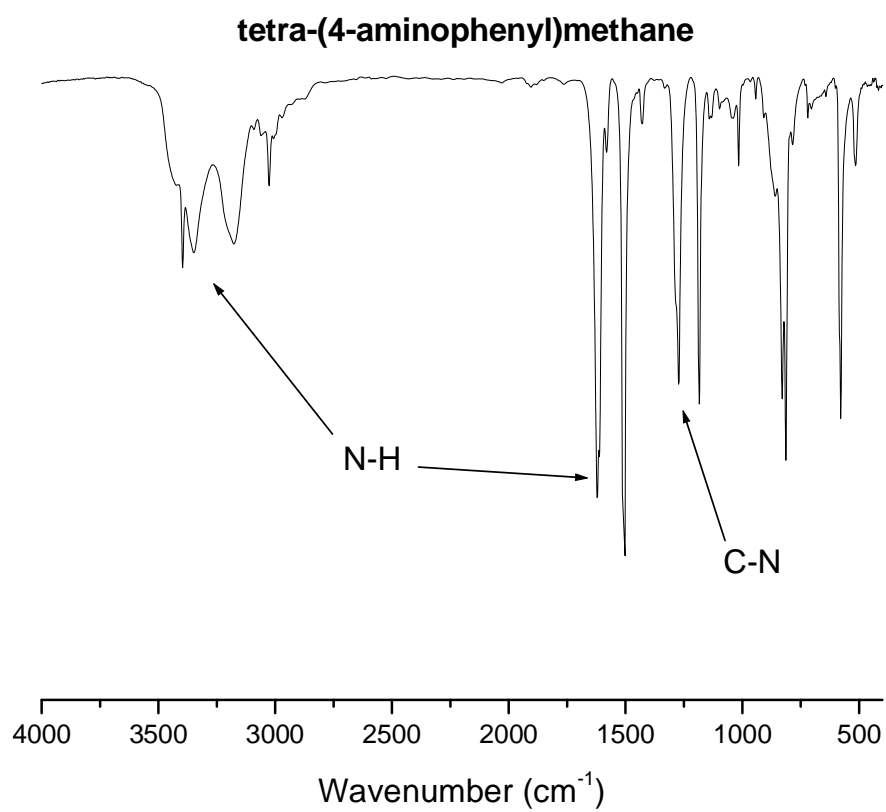


**Figure 17.** FT-IR Spectrum of BLP-1(Br). The C-N band at about  $1250\text{ cm}^{-1}$  overlaps with the large B-N band at about  $1400\text{ cm}^{-1}$ .

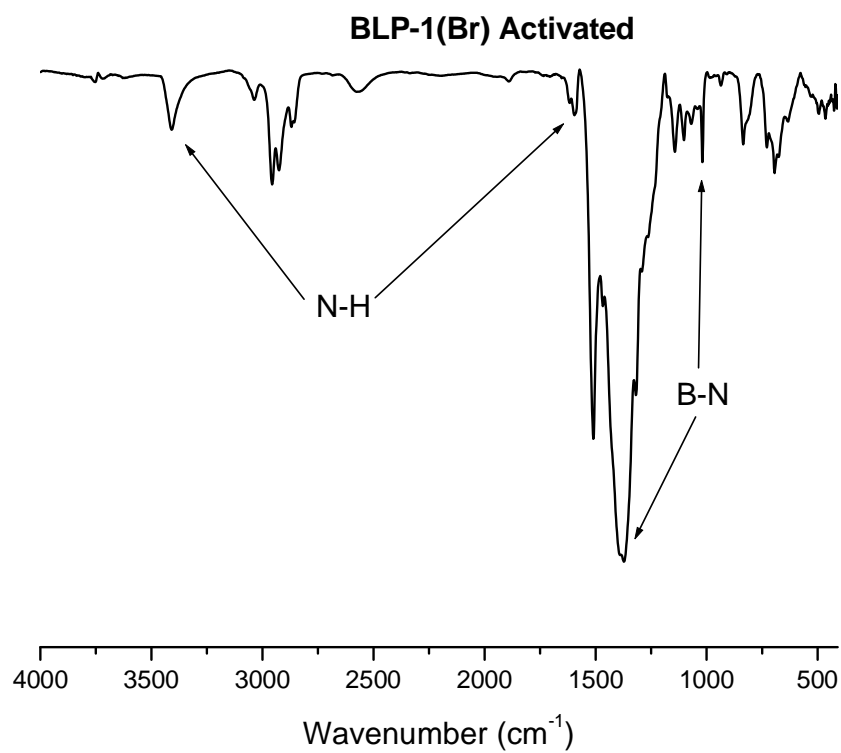




**Figure 18.** IR Spectra of BLP-1(Br) with Its Starting Material, p-phenylenediamine. The largely diminished amine stretching and bending bands indicate the consumption of the starting material, p-phenylenediamine. The peaks around 1400 and 1000  $\text{cm}^{-1}$  (blue arrows) indicate the closing into the ring system borazine.

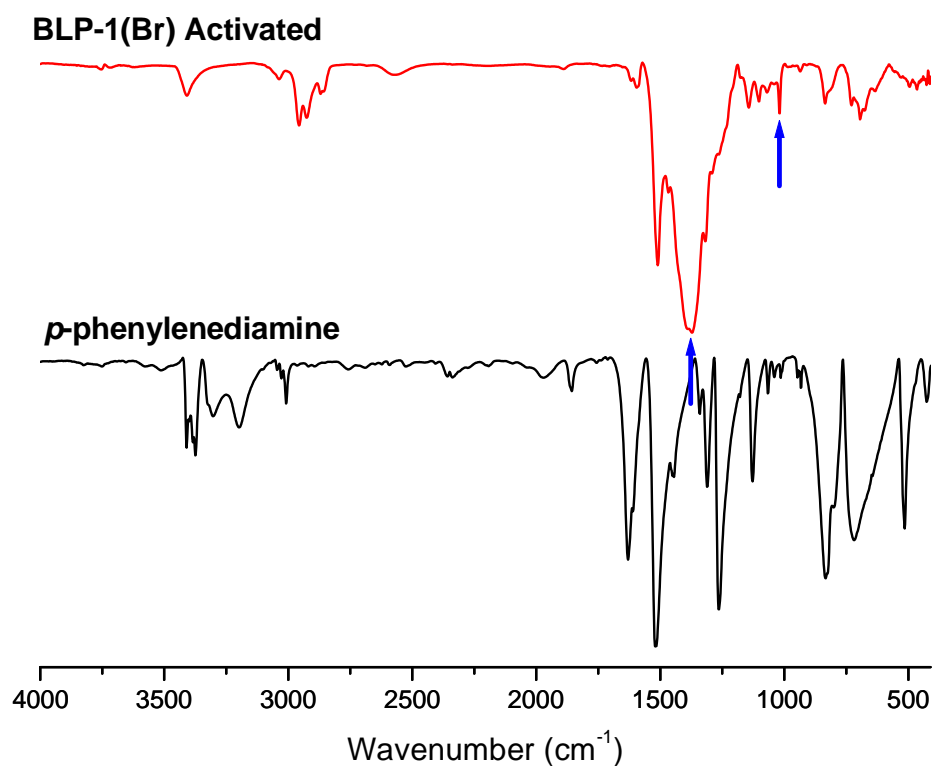


**Figure 19.** FT-IR Spectrum of BLP-1(Cl). The C-N band at about  $1250\text{ cm}^{-1}$  overlaps with the large B-N band at about  $1400\text{ cm}^{-1}$ .

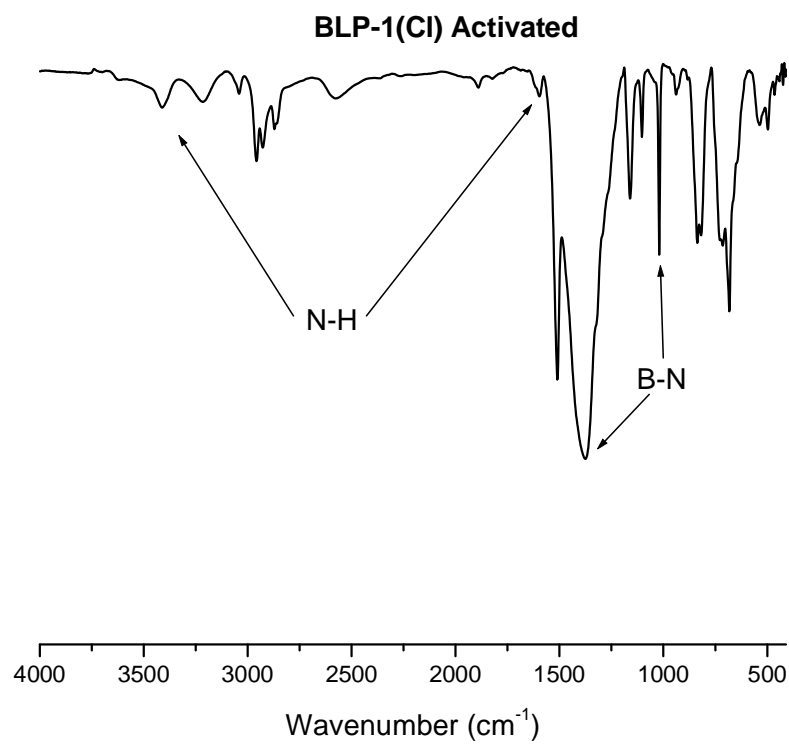


**Figure 20.** IR Spectra of BLP-1(Cl) with Its Starting Material, p-phenylenediamine. The largely diminished amine stretching and bending bands indicate the consumption of the starting material, p-phenylenediamine. The peaks around 1400 and 1000  $\text{cm}^{-1}$  (blue arrows) indicate the closing into the ring system borazine.

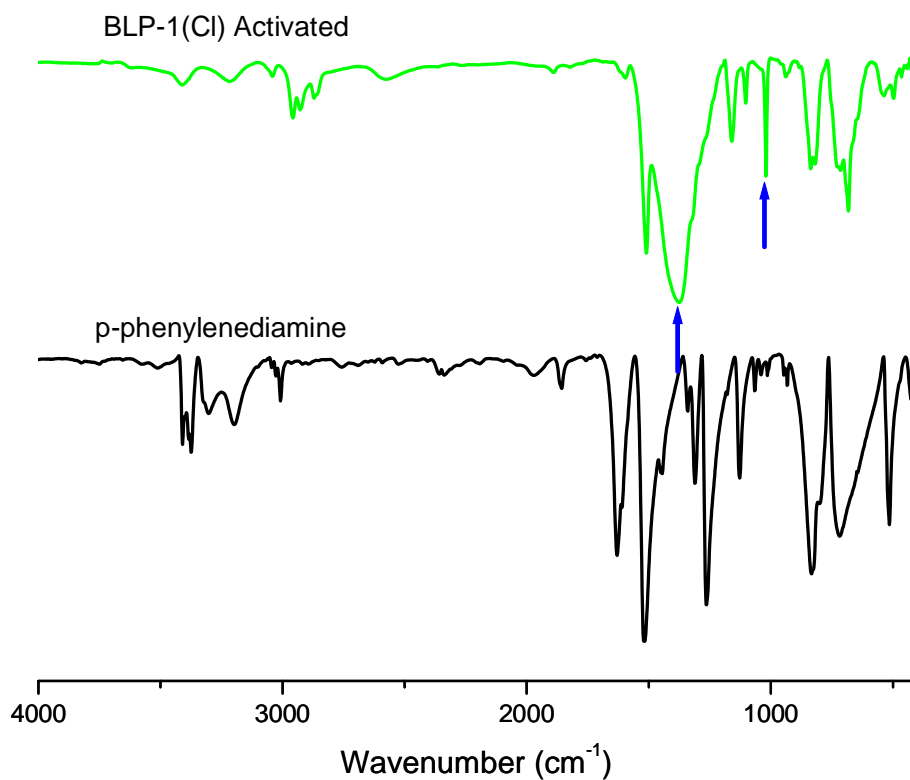


**Figure 21.** FT-IR Spectrum of BLP-2(Br). The C-N band at about  $1250\text{ cm}^{-1}$  overlaps with the large B-N band at about  $1400\text{ cm}^{-1}$ .

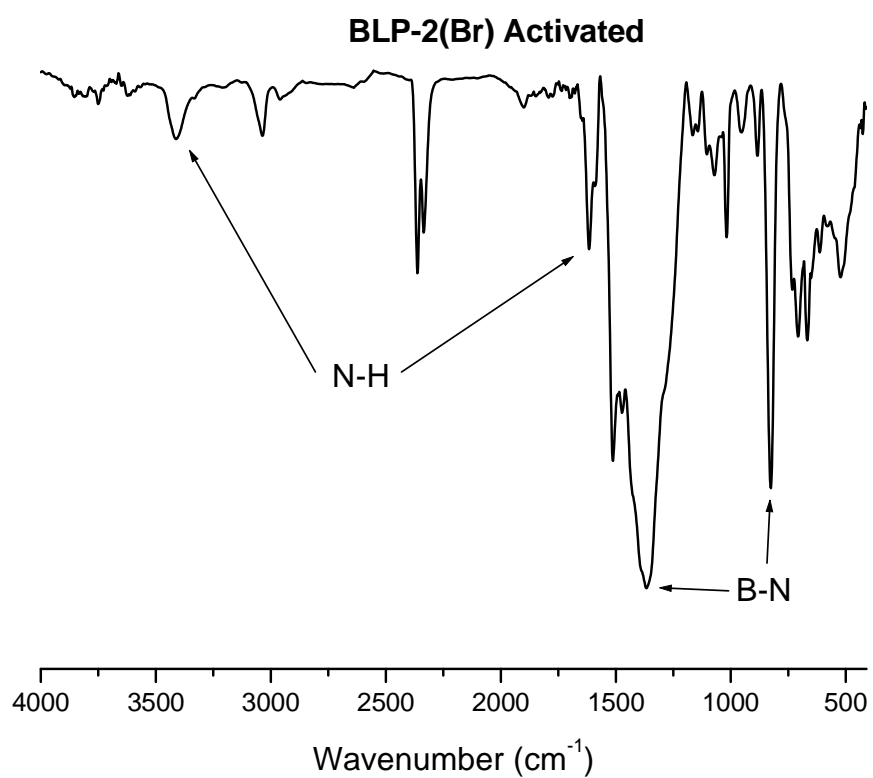


**Figure 22.** IR Spectra of BLP-2(Br) with Its Starting Material, 1,3,5-tris-(4-aminophenyl)benzene. The largely diminished amine stretching and bending bands indicate the consumption of the starting material, 1,3,5-tris-(4-aminophenyl)benzene. The peaks around 1400 and 1000  $\text{cm}^{-1}$  (blue arrows) indicate the closing into the ring system borazine.

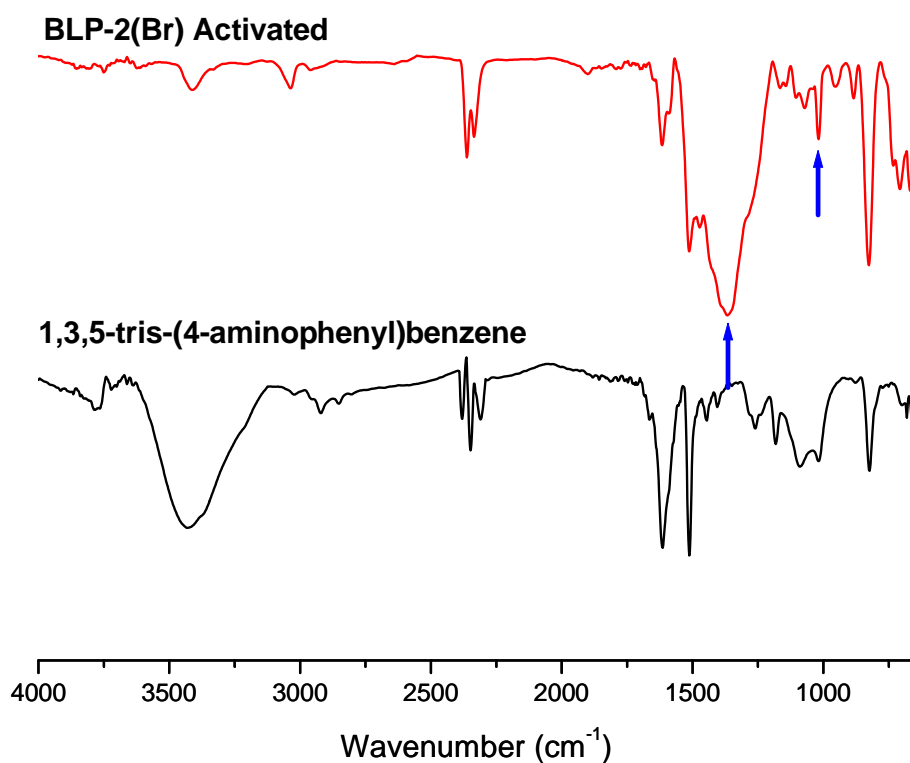


**Figure 23.** FT-IR Spectrum of BLP-2(Cl). The C-N band at about  $1250\text{ cm}^{-1}$  overlaps with the large B-N band at about  $1400\text{ cm}^{-1}$ .

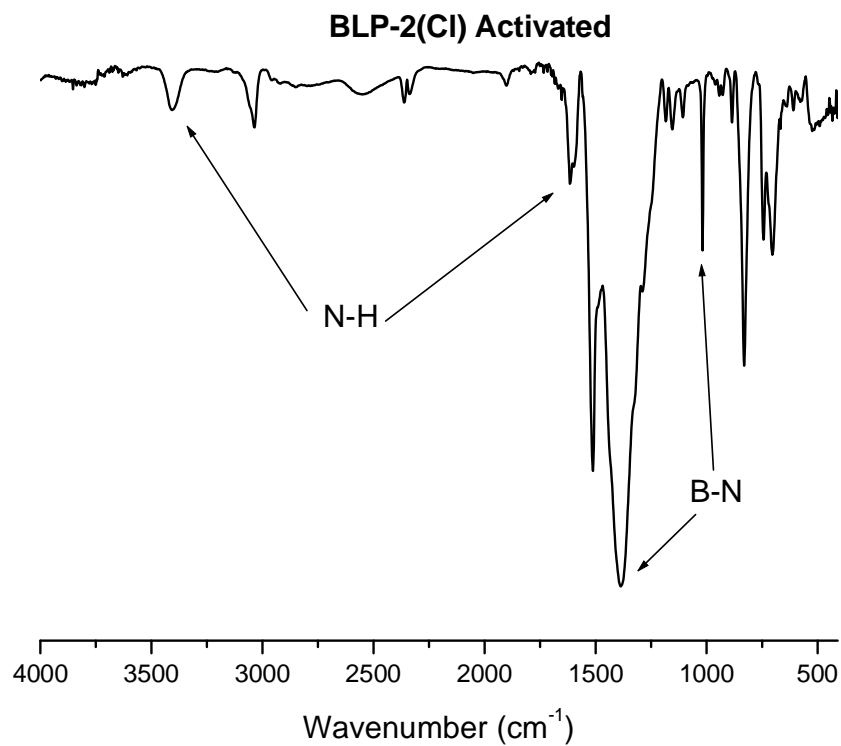


**Figure 24.** IR Spectra of BLP-2(Cl) with Its Starting Material, 1,3,5-tris-(4-aminophenyl)benzene. The largely diminished amine stretching and bending bands indicate the consumption of the starting material, 1,3,5-tris-(4-aminophenyl)benzene. The peaks around 1400 and 1000  $\text{cm}^{-1}$  (blue arrows) indicate the closing into the ring system borazine.

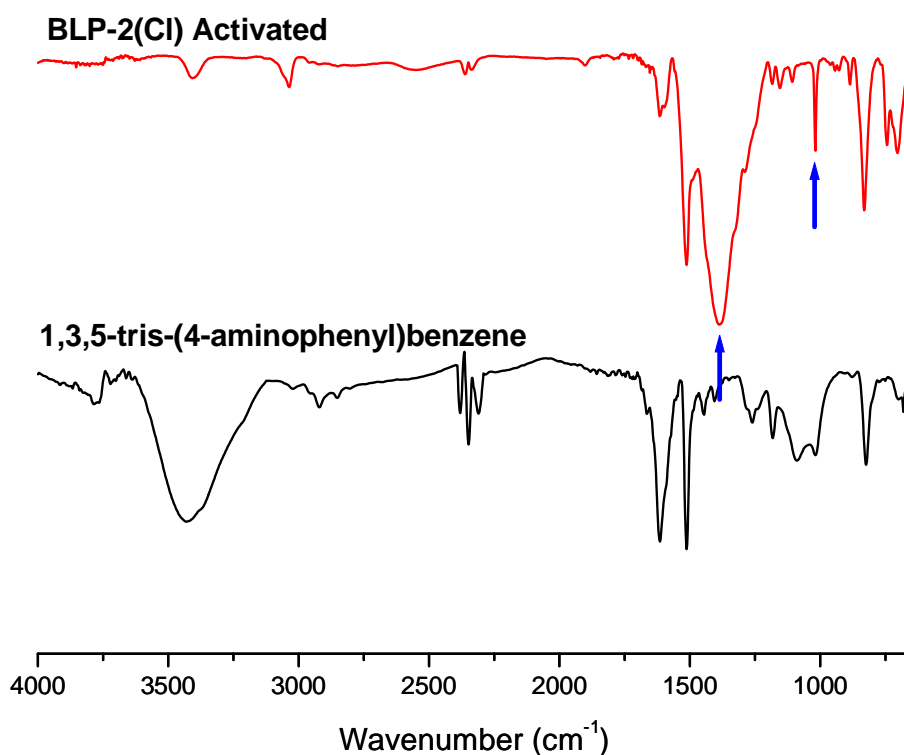


**Figure 25.** FT-IR Spectrum of BLP-10(Br). The C-N band at about  $1250\text{ cm}^{-1}$  overlaps with the large B-N band at about  $1400\text{ cm}^{-1}$ .

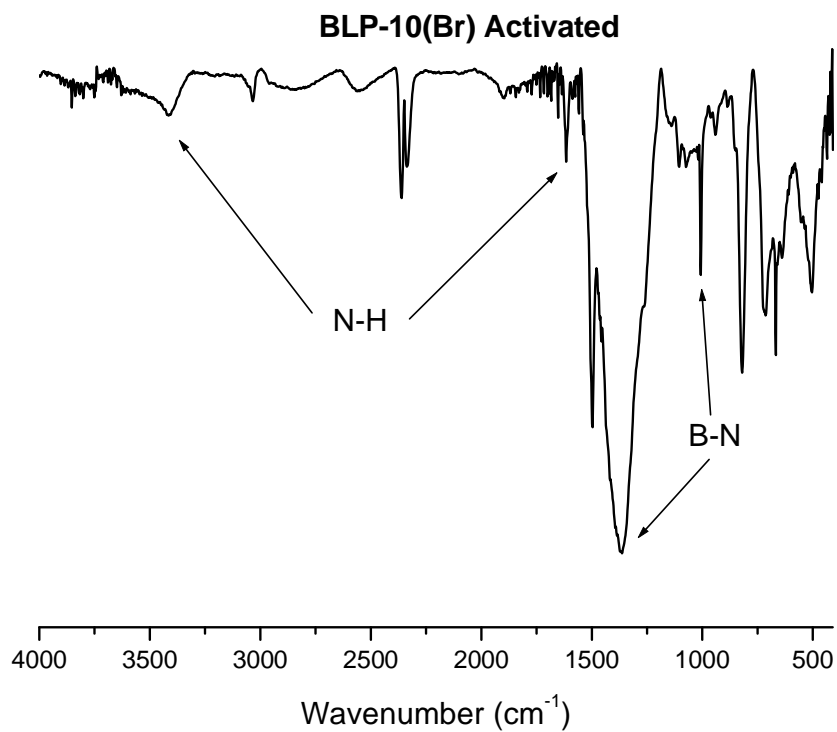




**Figure 26.** IR Spectra of BLP-10(Br) with Its Starting Material, benzidine. The largely diminished amine stretching and bending bands indicate the consumption of benzidine. The peaks around 1400 and 1000  $\text{cm}^{-1}$  (blue arrows) indicate the closing into the ring system borazine.

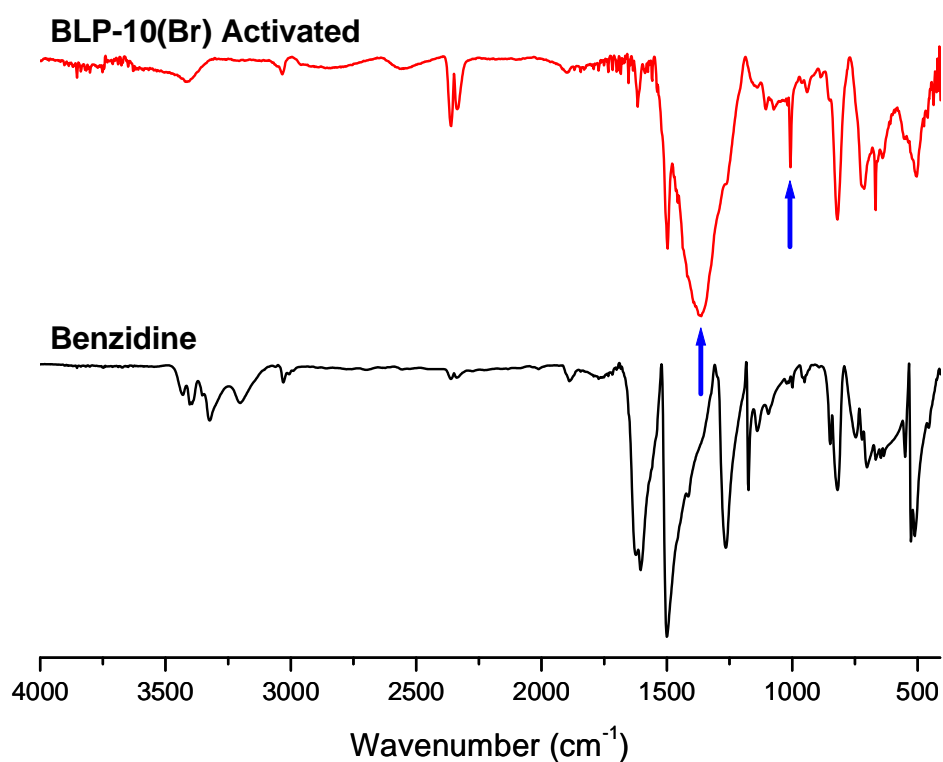


**Figure 27.** FT-IR Spectrum of BLP-10(Cl). The C-N band at about  $1250\text{ cm}^{-1}$  overlaps with the large B-N band at about  $1400\text{ cm}^{-1}$ .

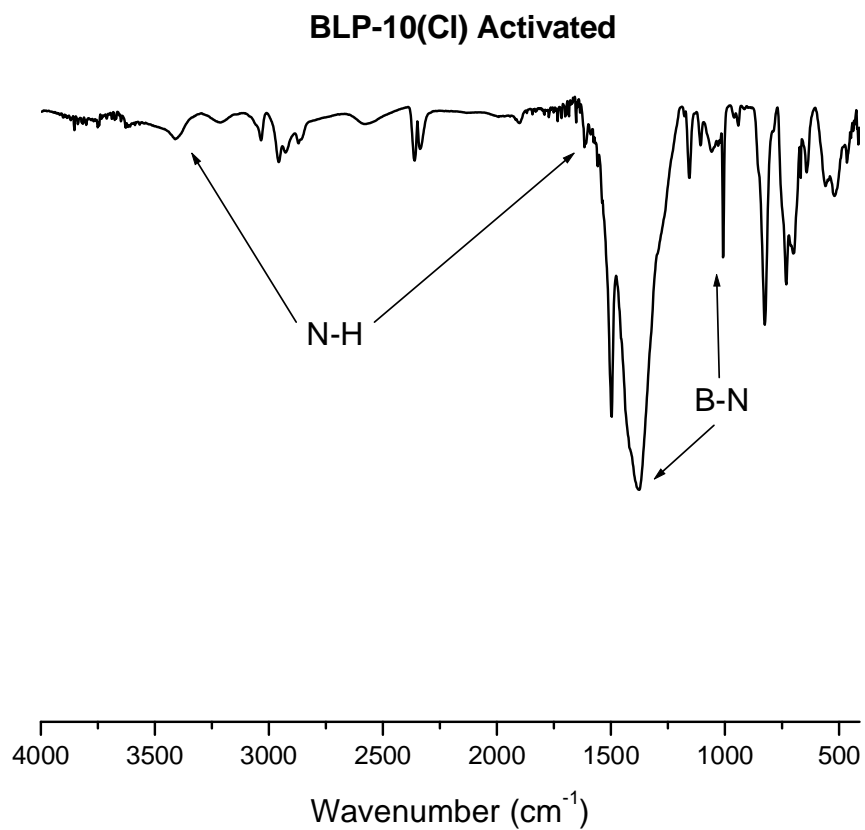


**Figure 28.** IR Spectra of BLP-10(Cl) with Its Starting Material, benzidine. The largely diminished amine stretching and bending bands indicate the consumption of benzidine. The peaks around 1400 and 1000  $\text{cm}^{-1}$  (blue arrows) indicate the closing into the ring system borazine.

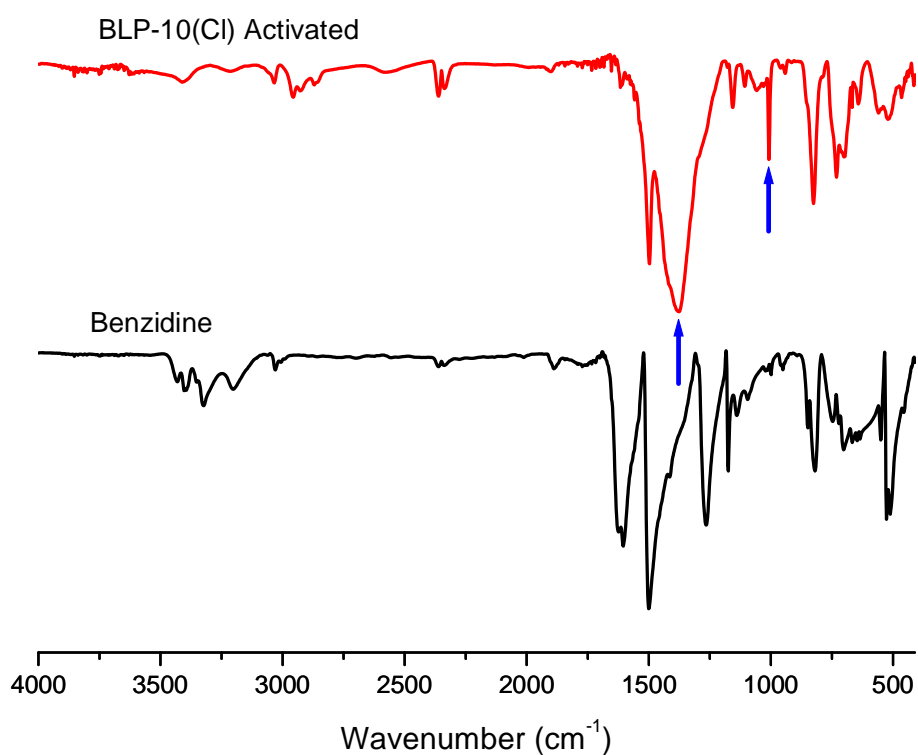


**Figure 29.** FT-IR Spectrum of BLP-12(Cl). The C-N band at about  $1250\text{ cm}^{-1}$  overlaps with the large B-N band at about  $1400\text{ cm}^{-1}$ .

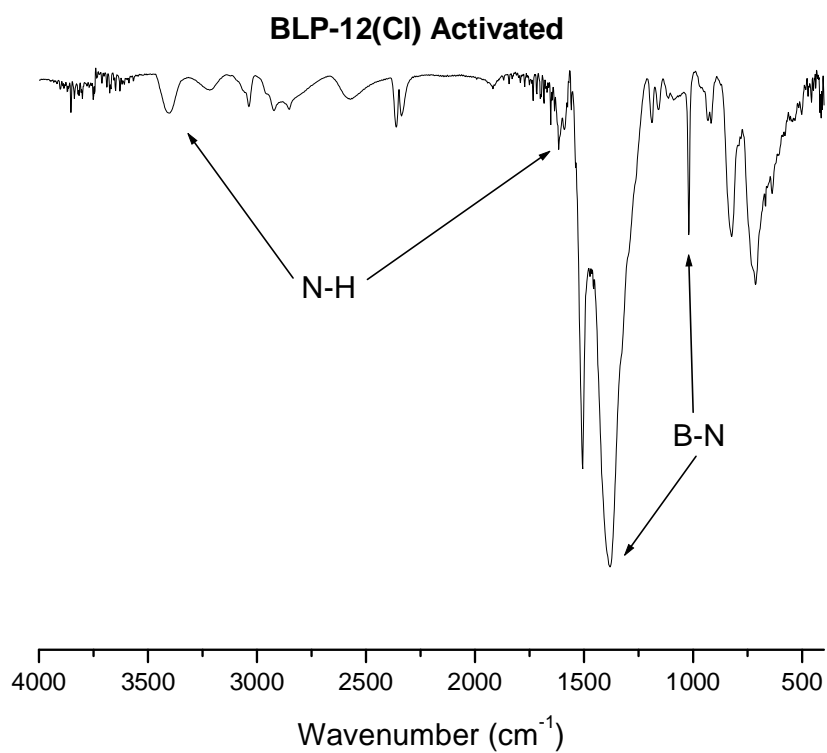
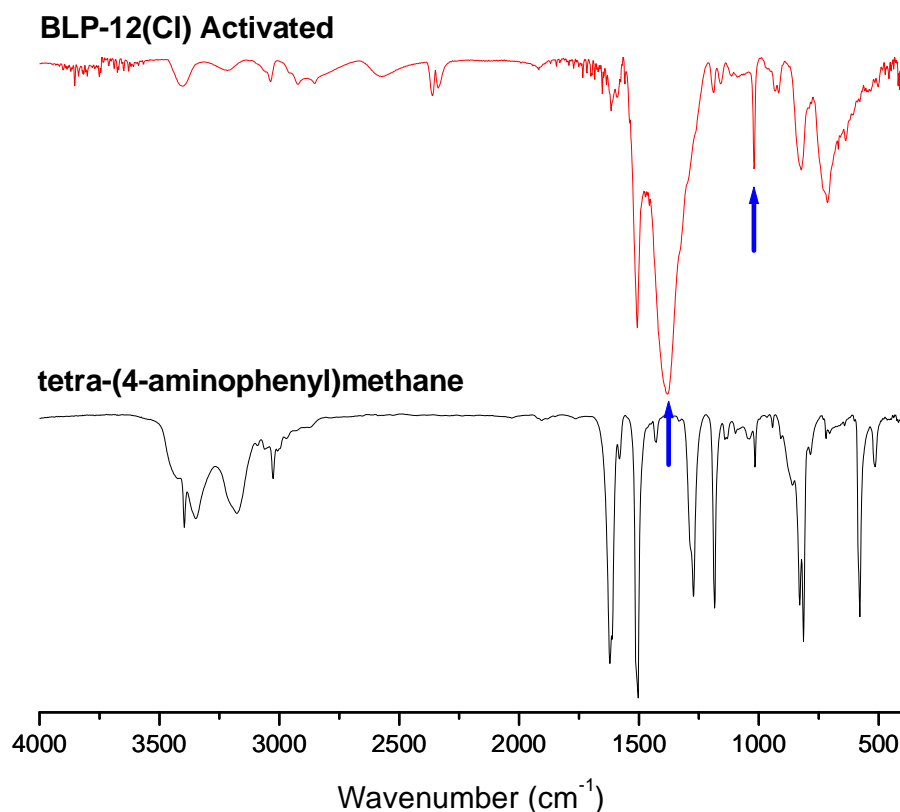


**Figure 30.** IR Spectra of BLP-12(Cl) with Its Starting Material, tetra-(4-aminophenyl)methane. The largely diminished amine stretching and bending bands indicate the consumption of amine. The peaks around 1400 and 1000  $\text{cm}^{-1}$  (blue arrows) indicate the closing into the ring system borazine.



Two representative materials were selected for  $^{11}\text{B}$  and  $^{13}\text{C}$  NMR experiments, BLP-1(Cl) and BLP-10(Cl). The BLP-1(Cl) spectra were recorded at ambient temperature on a Bruker DSX-300 spectrometer using a Bruker magic angle spinning (MAS) probe with 4 mm (O.D.) 80  $\mu\text{L}$  zirconia rotors with Kel-F drive caps packed under nitrogen. Cross-polarization with MAS (CPMAS) was used to acquire  $^{13}\text{C}$  data at 75.47 MHz. The  $^1\text{H}$  and  $^{13}\text{C}$  90° pulse widths were both 4  $\mu\text{s}$ , and the CP contact time was 1.5 ms. High power two-pulse phase modulation (TPPM)  $^1\text{H}$  decoupling was applied during data

acquisition. The decoupling frequency corresponded to 72 kHz. The MAS sample spinning rate was 10 kHz. Recycle delays between scans varied between 10 and 30 s, depending upon the compound as determined by observing no apparent loss in  $^{13}\text{C}$  signal intensity from one scan to the next. The  $^{13}\text{C}$  chemical shifts are given relative to tetramethylsilane as zero ppm, calibrated using the methane carbon signal of adamantane assigned to 29.46 ppm as a secondary reference. Multiple quantum MAS (MQMAS) spectroscopy was used to acquire  $^{11}\text{B}$  data at 96.29 MHz. The  $^{11}\text{B}$  solution-state  $90^\circ$  pulse width was 2  $\mu\text{s}$ . TPPM  $^1\text{H}$  decoupling was applied during data acquisition. The decoupling frequency corresponded to 72 kHz. The MAS spinning rate was 14.9 kHz. A recycle delay of 3 s was used. The  $^{11}\text{B}$  chemical shifts are given relative to  $\text{BF}_3$  etherate as zero ppm, calibrated using aqueous boric acid at pH = 4.4 assigned to -19.6 ppm as a secondary reference. Solid-state NMR spectra for BLP-10(Cl) were recorded at ambient temperature on a 360-1 instrument (8.5 T) by Spectral Data Services, Inc., in Champaign, IL.

The data, which are very sensitive to the boron magnetic and chemical environments, revealed one signal for BLP-1(Cl) at 30 ppm with a quadrupole coupling constant,  $Q_{cc}$ , of 2.39 MHz (Figures 31-33).<sup>221-223</sup> This signal falls in the reported range for tri-coordinated boron atoms in borazines, which usually appear at ~ 25 to 40 ppm, and are in sharp contrast to tetra-coordinated boron which appears upfield (0 to -45 ppm).<sup>224</sup> In addition, the  $Q_{cc}$  value, which depends on the boron site symmetry, is in agreement with trigonal sites ( $Q_{cc} = 2.8$  MHz).<sup>221</sup> The side hump in the  $^{11}\text{B}$  NMR for BLP-1(Cl) is most likely from a differing anisotropic environment resulting from changes in the stacking of the two-dimensional sheets.

**Figure 31.** Solid-State  $^{11}\text{B}$  NMR Spectrum of BLP-1(Cl).

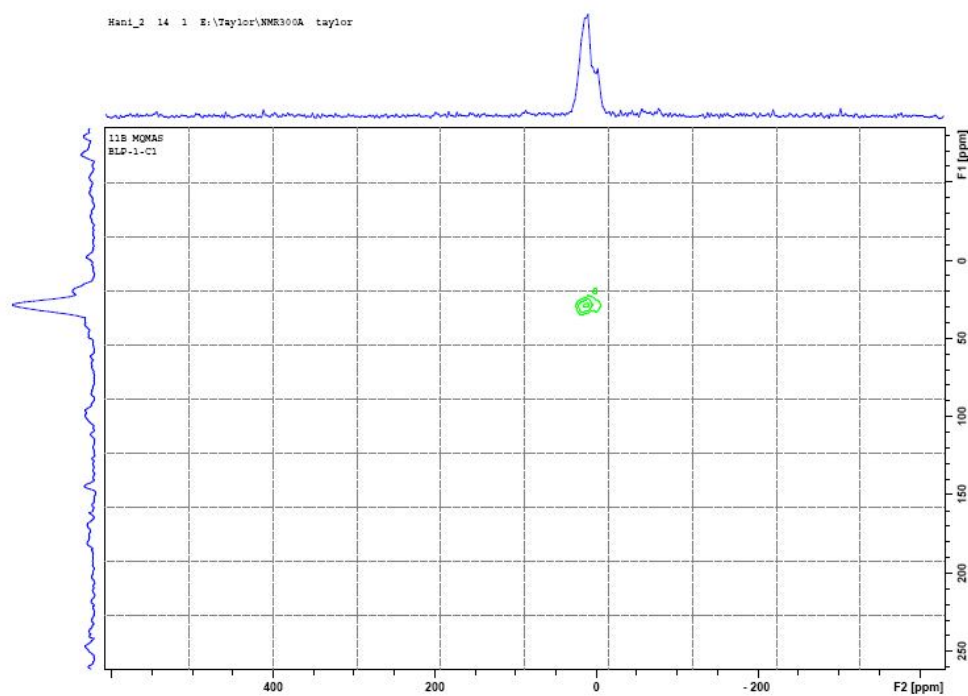


**Figure 32.** Solid-State  $^{11}\text{B}$  NMR Spectrum of BLP-1(Cl).

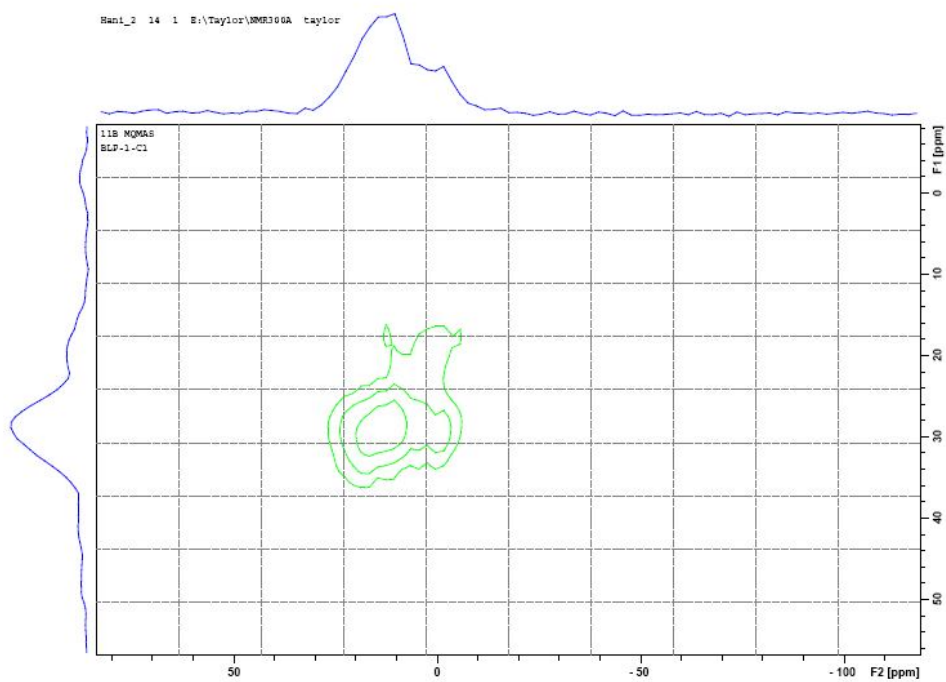
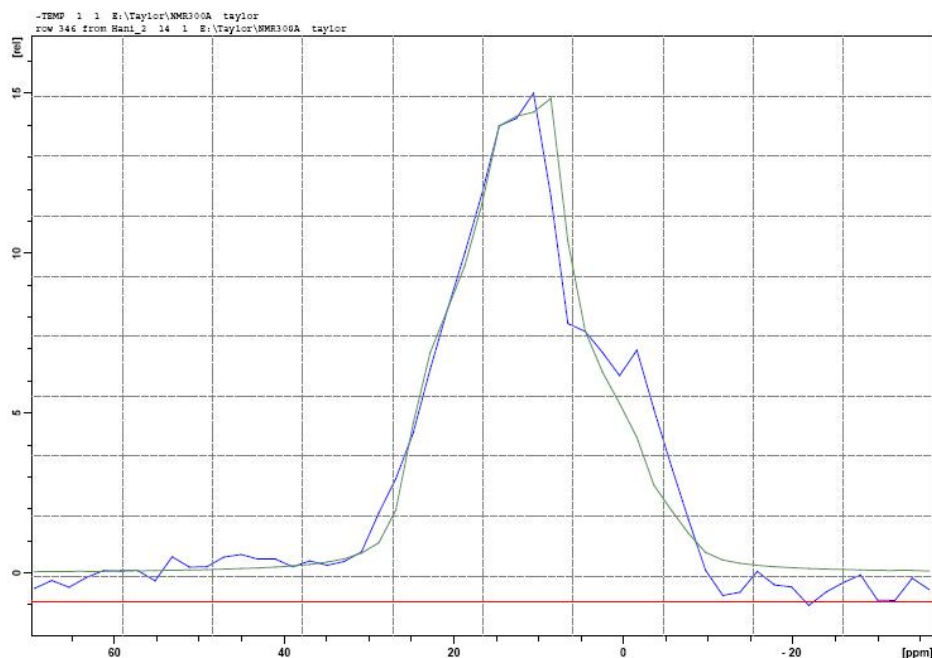


**Figure 33.** Solid-State  $^{11}\text{B}$  NMR Spectrum of BLP-1(Cl).



In the case of BLP-10(Cl) (Figure 34), the appearance of a single peak at 18.1 ppm in the  $^{11}\text{B}$  NMR is close to the values recorded for tri-coordinated boron and is also in sharp contrast to tetra-coordinated sites. Although this single peak does not fall exactly in the anticipated range for tri-coordinated boron atoms, this result is not completely unexpected. The low magnetic field capability for the NMR instrument used (8.5 T) can significantly contribute to an upfield shift. Additionally, an upfield shift compared to the standard boron peak for halogenated borazines is most likely the result of an anisotropic-induced magnetic field from the shielding cones radiating above and below the benzene rings.<sup>225</sup> An alignment of the neighboring layered sheets that would be necessary to create such a magnetic field would in fact be expected if the polymer exists in a staggered conformation—one of the potential formations for BLP-10(Cl). In



the  $^{13}\text{C}$  NMR spectroscopy of both BLP-1(Cl) and BLP-10(Cl) (Figures 35-36), the intact aryl peaks confirm the survival of the aromatic backbone.

**Figure 34.** Solid-State  $^{11}\text{B}$  NMR Spectrum of BLP-10(Cl).

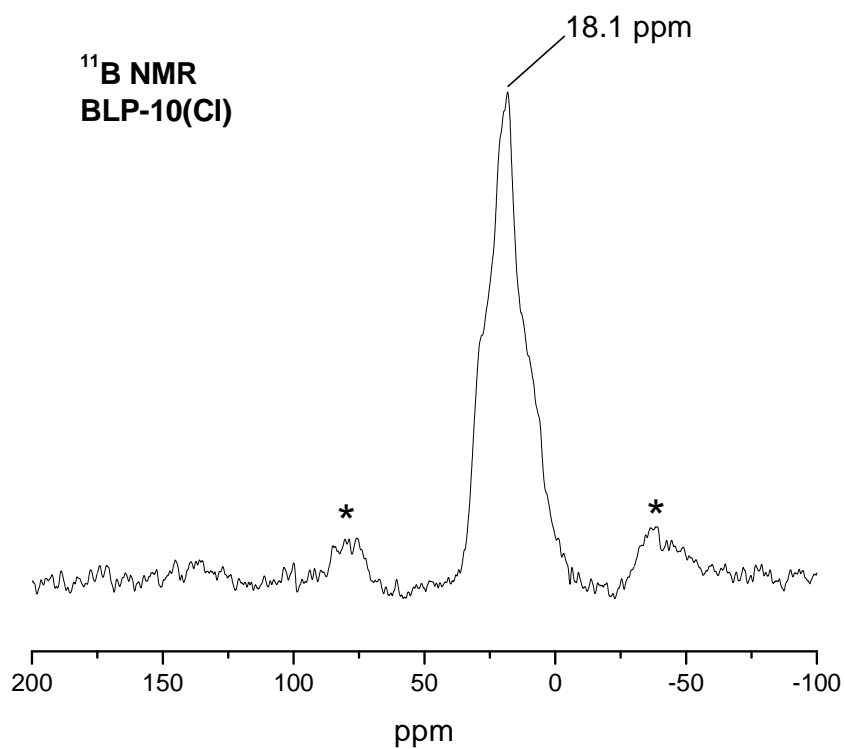
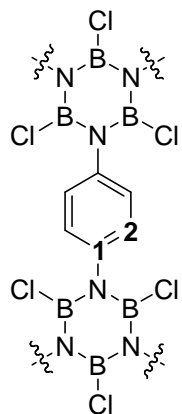
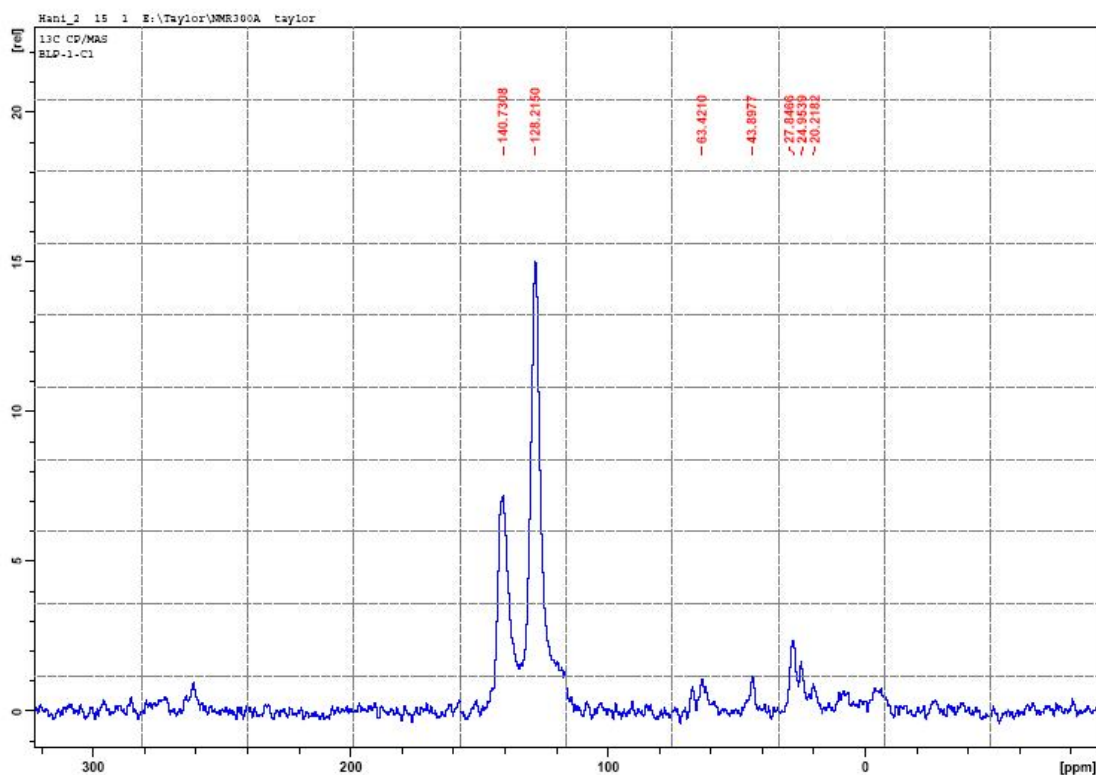
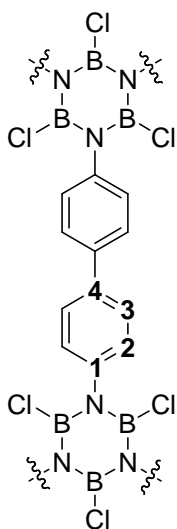
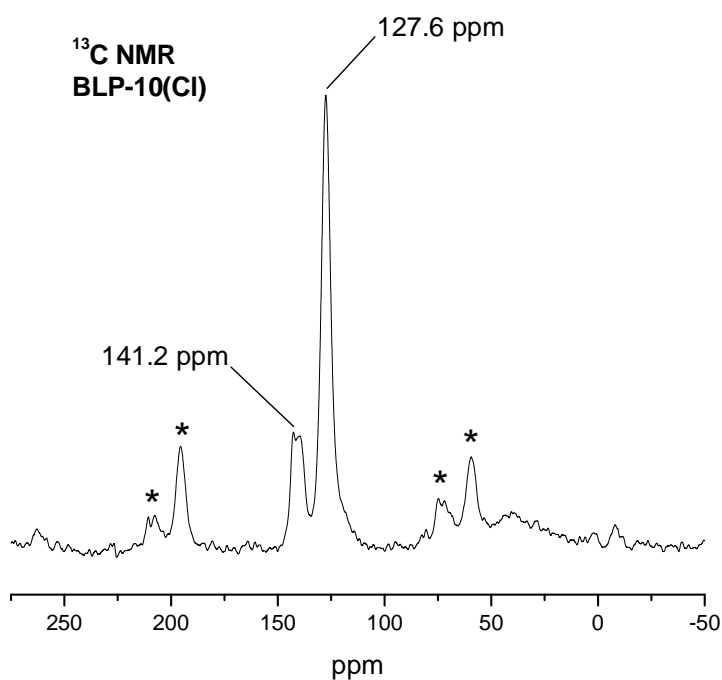


**Figure 35.** Solid-State  $^{13}\text{C}$  NMR Spectrum of BLP-1(Cl). Both of the expected peaks from the starting material are present in BLP-1(Cl). These peaks indicate that the backbone of the aryl-amine building block survived the reaction. Spinning side bands are also present in the spectrum as has been shown previously in COFs.<sup>121</sup>



Carbon	Chemical Shift (ppm)
1	140.73
2	128.21

**Figure 36.** Solid-State  $^{13}\text{C}$  NMR Spectrum of BLP-10(Cl). All of the expected peaks from the starting material are present in BLP-10(Cl), which indicates that the backbone of the aryl-amine building block survived the reaction. Some of the carbon signals are too close in chemical shift to be resolved. Peak assignments are shown. Spinning side bands are shown by asterisks.



Carbon	Chemical Shift (ppm)
1	141.2
2	127.6
3	127.6
4	127.6

The data collected from these spectral experiments in conjunction with elemental analysis results, which are very sensitive due to the high mass of the halide atoms, clearly illustrate the formation of the borazine building block for each of these polymers. Since the polymers' amorphous nature precluded their investigation by XRD, determination of the polymeric structure beyond the formation of the borazine building block is difficult. Among the possibilities is the formation of two-dimensional sheets in an eclipsed or staggered conformation as determined by Reticular Chemistry Structure Resource. However, such conformations would most likely produce legitimate peaks in the XRD pattern. Minimization of these peaks could result from limitations on the degree of order to short-ranged only. Deflecting of the benzene rings off the plane of polymerization to yield lower energy structures could also reduce the appearance of XRD peaks by limiting the capabilities of the two-dimensional sheets to stack. Nevertheless, neither of these occurrences can be confirmed, and, as such, conclusions on the precise orientation of the building blocks beyond the borazine formation and the survival of the aryl backbone cannot be made. Of important consideration is the possibility that these polymers form in a cross-linked linear fashion.

To assess the thermal stability for each of the BLPs, thermogravimetric analysis (TGA) was conducted under a flow of nitrogen on activated samples (Figures 37-43). The activation process for all samples involved multiple iterations of guest molecule exchange with dichloromethane followed by filtration and heating at 80 °C for 18 hours under vacuum ( $10^{-5}$  torr). The TGA results show a major weight loss in the range of 150 to 200 °C as well as a subsequent weight loss at about 450 °C. The former weight loss may result from halogen evolution due to boron-halide decomposition and the latter

from framework collapse as observed for covalent-organic frameworks and boron nitride formation.<sup>226</sup> Therefore, BLPs are thermally less stable than covalent organic frameworks or organic polymers which generally remain stable up to about 400 °C.

**Figure 37.** TGA for an Activated Sample of BLP-1(Br).

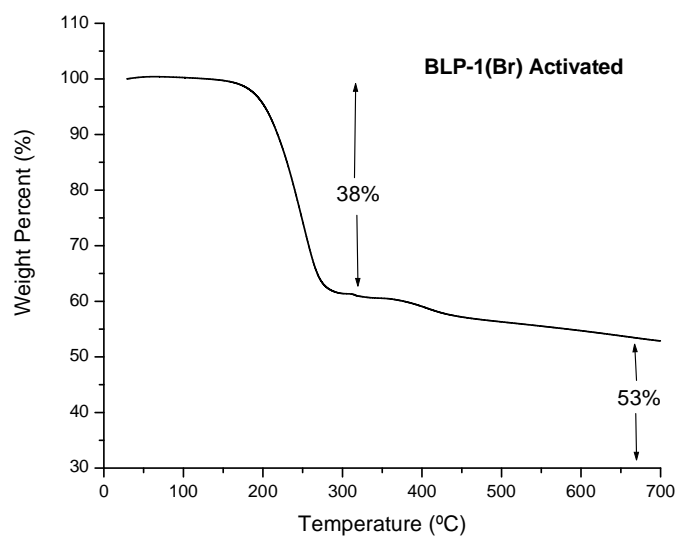


**Figure 38.** TGA for an Activated Sample of BLP-1(Cl).

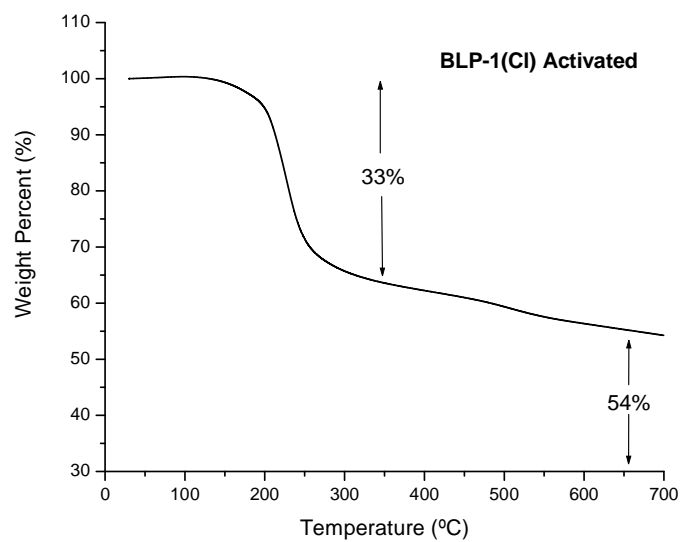


**Figure 39.** TGA for an Activated Sample of BLP-2(Br).

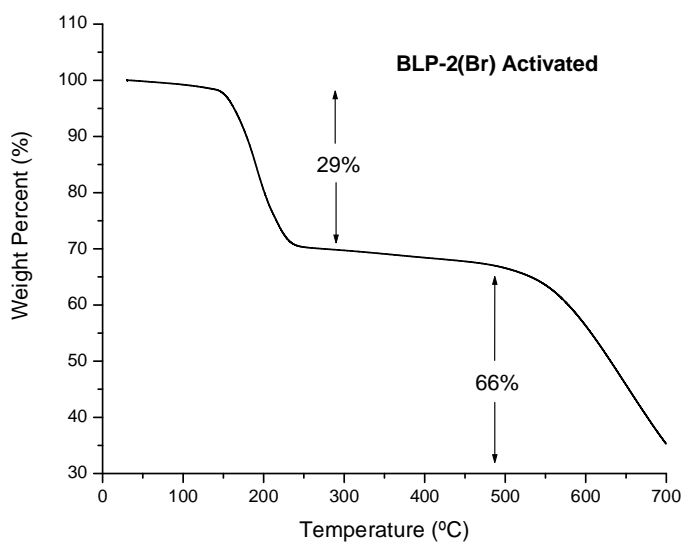


**Figure 40.** TGA for an Activated Sample of BLP-2(Cl).

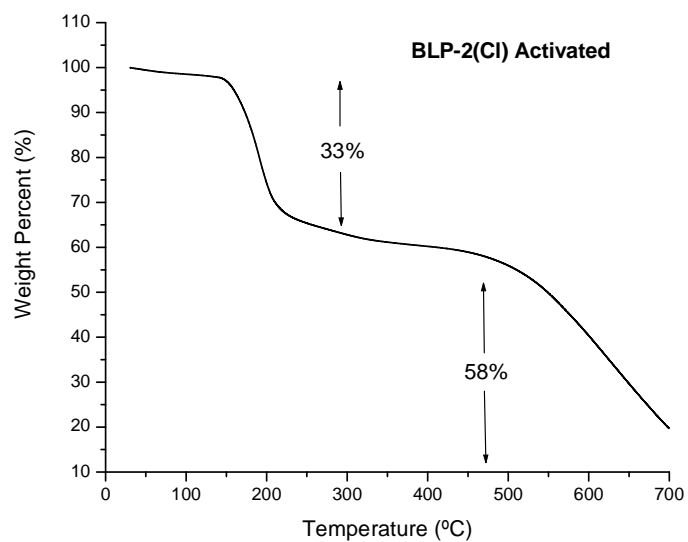


**Figure 41.** TGA for an Activated Sample of BLP-10(Br).

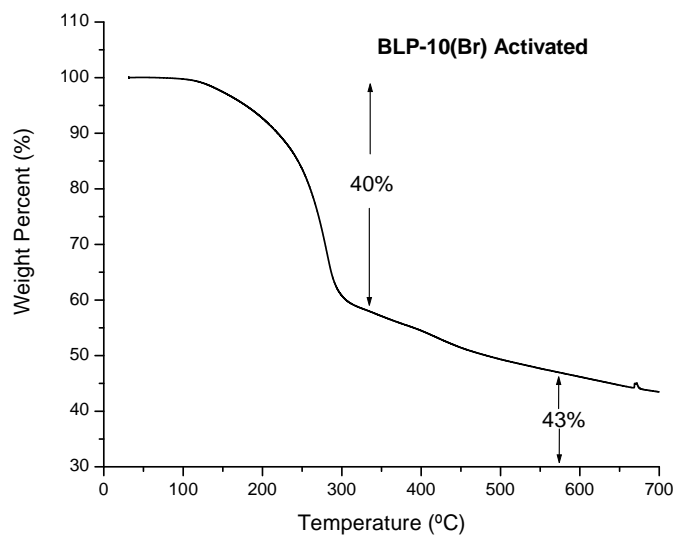


**Figure 42.** TGA for an Activated Sample of BLP-10(Cl).

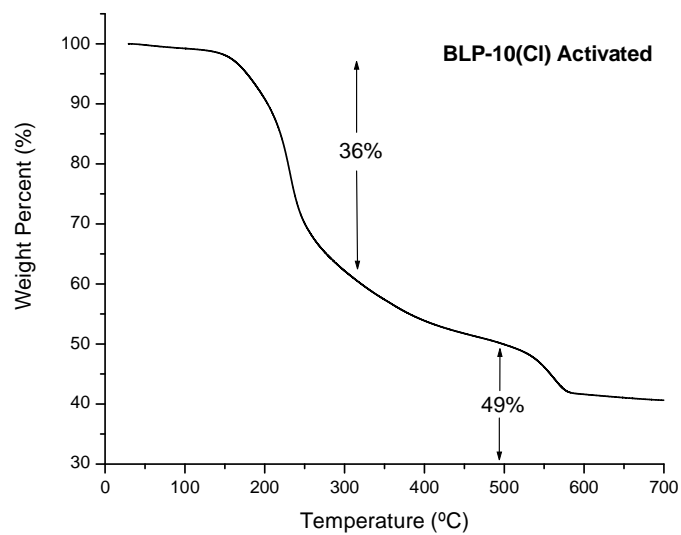
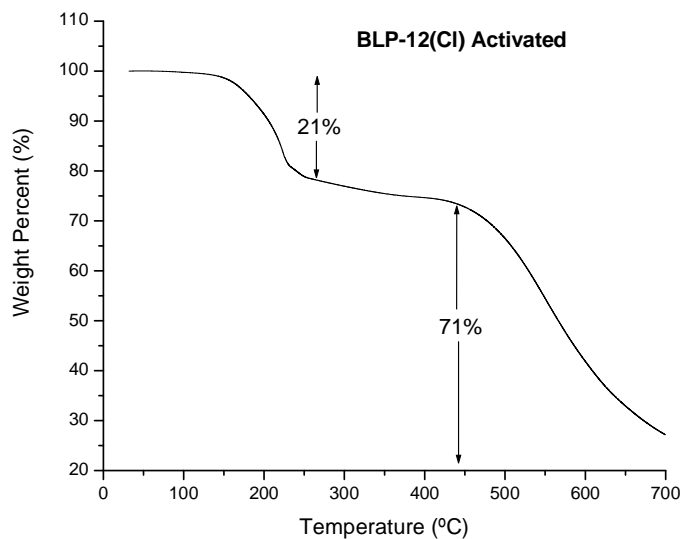


**Figure 43.** TGA for an Activated Sample of BLP-12(Cl).





## Chapter 4

### Porosity Measurements and Hydrogen, Carbon Dioxide, and Methane Gas Storage Capabilities of Halogenated Borazine-Linked Polymers

#### 4.1 Introduction

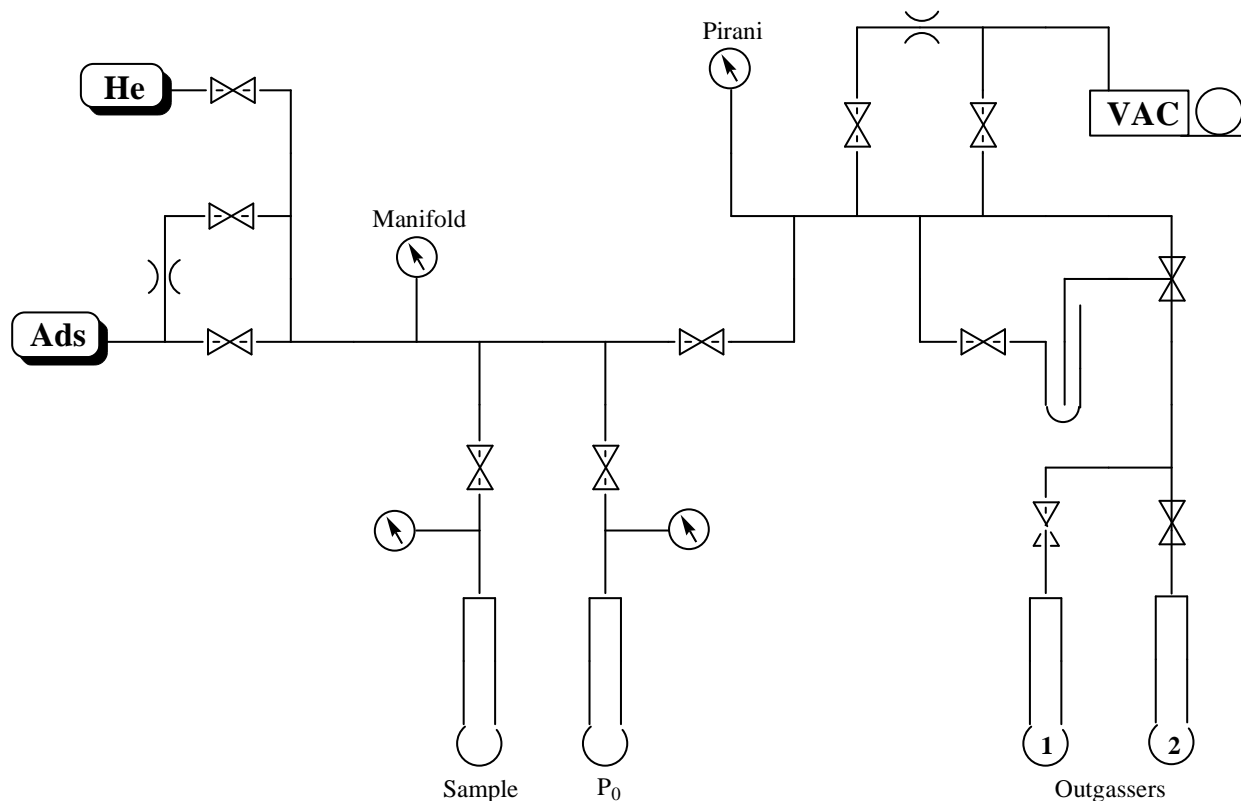
Great interest has been expressed in the gas storage capabilities of many porous media. Of particular interest as was discussed in Chapter 1 is hydrogen storage owing to its renewable and clean aspects that make it very attractive for future use in automotive applications.<sup>7</sup> The storage of methane, another alternative fuel, has received great interest as well. More recently, the storage of carbon dioxide has received increased attention for applications involving separation and sequestration. Prior to gas storage measurements, textural properties of BLPs were determined using nitrogen porosity measurements.

To assess gas storage capabilities, sorption equipment is employed. The applicable pressure range of this equipment varies from instrument to instrument but typically falls into one of two categories: (1) high pressure sorption equipment and (2) low pressure sorption equipment. High pressure equipment typically allows the user to assess gas storage capabilities from 1 bar (atmospheric pressure) to about 200 bar. This equipment can be outfitted to obtain lower pressure data (around  $10^{-4}$  bar); however, such an outfitting is typically undesirable as dedicated low pressure sorption equipment produces more reliable data at the low pressure range. The pressure range that dedicated low pressure sorption equipment can reach is typically around  $10^{-6}$  to 1 bar.

Higher pressures can be obtained, but, again, the reliability suffers compared to their high pressure brethren. High pressure gas sorption measurements are beyond the scope of this research; however, as is mentioned later in the concluding remarks, obtaining such data is part of the natural extension of this work.

Physisorption equipment is used to collect what is commonly called an isotherm. As one might expect from the name, isotherms are obtained at constant temperature. Applicable temperatures typically range from 77 K to 315 K. The choice of the temperature within this range is limited by the experimenter's capabilities to keep the temperature constant and consistent. For instance, submerging a sample in liquid nitrogen will keep the sample at 77 K until all of the nitrogen boils off. A similar comparison can be said for immersing a sample in ice water to keep the temperature at 273 K. The result of an isothermal experiment is a graph with pressure on the x-axis and gas uptake on the y-axis. As such, one might expect that the sorption equipment varies the pressure and measures the resulting gas uptake especially considering that the user requests certain pressures for the instrument to take. In fact, the opposite is true. The instrument inputs a known volume of gas and measures the corresponding pressure. In order to obtain the requested pressures, the instrument goes through a dosing process whereby it inputs the gas in repetitive small quantities until the threshold around the requested pressure is reached.

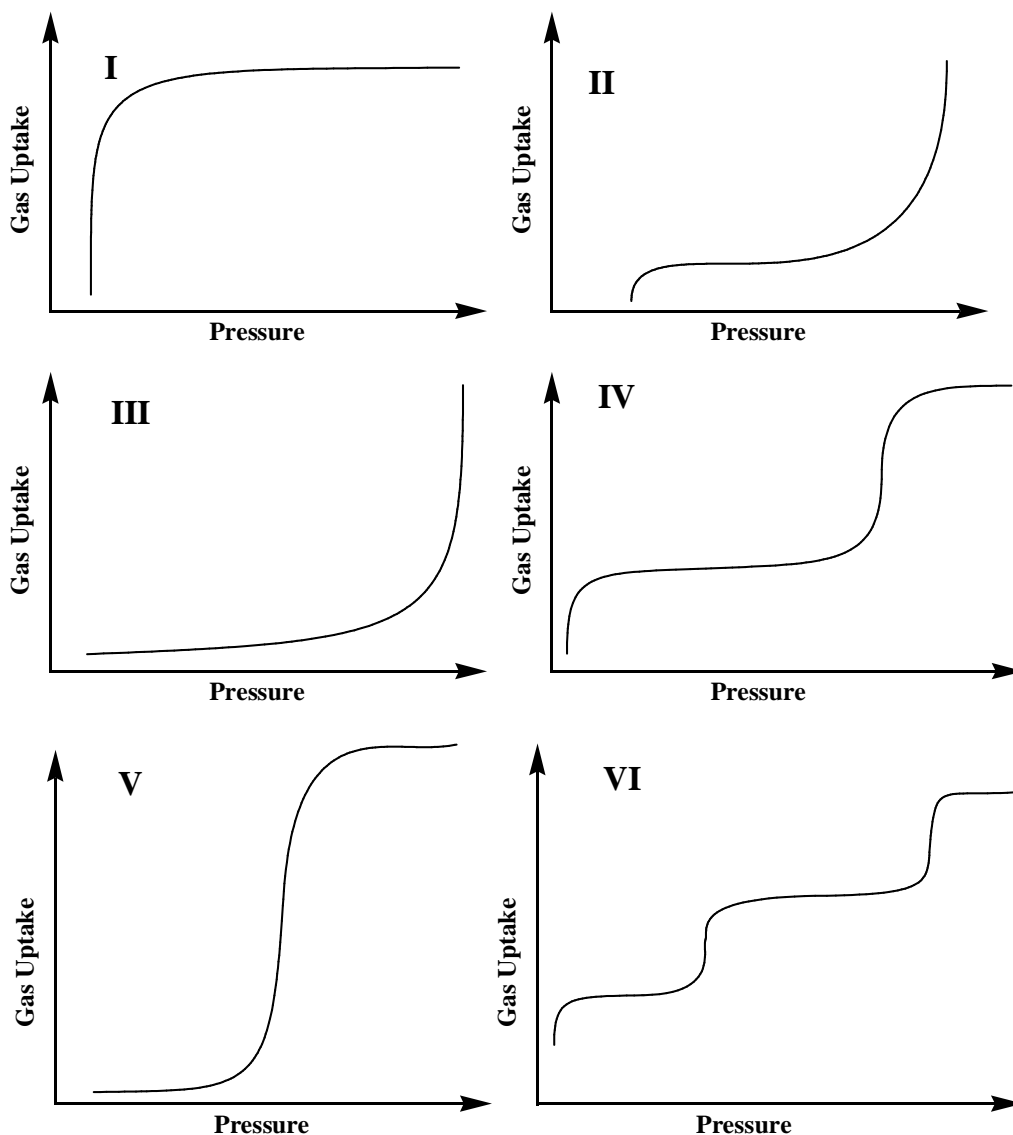
**Figure 44.** Schematic Representation for a Quantachrome Autosorb 1-C Low Pressure Sorption Instrument. He and Ads represent the inlets for helium gas and the adsorbate gas, respectively. VAC represents the vacuum. Circled arrows represent pressure gauges, and bow-tie shapes represent valves.  $\sim$  represents restriction valves for fine flow.



For this research, a Quantachrome Autosorb 1-C low pressure sorption instrument was used for all sorption experiments. Its schematic representation (Figure 44) shows that, at a base level, the adsorbate gas is introduced to the manifold. The amount of gas is measured through its pressure in a known manifold volume before being introduced to the sample. The pressure within the sample chamber is allowed to stabilize so that all adsorbed gas equilibrates with its surroundings. If the resultant

pressure does not reach the tolerance levels around the sought after pressure reading, another dose of gas is sent through the manifold and into the sample. The process is repeated until the appropriate pressure is reached. At which point, the instrument records the total amount of gas required to reach this pressure and updates the isotherm. The instrument then moves on to the next pressure reading until all steps are satisfied. Oftentimes, a desorption curve is requested. In such a case, gas is removed from the system until a requested pressure is reached. This aspect of the isotherm yields information on the reversibility of the adsorbate-media interaction by the presence (or absence) of hysteresis. Hysteresis results when the removal of the adsorbate from the media requires a lower pressure than when it was added and is represented as a higher gas uptake in the desorption branch of the isotherm than in the adsorption branch.

**Figure 45.** Brunauer, Deming, Deming, and Teller Isotherm Curves.



For nitrogen or argon experiments, a fully collected isotherm can tell a substantial amount of information regarding the sample beyond just its gas uptake capabilities. Firstly, the shape of the isotherm itself can help to describe different systems. In 1940, Brunauer, Deming, Deming, and Teller<sup>227</sup> reported six different types of isotherms (I through VI, Figure 45) to describe the experimental system, and this nomenclature was adopted by the International Union of Pure and Applied Chemistry (IUPAC). Type I

isotherms are indicative of microporous systems (pores less than 2 nm) while Type II isotherms result from experiments with macroporous (pores greater than 50 nm) or non-porous media. In the case of weak interactions as is seen with water vapor adsorbing onto graphite, Type III isotherms are produced. Mesoporous systems (pores between 2 and 50 nm) produce Type IV isotherms. Type V isotherms are the integration of type III and IV whereby a mesoporous system interacts weakly with the adsorbate. Finally, type VI isotherms are the result of a multilayer adsorption on a uniform, non-porous surface such as the interaction between argon and graphite at 77 K. The differences in the shapes of isotherms from microporous, mesoporous, and macroporous systems results from the relative contribution of the molecule-molecule and molecule-wall interactions. In the case of macroporous media, the majority of the adsorbate molecules is significantly apart from the walls of the media and exhibits relatively little of an interaction between them. As a result, the interactions among the molecules themselves dominate. For microporous samples where the pores are very small, the majority of the adsorbate molecules are suspect to surface interaction whereby limiting the molecule-molecule interactions and emphasizing the molecule-wall interactions. In the case of mesoporous media, both the molecule-molecule and molecule-wall interactions are statistically relevant. Of important note is that the curves in Figure 45 represent adsorption curves only. When hysteresis is present, it can give an indication of the nature of the pores whereby cylindrical-like, uniformly spherical, slit-shaped, and disordered pores exhibit unique hysteresis patterns.

A second important piece of information that nitrogen or argon sorption isotherms can convey is the surface area of the material, which is of importance since it

represents accessible area for binding. The surface area of a material can be calculated from a nitrogen or argon sorption isotherm taken at 77 K or 87 K, respectively. Other gases have been used to estimate surface area but are not traditionally practiced by industry standards. Two methods are traditionally used to assess surface area: Langmuir and BET.

The Langmuir model, which was pioneered in 1916 by Irving Langmuir, is determined by the equation:

$$\frac{1}{x} = \left( \frac{1}{K \cdot x_0} \right) \left( \frac{1}{P} \right) + \frac{1}{x_0}$$

where  $x$  is the surface area covered (i.e. the amount of gas put into the system),  $K$  is the ratio of the rate constant for adsorption over the rate constant for desorption,  $P$  is pressure, and  $x_0$  is the total surface area (i.e. the information sought after). This equation follows the style of  $y = mx + b$ ; therefore finding the intercept of the equation gives the reciprocal of the total surface area with an applicable range between 0.05 and 0.35  $P/P_0$ . Nevertheless, this equation is based on four assumptions:

1. The surface of the material is uniform.
2. Adsorbate molecules do not interact with each other.
3. All adsorption occurs by the same mechanism.
4. At the maximum adsorption, only a single layer is formed

In reality, these assumptions are rarely true. In most real-world samples, the surface of the material exhibits some level of non-ideality. Adsorbates do not conform precisely to the ideal gas law. Initial adsorption mechanisms can sometimes differ from the mechanisms in latter stages. And oftentimes adsorbate molecules will adhere to the

monolayer creating a multilayer scenario. To combat the fourth assumption, Brunauer, Emmett, and Teller published in 1938 their derivation of this equation and called it the BET theory.<sup>228</sup> Since the Langmuir model assumes that all gas adsorbed exists as a monolayer, it yields surface areas that are higher than what the BET model calculates. Since the level of interaction (complete, non-existent, or somewhere in between) for the monolayer and any other adsorbate gas molecules is debatable, both models are typically used. Often the Langmuir model is the highlighted number since it results in the higher value. These surface areas of course represent estimations; however, comparisons between porous media can often be made if the calculations were made with the same model on similar systems. One limitation to these comparisons, though, is that the surface area of mesoporous media cannot be calculated by these models. The reasoning for this limitation results from the third assumption which is shared by both theories; in mesoporous material, adsorption mechanisms occur both through molecule-molecule interactions and molecule-wall interactions. As a result, only the surface area for microporous material should be calculated by these methods although that restriction is often ignored at the researcher's peril.

A third piece of useful information that can be obtained from nitrogen or argon isotherms is the pore size distribution of the sample. Pore size distribution is a graphical analysis detailing how often pores of every size exists within a porous media. The thickness of the distribution can be an indication of the consistency of the network. Additionally, the pore size from the computer model of the network as discussed in Chapter 2 can be compared to the pore size distribution of nitrogen or argon isotherms to assess and confirm topological formations. Two methods are typically used to



calculate pore size distribution: Barrett-Joyner-Halenda (BJH) and Non-Local Density Functional Theory (NLDFT). BJH has a tendency to bias the distribution high and was not used within this research. For all synthesized BLPs within this work, NLDFT was used to calculate the pore size distribution.

#### **4.2 Nitrogen Sorption of Halogenated Borazine-Linked Polymers**

To investigate the permanent porosity of BLPs, nitrogen sorption data was acquired using a Quantachrome Autosorb 1-C at 77 K. Pore size distributions were calculated using the Non-Local Density Functional Theory (NLDFT)<sup>229</sup> on the adsorption branch with a cylindrical pore model for all BLPs except BLP-12(Cl), which used a cylindrical/spherical pore model on the adsorption branch. This model was used in conjunction with a similar model on the adsorption branch of the carbon dioxide isotherm at 273 K as has been reported previously in literature to obtain lower level pore size distributions.<sup>122, 230</sup> The choice of one model over another was determined by the shapes of the theoretical computer-generated models. For all models except BLP-12(Cl), the stacking of the two-dimensional sheets suggested pores of potentially cylindrical shape. In the case of BLP-12(Cl), which does not form two-dimensional sheets, the ordering suggests pores of a spherical shape. However, a cylindrical duality to the NLDFT model was chosen owing to the cylindrical appearance when several unit cells are combined. Nitrogen sorption studies were performed on activated samples. The activation process for all samples involved multiple iterations of guest molecule exchange with dichloromethane (DCM) followed by filtration and heating at 80 °C for 18 hours under vacuum ( $10^{-5}$  torr).

The N<sub>2</sub> uptakes (Figures 46 and 47) display Type I isotherms as described by Brunauer, Deming, Deming, and Teller with a sharp increase in the  $P/P_0 = 0$  to 0.1 range which is indicative of their microporous nature. The final rise at  $P/P_0 = 0.9$  to 1.0 is due to nitrogen condensation in the macroporous and mesoporous interparticulate cavities. Additionally, a minor hysteresis for all samples is consistent with their fine powder and microporous nature.

**Figure 46.** Nitrogen Uptake Isotherms for Chlorine-Lined BLPs; adsorption (filled) and desorption (empty) data points were taken at 77 K and 0-1 bar.

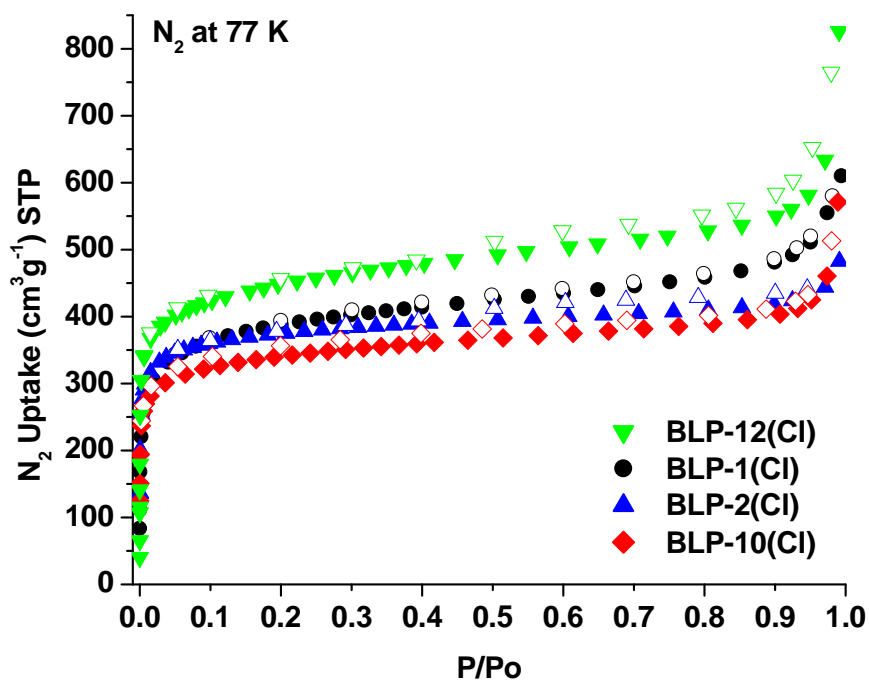


**Figure 47.** Nitrogen Uptake Isotherms for Bromine-Lined BLPs; adsorption (filled) and desorption (empty) data points were taken at 77 K and 0-1 bar.

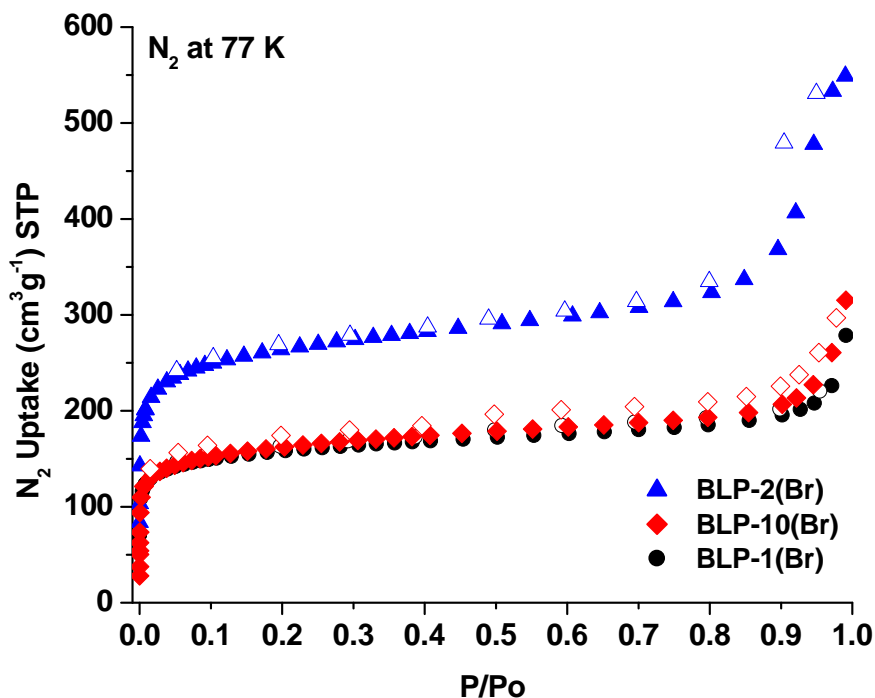


**Table 18.** Porous Textural Properties of BLPs. <sup>a</sup>Calculated by the Langmuir and BET methods. <sup>b</sup>Calculated from nitrogen adsorption at  $P/P_o = 0.9$ . <sup>c</sup>Calculated from NLDFT.

Polymer	$SA_{Lang} (m^2 g^{-1})^a$	$SA_{BET} (m^2 g^{-1})^a$	$P_{vol} (cm^3 g^{-1})^b$	PSD (nm) <sup>c</sup>
BLP-1(Cl)	1828	1364	0.746	1.33
BLP-1(Br)	730	503	0.303	1.27
BLP-2(Cl)	1699	1174	0.649	1.27
BLP-2(Br)	1221	849	0.571	1.27
BLP-10(Cl)	1581	1205	0.626	1.26
BLP-10(Br)	755	520	0.321	1.06
BLP-12(Cl)	2091	1569	0.853	1.13

The BET-calculated surface areas (Table 18) were higher for Cl-decorated materials, BLP-12(Cl): 1569, BLP-1(Cl): 1364, BLP-10(Cl): 1205, and BLP-2(Cl): 1174 m<sup>2</sup>g<sup>-1</sup> than the corresponding Br-decorated polymers, BLP-2(Br): 849, BLP-10(Br): 520, and BLP-1(Br): 503 m<sup>2</sup>g<sup>-1</sup>. The Langmuir-calculated surface areas also exhibited this observation. Of important note is that the BET surface area of BLP-1(Cl) (1364 m<sup>2</sup>g<sup>-1</sup>) far exceeds the values for the analogous COF-1 (711 m<sup>2</sup>g<sup>-1</sup>)<sup>122</sup> and CTF-1 (791 m<sup>2</sup>g<sup>-1</sup>)<sup>124</sup> despite the fact that BLP-1(Cl) is amorphous while COF-1 and CTF-1 exhibit crystalline behavior. As stated earlier, this finding could be the result of an aversion with BLPs to stack their two-dimensional sheets owing to their large halide atoms. The trend with chlorinated BLPs exhibiting higher surface areas than their brominated counterparts is unsurprising. Since bromine atoms are more massive than chlorine, the surface area on a per weight basis of polymers utilizing bromine would naturally decrease. The larger atomic size of bromine also contributes to reducing the overall surface area by shielding previously accessible areas. Although the trend between chlorinated and brominated BLPs is unsurprising, the trend within the chlorinated BLPs is. According to the Connolly expectations from Chapter 2, BLP-2(Cl) should exhibit a higher surface area than BLP-1(Cl). However, these polymers do not conform to such expectations hence their amorphous nature. The irregular trend in surface area values may arise from solid state packing that can lead to a more accessible surface as indicated by a recent theoretical investigation of 2D COFs.<sup>207</sup>

The pore volumes, which were calculated at P/P<sub>0</sub> of 0.9, showed a significant halide dependence as each of the chlorinated polymers yielded higher pore volumes than their brominated counterparts. This finding is consistent with the smaller atomic size of

chlorine when compared to bromine. The pore size distributions (Figures 48-54) were found to be centered about 1.1 nm for BLP-10(Br) and BLP-12(Cl) and centered about 1.3 nm for the other five BLPs. These values are in line with two-dimensional COFs such as CTF-1 (1.2 nm) and COF-1 (0.9 nm).

**Figure 48.** Pore Size Distribution for BLP-1(Br).

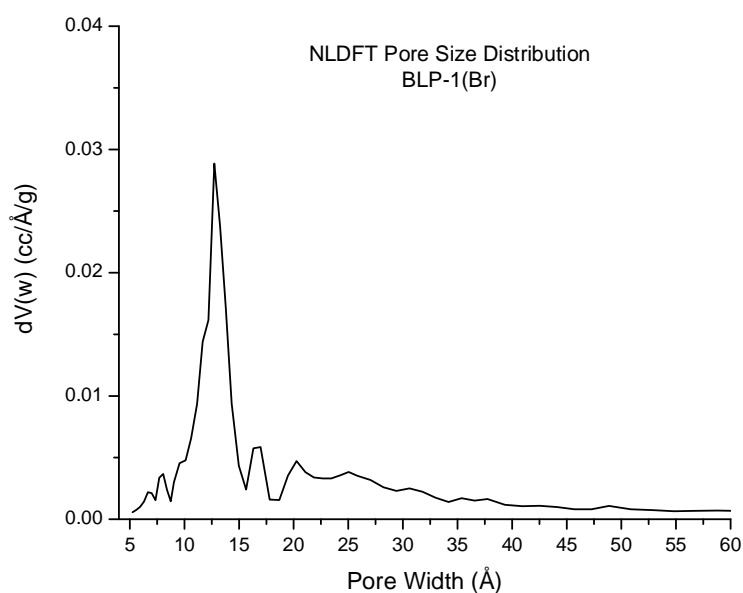


**Figure 49.** Pore Size Distribution for BLP-1(Cl).

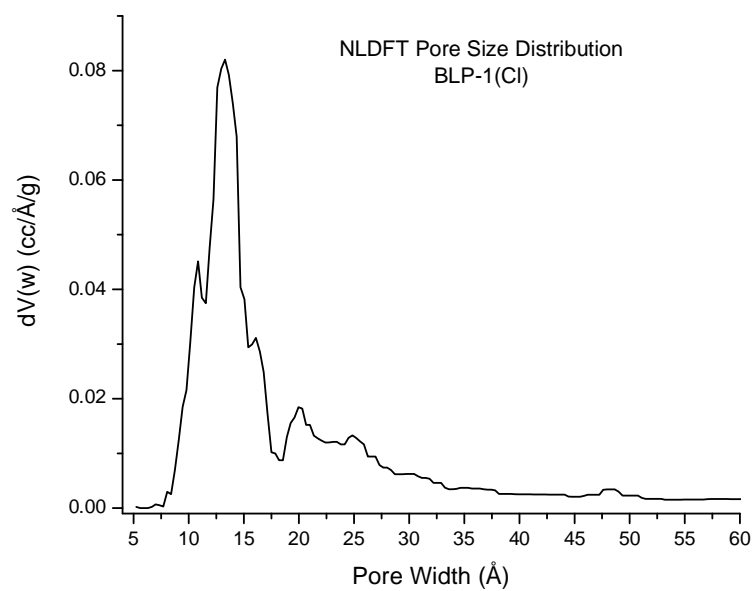


**Figure 50.** Pore Size Distribution for BLP-2(Br).

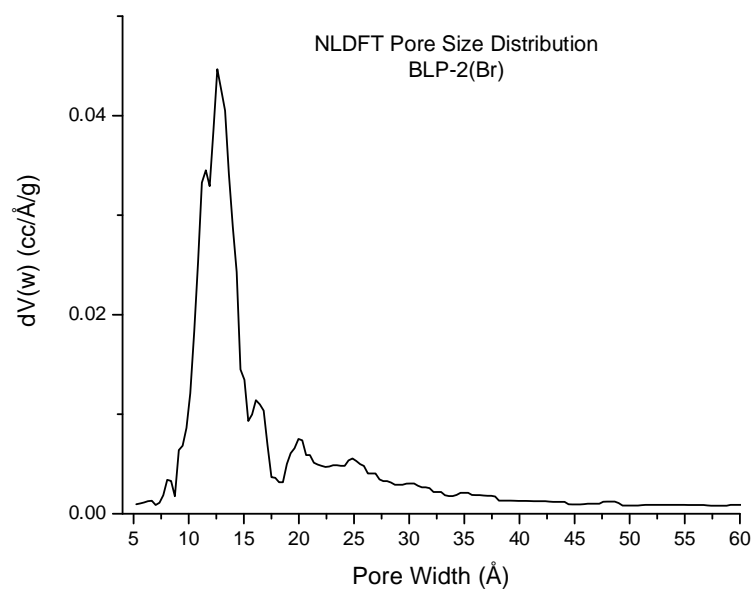


**Figure 51.** Pore Size Distribution for BLP-2(Cl).

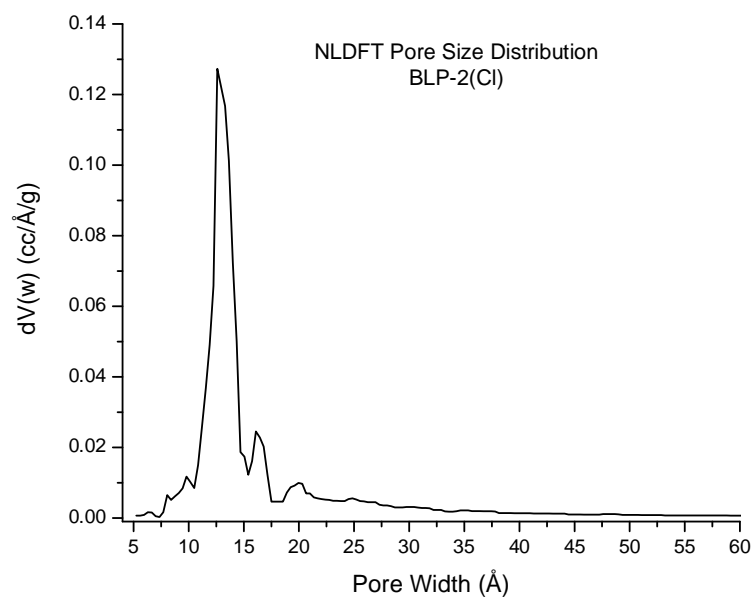


**Figure 52.** Pore Size Distribution for BLP-10(Br).

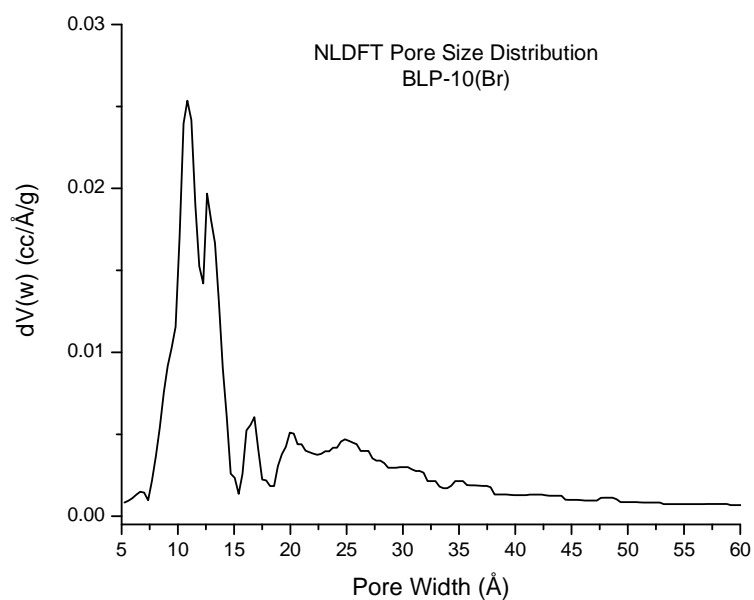


**Figure 53.** Pore Size Distribution for BLP-10(Cl).

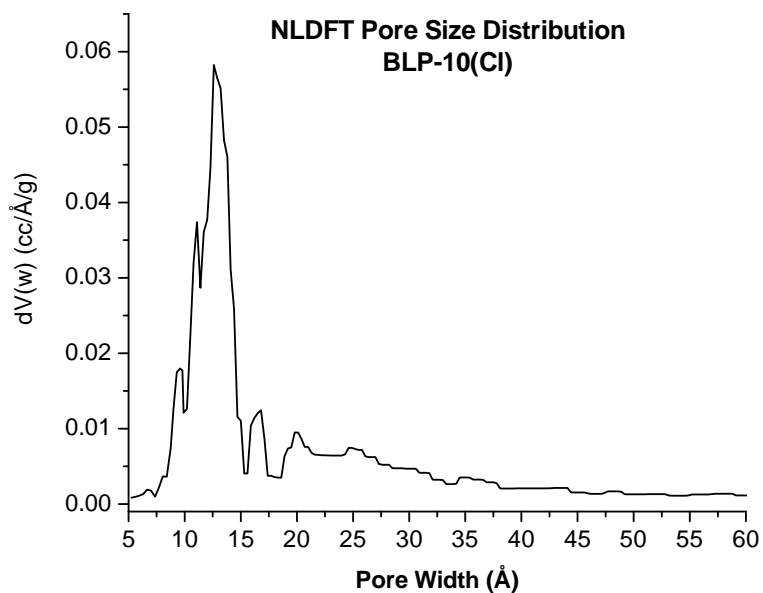
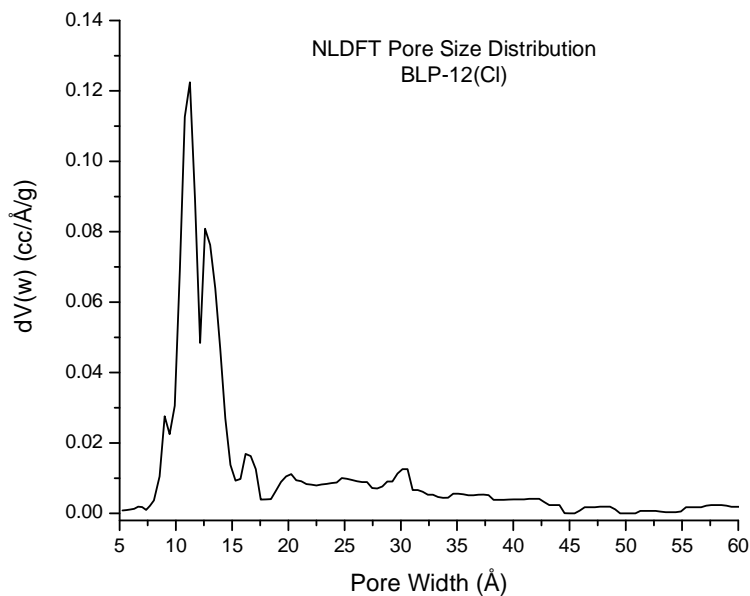


**Figure 54.** Pore Size Distribution for BLP-12(Cl).



As stated earlier, the calculation of both Langmuir and BET surface areas are based on the intercept of a  $y = mx + b$  type of curve. Additionally, the calculations of pore size



distribution by NLDFT are based on the applicability of the method to fit to the experimental data. As such, the graphical comparison for the method fitting of the NLDFT calculations as well as the curves for both Langmuir and BET calculations are shown in Figures 55-75.

**Figure 55.** NLDFT calculated isotherm for BLP-1(Br) overlaid with the experimental nitrogen isotherm. A fitting error less than 1% indicates validity of the model.

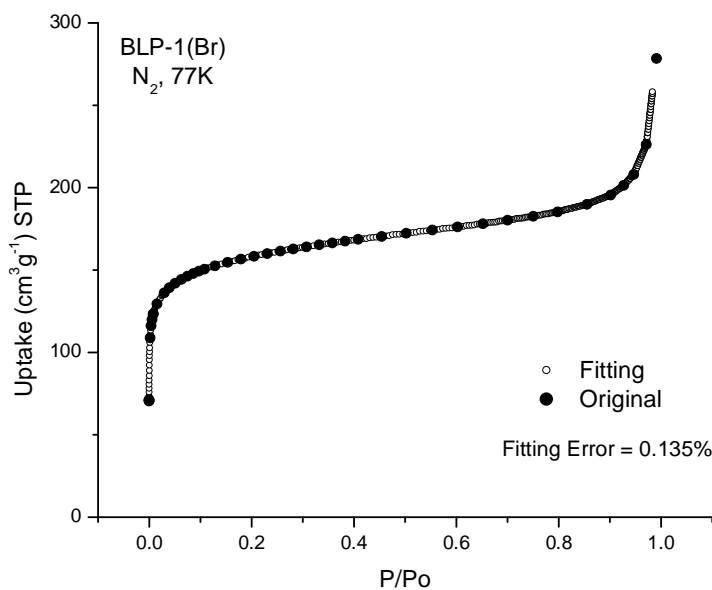


**Figure 56.** Langmuir plot for BLP-1(Br) calculated from the nitrogen adsorption in the range 0.06-0.30  $P/P_o$ .

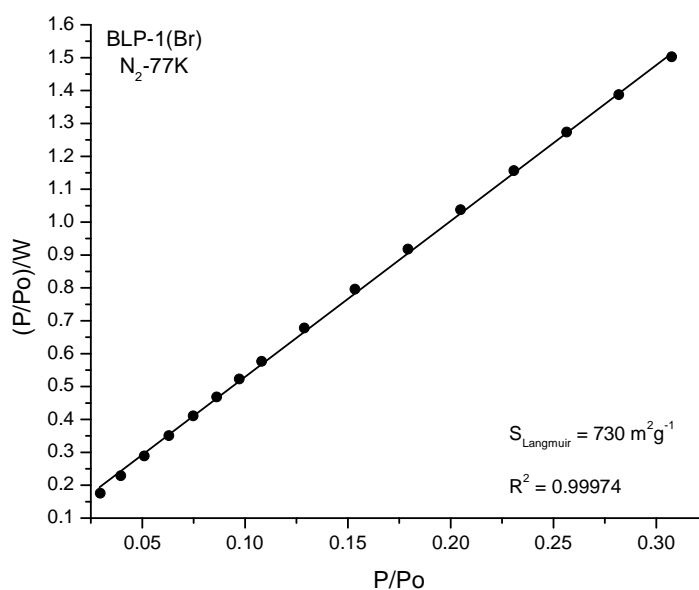


**Figure 57.** Multipoint BET plot for BLP-1(Br) calculated from the nitrogen adsorption in the range 0.02-0.20  $P/P_o$ .

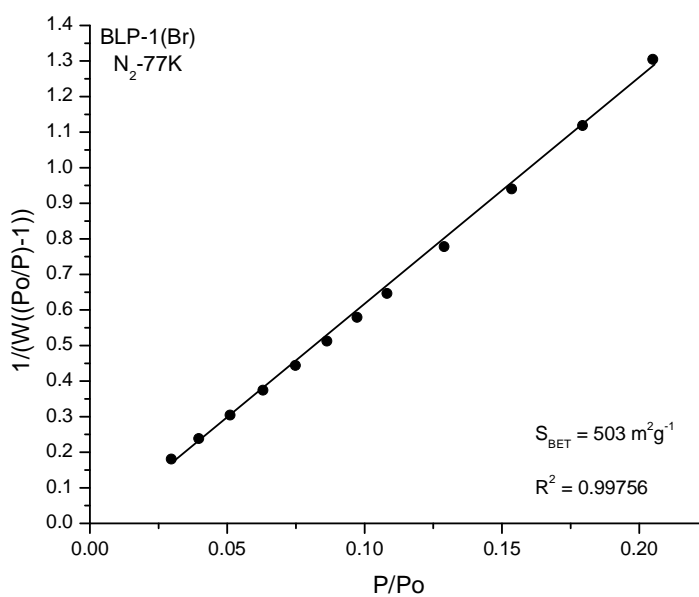


**Figure 58.** NLDFT calculated isotherm for BLP-1(Cl) overlaid with the experimental nitrogen isotherm. A fitting error less than 1% indicates validity of the model.

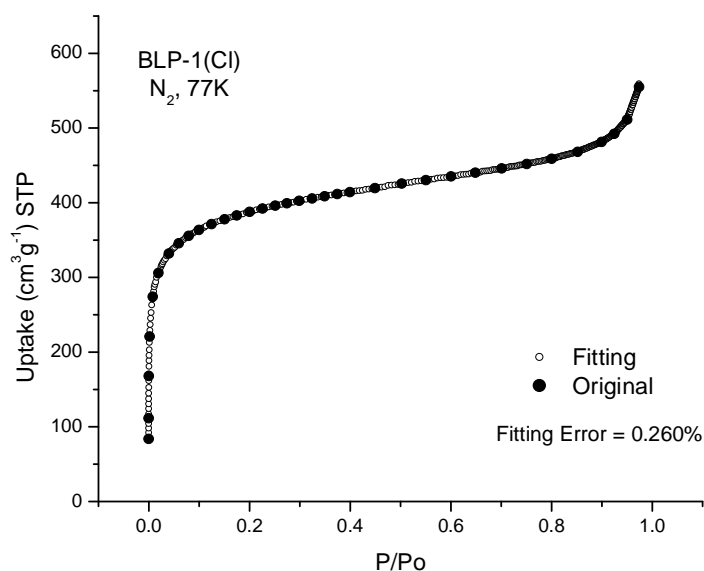


**Figure 59.** Langmuir plot for BLP-1(Cl) calculated from the nitrogen adsorption in the range 0.06-0.30 P/P<sub>0</sub>.

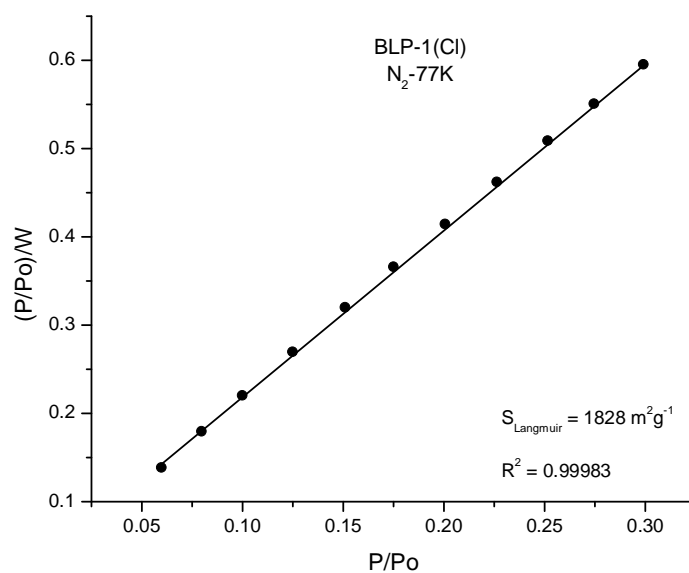


**Figure 60.** Multipoint BET plot for BLP-1(Cl) calculated from the nitrogen adsorption in the range 0.02-0.20  $P/P_o$ .

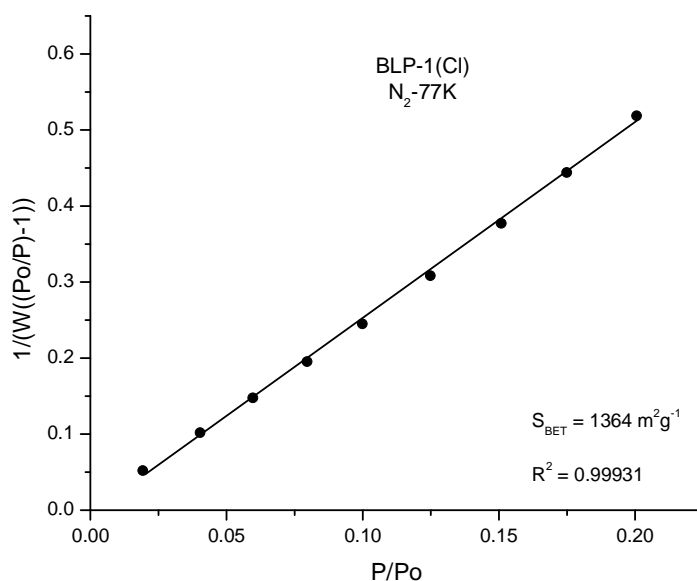


**Figure 61.** NLDFT calculated isotherm for BLP-2(Br) overlaid with the experimental nitrogen isotherm. A fitting error less than 1% indicates validity of the model.

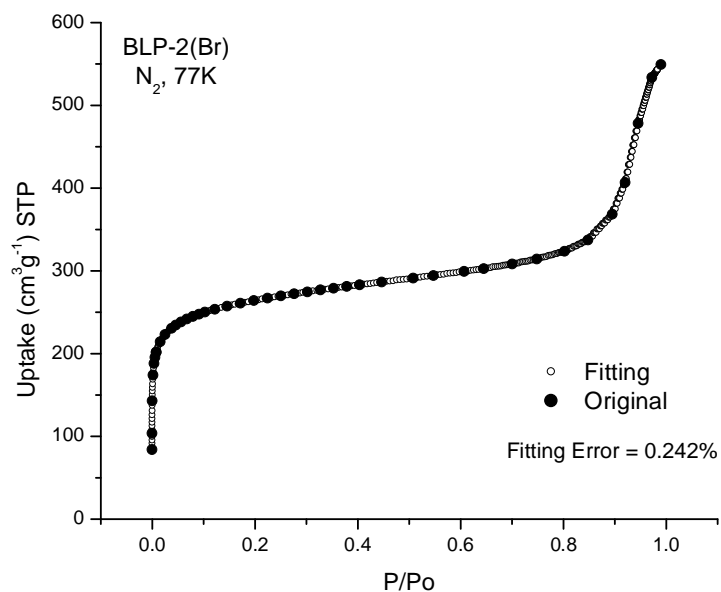


**Figure 62.** Langmuir plot for BLP-2(Br) calculated from the nitrogen adsorption in the range 0.06-0.30  $P/P_o$ .

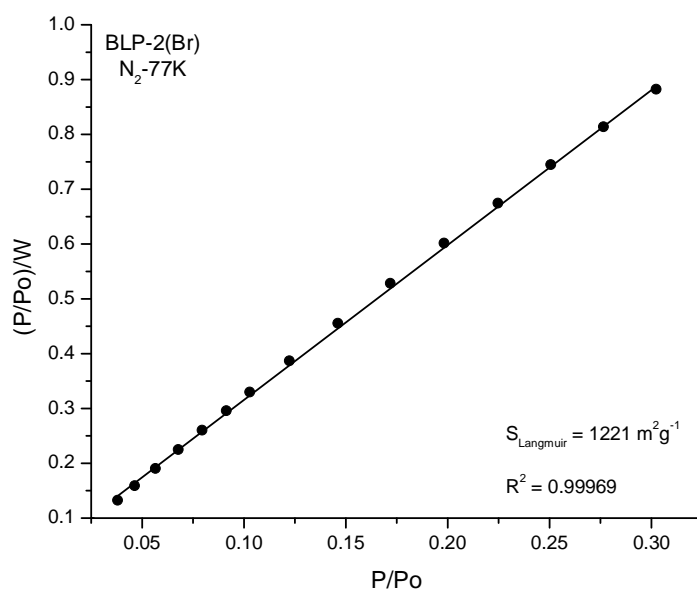


**Figure 63.** Multipoint BET plot for BLP-2(Br) calculated from the nitrogen adsorption in the range 0.02-0.20  $P/P_o$ .

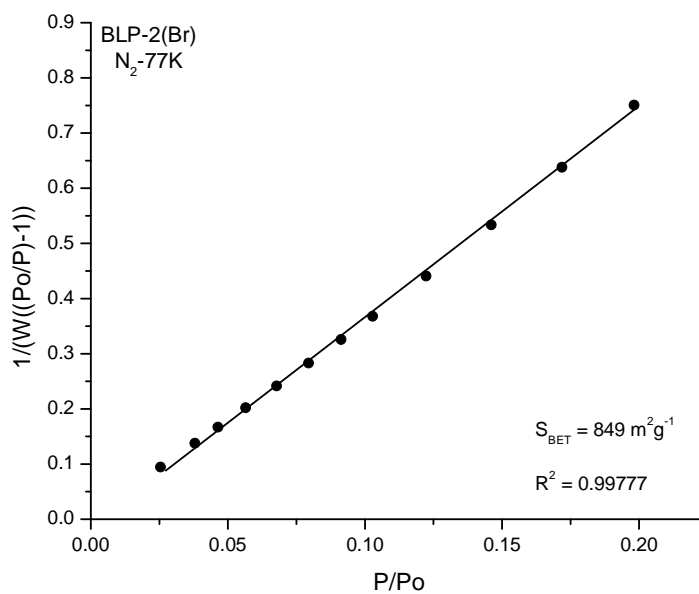


**Figure 64.** NLDFT calculated isotherm for BLP-2(Cl) overlaid with the experimental nitrogen isotherm. A fitting error less than 1% indicates validity of the model.

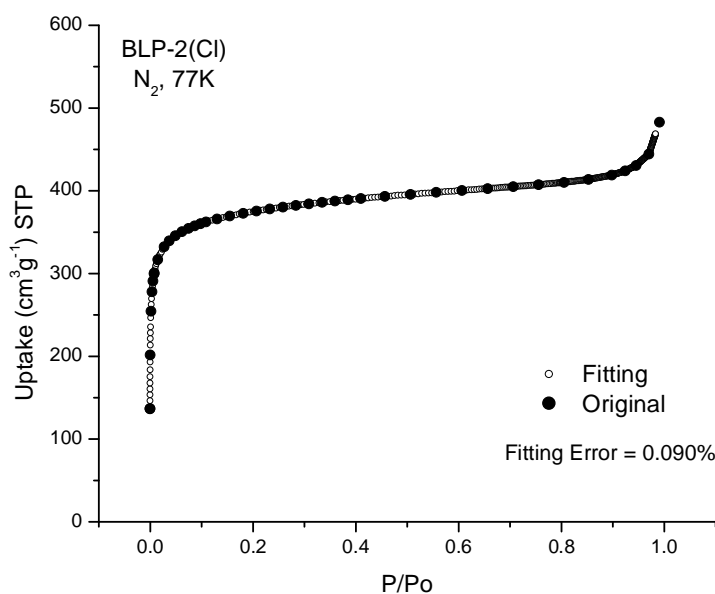


**Figure 65.** Langmuir plot for BLP-2(Cl) calculated from the nitrogen adsorption in the range 0.06-0.30 P/P<sub>0</sub>.

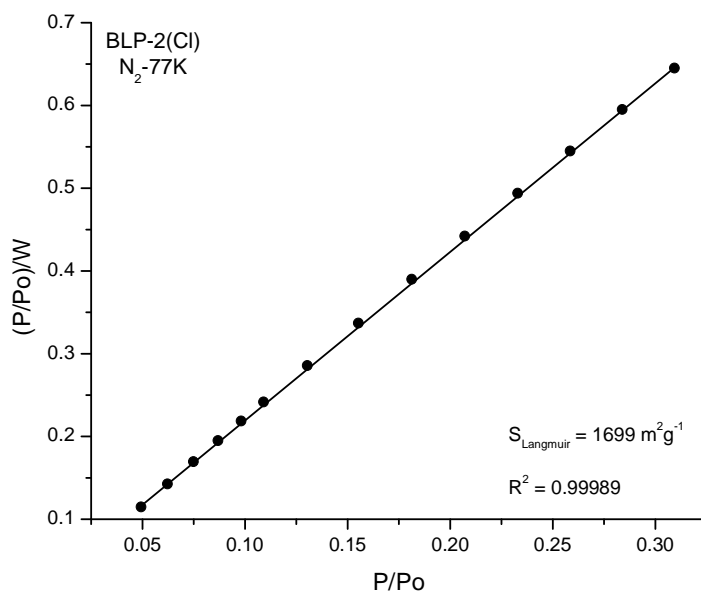


**Figure 66.** Multipoint BET plot for BLP-2(Cl) calculated from the nitrogen adsorption in the range 0.02-0.20  $P/P_o$ .

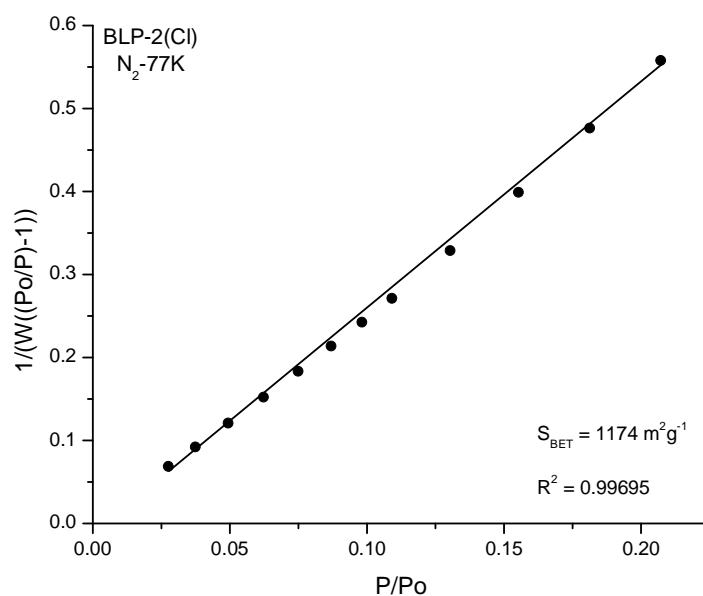


**Figure 67.** NLDFT calculated isotherm for BLP-10(Br) overlaid with the experimental nitrogen isotherm. A fitting error less than 1% indicates validity of the model.

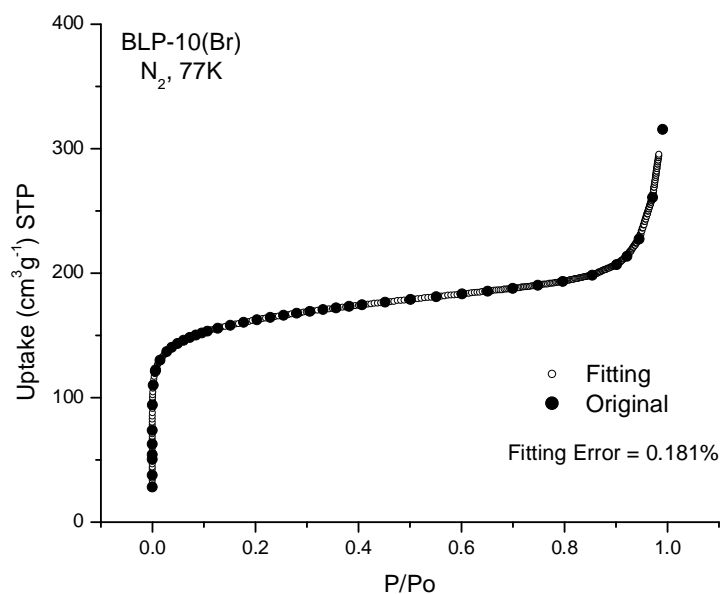


**Figure 68.** Langmuir plot for BLP-10(Br) calculated from the nitrogen adsorption in the range 0.06-0.30  $P/P_o$ .

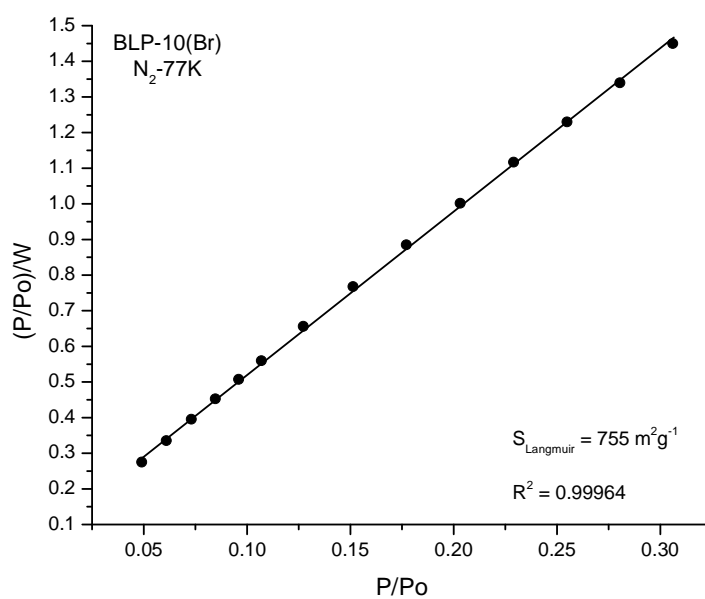


**Figure 69.** Multipoint BET plot for BLP-10(Br) calculated from the nitrogen adsorption in the range 0.02-0.20  $P/P_o$ .

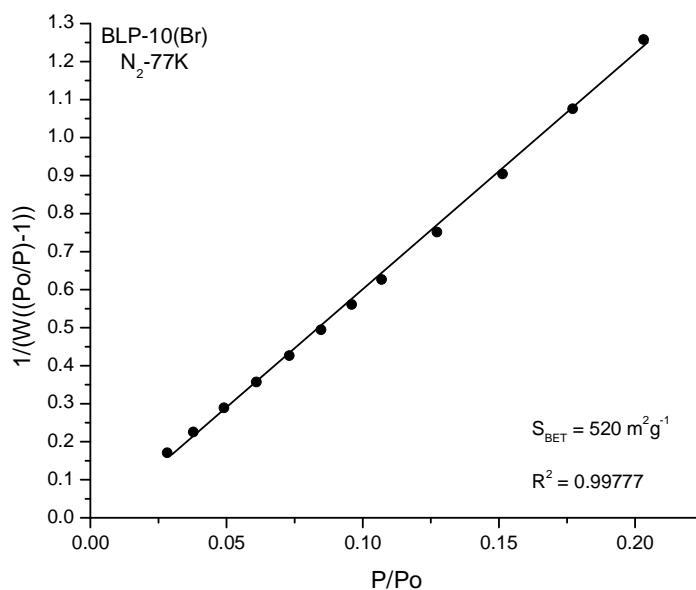




**Figure 70.** NLDFT calculated isotherm for BLP-10(Cl) overlaid with the experimental nitrogen isotherm. A fitting error less than 1% indicates validity of the model.

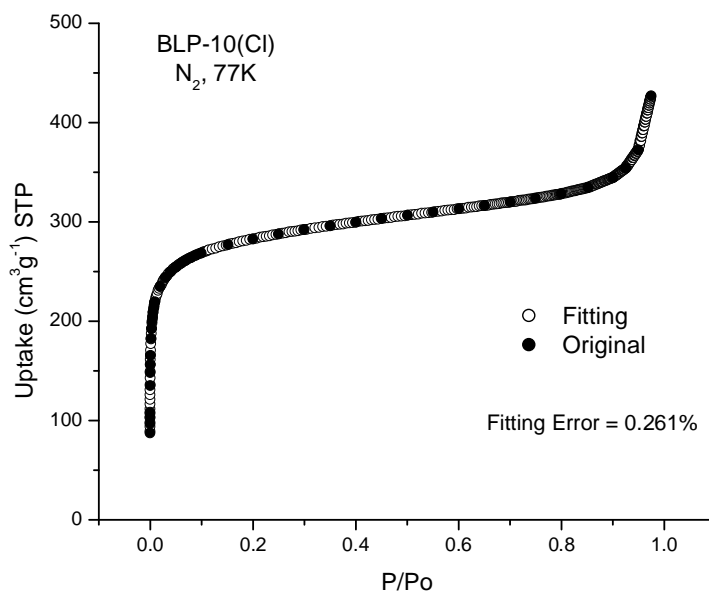


**Figure 71.** Langmuir plot for BLP-10(Cl) calculated from the nitrogen adsorption in the range 0.06-0.30 P/P<sub>0</sub>.

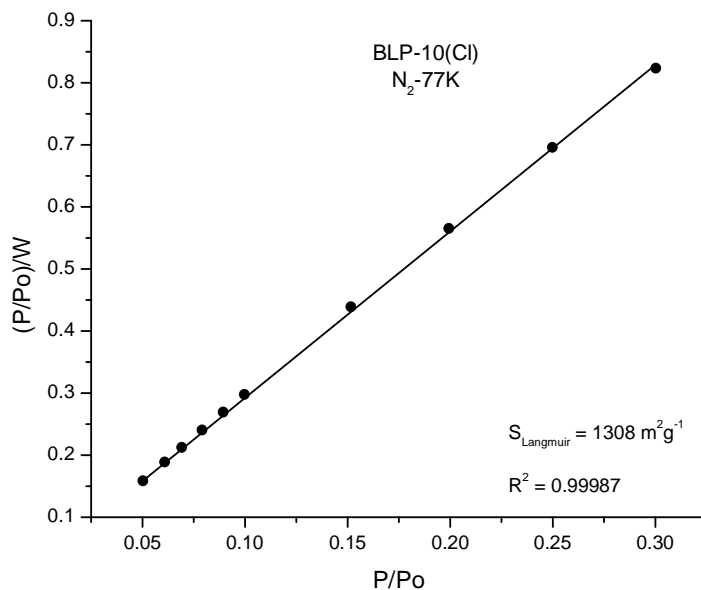


**Figure 72.** Multipoint BET plot for BLP-10(Cl) calculated from the nitrogen adsorption in the range 0.02-0.20  $P/P_o$ .

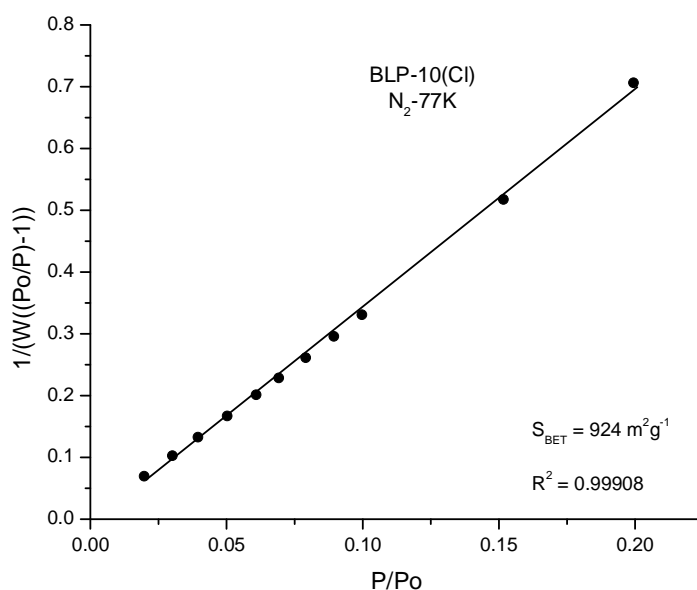


**Figure 73.** NLDFT calculated isotherm for BLP-12(Cl) overlaid with the experimental nitrogen isotherm. A fitting error less than 1% indicates validity of the model.

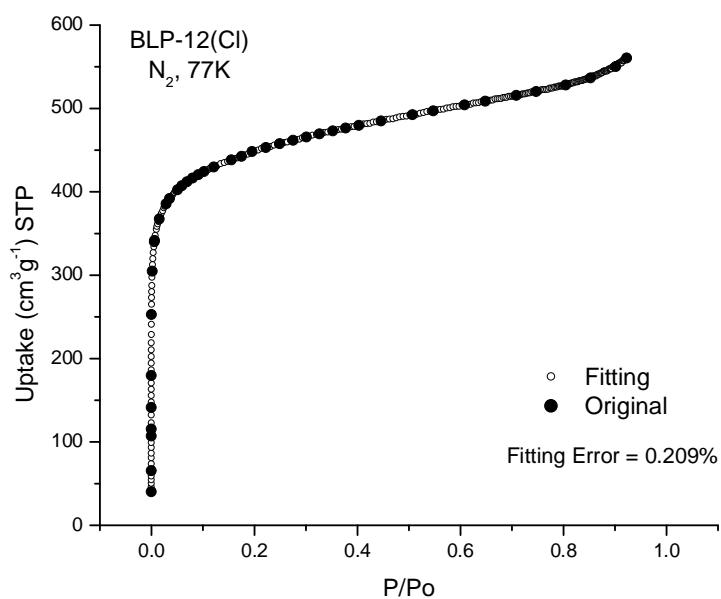


**Figure 74.** Langmuir plot for BLP-12(Cl) calculated from the nitrogen adsorption in the range 0.06-0.30  $P/P_o$ .

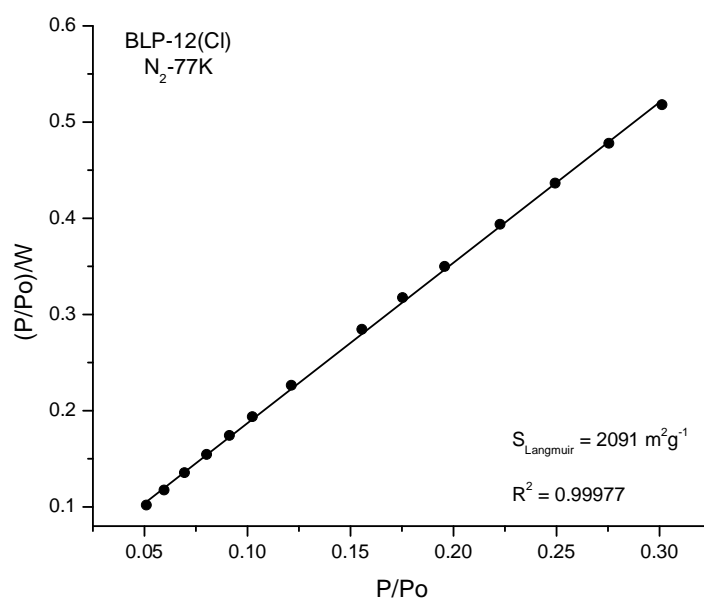
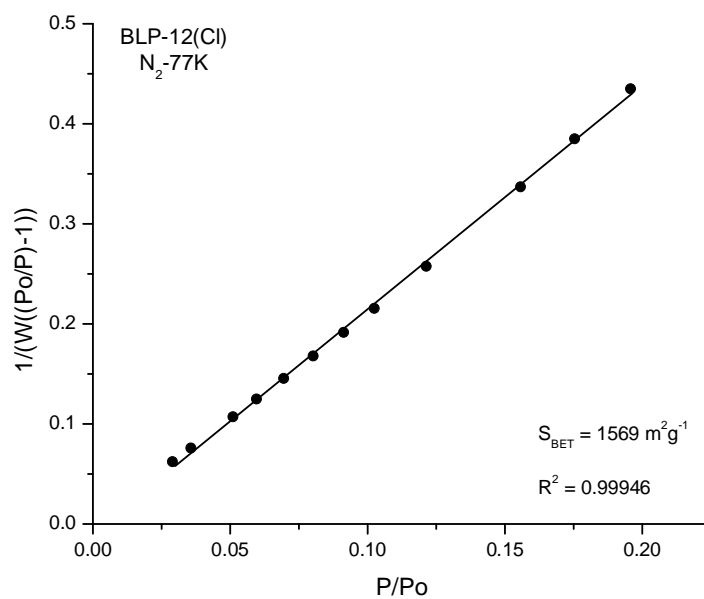


**Figure 75.** Multipoint BET plot for BLP-12(Cl) calculated from the nitrogen adsorption in the range 0.02-0.20  $P/P_o$ .



### 4.3 Hydrogen, Carbon Dioxide, and Methane Sorption of Halogen-Decorated Borazine-Linked Polymers

To investigate the potential of BLPs in the storage of other gases, sorption experiments on activated samples for hydrogen, carbon dioxide, and methane were performed. Hydrogen isotherms were performed at 77 and 87 K whereas carbon dioxide and methane isotherms were each performed at 273 and 298 K. The combined isotherms for H<sub>2</sub> (Figures 76 and 77), CO<sub>2</sub> (Figures 78 and 79), and CH<sub>4</sub> (Figures 80 and 81) are all fully reversible illustrating the facile gaseous release typical for organic polymers which makes them energetically attractive for gas storage applications.

**Figure 76.** Hydrogen isotherms for BLPs at 77K.

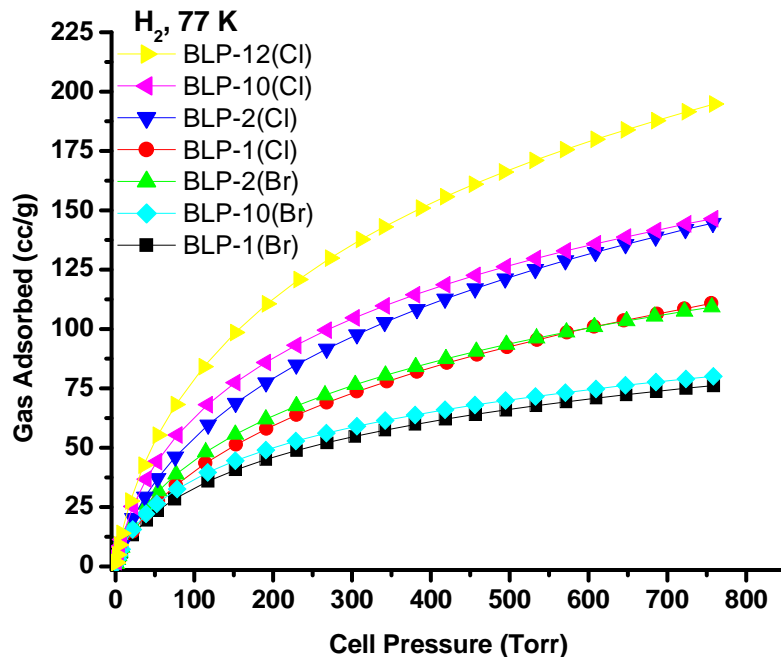


**Figure 77.** Hydrogen isotherms for BLPs at 87K.

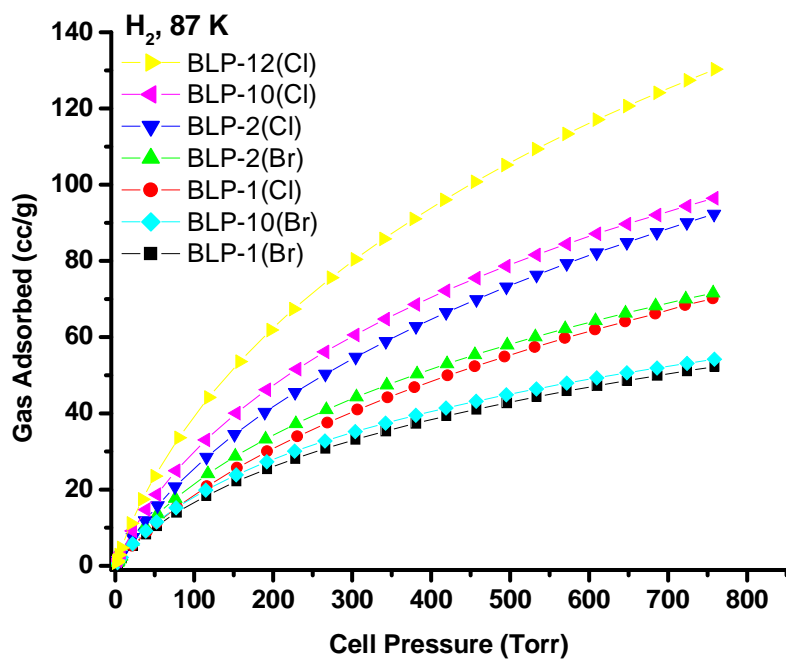


**Figure 78.** Carbon dioxide isotherms for BLPs at 273K.

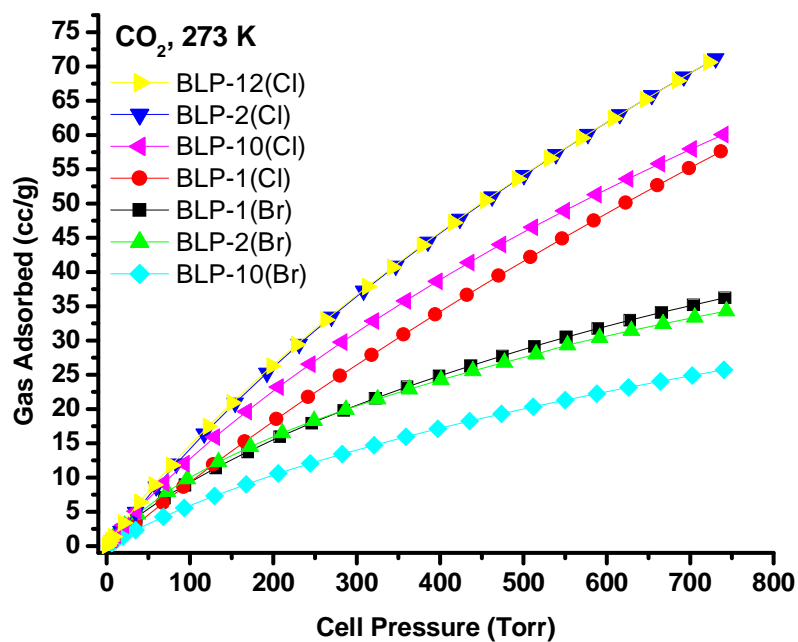


**Figure 79.** Carbon dioxide isotherms for BLPs at 298K.

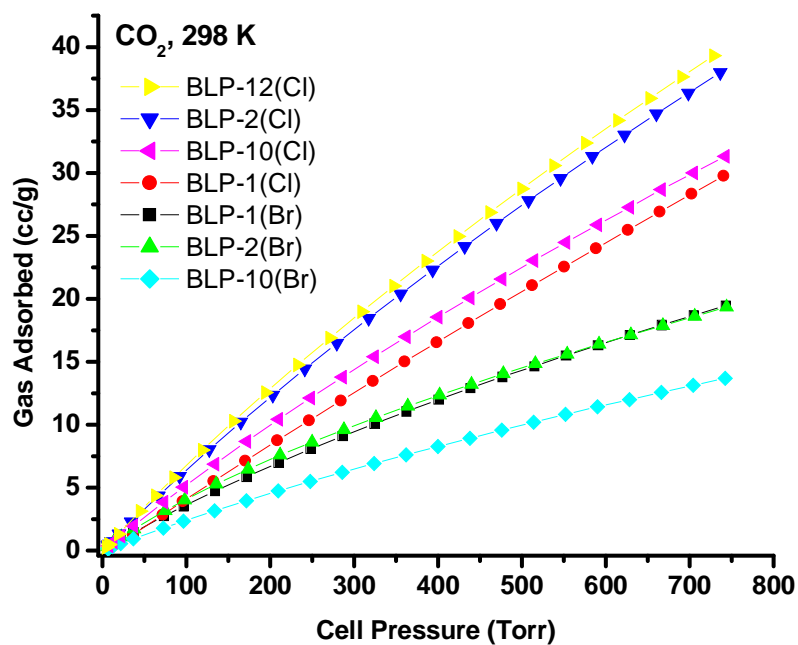


**Figure 80.** Methane isotherms for BLPs at 273K.

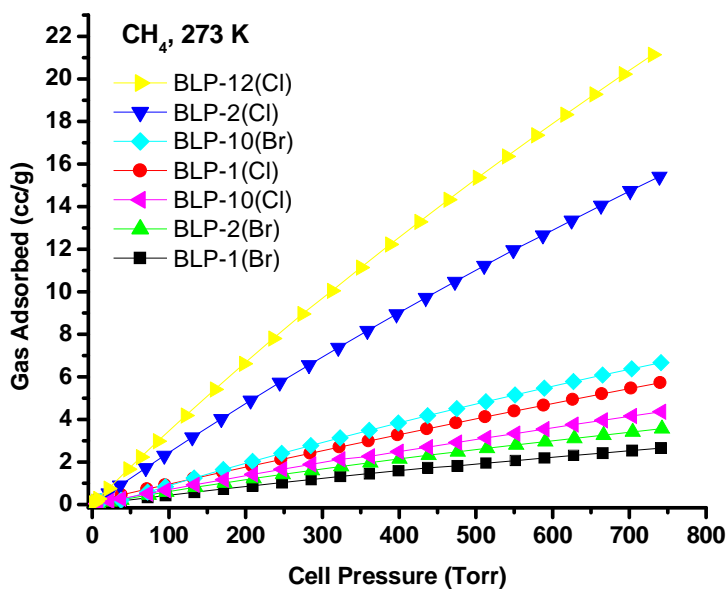


**Figure 81.** Methane isotherms for BLPs at 298K.

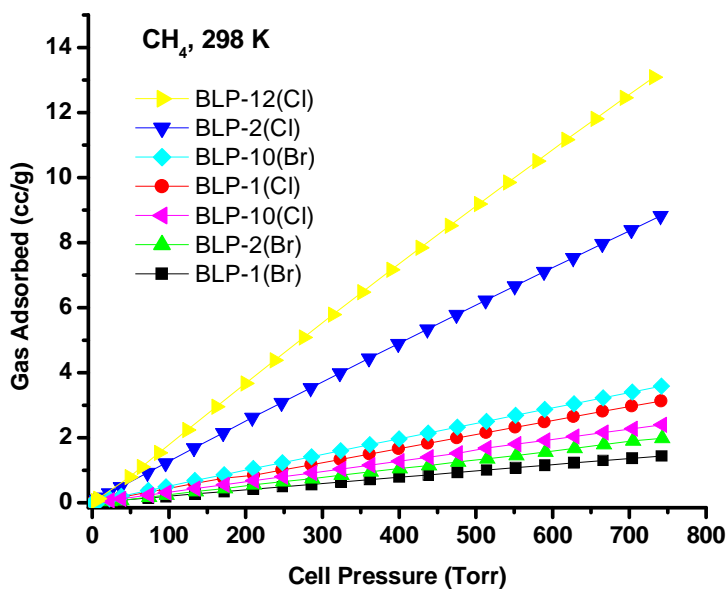


**Table 19.** H<sub>2</sub>, CO<sub>2</sub>, and CH<sub>4</sub> Gas Sorption Uptakes of BLPs.

Polymer	H <sub>2</sub> , 77 K		CO <sub>2</sub> , 273 K		CH <sub>4</sub> , 273 K	
	(wt%)	cc/g	(mg/g)	cc/g	(mg/g)	cc/g
BLP-1(Cl)	1.00	110.8	114	57.6	4.1	5.7
BLP-1(Br)	0.68	76.2	72	36.2	1.9	2.7
BLP-2(Cl)	1.30	144.6	141	71.2	11.1	15.4
BLP-2(Br)	0.98	109.2	68	34.3	2.6	3.6
BLP-10(Cl)	1.32	146.5	119	60.1	3.1	4.4
BLP-10(Br)	0.72	80.0	51	25.7	4.8	6.7
BLP-12(Cl)	1.75	194.8	140	70.6	15.2	21.1

The H<sub>2</sub> uptakes at 77 K listed in Table 19 were generally, but not universally, higher for BLPs of higher surface area, and the extent of halogen decoration seems to have a modest impact on the final uptake. These uptake values for 77 K and 87 K range

between 0.68-1.75 wt% and 0.47-1.15 wt%, respectively. The type of halogen incorporated into the polymer does seem to have an impact as the chlorinated BLPs exhibited higher hydrogen uptake than brominated BLPs in all cases. This observation could potentially be the result of the differences in the electronegativity and spatiality between chlorine and bromine. The higher electronegative chlorine can more readily polarize the dihydrogen molecules allowing for an increase in storage capacity whereas the larger bromine atom sterically shields dihydrogen from adsorbing as efficiently as with chlorine. However, it is not clear how much this contribution is since the higher surface area of chlorinated BLPs versus their brominated counterparts could also affect hydrogen storage.

Despite their amorphous nature, the performance of BLPs in hydrogen storage is very comparable with other organic polymers of similar surface areas.<sup>16, 231-232</sup> For example, under similar conditions the analogous crystalline COF-1 and CTF-1 store 1.28 and 1.55 wt% of H<sub>2</sub>, respectively.<sup>124, 131-132</sup> It is also relevant to compare the hydrogen uptake by BLPs with those of purely organic polymers such as hyper-crosslinked polymer networks synthesized by the self-condensation of bis-chloromethyl monomers (0.89-1.69 wt%),<sup>233</sup> nitrogen-linked nanoporous networks of aromatic rings (0.01-0.85 wt%),<sup>234</sup> and polymers of intrinsic microporosity (PIMs) which recently have been reported to be among the best organic polymers for hydrogen uptake (0.74-1.83 wt%).<sup>235</sup> Moreover, BLPs show similar H<sub>2</sub> uptake as those reported for crystalline and high surface area COFs (0.9-1.2 wt%) and the amorphous porous aromatic framework, PAF-1 (1.5 wt%).<sup>132, 236</sup> In contrast, activated carbons such as PICACTIF-SC, AX-21, and zeolitic-templated carbons show a noticeably higher uptake (1.90, 2.40, and 2.60



wt%, respectively) due to their ultrafine pores which are typically less than 1 nm in size.<sup>143</sup>

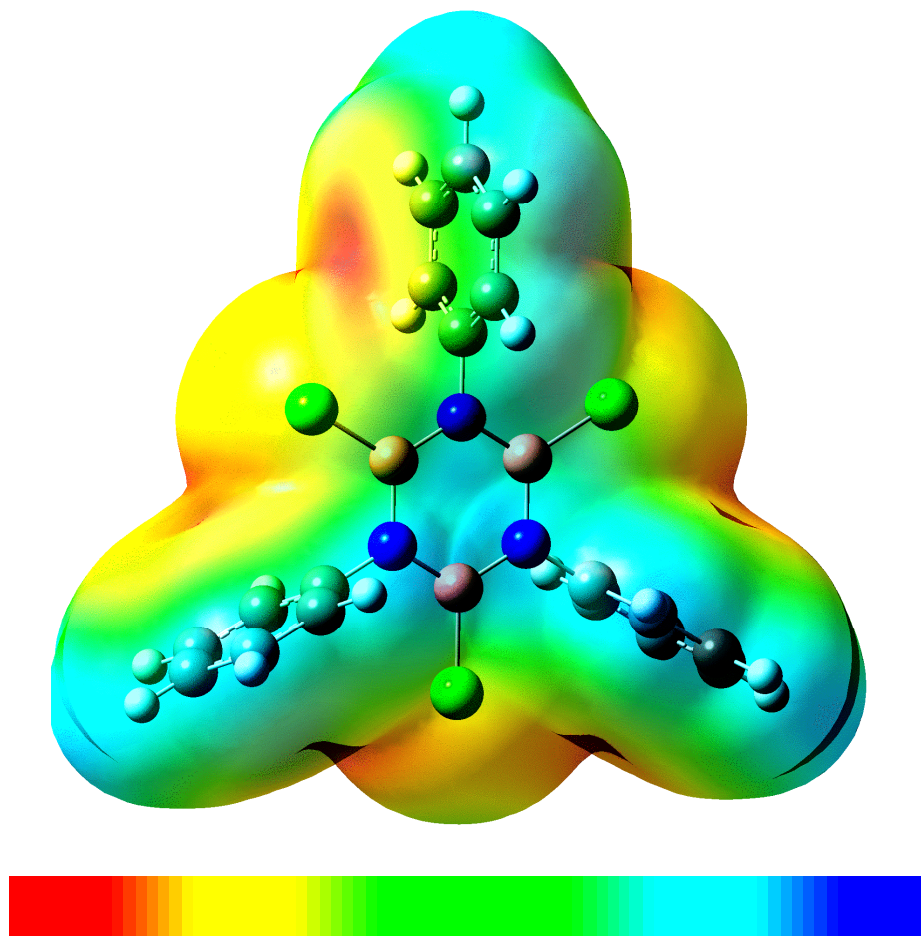
The order with which BLPs store CO<sub>2</sub> at 273 K (Table 19) is in much the same fashion as in the case of H<sub>2</sub>. The CO<sub>2</sub> values were generally, but not universally, higher for BLPs of higher surface area, and again the extent of halogen decoration seems to have a modest impact on the final uptake. These values range between 51-141 mg/g and 27-78 mg/g at 273 K and 298 K, respectively. Additionally just like for hydrogen, the type of halogen incorporated into the polymer does seem to have an impact as the chlorinated BLPs exhibit higher carbon dioxide uptake than brominated BLPs in all cases. These uptakes are comparable to the values reported for COFs,<sup>132</sup> imine-lined organic cages,<sup>237</sup> ZIFs,<sup>238-240</sup> supramolecular organic frameworks (SOFs),<sup>241</sup> and diimide polymers<sup>242</sup> but are less than that of benzimidazole-linked polymers (BILPs),<sup>156</sup> CO<sub>2</sub>-selective MOFs,<sup>151-155, 243</sup> and ZTFs.<sup>150</sup>

The CH<sub>4</sub> isotherms, however, reveal that BLPs exhibit only a meager methane uptake. These values (Table 19) in the range of 1.9-15.2 mg/g and 1.0-9.4 mg/g at 273 and 298 K, respectively, make BLPs largely unremarkable as a methane storage media with many porous polymers having been shown to exhibit higher values including COFs,<sup>132</sup> MOFs,<sup>244-246</sup> porous coordinated networks (PCNs),<sup>247</sup> and commercially available carbons.<sup>248</sup> However, the great disparity in methane uptake versus carbon dioxide uptake makes BLPs good candidates for CO<sub>2</sub>/CH<sub>4</sub> selectivity as is discussed in Chapter 6.

As mentioned in Chapter 1, the polarity of the surface of a polymer can have a significant impact on the overall uptakes for polarizable gas molecules. Among these

molecules are hydrogen and carbon dioxide. As such, a pictorial assessment of the electron density of the borazine building block was investigated (Figure 82). In the interest of simplification, a chlorinated borazine monomer surrounded by three phenyl rings was used. In Figure 82, which shows areas of high electron density in red and yellow, the regions surrounding the chlorine atoms exhibit high levels of electron density. Coupling this region with the low electron density shown for the borazine ring itself illustrates areas of exceptional polarity for gas storage potential. This concept of molecular affinity with the borazine ring is extrapolated in Section 5.3 of Chapter 5.

**Figure 82.** Electron Density of a Monomeric Chlorinated Borazine. Red represents areas of high electron density. Blue atoms: N; adjacent pink/orange atoms: B; lime green atoms: chlorine; with kaleidoscopic phenyl rings bonded through the N atoms.



## Chapter 5

# Experimental and Theoretical Calculations for the Isostatic Heat of Adsorption of Hydrogen, Carbon Dioxide, and Methane with Halogenated Borazine-Linked Polymers

### 5.1 Introduction

Isostatic heat of adsorption,  $Q_{st}$ , represents a useful tool to assess a polymer's capabilities to store a particular gas. Whereas the actual storage capabilities are similar in concept to the application-based targets for storage media, oftentimes the storage numbers reported in literature can be misleading. A great example of this effect is with hydrogen storage. The United States Department of Energy has set forth performance targets for the storage of enough hydrogen to overcome these limitations at 5.5 wt%  $H_2$  and 40 g  $H_2$ /L by 2015 and at 7.5 wt%  $H_2$  and 70 g  $H_2$ /L as an ultimate goal. These system targets require energetically favorable conditions (i.e. under ambient temperatures). The industry standard for reported hydrogen storage values in literature, however, is at 77 K. Although many of these reported values meet and exceed the Department of Energy's targets, the storage capabilities of these media under ambient temperatures is meager compared to the final goals. As a means of standardization, isosteric heat of adsorption is used. Of important note is that according to a report by Svec et. al.,<sup>232</sup> the necessary hydrogen isosteric heat of adsorption for sufficient performance is between 13-20 kJ/mol. This number agrees well with another

approximation by Bhatia that estimated a requisite value of 15.1 kJ/mol.<sup>249</sup> Current investigations are still well below these values as is expected owing to the low room temperature hydrogen uptakes reported thus far.

Calculation of isosteric heat of adsorption is based on experimental isotherms. Often, these isotherms are fitted to mathematical models that are intended to describe the data. In some cases, more than one isotherm is required to calculate  $Q_{st}$ . For others using more than one isotherm is encouraged to enhance the accuracy of the isothermal fitting parameters.

Calculating isosteric heat of adsorption is typically accomplished by one of three methods: (1) Langmuir model, (2) Langmuir-Freundlich model, and (3) virial model. In the first two cases, the use of the Clausius-Clapeyron equation evaluates the fitted model. Previously reported investigations<sup>250-251</sup> into the use of the Clausius-Clapeyron equation is based on the following formula:

$$\frac{dP}{dT} = \frac{L}{T^*\Delta V}$$

Here, P is pressure, T is temperature, L is latent heat, and  $\Delta V$  is the change in volume of the phase transition. When applied to the application of gas adsorbed onto the surface of a storage media, the equation derives to:

$$\ln\left(\frac{P_2}{P_1}\right) = \frac{\Delta H_{vap}}{R} \left(\frac{1}{T_1} - \frac{1}{T_2}\right)$$

or

$$\left[ \frac{\delta \ln P}{\delta \ln (1/T)} \right]_V = \frac{-Q_{st}}{R}$$

The partial derivative of the Langmuir or Langmuir-Freundlich model yields a calculable isosteric heat of adsorption,  $Q_{st}$ , based on the fitting parameters. The fitted models are then evaluated for isotherms taken at multiple temperatures and analyzed by the above equation. In the case of the Langmuir model, experimental data is fitted according to the equation:

$$q = \frac{q_{sat} * bp}{1 + bp}$$

In this equation,  $q$  is the gas uptake,  $q_{sat}$  is the saturation gas uptake,  $p$  is pressure, and  $b$  is a temperature-dependent fitting parameter. Rearrangement of the above equation in conjunction with derivation from the Clausius-Clapeyron equation yields:<sup>252-253</sup>

$$Q_{st} = RT^2 \left( \frac{\delta \ln p}{\delta T} \right)_q$$

In this author's opinion, however, the use of the Langmuir model is insufficient to describe most isothermal data within the realm of gas storage on porous media. Visual inspection of the graphical fittings reveals that such practices typically ill-describes the early and later stages of the isotherms while overcompensating for the intermediate stages.<sup>254</sup> Employing the use of the Langmuir-Freundlich model, which is a slight deviation from the base Langmuir fitting, affords a much more accurate description of the data from both a graphical as well as statistical standpoint. This model is represented in the following formula:

$$q = \frac{q_{sat} * bp^{(1/c)}}{1 + bp^{(1/c)}}$$

From this formula where  $c$  is a new fitting parameter, the Clausius-Clapeyron equation can be applied.

Another means of calculating isosteric heat of adsorption is through the virial method.<sup>255-258</sup> A virial expansion is a summation equation for which, in this case, the number of summation iterations is unknown:

$$\ln P = \ln N + (1/T) \sum_{i=0}^m a_i N^i + \sum_{i=0}^n b_i N^i$$

In this equation,  $P$  is pressure in torr,  $T$  is temperature in Kelvin, and  $N$  is the mmol of gas adsorbed per gram of sample. The values for  $m$  and  $n$  are undefined (hence, the unknown number of summation iterations) and are varied such that  $m \geq n$  and result in the best fit as determined by the sum of the squares of the errors. The values for  $a_0$ ,  $a_1, \dots, a_m$  and  $b_0$ ,  $b_1, \dots, b_n$  are fitting parameters for the virial expansion. Following the appropriate fitting, the values for  $a_0$ ,  $a_1, \dots, a_m$  are used in the calculation for the isosteric heat of adsorption,  $Q_{st}$ :

$$Q_{st} = -R \sum_{i=0}^m a_i N^i$$

The value of  $m$  in this case matches the value found for the preceding equation such that all  $a_i$  values are used. The calculated values are then plotted as they relate to the surface coverage,  $N$ , while the isosteric heat of adsorption at the point of zero-coverage is typically reported as a means of comparison.

In the case of the virial-type calculation for the isosteric heat of adsorption, only one temperature is necessary to perform the full calculation. However, the large combination of  $a_i$  and  $b_i$  values for varying  $m$  and  $n$  values results in a very subjective

approach from the researcher's perspective. In order to mitigate, the subjective human element in these calculations, a minimum of two isotherms taken at different temperatures should be performed when utilizing the virial method. This practice of multiple temperature-isotherms would drop the subjectivity of the calculations for the virial method to the point encountered for the Langmuir and Langmuir-Freundlich methods; however, it should be noted that for all three methods, a base level of subjectivity (and consequently ethical dilemmas) still exist. It should also be noted that owing to the larger potential number of fitting parameters, the virial method tends to give a better description of the isothermal data than what is found utilizing the Langmuir or Langmuir-Freundlich models.

## **5.2 Experimental Isostatic Heat of Adsorption of Hydrogen, Carbon Dioxide, and Methane with Halogenated Borazine-Linked Polymers**

Experimental isosteric heat of adsorption for all gases was calculated via the virial method from experimental isotherms. For hydrogen, isotherms were taken at 77 and 87 K; while for carbon dioxide and methane, isotherms were each taken 273 and 298 K. The virial coefficients for all BLPs with all three gases are shown in Table 20 and were calculated with the computational help of Dr. Enrique Campos-Nanez at George Washington University. The resulting zero-coverage  $Q_{st}$  values for hydrogen, carbon dioxide, and methane are relayed in Table 21.



**Table 20.** Virial fitting coefficients of BLPs.

Polymer	Gas	$a_0$	$a_1$	$a_2$	$a_3$	$a_4$	$b_0$	$b_1$	$b_2$	$b_3$
BLP-1(Br)	H <sub>2</sub>	-864	102	-15.2	1.10		14.3	-0.46	0.09	
	CO <sub>2</sub>	-3711	668	-91.3	21.8		18.8	-1.53		
	CH <sub>4</sub>	-2539	1779	-252	79.9	-16.0	17.8	-4.49		
BLP-1(Cl)	H <sub>2</sub>	-859	87.8	-10.4	0.46		14.3	-0.55	-0.06	
	CO <sub>2</sub>	-2686	137	3.99			15.3	-0.46		
	CH <sub>4</sub>	-2337	308	-13.7	9.10		16.4	-0.93	1.38	
BLP-2(Br)	H <sub>2</sub>	-906	96.8	-13.1	0.51		14.6	-0.60	0.09	
	CO <sub>2</sub>	-3839	755	-156	40.0		19.0	-1.42		
	CH <sub>4</sub>	-2606	1818	169	44.8	8.01	17.7	-5.24		
BLP-2(Cl)	H <sub>2</sub>	-872	73.2	-7.77	0.22		14.1	-0.47	0.06	
	CO <sub>2</sub>	-2905	128	-44.3	17.1	-2.34	15.5	-0.15		
	CH <sub>4</sub>	-2136	286	-56.3			14.6	-0.61	-0.03	
BLP-10(Br)	H <sub>2</sub>	-925	85.4	-7.90	0.51		14.9	-0.31	0.04	
	CO <sub>2</sub>	-3451	765	-7.08			18.3	-1.91	-0.19	
	CH <sub>4</sub>	-2062	220	-27.8	0.26		15.3	-0.68	0.02	
BLP-10(Cl)	H <sub>2</sub>	-901	46.1	-2.80	0.12		14.2	-0.17	0.01	
	CO <sub>2</sub>	-3423	392	-13.5	0.80		17.5	-1.09		
	CH <sub>4</sub>	-2432	776	-29.4			17.0	-1.90		
BLP-12(Cl)	H <sub>2</sub>	-855	49.9	-3.99	0.10		13.4	-0.28	0.03	
	CO <sub>2</sub>	-2843	209	-158	70.3	1.03	15.3	-0.57	0.61	-0.28
	CH <sub>4</sub>	-2245	965	-415	-55.6	9.46	14.7	-3.95	2.97	-0.75

**Table 21.** Zero-coverage isosteric heats of adsorption,  $Q_{st}$ , of  $H_2$ ,  $CO_2$ , and  $CH_4$  for BLPs.

Polymer	$H_2$ (kJ/mol)	$CO_2$ (kJ/mol)	$CH_4$ (kJ/mol)
BLP-1(Cl)	7.06	22.2	19.4
BLP-1(Br)	7.14	30.7	21.0
BLP-2(Cl)	7.19	24.1	17.7
BLP-2(Br)	7.49	31.7	21.7
BLP-10(Cl)	7.46	28.3	20.2
BLP-10(Br)	7.65	28.6	17.1
BLP-12(Cl)	7.08	23.6	18.6

At zero-coverage, the hydrogen isosteric heat of adsorption ranges from 7.06 to 7.65 kJ/mol and drops gradually with increasing surface coverage to reach values that fall between 5.2 and 5.7 kJ/mol as is illustrated in Figure 83. These  $Q_{st}$  values are similar to values reported for organic polymers such as POFs (5.8-8.3 kJ/mol),<sup>146-147</sup> 2D COFs (6.0-7.0 kJ/mol),<sup>132</sup> polyimide networks (5.3-7.0 kJ/mol),<sup>259</sup> PPNs (5.5-7.6 kJ/mol),<sup>260</sup> BILP-1 (7.9 kJ/mol),<sup>156</sup> and BPL carbon (8.0 kJ/mol);<sup>141, 255, 257-258</sup> furthermore, these values are much higher than what has been reported for the 3D COFs COF-102 (3.9 kJ/mol) and COF-103 (4.4 kJ/mol)<sup>132</sup> as well as the carbon-based porous aromatic framework PAF-1 (4.6 kJ/mol).<sup>236</sup>

The  $CO_2$  zero-coverage  $Q_{st}$  values for BLPs (Figure 84) range from 22.2 to 31.7 kJ/mol. These values typically drop off in a near-linear fashion with the exception of BLP-12(Cl) which exhibits a progressively steepening drop in affinity beginning around

80 mg/g of CO<sub>2</sub> coverage. These zero-coverage values, particularly those on the higher end, are comparable to BILPs,<sup>156</sup> CO<sub>2</sub>-selective MOFs,<sup>151-152</sup> and ZTFs which feature amine functionality that enhances CO<sub>2</sub> affinity.<sup>150</sup> The CH<sub>4</sub> zero-coverage isosteric heats of adsorption for BLPs (17.1-21.7 kJ/mol) (Figure 85) are again comparable to COFs (8-19 kJ/mol),<sup>132</sup> BILPs (13.2-16.6 kJ/mol),<sup>156</sup> and BPL carbon (20 kJ/mol).<sup>257-258</sup> The higher affinity in BLPs for carbon dioxide over methane results from the non-polar nature of methane versus the polarizability of carbon dioxide. Interestingly, this difference in polarizability contributes positively to BLPs' capabilities in CO<sub>2</sub>/CH<sub>4</sub> selectivity and separation studies.

**Figure 83.** Hydrogen isosteric heat of adsorption curves of BLPs.

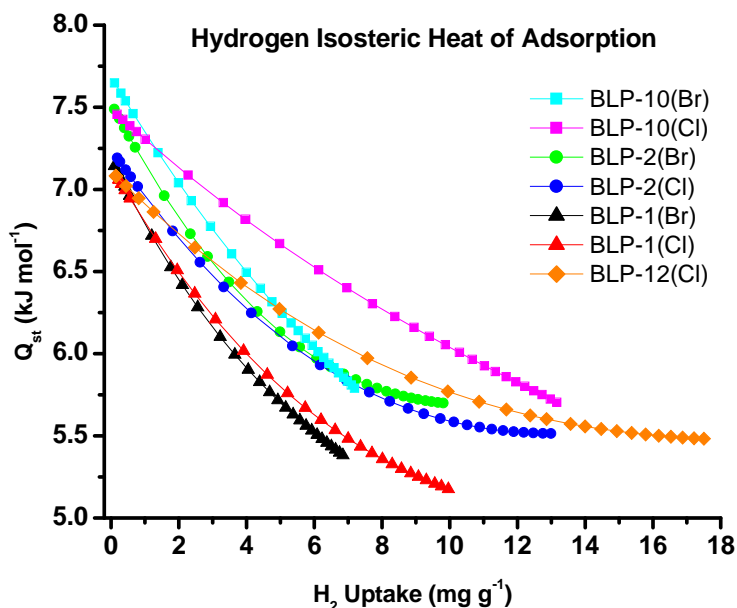


**Figure 84.** Carbon dioxide isosteric heat of adsorption curves of BLPs.

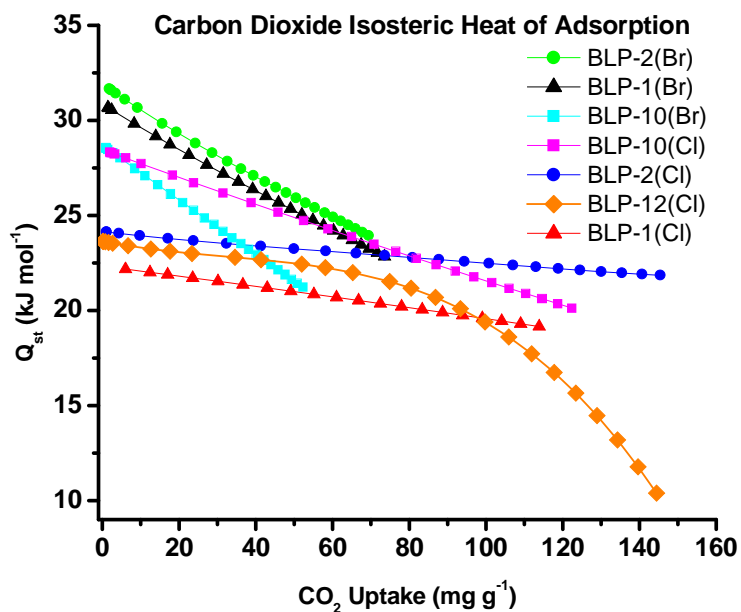
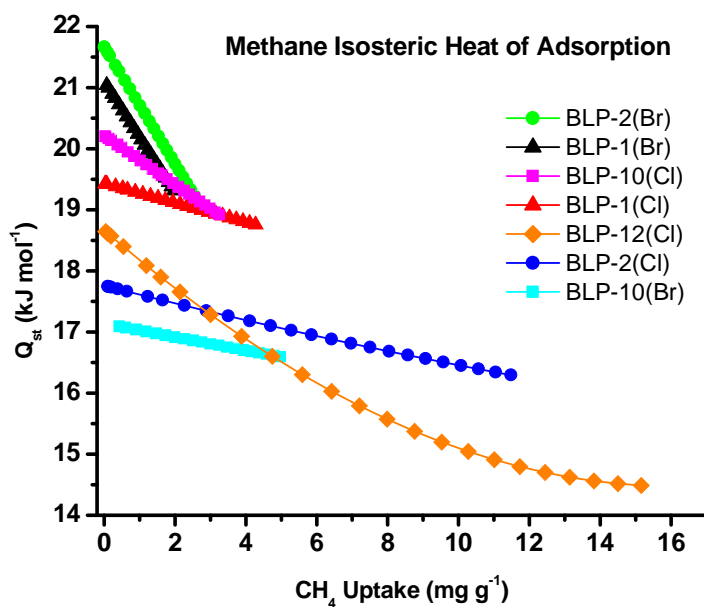


**Figure 85.** Methane isosteric heat of adsorption curves of BLPs.



### 5.3 Theoretical Calculations for the Isothermic Heat of Adsorption of Hydrogen, Carbon Dioxide, and Methane with Halogenated Borazine-Linked Polymers

To gain a greater insight into the binding of small gases (i.e.  $\text{H}_2$ ,  $\text{CO}_2$ , and  $\text{CH}_4$ ) with BLPs, Dr. Jena's group at Virginia Commonwealth University performed computational investigations for BLPs with  $\text{H}_2$ ,  $\text{CO}_2$ , and  $\text{CH}_4$ . To ease the computational load by reducing the number of applicable atoms, the polymeric system was simplified to a monomeric chlorinated borazine bound to three phenyl rings through the nitrogen atoms. As a result, this system is designed to mimic the binding with small gases to BLP-10(Cl). The binding affinities,  $E_b$ , of hydrogen, carbon dioxide, and methane molecules attached to the chlorinated borazine ring were calculated by determining the equilibrium geometries and corresponding total energies of these complexes. The binding affinity,  $E_b$ , is defined as the total energy of the chlorinated borazine interacting with the small molecules less the total energies of the individual chlorinated borazine and small gas molecule. All calculations were performed using the density functional theory (DFT) with three different forms for the exchange-correlation potential. These different forms are: (1) the Becke's three parameter hybrid functional for exchange and Lee-Yang-Parr functional for correlation (B3LYP),<sup>261</sup> (2) the local density approximation (LDA) for exchange-correlation potential prescribed by Vosko-Wilk-Nusair (SVWN),<sup>262</sup> and (3) the functional of Zhao and Truhlar (M06)<sup>263</sup> that includes corrections for long range dispersive forces. It should be noted that since the interaction of  $\text{H}_2$ ,  $\text{CO}_2$  or  $\text{CH}_4$  with the chlorinated borazine substrate is expected to be weak, it is necessary to go beyond the generalized gradient functionals that do not include van der Waal's terms and hence underestimate the binding affinities. While LDA also does not include long range

dispersive forces, it is known to over-bind. Thus, it is possible that due to the cancellation of errors, LDA may yield binding affinities that are closer to experiment than the GGA functionals. The *Gaussian 09* package<sup>264</sup> and 6-311+G\*<sup>265-266</sup> basis sets were used for all computations. The convergence in the total energy and force were set at  $1 \times 10^{-6}$  eV and  $1 \times 10^{-2}$  eV/Å, respectively, and the output symmetries were kept at a tolerance of 0.1 using GaussView.

Several initial geometries were taken where the molecules were allowed to approach different sites of the chlorinated borazine ring including the top of the borazine ring and the bridge sites as well as on top of B and N atoms. The molecules were further allowed to align perpendicular or parallel to the ring surface. The geometries were first optimized without symmetry constraint at the B3LYP level of theory. These geometries were used again as starting configurations with the other functionals, M06 and SVWN, and re-optimized. All optimization were followed by frequency calculations to confirm that the structures represent genuine minima in the potential energy surface. The atomic charges have been evaluated by applying the Natural Bonding Orbital method (NBO).<sup>267</sup> The theoretically calculated binding affinities ( $E_b$ ) using different methods are compared with the experimental results of BLP-10(Cl) and are shown in Table 22. Since the B3LYP results were unphysical for H<sub>2</sub> and CH<sub>4</sub>, the calculation for CO<sub>2</sub> was not repeated.

**Table 22.** Theoretically Calculated Binding Affinities of H<sub>2</sub>, CO<sub>2</sub>, and CH<sub>4</sub> with Chlorinated Borazine and the Respective Experimental Values.

Small Gas	Expt (kJ/mol)	B3LYP/6- 311+G* (kJ/mol)	M06/6- 311+G* (kJ/mol)	SVWN/6- 311+G* (kJ/mol)
H <sub>2</sub>	7.46	-2.33	9.05	10.39
CO <sub>2</sub>	28.28	-	15.46	25.95
CH <sub>4</sub>	20.2	-0.22	20.22	20.30

In the case of a dihydrogen molecule interacting with the chlorinated borazine based with the M06 methodology, the H<sub>2</sub> is bound molecularly with a bond length of 0.75 Å and at a distance of 2.76 Å from the boron site. CO<sub>2</sub> and CH<sub>4</sub>, on the other hand, interact with the central ring system of borazine at a distance of 3.12 Å and 3.33 Å, respectively. The bond length between the carbon and oxygen atoms of CO<sub>2</sub> is 1.16 Å while the distance between the carbon and hydrogen atoms of CH<sub>4</sub> is 1.10 Å. Figure 86 gives the geometries obtained from the M06 functional while the geometries obtained from SVWN and B3LYP are shown in Figure 87 and 88, respectively. The result obtained from M06 agree well with experiment except for CO<sub>2</sub> interacting with the chlorinated borazine. Surprisingly, the binding affinities calculated at the SVWN level of theory agrees best with the experimental results even though this functional does not take into account van der Waals' interactions. The results obtained using B3LYP do not show any binding which demonstrates the importance of taking into account dispersive forces while dealing with weakly bound systems.

**Figure 86.** Optimized geometries of (a)  $\text{H}_2$ , (b)  $\text{CO}_2$  and (c)  $\text{CH}_4$  adsorbed on chlorinated borazine calculated at M06/6-311+G\* level of theory. The bond lengths are in Å. Front and side views are given (left and right panel, respectively). The blue, pink, green, grey, white, and red colors stand for N, B, Cl, C, H, and O atoms, respectively.

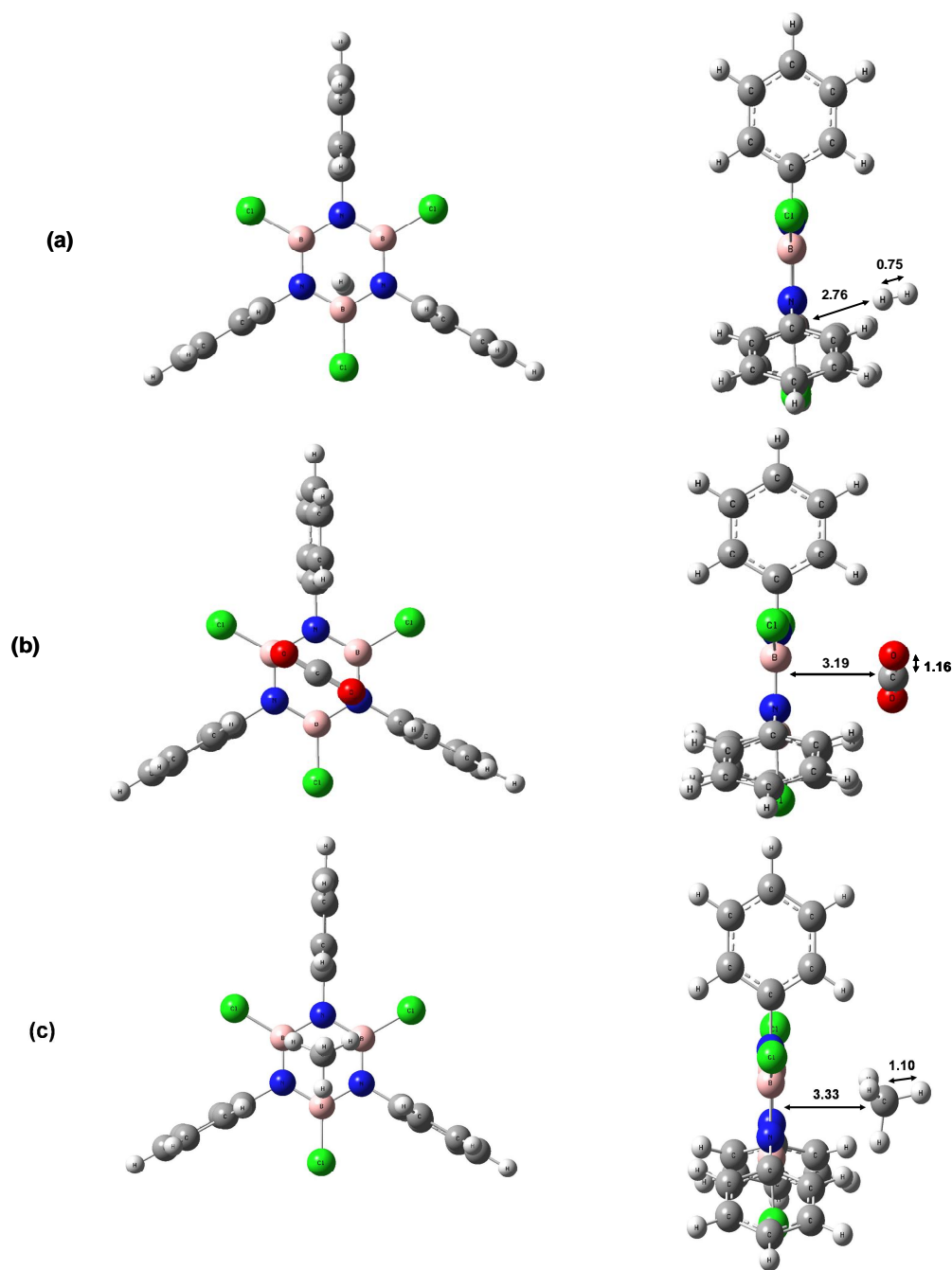




**Figure 87.** Optimized geometries of (a)  $\text{H}_2$ , (b)  $\text{CO}_2$  and (c)  $\text{CH}_4$  adsorbed on chlorinated borazine calculated at SVWN/6-311+G\* level of theory. The bond lengths are in Å. Front and side views are given on the left and right panel, respectively. The blue, pink, green, grey, white, and red colors stand for N, B, Cl, C, H, and O atoms, respectively.

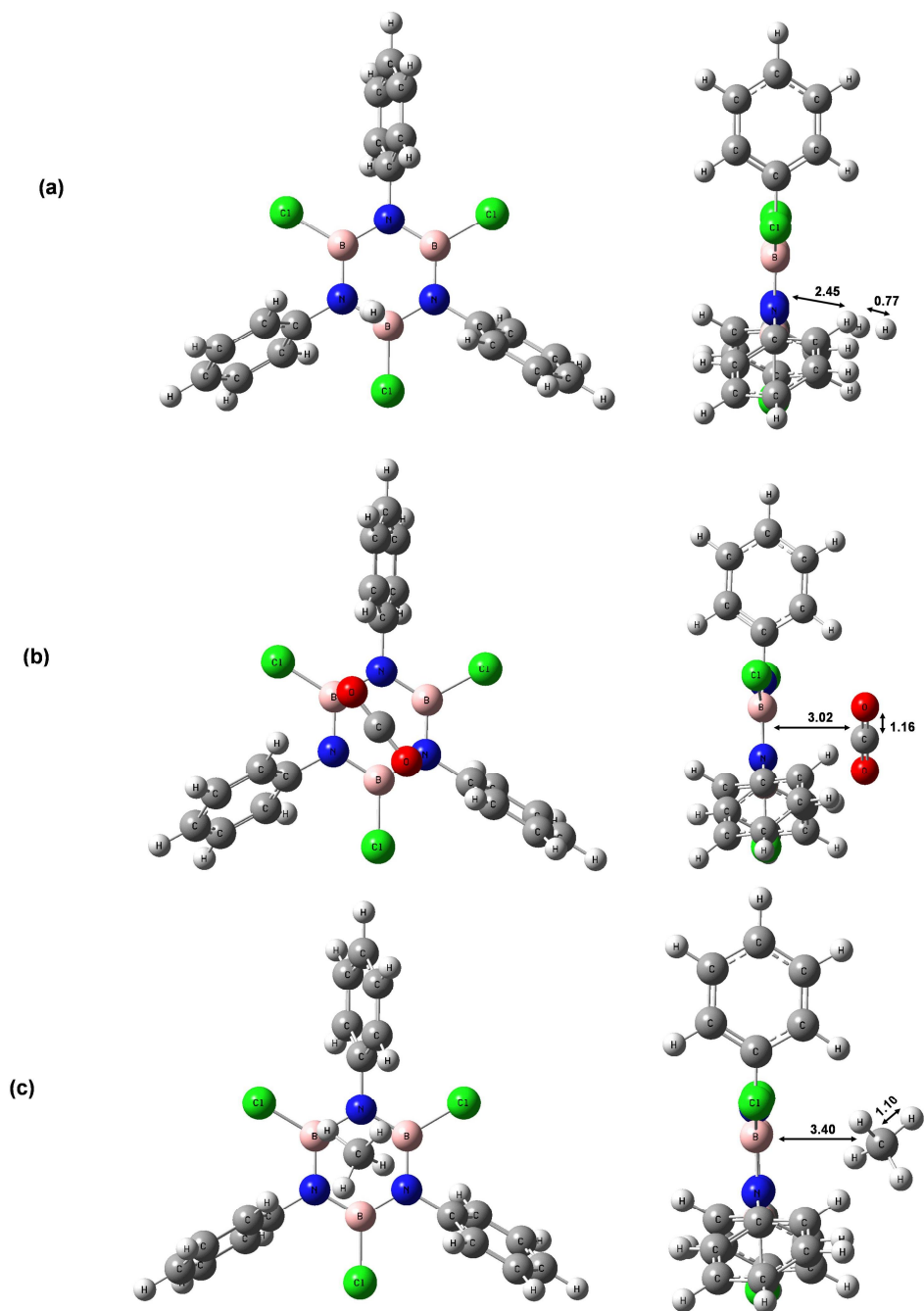
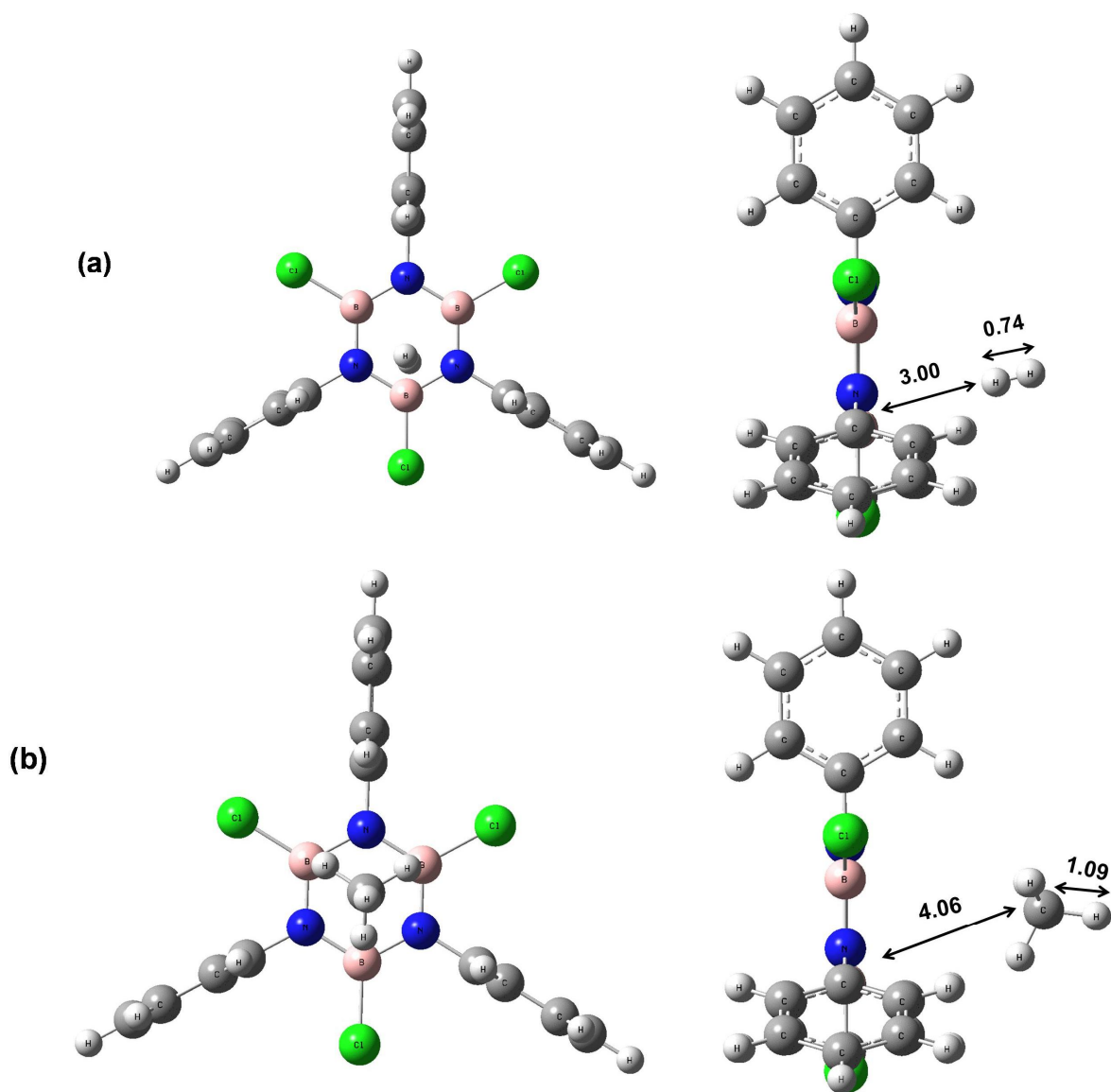


**Figure 88.** Optimized geometries of (a) H<sub>2</sub>, (b) CH<sub>4</sub> adsorbed on chlorinated borazine calculated at B3LYP/6-311+G\* level of theory. The bond lengths are in Å. Front and side views are given on the left and right panel, respectively. The blue, pink, green, grey, white, and red colors stand for N, B, Cl, C, H, and O atoms, respectively.



## Chapter 6

### Gas Separation and Selectivity Capabilities for Benzimidazole-Linked Polymers and Halogenated Borazine-Linked Polymers

#### 6.1 Introduction

As a result of the economical and environmental impacts of gaseous impurities, gas separation and selectivity continues to garner great attention among the scientific community.<sup>256, 268-296</sup> Of particular interest is in the selectivity and separation of CO<sub>2</sub> from N<sub>2</sub>, CH<sub>4</sub>, and H<sub>2</sub>. More specifically, carbon dioxide exists as an impurity in flue gases as well as in natural gas. Advancements in this area can result in a reduction in atmospheric greenhouse gases as well as providing a facile approach to the production of high purity natural gas. Owing to their differences in gas uptakes for different gases, porous polymers are an attractive method for this purification. Calculations for the separation and selectivity capabilities of a porous polymer media are performed based on the polymer's pure gas isotherms. Typically, there are three different methods for calculating selectivity: (1) initial slopes method, (2) Henry's Law constants, and (3) ideal adsorbed solution theory (IAST).

The initial slopes method<sup>297</sup> for calculating selectivity employs the varying levels of gas uptake in the low pressure range (typically from 0 to about 0.1 bar). In this pressure range, the isotherms are assumed to be linear. As such, data points in this range are fit according to the linear equation:  $y = mx + b$ , where  $y$  is the gas uptake in mmol/g, and  $x$

is pressure in bar,  $m$  is the slope of the curve, and  $b$  is the y-intercept of the curve. Selectivity is then calculated based on the ratio of the slopes of the curves for the respective gases. Selectivities based on this method are pursued based on the fact that it represents the simplest and fastest method of the three. Nevertheless, the requisite assumption that the isotherms are linear in the low pressure range is suspect. Additionally, the applicable pressure range is very subjective hindering the calculation's reliability. As a result, utilizing the initial slopes method is typically performed as a quick assessment to pursue selectivity for the polymer or as a confirmation of one of the other two calculation methods.

Performing selectivity calculations based on the Henry's Law constants<sup>256, 298</sup> helps to alleviate some of the subjectivity inherent in the initial slopes calculations. This method utilizes parameters of the virial-type expansion that was mentioned in Chapter 5 for the calculation of isosteric heat of adsorption. At its core, the use of Henry's Law constants is an initial slopes calculation method; however, the mathematical sophistication gives this method a more precise measure of the true initial slope of each gas isotherm. Calculation by this method begins with the fitting of each isothermal data set to the virial equation:

$$\ln P = \ln N + (1/T) \sum_{i=0}^m a_i N^i + \sum_{i=0}^n b_i N^i$$

In this equation, again,  $P$  is pressure in torr,  $T$  is temperature in Kelvin, and  $N$  is the mmol of gas adsorbed per gram of sample. Also again, the values for  $m$  and  $n$  are varied such that  $m \geq n$  and result in the best fit as determined by the sum of the squares of the errors where the values for  $a_0, a_1, \dots, a_m$  and  $b_0, b_1, \dots, b_n$  are fitting parameters for

the virial expansion. From these results, the Henry's constant ( $K_H$ ) can be calculated at temperature  $T$  in Kelvin by:

$$K_H = \exp(-b_0) * \exp(-a_0/T)$$

The Henry's Law selectivity for a gas component  $i$  over  $j$  is calculated by the equation:

$$S_{ij} = K_{Hi} / K_{Hj}$$

The use of the first parameters for both  $a$  and  $b$  indicates that this method approximates the selectivity based on the "true" initial slopes of the isotherms. Although this method is much more time consuming than by the initial slopes method, it is typically more reliable.

For both the initial slopes method and the Henry's Law constants method, selectivity results are just a single number whereas the true separation capabilities of a porous polymer can vary with changing pressure and molar ratio. Neither of these calculation methods allow for such variability. However, calculations based on the ideal adsorbed solution theory (IAST)<sup>299-311</sup> do allow for it and has been studied extensively for a number of gas mixture systems and media.<sup>312-318</sup> This theory is based on the fact that "in an ideal solution the partial pressure of an adsorbed component is given by the product of its mole fraction in the adsorbed phase and the pressure which it would exert as a pure adsorbed component at the same temperature and spreading pressure as those of the mixture."<sup>299</sup> From there, mathematical derivations based on classical surface thermodynamics can be made. The resulting calculations yield the formula:

$$\int_{t=0}^{\frac{Py_1}{x_1}} F_1(t) d \ln t = \int_{t=0}^{\frac{Py_2}{x_2}} F_2(t) d \ln t$$

where:

P is the total pressure

$y_1$  and  $y_2$  are the bulk phase molar ratio of gases 1 and 2, respectively

$x_1$  and  $x_2$  are the adsorbed phase molar ratio of gases 1 and 2, respectively

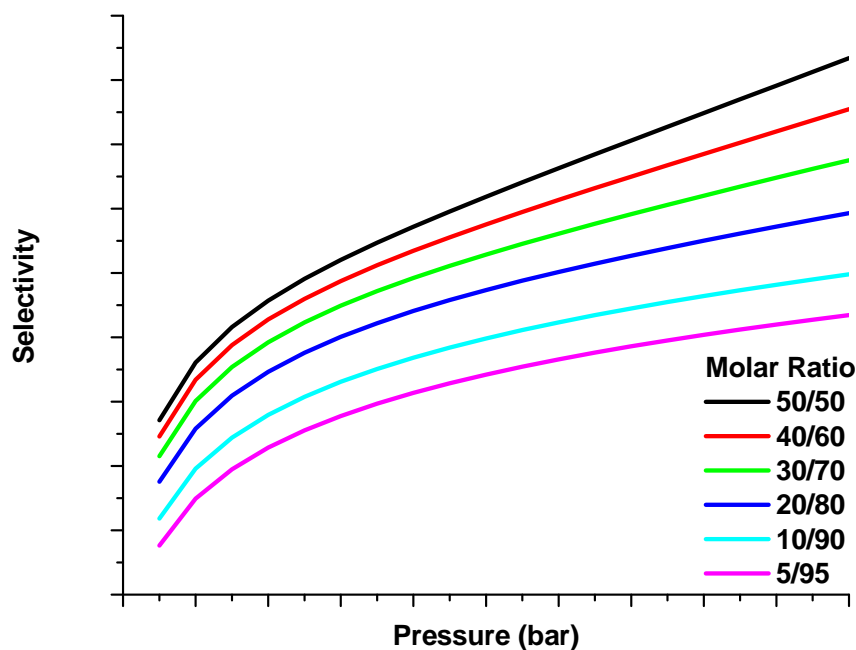
$F_1(t)$  and  $F_2(t)$  are the fitting functions of the isothermal data of gas uptake versus pressure for gases 1 and 2, respectively

Since  $x_2 = 1 - x_1$  and  $y_2 = 1 - y_1$ , the above equation yields three unknowns. Therefore, by specifying one value and varying a second, the third value can be calculated. Selectivity can then be calculated by:

$$s_{1,2} = \frac{x_1/y_1}{x_2/y_2}$$

From these calculations, a graph of the selectivity versus the varying second parameter can be achieved. Additionally, the specified first value can be adjusted as well to give a single graph of many specified first values (for example Figure 89). Selectivity can also be calculated such that molar ratio is on the x-axis while the different lines represent different pressures.

**Figure 89.** Example IAST Graph of Selectivity versus Pressure at Different Molar Ratios.



A drawback to IAST has to do with the assumption that the system is ideal. As a result, any heterogeneity of the system would create non-ideality thus denying the applicability. In reality, no polymeric system is completely homogeneous as even highly crystalline polymers exhibit heterogeneous chain ends. However, with sufficient purity, this non-ideality is negligible. Oftentimes, comparing IAST results against values calculated by the initial slopes or Henry's Law constants method can help to confirm the applicability of IAST to a particular system. Since both of these methods are based on selectivity at the low pressure range, only the IAST results that are also within the low pressure range can be compared.

For the research presented in this dissertation, IAST was used to calculate selectivities. These values were compared to values calculated by the initial slopes method to confirm that these types of polymer systems conform to the necessary ideality level requirements. In Section 6.2, IAST results from a number of benzimidazole-linked polymers (BILPs) are presented. In Section 6.3, a detailed explanation for how the IAST integration was performed as well as the fitting methods for the pure component isotherms is included. In Section 6.4, IAST results from all seven of the borazine-linked polymers (BLPs) are presented.

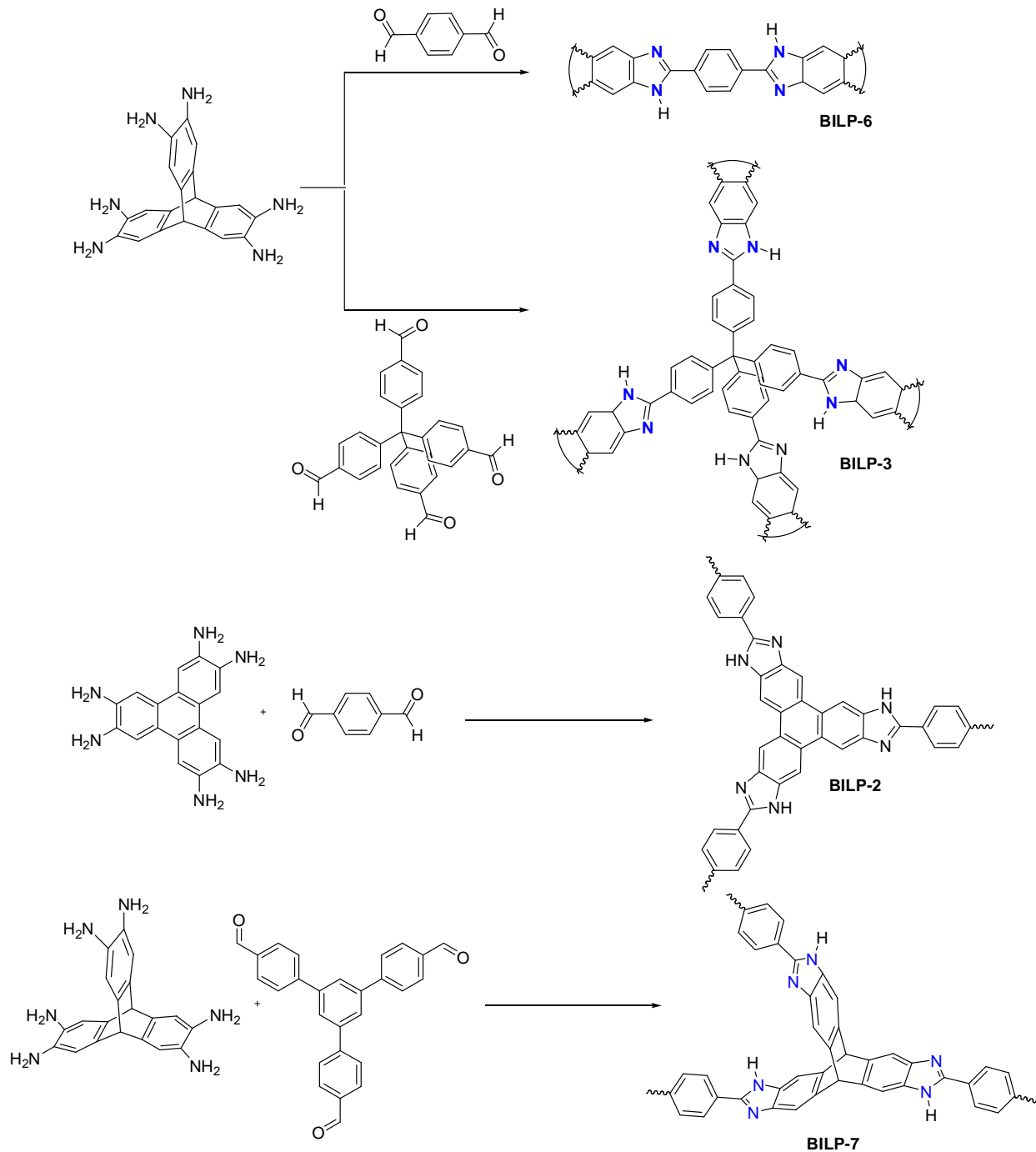
## **6.2 IAST Calculations for Benzimidazole-Linked Polymers**

IAST calculations were performed on benzimidazole-linked polymers (BILPs) to assess their capabilities for gas separation applications. All BILPs were synthesized and characterized by Dr. Mohammad Rabbani in the El-Kaderi group at Virginia Commonwealth University. All polymers are based on the building block benzimidazole whereby a benzene ring is fused with imidazole and were synthesized as shown in Figure 90. Extension of the aryl backbone through the benzene ring is permitted through fused or bonded aryl groups.

For BILP-1, a dropwise treatment of a suspension of 2,3,6,7,10,11-hexaaminotriphenylene (HATP) in N,N-dimethylformamide (DMF) with a homogenous solution of tetrakis(4-formylphenyl)methane (TFPM) in DMF over 3 hours at -30 °C followed by stirring at room temperature for 6 hours afforded a yellow suspension. The resulting suspension was bubbled with oxygen and then heated in a sealed Schlenk flask at 130 °C for 3 days to afford BILP-1 (70%) as a yellow powder after filtration and drying at 120 °C and  $1.0 \times 10^{-5}$  Torr for 12 hours.<sup>156</sup>



**Figure 90.** Selected Benzimidazole-Linked Polymers used in IAST studies.



BILP-2 was synthesized through a similar type of reaction by the condensation of HATP with terephthalaldehyde. BILPs-3, 6, and 7 were also synthesized through a

similar type of reaction by the condensation of triptycene with TFPM, terephthalaldehyde, and 1,3,5-tris(4-formylphenyl)benzene, respectively. One of the many attractive features of BILPs is their stability in aerobic conditions—a downfall to many porous organic and coordination polymers. Even after storage in air for one month or by treatment of a 2M solution of HCl or NaOH, BILPs suffered from only a minor color change from yellow to brown which is attributed to the oxidation of unreacted amine sites on the surface of the polymer. Following standard characterization techniques to confirm the formation of the benzimidazole building unit as well as the survival of the aryl backbone, four BILPs (2, 3, 6, and 7) for IAST study were subjected to gas sorption experiments. Nitrogen, hydrogen, carbon dioxide, and methane sorption experiments were all performed at 273 K and 298 K.

From these pure component sorption isotherms, IAST calculations can be made to predict how these BILPs would perform with gas mixture systems of  $\text{CO}_2\text{:CH}_4$ ,  $\text{CO}_2\text{:N}_2$ , and  $\text{CO}_2\text{:H}_2$ . As mentioned in Section 6.1, a very detailed explanation for how these calculations were performed is given in Section 6.3. In brief, the simultaneous integrations were performed with two different approaches. First, the selectivities were calculated with pressure on the x-axis from 0 to 1 bar for  $\text{CO}_2\text{:X}$  molar ratios of 50:50, 40:60, 30:70, 20:80, 10:90, and 5:95 where X is  $\text{CH}_4$ ,  $\text{N}_2$ , or  $\text{H}_2$ . Second, selectivities were calculated with molar ratio of the non- $\text{CO}_2$  gas on the x-axis from 0.5 to 0.975 for pressures of 0.2, 0.4, 0.6, 0.8, and 1.0 bar. In essence, the resulting graphs are two different ways to look at the same data set. Since two graphs are generated for each of two different temperatures for each of three types of selectivities, a total of 12 graphs for each BILP are generated and are shown in Figures 91-138. In none of the BILPs are

the selectivity numbers exceptional for CO<sub>2</sub>/CH<sub>4</sub>. In fact for BILP-3 and BILP-6, these values only range from 8-8.5 for most molar ratios which are comparable to diimide polymers<sup>242, 319</sup> and PPNs<sup>260</sup> but are less than BLPs as will be conveyed in Section 6.4. However, the selectivities for CO<sub>2</sub>/N<sub>2</sub> reach more appreciable levels. At 273 K, the CO<sub>2</sub>/N<sub>2</sub> selectivity for both BILP-3 and BILP-6 are greater than 73 even at very low pressures. These values are in line with that of NPMs and Bio-MOF-11 and again surpass the values for activated carbons and ZIFs. Moreover, with increasing pressure, the nitrogen uptake approaches saturation much quicker than carbon dioxide, and as a result, the selectivity values increase dramatically with pressure for all molar ratios. Interestingly, the selectivity obtained from IAST calculations for CO<sub>2</sub>/CH<sub>4</sub> and CO<sub>2</sub>/N<sub>2</sub> at very low pressures are consistent with the values obtained from initial slope calculations. The selectivity values for CO<sub>2</sub>/H<sub>2</sub> are also appreciably high. At low pressures and 273 K, these values range from 215 up to 900 for BILP-2 which is comparable to the values of MOFs, zeolites, and activated carbons.<sup>300</sup> Additionally, the uptake for hydrogen appears to approach saturation much quicker than carbon dioxide as was the case for CO<sub>2</sub>/N<sub>2</sub>. As a result, the selectivity values also increase dramatically with pressure for all molar ratios.

Since all BILPs like BLPs are amorphous, their effective use of IAST in predicting gas pair mixture separation may be limited.<sup>320</sup> As a result, selectivity based on the initial slopes method of calculation was also performed. In all cases, the selectivity values of the initial slopes method were in good agreement to the values found at the low pressure regime for IAST. As such, IAST should be a useful tool for calculating the selectivity in BILPs.

Of particular note regarding the CO<sub>2</sub>/N<sub>2</sub> selectivity in BILPs is the fact that for many of these polymers the selectivities increase dramatically to levels reaching several tens of thousands at 1 bar. Although saturation of nitrogen is the attributing factor for this occurrence, the reliability of this data is not without concern. As a result, only the selectivity values calculated from the initial slopes method (which agreed well with the low pressure IAST data) was reported. In order to enhance the reliability of these IAST calculations for BILPs, two approaches would need to be pursued. First, high pressure data for carbon dioxide and nitrogen would need to be collected. From this high pressure data in conjunction with low pressure isotherms, a more precise fitting to the data can be made. With a better fit, IAST can be performed with more confidence. And second, experimental data utilizing a gas mixture on BILPs would need to be performed to confirm the applicability of IAST to BILPs and assess their true capabilities in gas separation applications.

**Figure 91.** BILP-2 CO<sub>2</sub>/CH<sub>4</sub> Selectivity versus Pressure at 273 K.

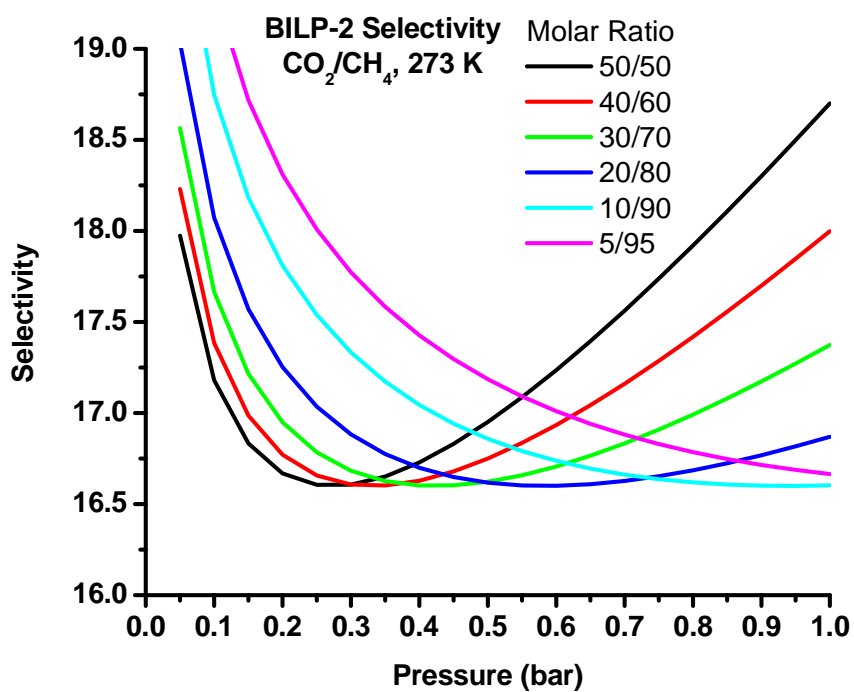


**Figure 92.** BILP-2 CO<sub>2</sub>/CH<sub>4</sub> Selectivity versus Molar Ratio of CH<sub>4</sub> at 273 K.

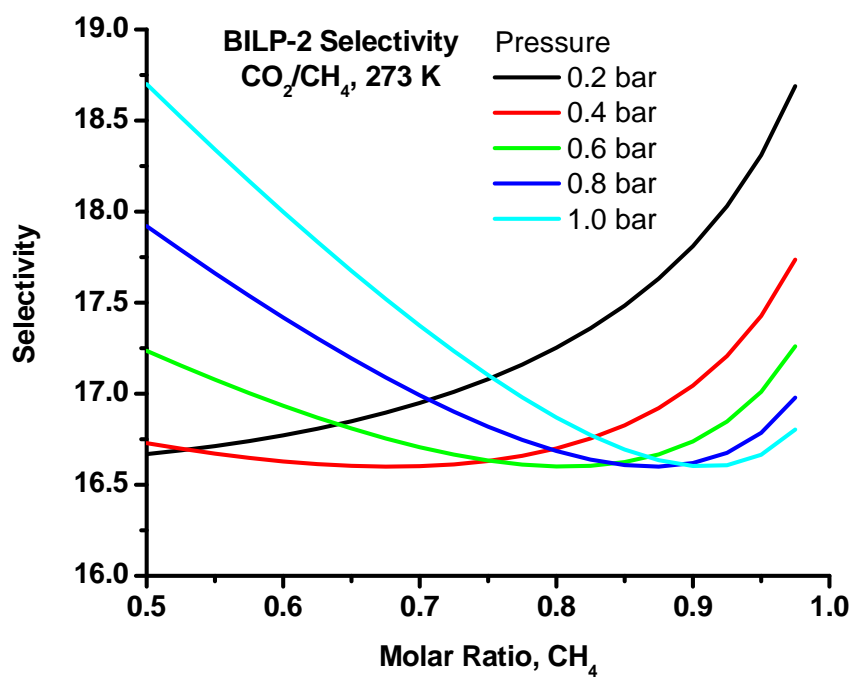


**Figure 93.** BILP-2 CO<sub>2</sub>/CH<sub>4</sub> Selectivity versus Pressure at 298 K.

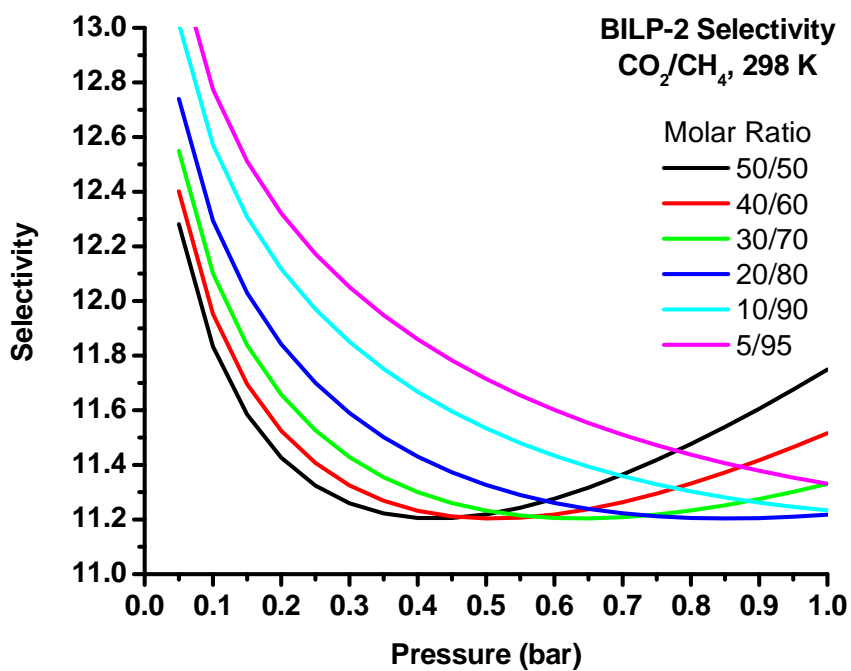


**Figure 94.** BILP-2 CO<sub>2</sub>/CH<sub>4</sub> Selectivity versus Molar Ratio of CH<sub>4</sub> at 298 K.

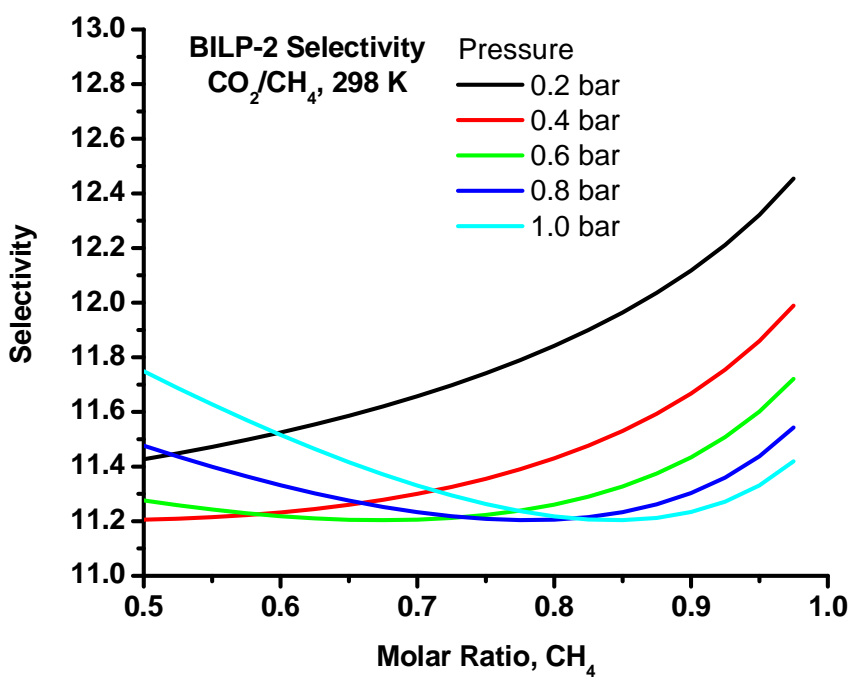


**Figure 95.** BILP-2 CO<sub>2</sub>/N<sub>2</sub> Selectivity versus Pressure at 273 K.

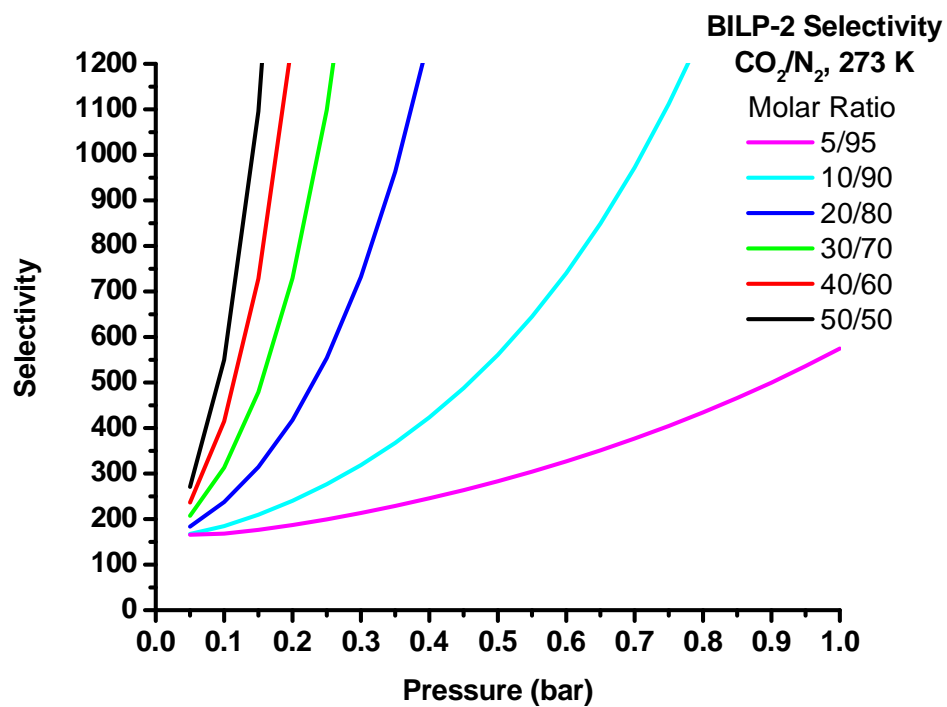


**Figure 96.** BILP-2 CO<sub>2</sub>/N<sub>2</sub> Selectivity versus Molar Ratio of N<sub>2</sub> at 273 K.

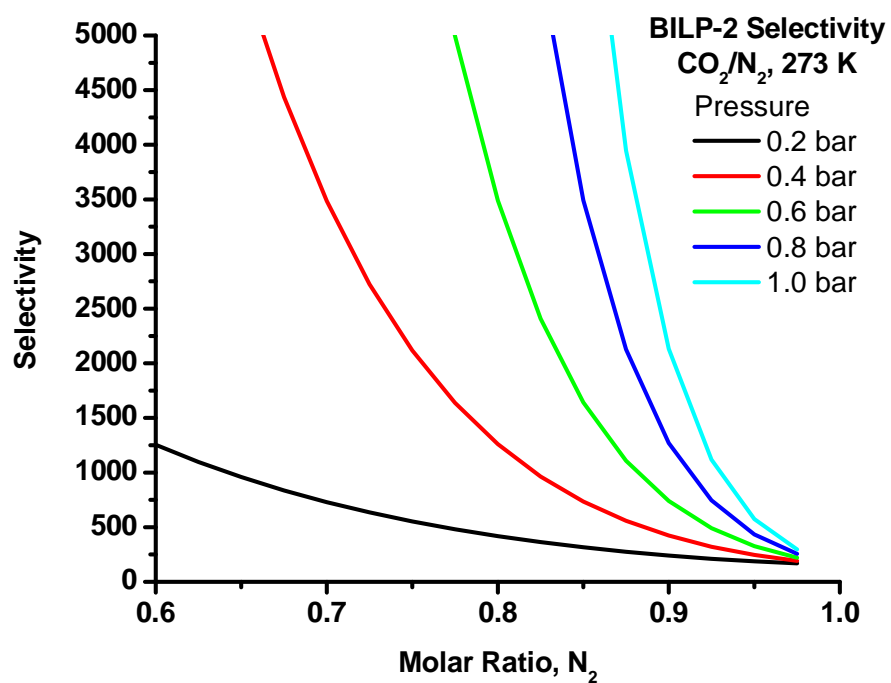


**Figure 97.** BILP-2 CO<sub>2</sub>/N<sub>2</sub> Selectivity versus Pressure at 298 K.

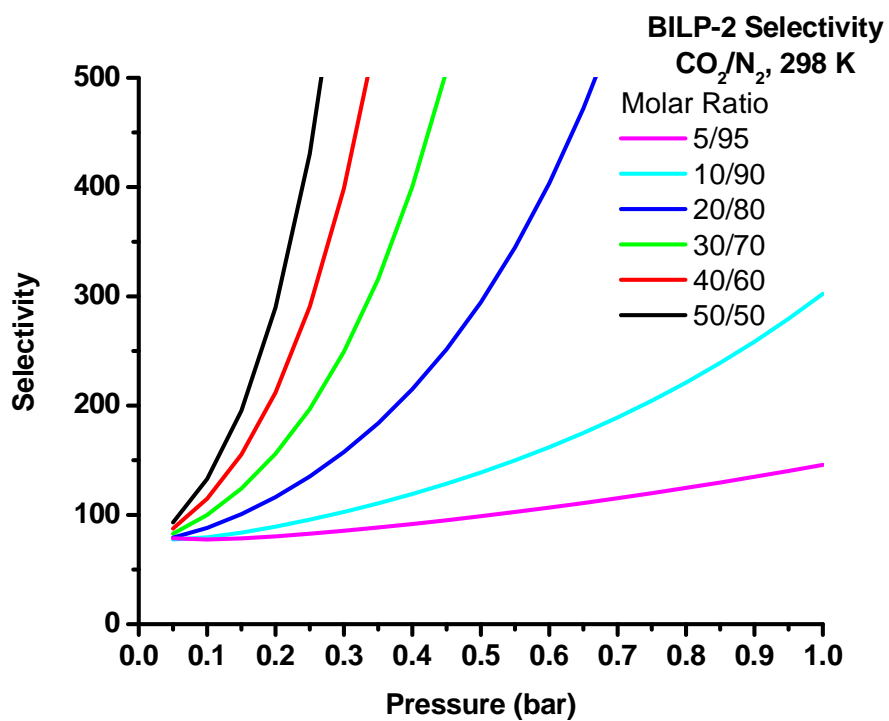


**Figure 98.** BILP-2 CO<sub>2</sub>/N<sub>2</sub> Selectivity versus Molar Ratio of N<sub>2</sub> at 298 K.

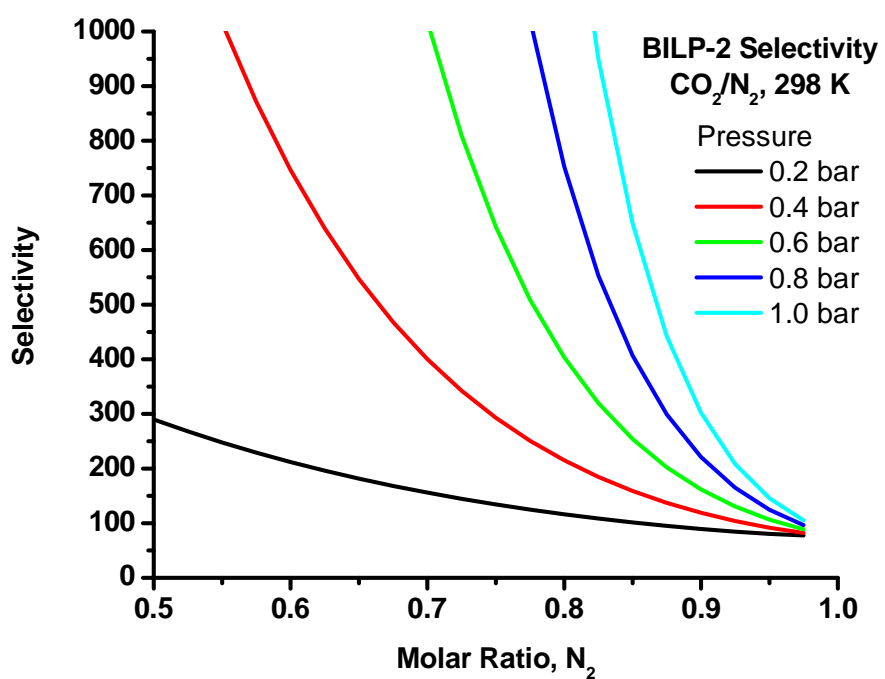




**Figure 99.** BILP-2 CO<sub>2</sub>/H<sub>2</sub> Selectivity versus Pressure at 273 K.

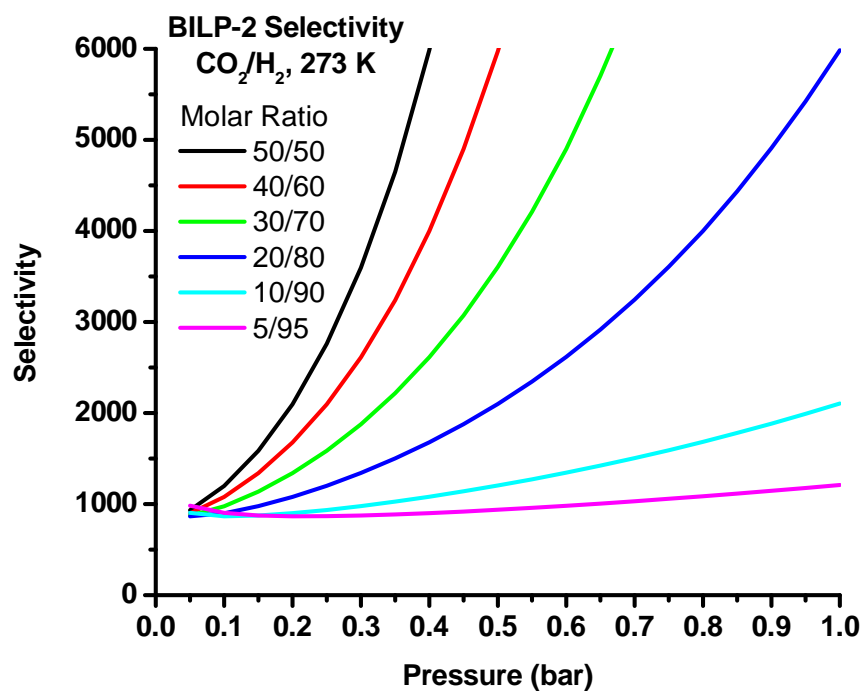


**Figure 100.** BILP-2 CO<sub>2</sub>/H<sub>2</sub> Selectivity versus Molar Ratio of H<sub>2</sub> at 273 K.

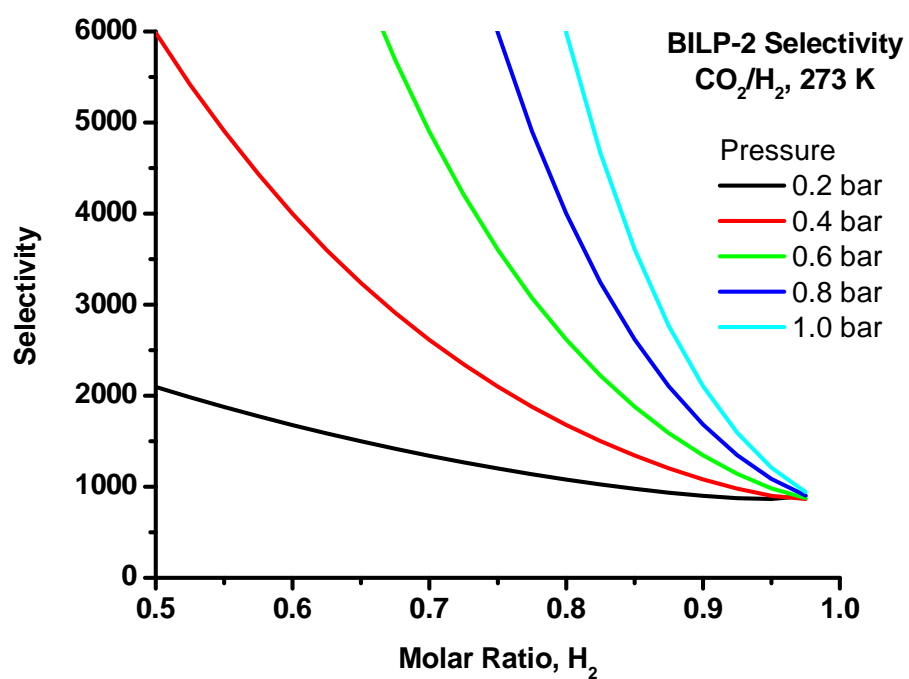


**Figure 101.** BILP-2 CO<sub>2</sub>/H<sub>2</sub> Selectivity versus Pressure at 298 K.

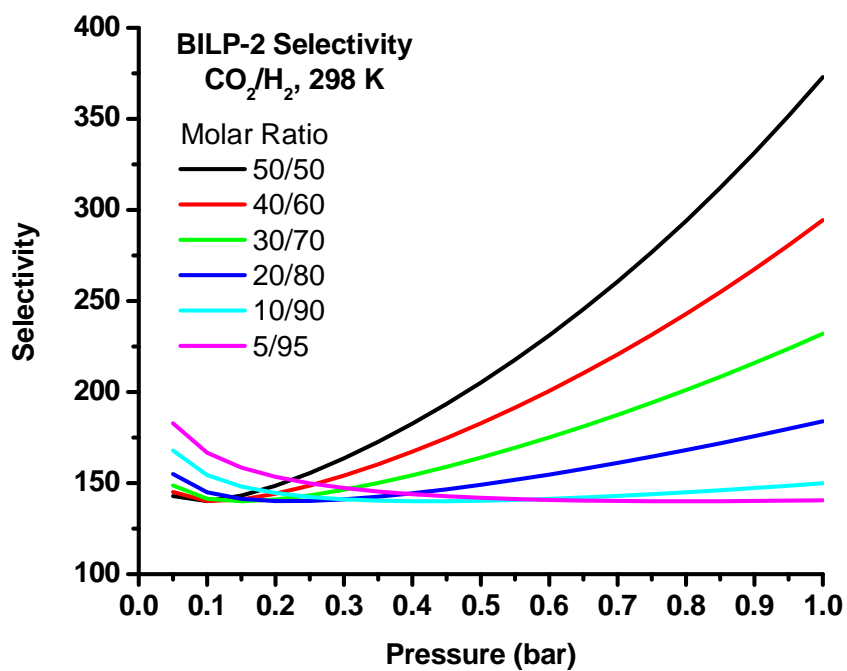


**Figure 102.** BILP-2 CO<sub>2</sub>/H<sub>2</sub> Selectivity versus Molar Ratio of H<sub>2</sub> at 298 K.

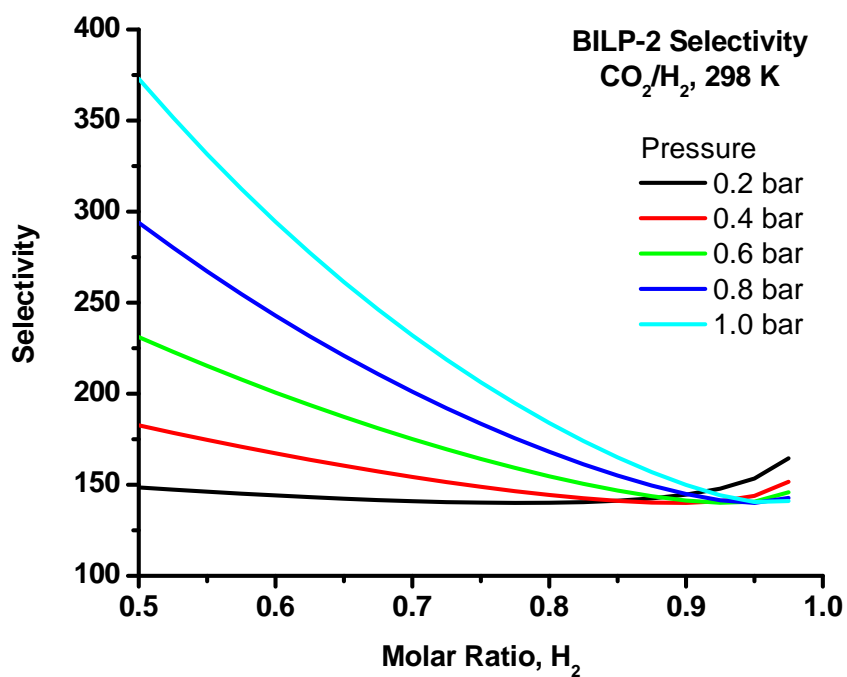


**Figure 103.** BILP-3 CO<sub>2</sub>/CH<sub>4</sub> Selectivity versus Pressure at 273 K.

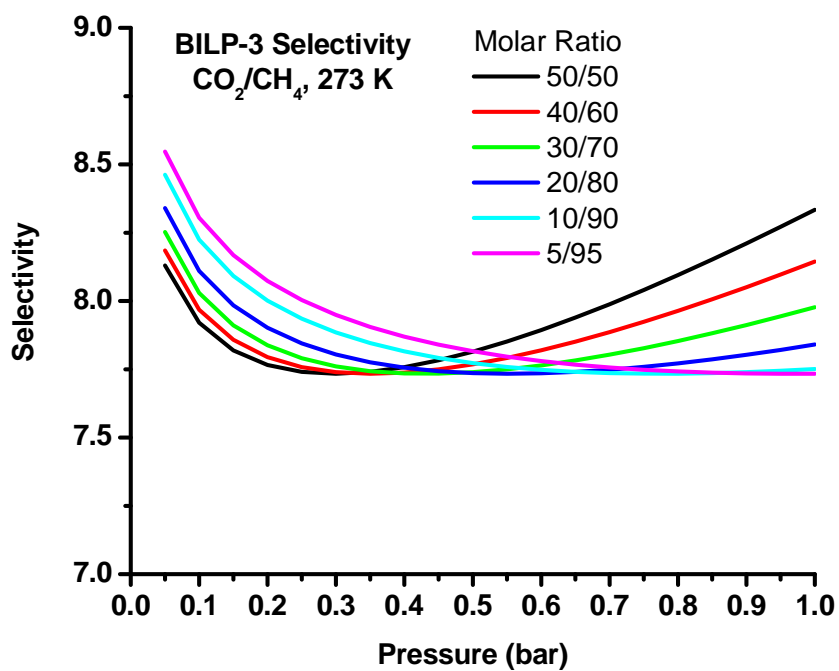


**Figure 104.** BILP-3 CO<sub>2</sub>/CH<sub>4</sub> Selectivity versus Molar Ratio of CH<sub>4</sub> at 273 K.

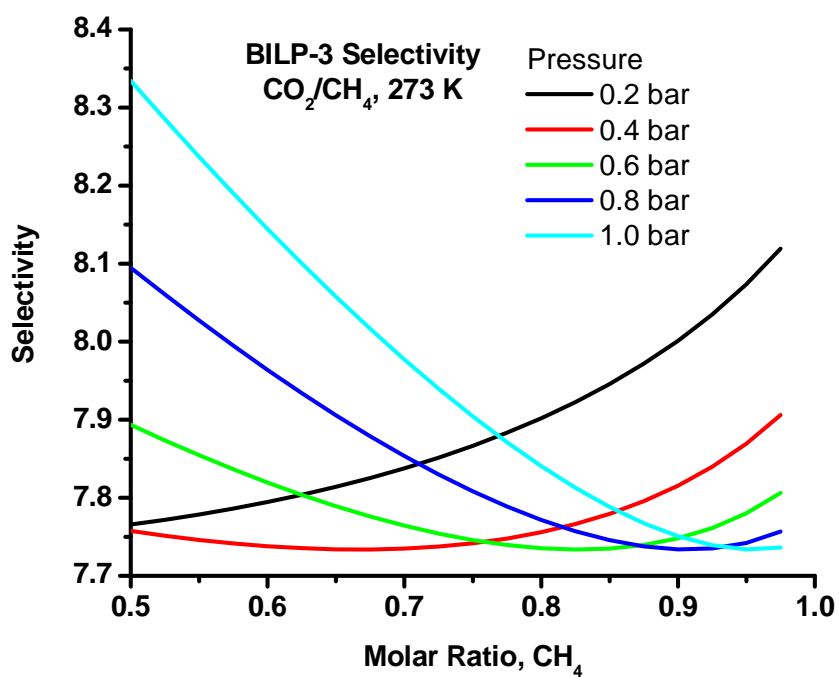


**Figure 105.** BILP-3 CO<sub>2</sub>/CH<sub>4</sub> Selectivity versus Pressure at 298 K.

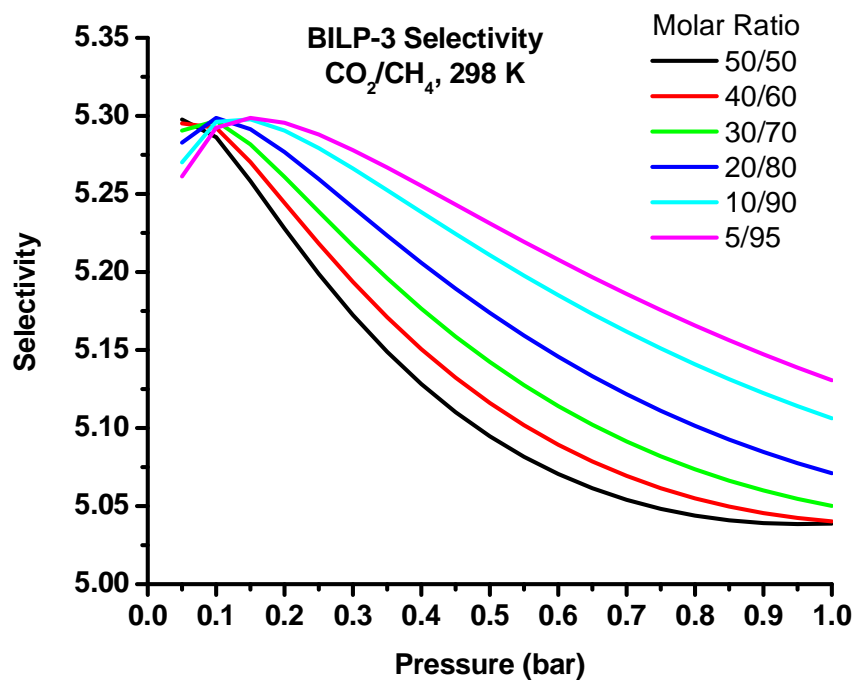


**Figure 106.** BILP-3 CO<sub>2</sub>/CH<sub>4</sub> Selectivity versus Molar Ratio of CH<sub>4</sub> at 298 K.

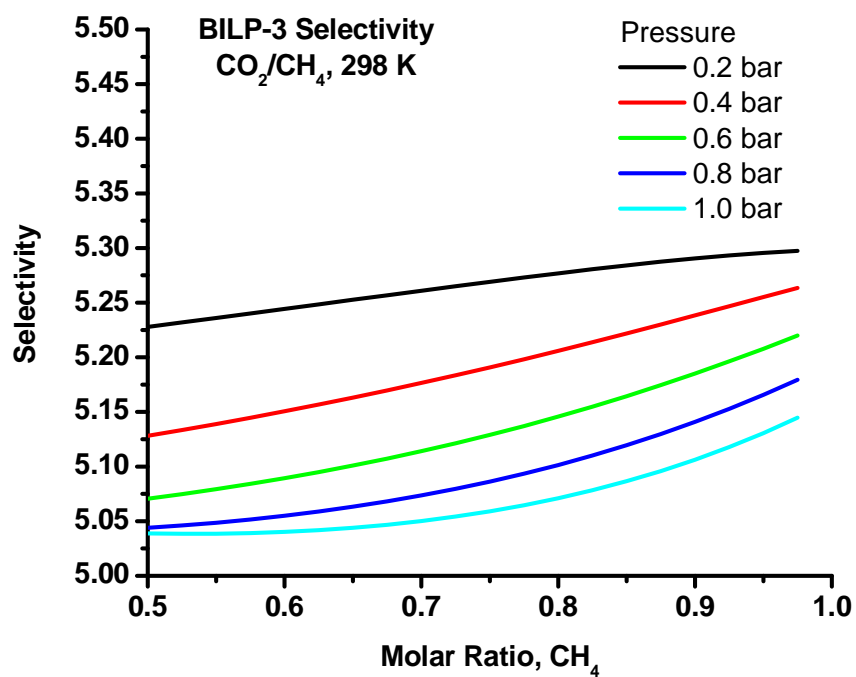


**Figure 107.** BILP-3 CO<sub>2</sub>/N<sub>2</sub> Selectivity versus Pressure at 273 K.

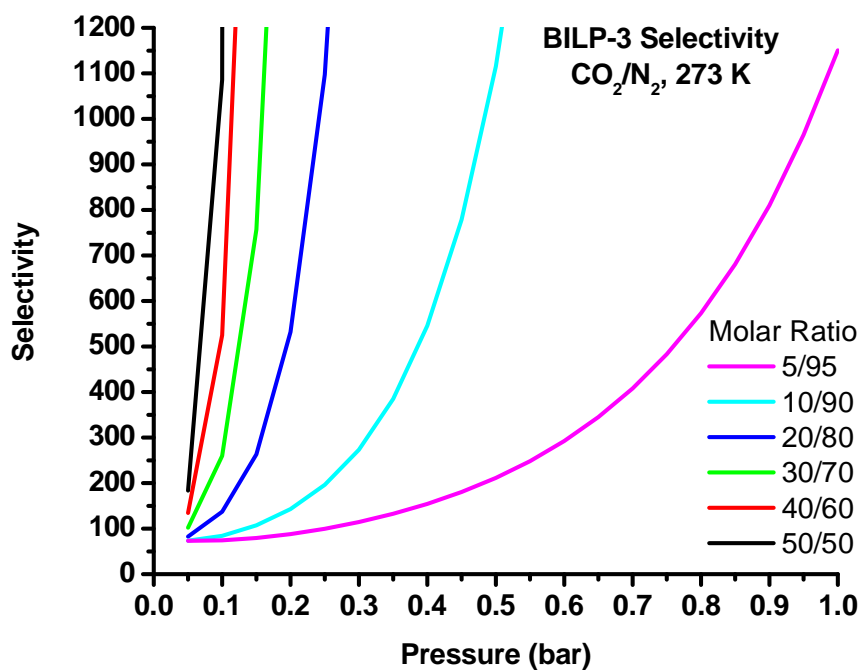


**Figure 108.** BILP-3 CO<sub>2</sub>/N<sub>2</sub> Selectivity versus Molar Ratio of N<sub>2</sub> at 273 K.

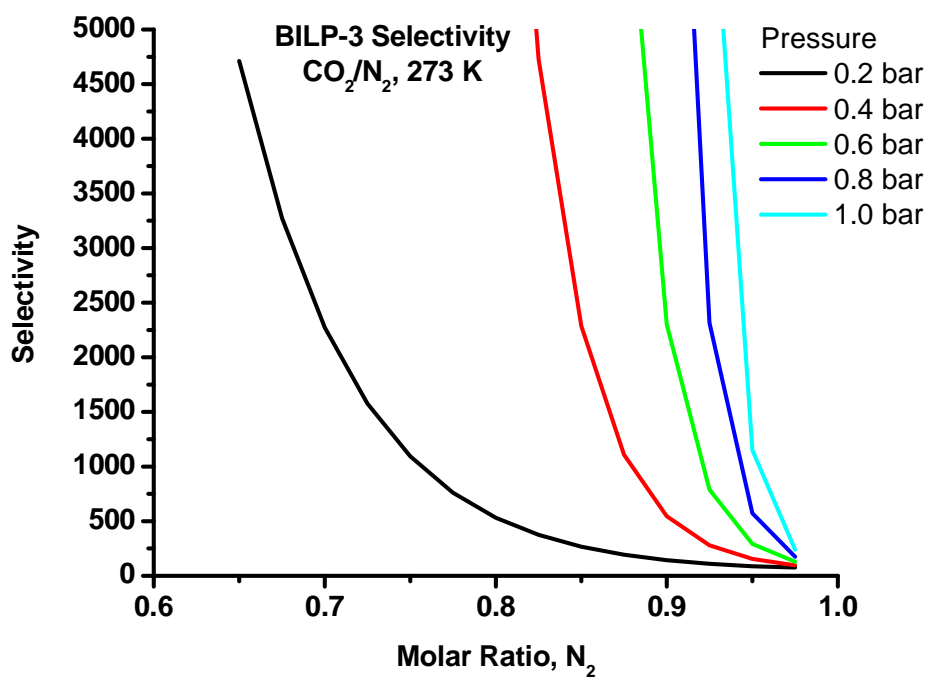


**Figure 109.** BILP-3 CO<sub>2</sub>/N<sub>2</sub> Selectivity versus Pressure at 298 K.

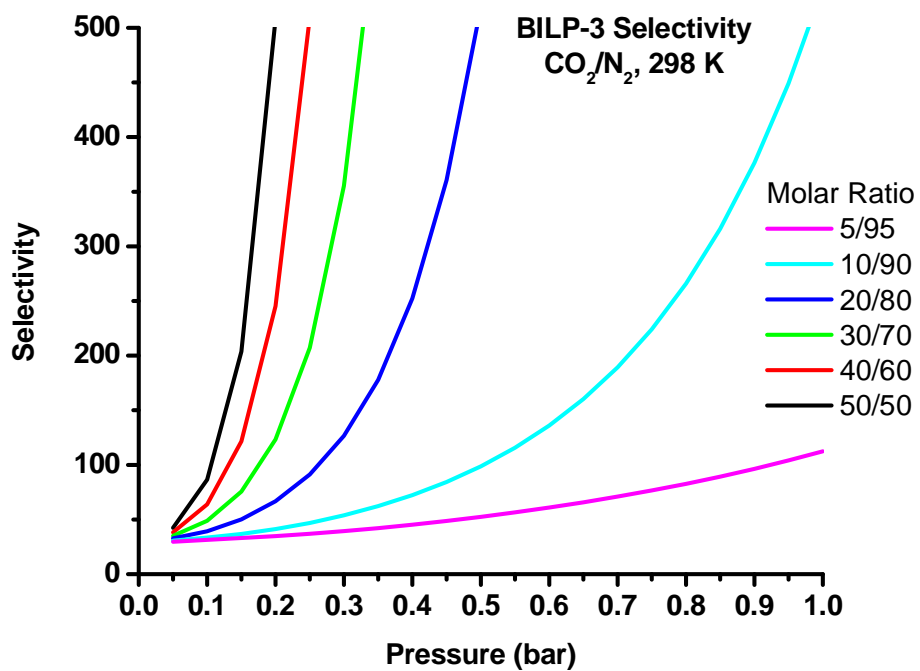


**Figure 110.** BILP-3 CO<sub>2</sub>/N<sub>2</sub> Selectivity versus Molar Ratio of N<sub>2</sub> at 298 K.

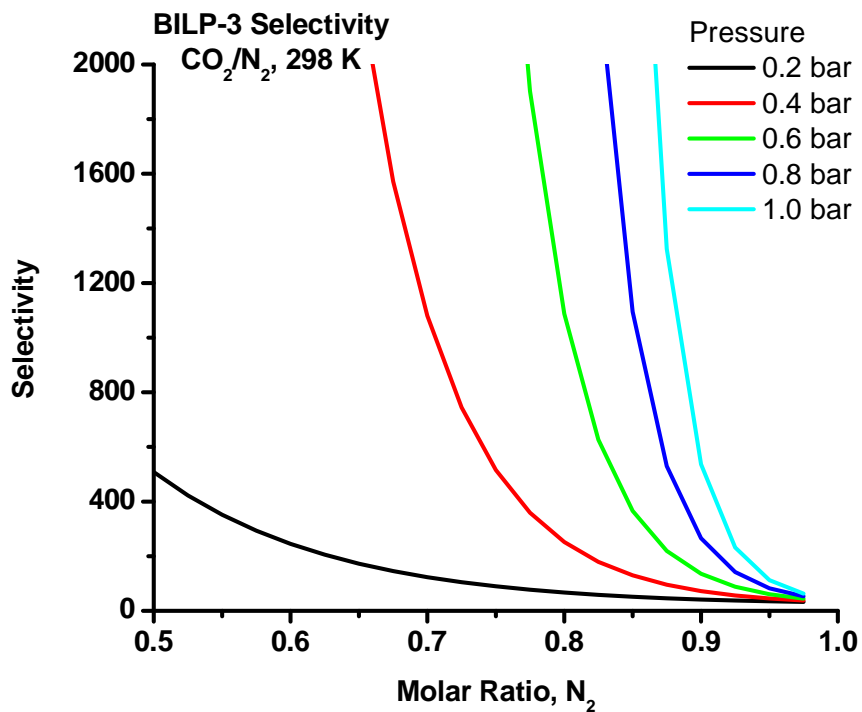


**Figure 111.** BILP-3 CO<sub>2</sub>/H<sub>2</sub> Selectivity versus Pressure at 273 K.

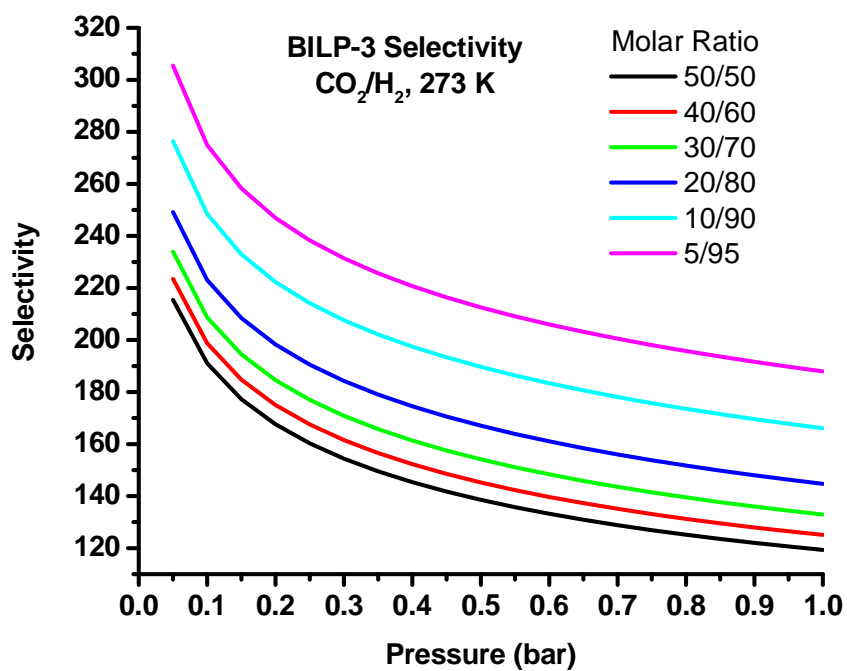


**Figure 112.** BILP-3 CO<sub>2</sub>/H<sub>2</sub> Selectivity versus Molar Ratio of H<sub>2</sub> at 273 K.

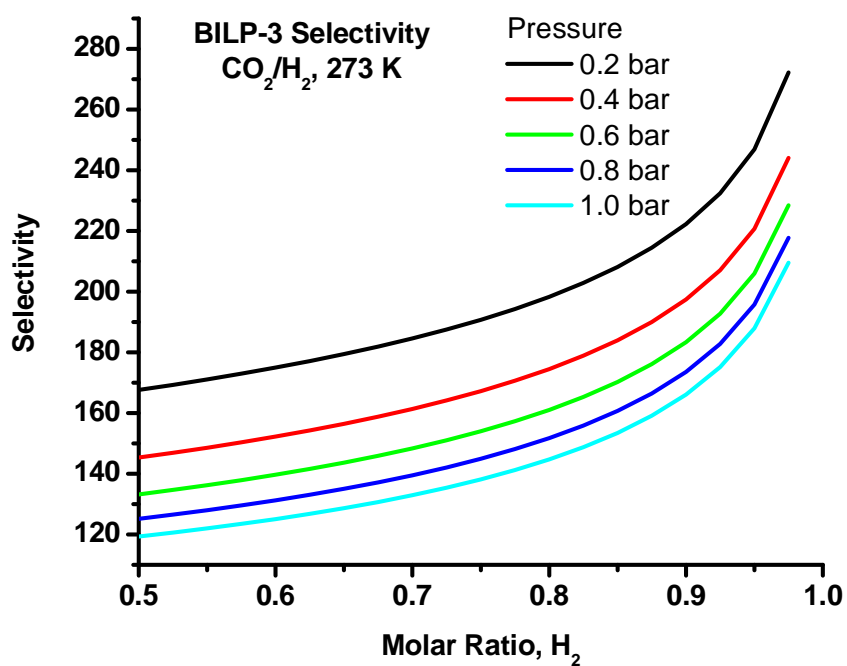


**Figure 113.** BILP-3 CO<sub>2</sub>/H<sub>2</sub> Selectivity versus Pressure at 298 K.

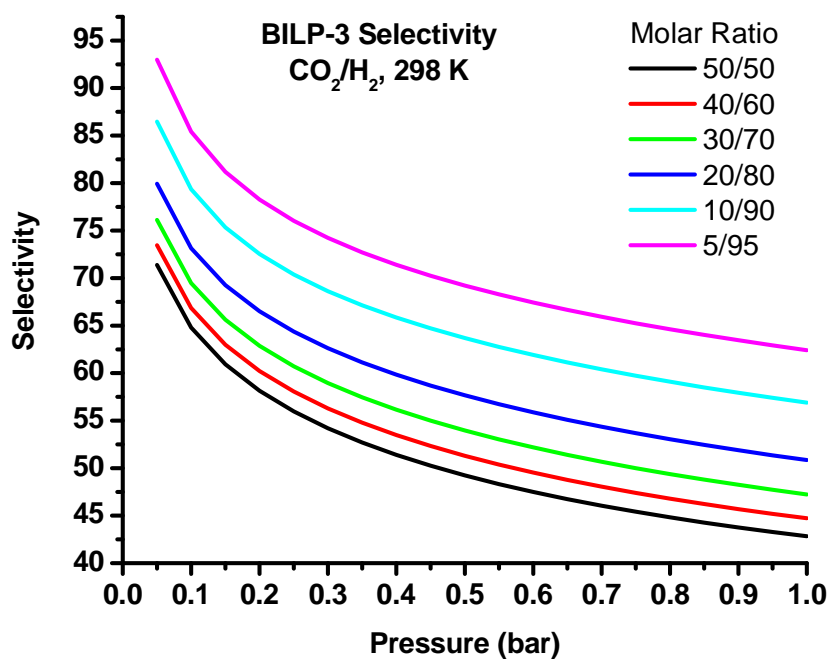


**Figure 114.** BILP-3 CO<sub>2</sub>/H<sub>2</sub> Selectivity versus Molar Ratio of H<sub>2</sub> at 298 K.

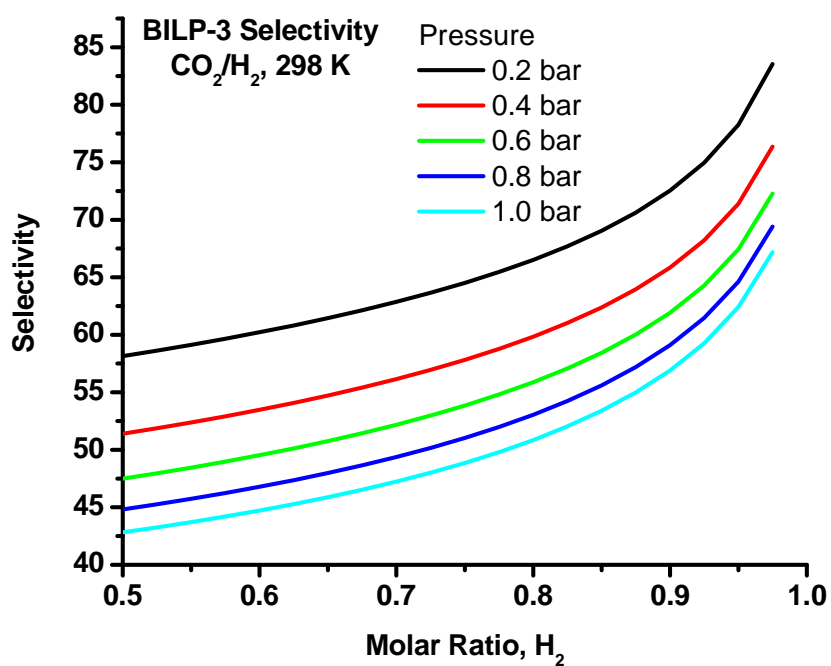




**Figure 115.** BILP-6 CO<sub>2</sub>/CH<sub>4</sub> Selectivity versus Pressure at 273 K.

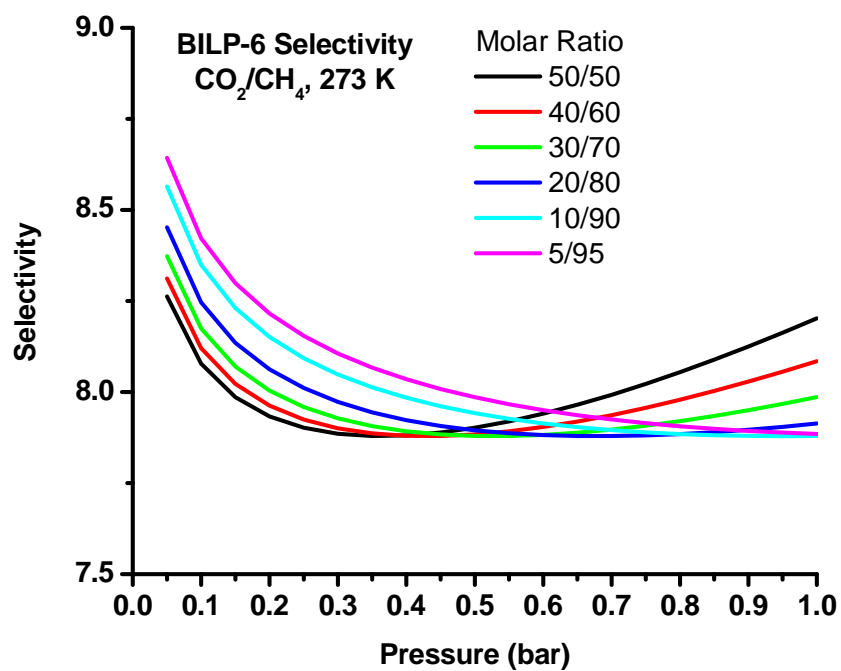


**Figure 116.** BILP-6 CO<sub>2</sub>/CH<sub>4</sub> Selectivity versus Molar Ratio of CH<sub>4</sub> at 273 K.

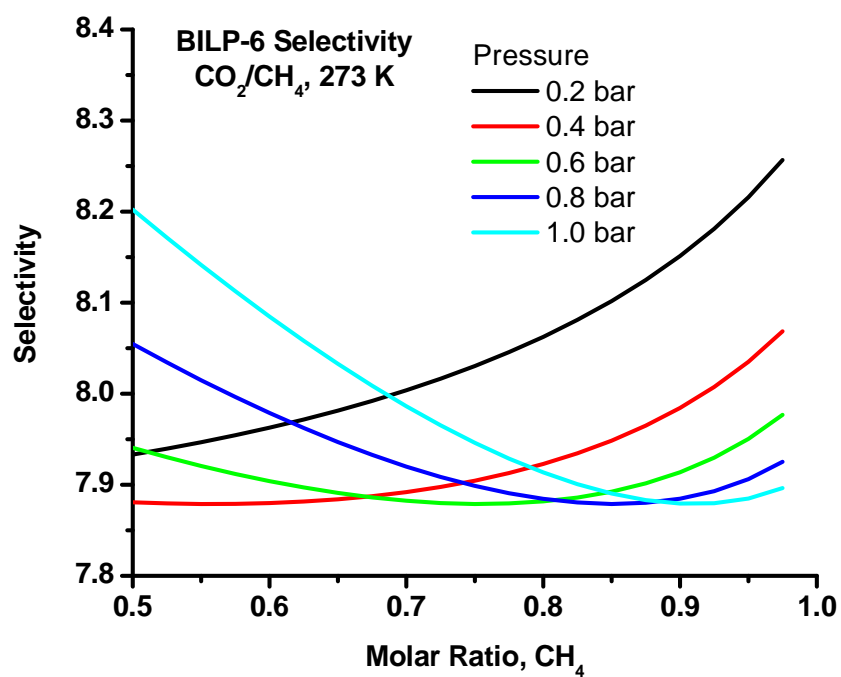


**Figure 117.** BILP-6 CO<sub>2</sub>/CH<sub>4</sub> Selectivity versus Pressure at 298 K.

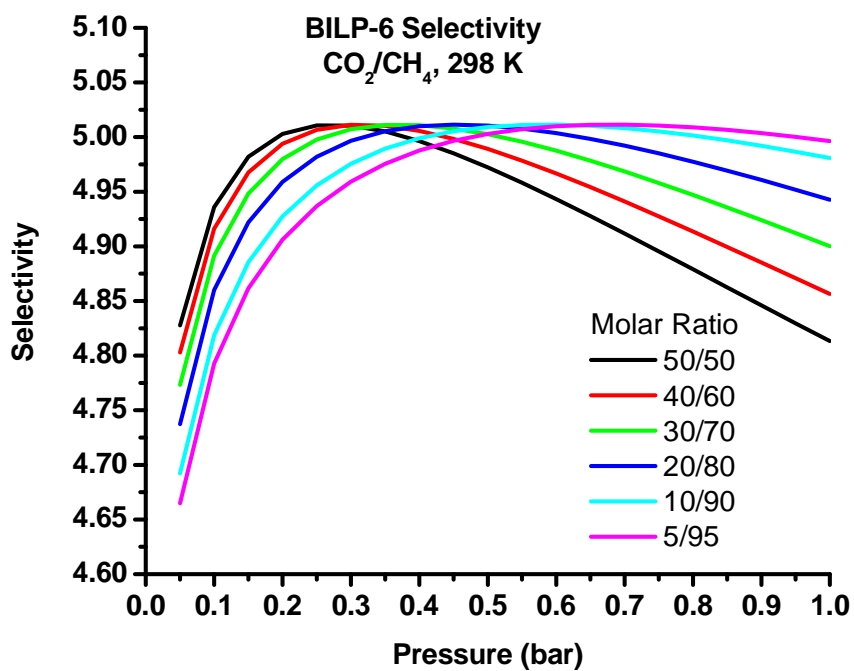


**Figure 118.** BILP-6 CO<sub>2</sub>/CH<sub>4</sub> Selectivity versus Molar Ratio of CH<sub>4</sub> at 298 K.

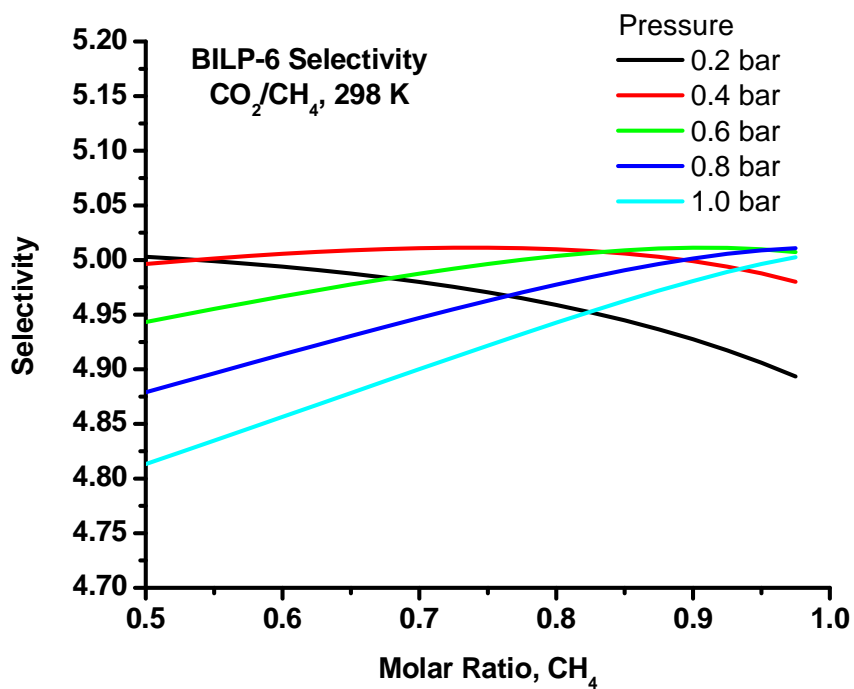


**Figure 119.** BILP-6 CO<sub>2</sub>/N<sub>2</sub> Selectivity versus Pressure at 273 K.

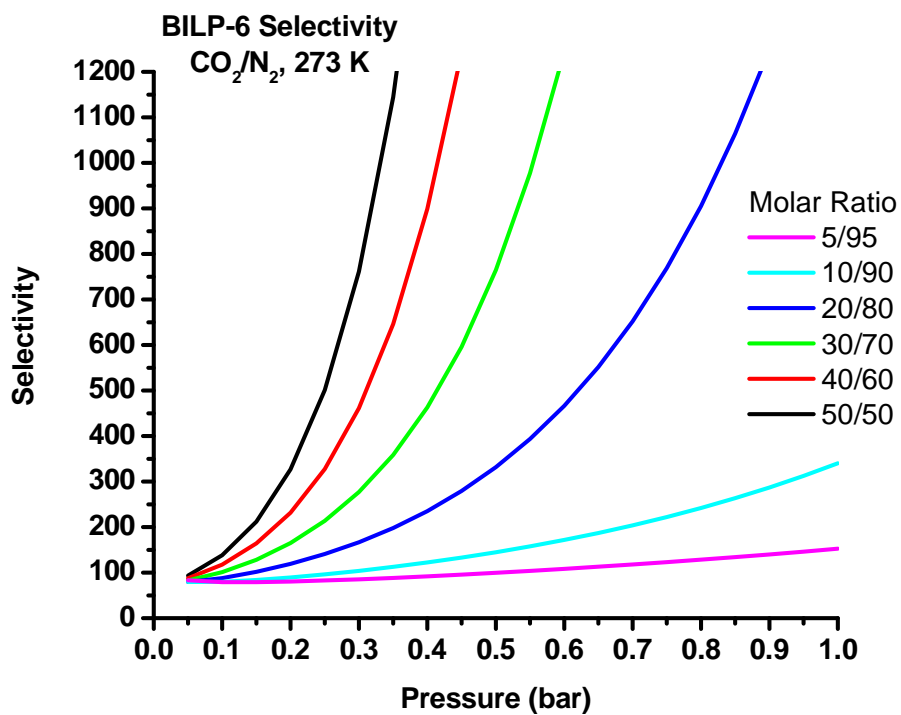


**Figure 120.** BILP-6 CO<sub>2</sub>/N<sub>2</sub> Selectivity versus Molar Ratio of N<sub>2</sub> at 273 K.

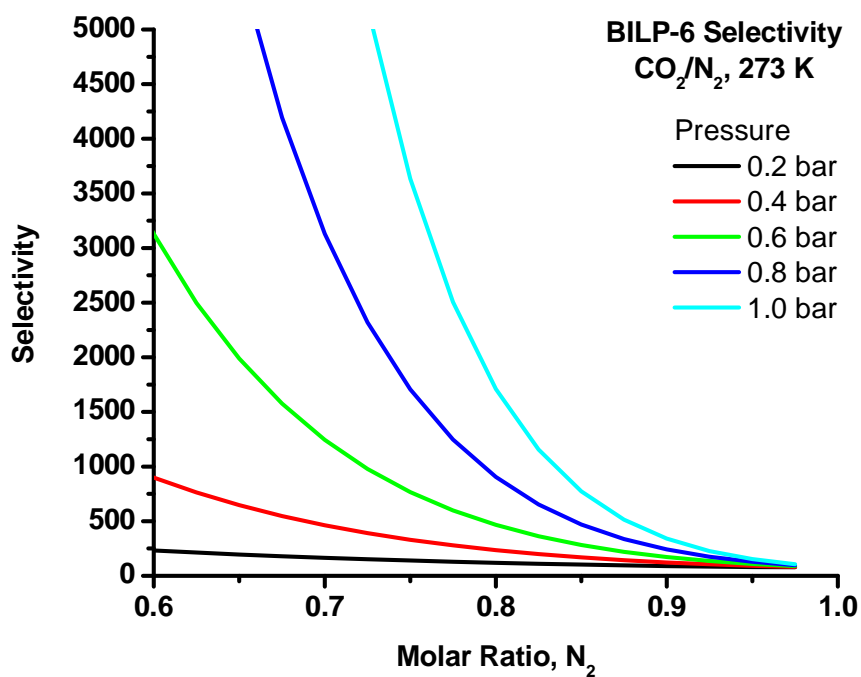


**Figure 121.** BILP-6 CO<sub>2</sub>/N<sub>2</sub> Selectivity versus Pressure at 298 K.

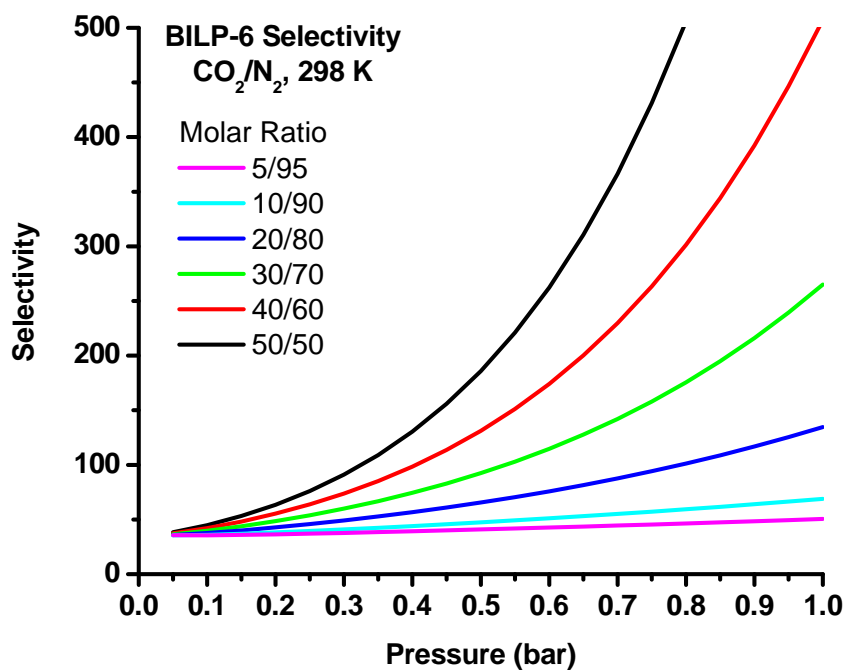


**Figure 122.** BILP-6 CO<sub>2</sub>/N<sub>2</sub> Selectivity versus Molar Ratio of N<sub>2</sub> at 298 K.

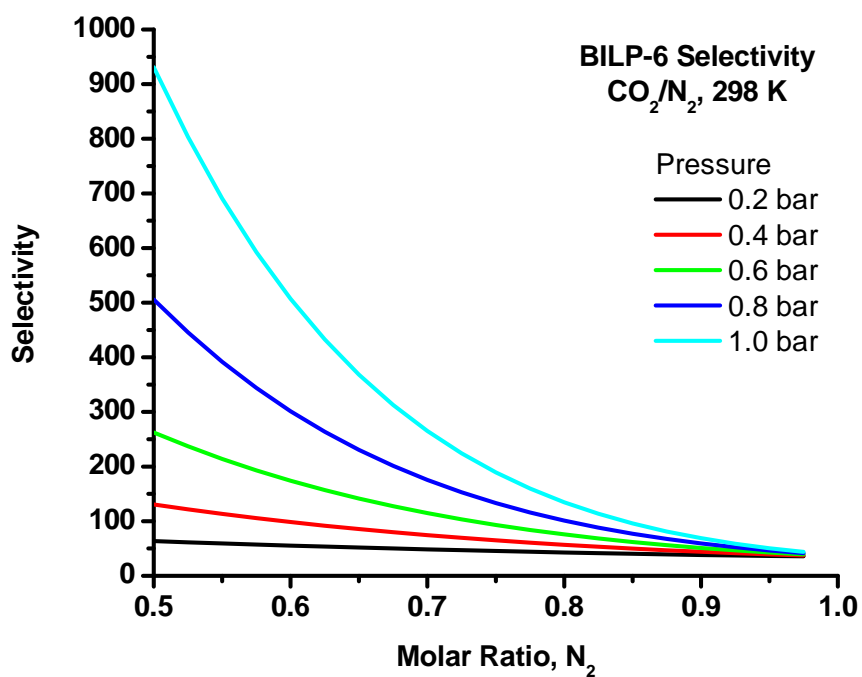


**Figure 123.** BILP-6 CO<sub>2</sub>/H<sub>2</sub> Selectivity versus Pressure at 273 K.

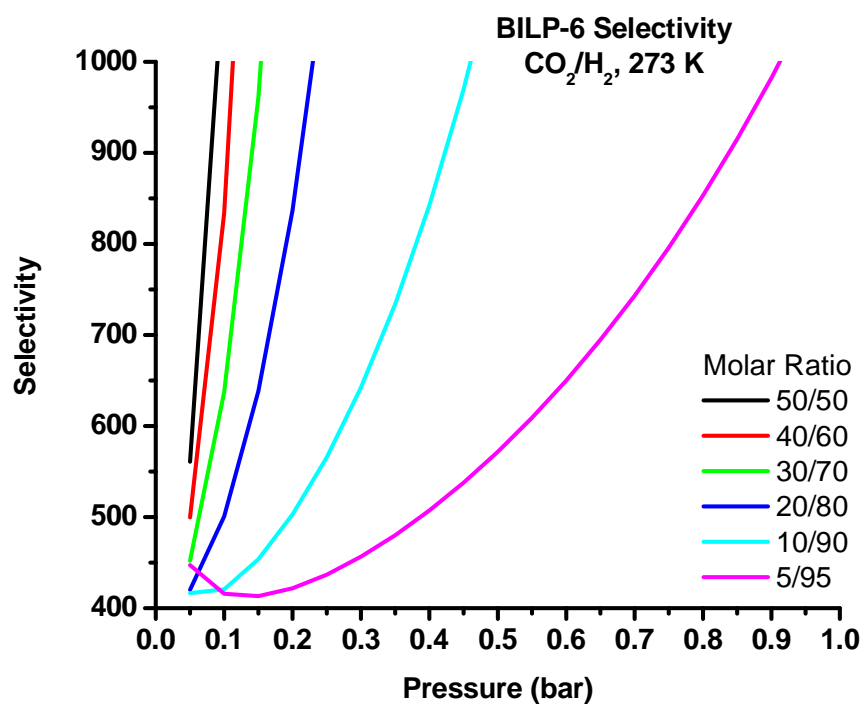


**Figure 124.** BILP-6 CO<sub>2</sub>/H<sub>2</sub> Selectivity versus Molar Ratio of H<sub>2</sub> at 273 K.

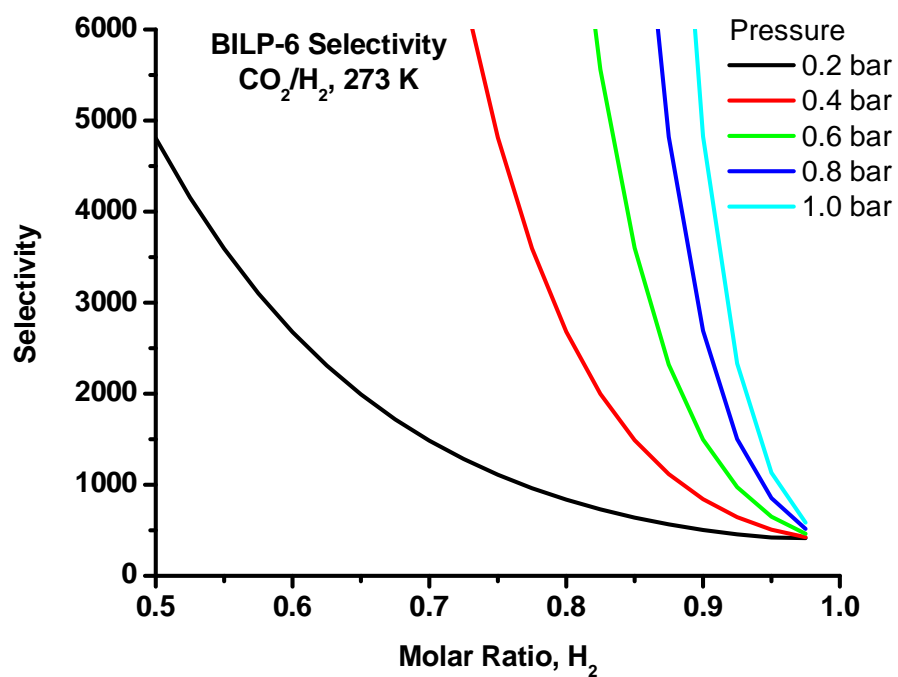


**Figure 125.** BILP-6 CO<sub>2</sub>/H<sub>2</sub> Selectivity versus Pressure at 298 K.

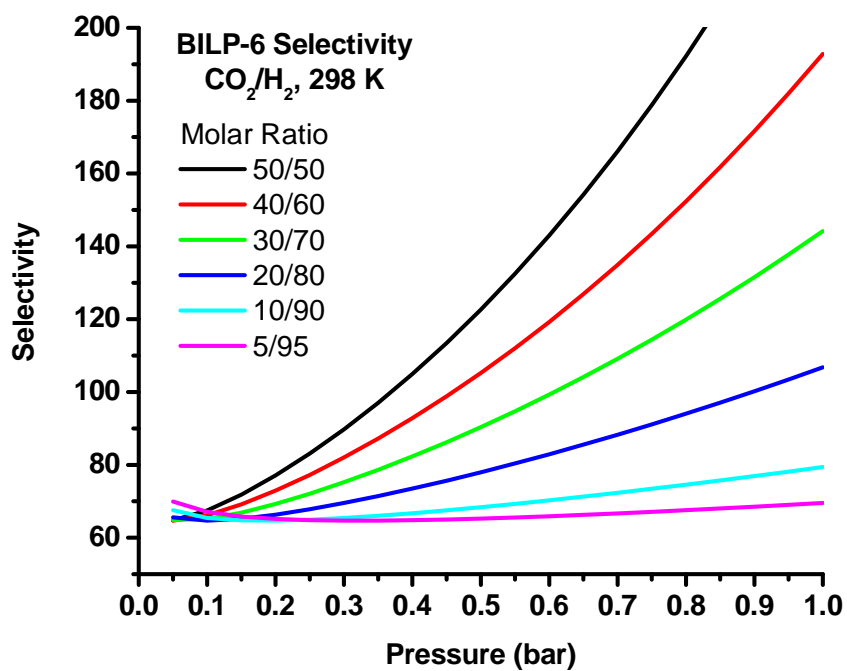


**Figure 126.** BILP-6 CO<sub>2</sub>/H<sub>2</sub> Selectivity versus Molar Ratio of H<sub>2</sub> at 298 K.

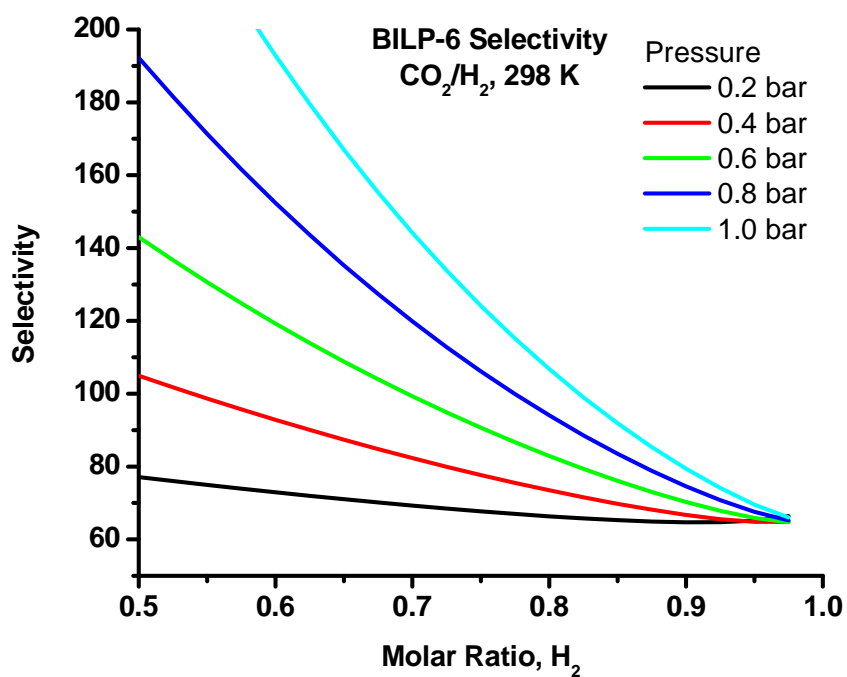


**Figure 127.** BILP-7 CO<sub>2</sub>/CH<sub>4</sub> Selectivity versus Pressure at 273 K.

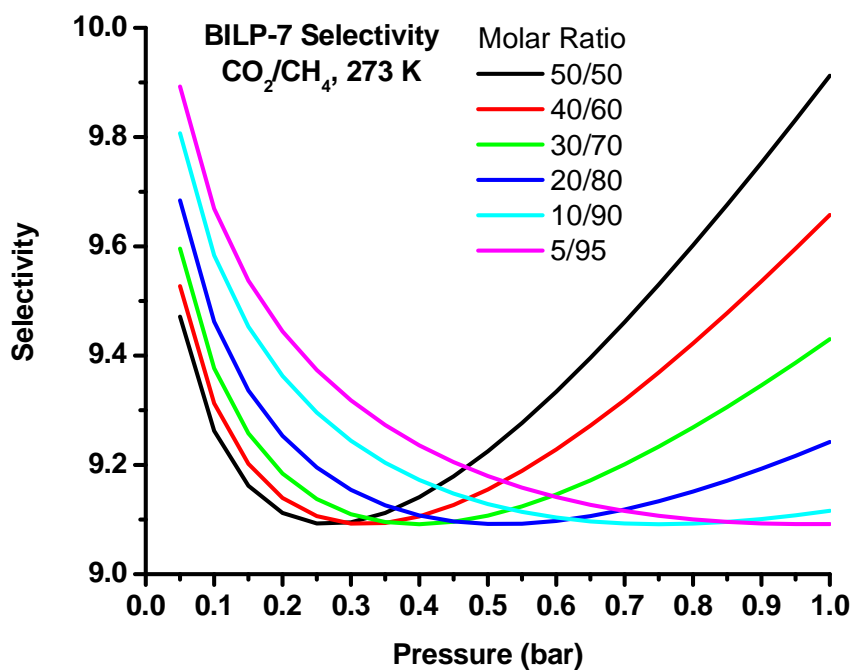


**Figure 128.** BILP-7 CO<sub>2</sub>/CH<sub>4</sub> Selectivity versus Molar Ratio of CH<sub>4</sub> at 273 K.

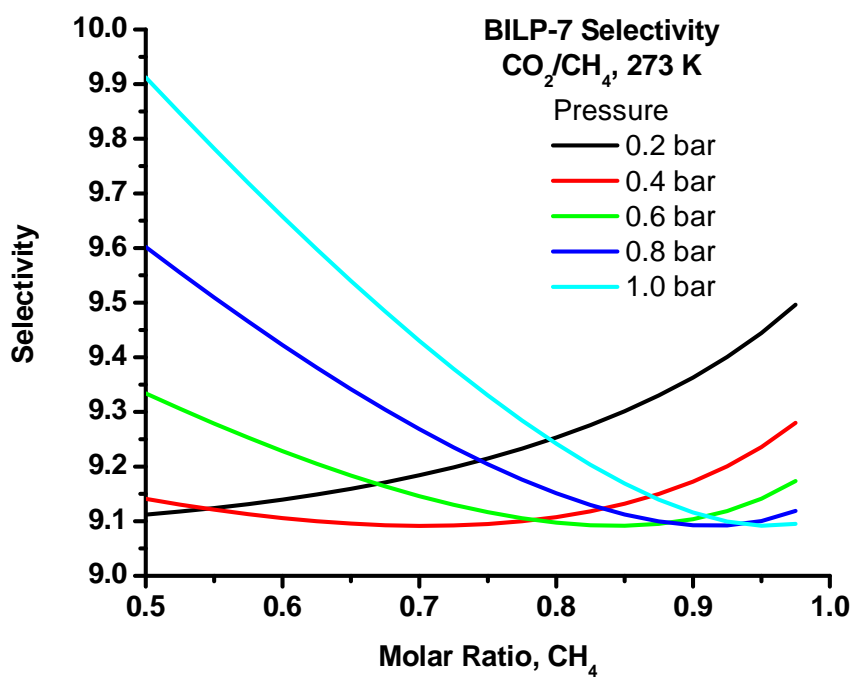


**Figure 129.** BILP-7 CO<sub>2</sub>/CH<sub>4</sub> Selectivity versus Pressure at 298 K.

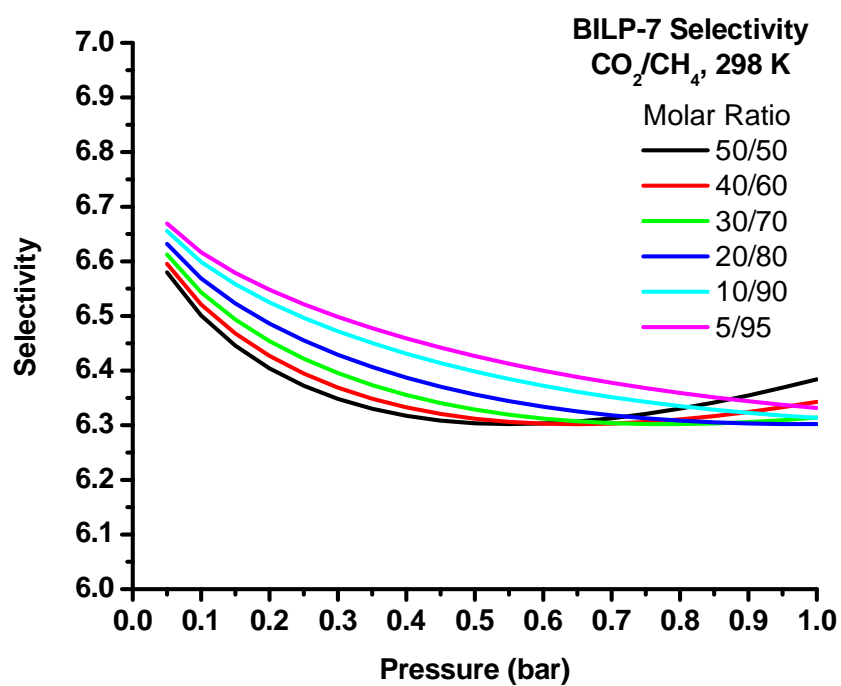


**Figure 130.** BILP-7 CO<sub>2</sub>/CH<sub>4</sub> Selectivity versus Molar Ratio of CH<sub>4</sub> at 298 K.

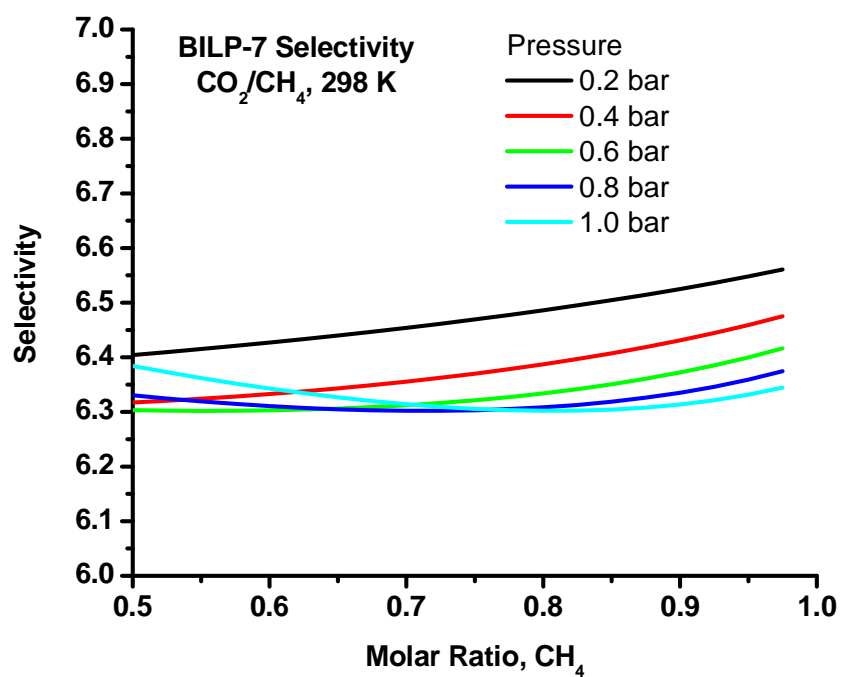




**Figure 131.** BILP-7 CO<sub>2</sub>/N<sub>2</sub> Selectivity versus Pressure at 273 K.

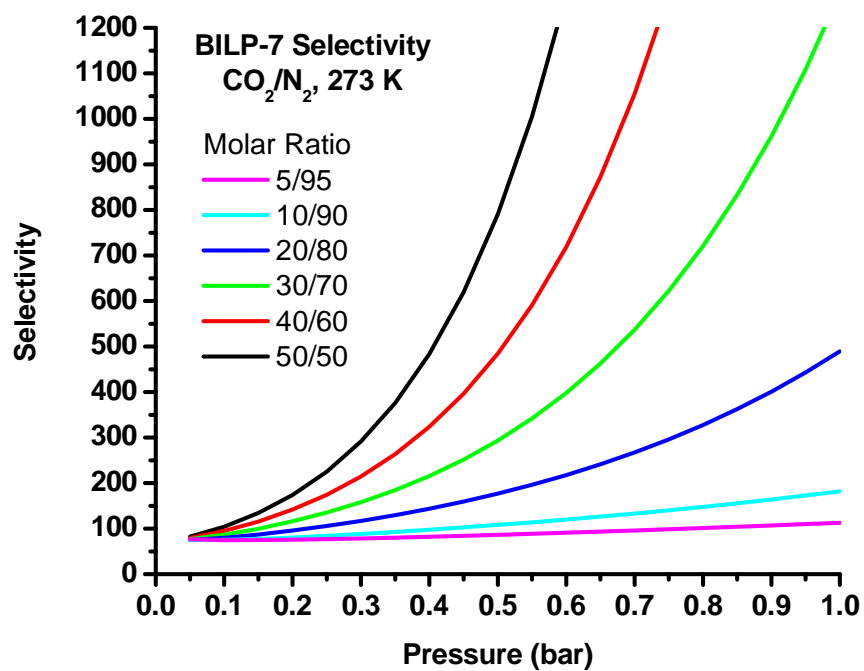


**Figure 132.** BILP-7 CO<sub>2</sub>/N<sub>2</sub> Selectivity versus Molar Ratio of N<sub>2</sub> at 273 K.

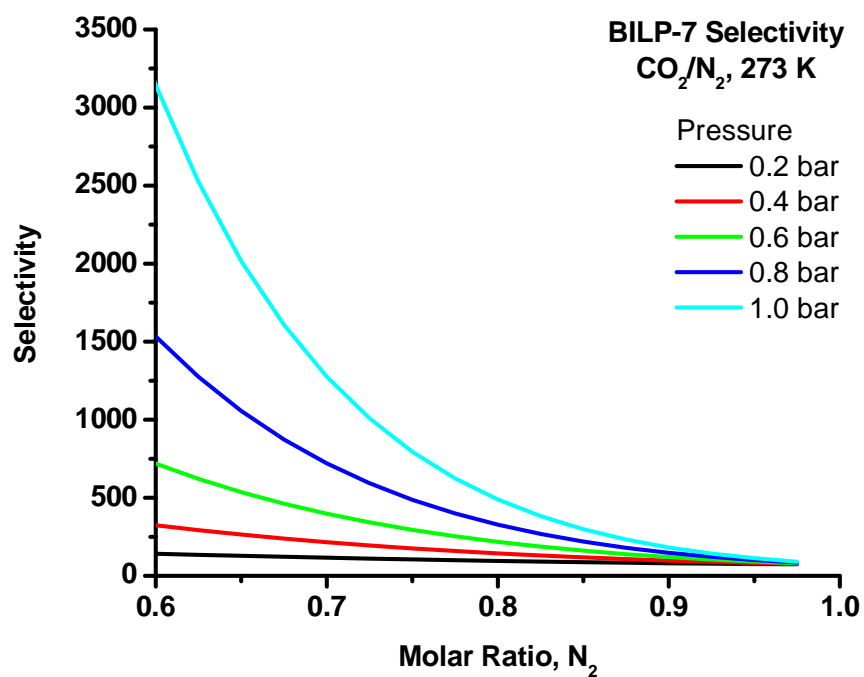


**Figure 133.** BILP-7 CO<sub>2</sub>/N<sub>2</sub> Selectivity versus Pressure at 298 K.

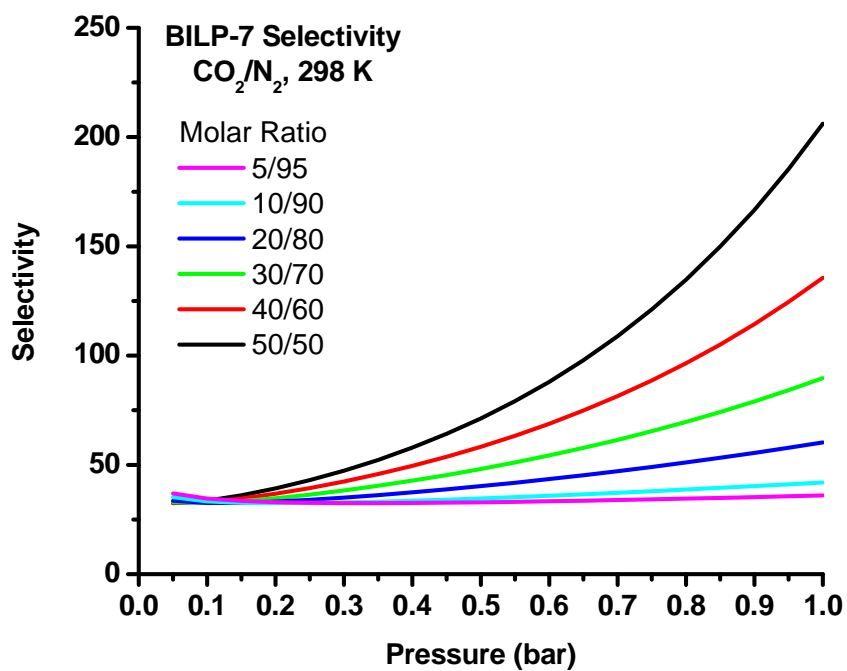


**Figure 134.** BILP-7 CO<sub>2</sub>/N<sub>2</sub> Selectivity versus Molar Ratio of N<sub>2</sub> at 298 K.

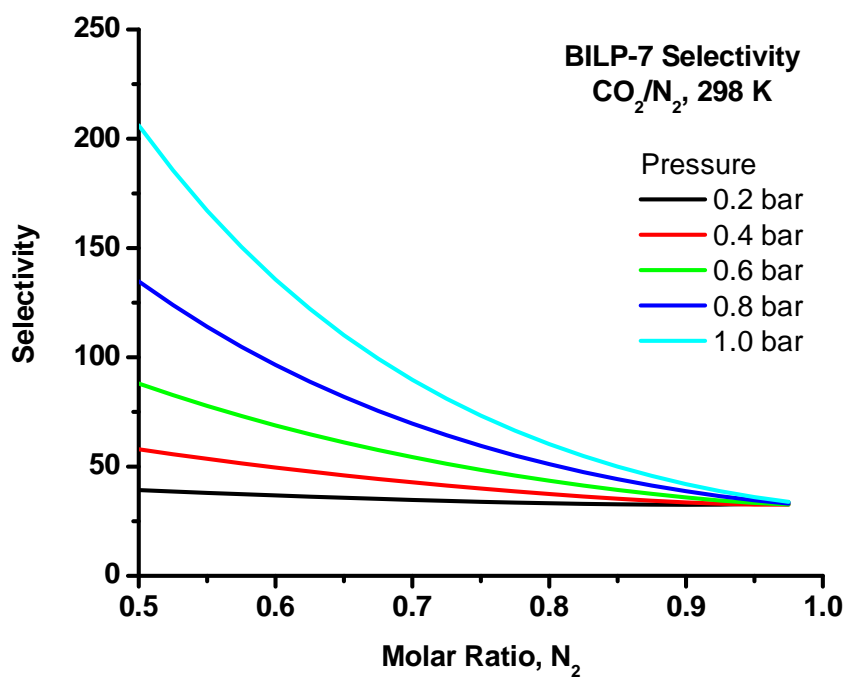


**Figure 135.** BILP-7 CO<sub>2</sub>/H<sub>2</sub> Selectivity versus Pressure at 273 K.

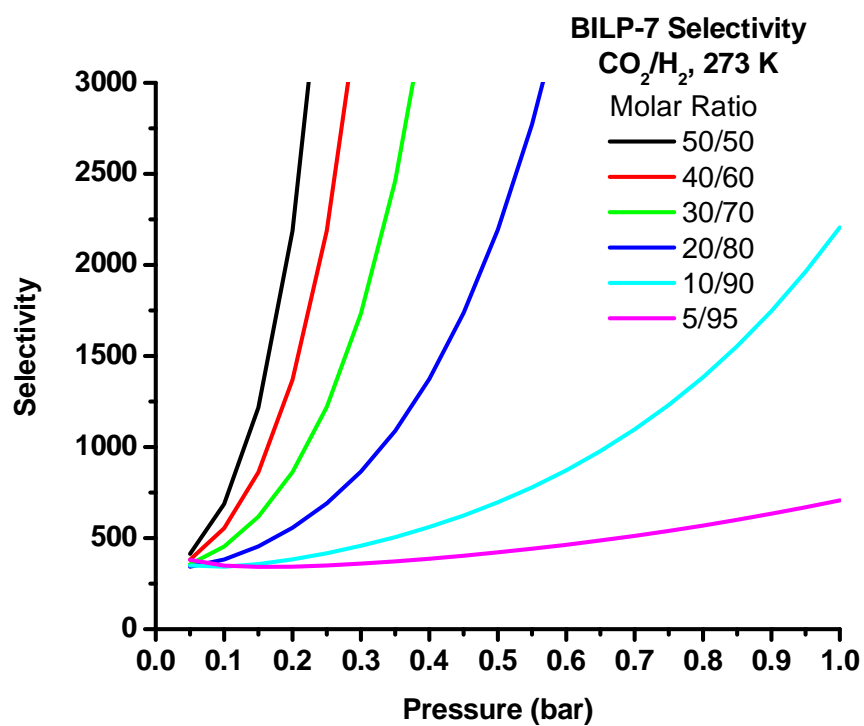


**Figure 136.** BILP-7 CO<sub>2</sub>/H<sub>2</sub> Selectivity versus Bulk Phase Molar Ratio of H<sub>2</sub> at 273 K.

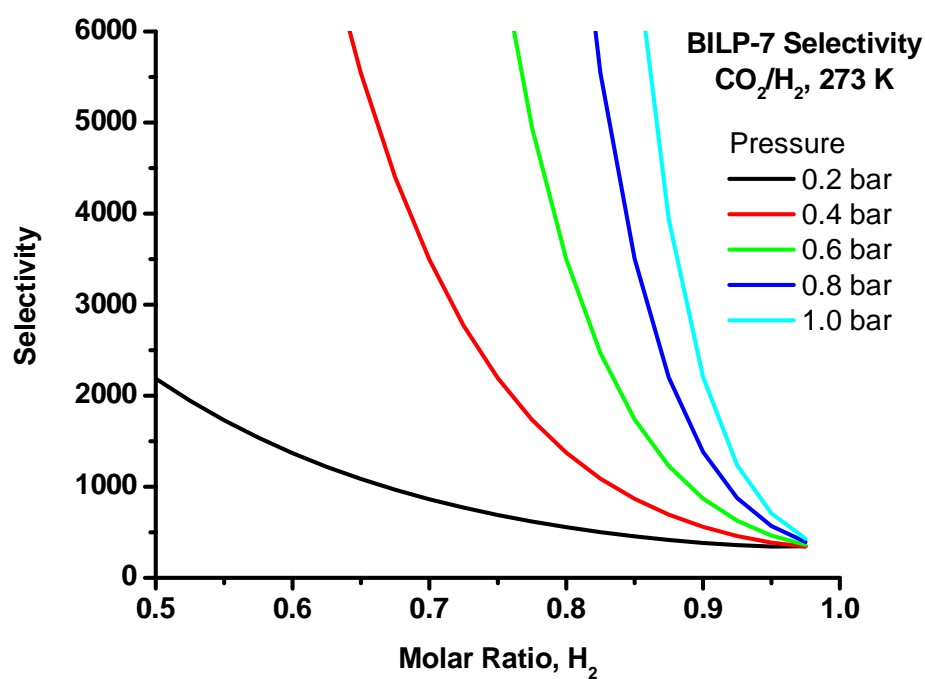


**Figure 137.** BILP-7 CO<sub>2</sub>/H<sub>2</sub> Selectivity versus Pressure at 298 K.

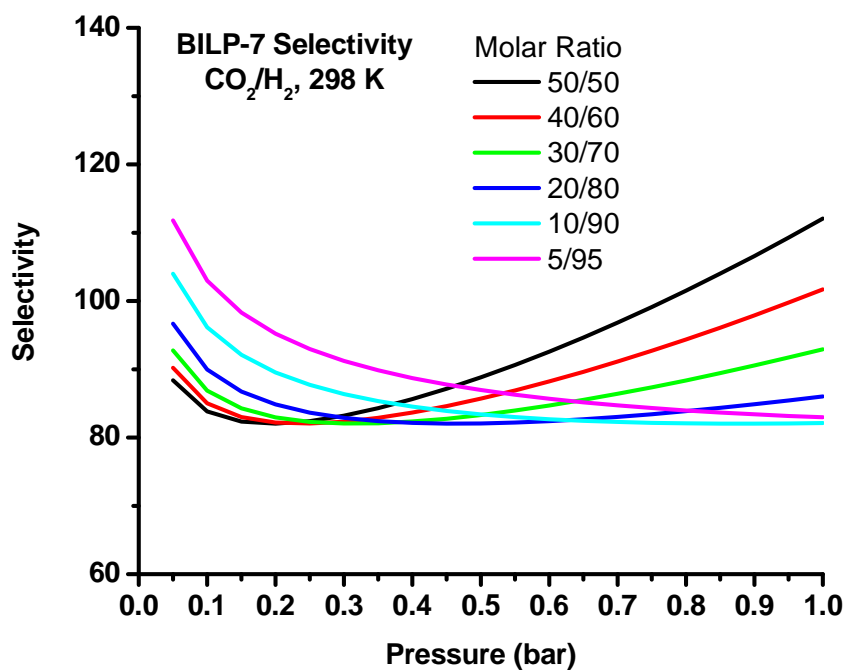
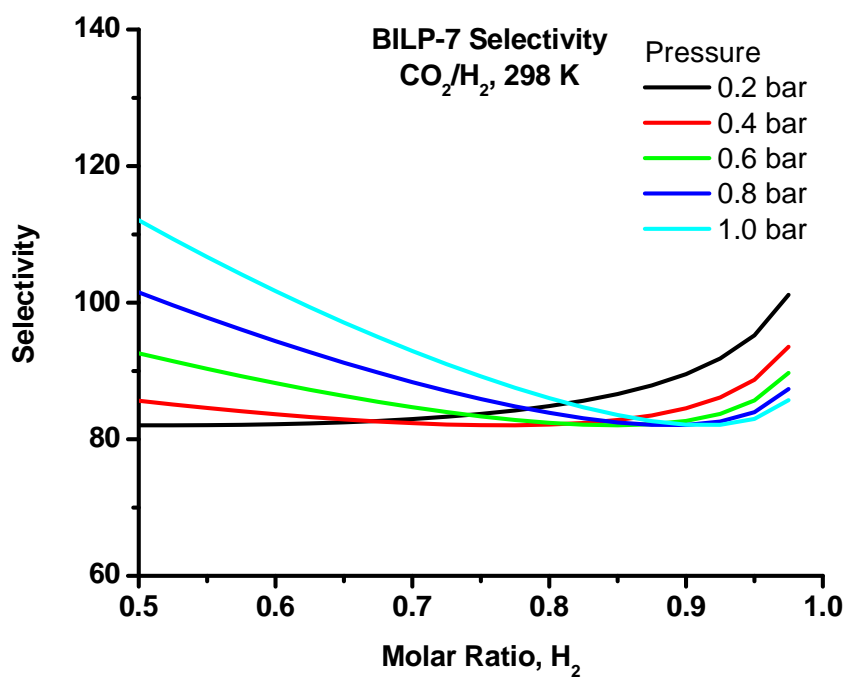


**Figure 138.** BILP-7 CO<sub>2</sub>/H<sub>2</sub> Selectivity versus Bulk Phase Molar Ratio of H<sub>2</sub> at 298 K.



### 6.3 Detailed Methodology for the Calculation of Selectivity by the Ideal Adsorbed Solution Theory

As mentioned in Section 6.1, ideal adsorbed solution theory<sup>299</sup> calculations were performed based on the mathematical integration:

$$\int_{t=0}^{\frac{Py_1}{x_1}} F_1(t) d \ln t = \int_{t=0}^{\frac{Py_2}{x_2}} F_2(t) d \ln t$$

In this equation, P is the total pressure,  $y_i$  is the bulk phase molar ratio of gas i,  $x_i$  is the adsorbed phase molar ratio of gas i, and the function,  $F_i(t)$ , is a fitting function for the pure component i based on the Langmuir-Freundlich equation:

$$n = \frac{a*b*p^{1/c}}{1+b*p^{1/c}} + \frac{d*e*p^{1/f}}{1+e*p^{1/f}}$$

In this equation, n is the gas uptake in mmol/g, p is the pressure in bar, and a, b, c, d, e, and f are the fitting parameters. Note that this equation is based on the dual-site Langmuir-Freundlich equation. If the single-site fitting gives a more appropriate result, d and e become 0, and f becomes 1. Since  $x_1 = 1 - x_2$  and  $y_1 = 1 - y_2$ , the integration equation nets only three unknowns. Therefore, by specifying one value and varying a second, the third value can be calculated. Selectivity can then be calculated as:

$$s_{1,2} = \frac{x_1/y_1}{x_2/y_2}$$

As a detailed example of how the process was performed, the calculation for the selectivity of CO<sub>2</sub>/CH<sub>4</sub> at 273 K for BLP-10(Cl) is included. The dual-site or single-site Langmuir-Freundlich equation was used to calculate the fitting as appropriate. Table 23

(at the end of this section) shows the data points for the isotherms of CO<sub>2</sub> and CH<sub>4</sub> at 273 K for BLP-10(CI), and Table 24 (also at the end of this section) shows the corresponding Langmuir-Freundlich coefficients. The corresponding selectivity graphs can be found in Section 6.4. To find the root of the integration, Wolfram Mathematica 8.0 was used.<sup>321</sup> First, the indefinite integral was solved for the Langmuir-Freundlich coefficients for CO<sub>2</sub> at 273 K by inputting the following command:

```
Integrate[ ((5.069818517 * (0.476625513) * p^(1/0.740709345)) / (1 + (0.476625513) * p^(1/0.740709345))) +  
(1.527817039 * 2.642546179 * p^(1/1.045857825)) / (1 + (2.642546179 * p^(1/1.045857825)))) / p, p]
```

where p is the indefinite pressure. This command gives the result:

$$1.59788 \log[1. + 2.64255 p^{0.956153}] + 3.75526 \log[1. + 0.476626 p^{1.35006}]$$

Note that the Langmuir-Freundlich equation is divided by p before the indefinite integral is solved since the integration of the IAST method is by  $(d \ln t)$  and not  $(dt)$ . The process was repeated for CH<sub>4</sub> at 273 K:

```
Integrate[ ((3.681148701 * (0.05704397) * p^(1/1.080128572)) / (1 + ((0.05704397) * p^(1/1.080128572)))) / p, p]  
3.97611 Log[1. + 0.057044 p0.925816]
```

The definite integral was then solved according to IAST by the command:

```
Grid[Table[FindRoot[
  (1.59788 Log[1. + 2.64255 (0.4 Q / x)^0.956153] + 3.75526 Log[1. + 0.476626 (0.4 Q / x)^1.35006]) -
  (1.59788 Log[1. + 2.64255 * 0^0.956153] + 3.75526 Log[1. + 0.476626 * 0^1.35006])
  == (3.97611 Log[1. + 0.057044 * (0.6 Q / (1 - x))^0.925816] - (3.97611 Log[1. + 0.057044 * 0^0.925816])),
  {x, .999}], {Q, 0.05, 1, 0.05}]]
```

In this command, Q represents the pressure and is varied from 0.05 to 1 bar with a step size of 0.05 bar. The value of x represents  $x_1$ , and the value for  $x_2$  is replaced with (1-x). Additionally, the values 0.4 and 0.6 before each Q represent the bulk phase molar ratios  $y_1$  and  $y_2$ , respectively. This command generates the results:

```
x → 0.937393
x → 0.939612
x → 0.940897
x → 0.94181
x → 0.942527
x → 0.943127
x → 0.943652
x → 0.944124
x → 0.944558
x → 0.944966
x → 0.945352
x → 0.945722
x → 0.946079
x → 0.946425
x → 0.946763
x → 0.947093
x → 0.947417
x → 0.947736
x → 0.94805
x → 0.948359
```

These  $x_1$  values correspond to the values with increasing pressure, Q, and were used to calculate the selectivity at this bulk phase composition. The process was also repeated for bulk phase compositions of CO<sub>2</sub>:CH<sub>4</sub> mixtures at 50:50, 30:70, 20:80, 10:90, and

5:95 molar ratios. In order to calculate selectivity at a particular pressure with varying bulk phase composition (the second method for visualizing the selectivity data), the following command was entered into Mathematica:

```
Grid[Table[FindRoot[
  (1.59788 Log[1. + 2.64255 (y*0.2/x)^0.956153] + 3.75526 Log[1. + 0.476626 (y*0.2/x)^1.35006]) -
  (1.59788 Log[1. + 2.64255 * 0^0.956153] + 3.75526 Log[1. + 0.476626 * 0^1.35006])
  == (3.97611 Log[1. + 0.057044 * ((1-y)*0.2/(1-x))^0.925816]) - (3.97611 Log[1. + 0.057044 * 0^0.925816]),
  {x, .999}], {y, 0.5, 0.025, -0.025}]]
```

The bulk phase composition of CO<sub>2</sub>, characterized as y, was varied from 0.5 down to 0.025 (i.e. an increasing mole fraction for CH<sub>4</sub>). The 0.2 value following the bulk phase compositions represents a pressure of 0.2 bar. This command yields:

```
x → 0.960893
x → 0.956837
x → 0.952354
x → 0.947373
x → 0.94181
x → 0.935557
x → 0.928481
x → 0.920413
x → 0.911134
x → 0.900354
x → 0.887688
x → 0.872605
x → 0.854358
x → 0.831862
x → 0.803477
x → 0.766615
x → 0.71693
x → 0.64657
x → 0.539794
x → 0.360032
```



These  $x_1$  values were used to calculate the selectivity at this pressure with varying bulk phase composition. The process was also repeated for pressures of 0.4, 0.6, 0.8, and 1.0 bar.

To ease the redundancy in the Mathematica calculations, more encompassing parameters can be used. For selectivity calculations with pressure on the x-axis at certain molar ratios, the following formula was used:

```
Grid[Table[FindRoot[
  (1.59788 Log[1. + 2.64255 (0.4 Q / x)^0.956153] + 3.75526 Log[1. + 0.476626 (0.4 Q / x)^1.35006]) -
  (1.59788 Log[1. + 2.64255 * 0^0.956153] + 3.75526 Log[1. + 0.476626 * 0^1.35006])
  == (3.97611 Log[1. + 0.057044 * (0.6 Q / (1 - x))^0.925816]) - (3.97611 Log[1. + 0.057044 * 0^0.925816]),
  {x, .999}], {Q, 0.05, 1, 0.05}]]
```

Instead of manually re-entering the molar ratios for values other than a 40:60 mixture, the following input can be applied:

```
Grid[Table[Grid[Table[FindRoot[
  (1.59788 Log[1. + 2.64255 (y * Q / x)^0.956153] + 3.75526 Log[1. + 0.476626 (y * Q / x)^1.35006]) -
  (1.59788 Log[1. + 2.64255 * 0^0.956153] + 3.75526 Log[1. + 0.476626 * 0^1.35006])
  == (3.97611 Log[1. + 0.057044 * ((1 - y) * Q / (1 - x))^0.925816]) -
  (3.97611 Log[1. + 0.057044 * 0^0.925816]),
  {x, .999}], {Q, 0.05, 1, 0.05}]], {y, {0.5, 0.4, 0.3, 0.2, 0.1, 0.05}}]]
```

In this equation,  $x$  still represents the adsorbed phase mole fraction of  $\text{CO}_2$ , and  $Q$  still represents pressure. The new term,  $y$ , represents the bulk phase mole fraction of  $\text{CO}_2$ . This equation yields the output:

	x → 0.957824	x → 0.937393	x → 0.904703	x → 0.844684	x → 0.701831	x → 0.522179
	x → 0.959362	x → 0.939612	x → 0.907932	x → 0.849517	x → 0.709287	x → 0.530784
	x → 0.960253	x → 0.940897	x → 0.909808	x → 0.852353	x → 0.713744	x → 0.536012
	x → 0.960893	x → 0.94181	x → 0.911134	x → 0.854358	x → 0.71693	x → 0.539794
	x → 0.961403	x → 0.942527	x → 0.912165	x → 0.85591	x → 0.719408	x → 0.54276
	x → 0.961836	x → 0.943127	x → 0.913015	x → 0.85718	x → 0.721435	x → 0.545201
	x → 0.962222	x → 0.943652	x → 0.913746	x → 0.858257	x → 0.72315	x → 0.547275
	x → 0.962574	x → 0.944124	x → 0.914393	x → 0.859198	x → 0.724637	x → 0.549078
	x → 0.962904	x → 0.944558	x → 0.914979	x → 0.860036	x → 0.725951	x → 0.550673
Grid[	{ x → 0.963216	x → 0.944966	x → 0.91552	x → 0.860797	x → 0.72713	x → 0.552103 }
	{ x → 0.963516	x → 0.945352	x → 0.916025	x → 0.861497	x → 0.7282	x → 0.5534 }
	x → 0.963806	x → 0.945722	x → 0.916503	x → 0.862147	x → 0.729181	x → 0.554587
	x → 0.964087	x → 0.946079	x → 0.916958	x → 0.862758	x → 0.730089	x → 0.555681
	x → 0.964362	x → 0.946425	x → 0.917396	x → 0.863337	x → 0.730936	x → 0.556698
	x → 0.964632	x → 0.946763	x → 0.917819	x → 0.863888	x → 0.73173	x → 0.557647
	x → 0.964896	x → 0.947093	x → 0.918229	x → 0.864416	x → 0.732479	x → 0.558537
	x → 0.965157	x → 0.947417	x → 0.91863	x → 0.864925	x → 0.73319	x → 0.559377
	x → 0.965413	x → 0.947736	x → 0.919021	x → 0.865417	x → 0.733867	x → 0.560173
	x → 0.965666	x → 0.94805	x → 0.919404	x → 0.865896	x → 0.734515	x → 0.560928
	x → 0.965916	x → 0.948359	x → 0.919781	x → 0.866361	x → 0.735137	x → 0.561649

These values all represent  $x_1$  (the adsorbed mole fraction of  $\text{CO}_2$ ). Moving down a column is the values associated with increasing pressure. Each column represents a unique molar ratio. By moving left to right, the  $\text{CO}_2:\text{CH}_4$  bulk phase molar ratios are 50:50, 40:60, 30:70, 20:80, 10:90, and 5:95. Applying the same idea of reducing the redundancy of entering more values than is necessary to the situation of selectivity versus molar ratio on the x-axis demands the input and subsequent output:

```
Grid[Table[Grid[Table[FindRoot[
  (1.59788 Log[1. + 2.64255 (y * Q / x) ^ 0.956153] + 3.75526 Log[1. + 0.476626 (y * Q / x) ^ 1.35006]) -
  (1.59788 Log[1. + 2.64255 * 0 ^ 0.956153] + 3.75526 Log[1. + 0.476626 * 0 ^ 1.35006])
  == (3.97611 Log[1. + 0.057044 * ((1 - y) * Q / (1 - x)) ^ 0.925816]) -
  (3.97611 Log[1. + 0.057044 * 0 ^ 0.925816]) ,
  {x, .999}], {y, 0.5, 0.025, -0.025}], {Q, {0.2, 0.4, 0.6, 0.8, 1}}]]
```

	x → 0.960893	x → 0.962574	x → 0.963806	x → 0.964896	x → 0.965916
	x → 0.956837	x → 0.958657	x → 0.959972	x → 0.961129	x → 0.962207
	x → 0.952354	x → 0.954324	x → 0.955727	x → 0.956952	x → 0.958092
	x → 0.947373	x → 0.949508	x → 0.951004	x → 0.952301	x → 0.953503
	x → 0.94181	x → 0.944124	x → 0.945722	x → 0.947093	x → 0.948359
	x → 0.935557	x → 0.938069	x → 0.939777	x → 0.941228	x → 0.94256
	x → 0.928481	x → 0.931215	x → 0.933043	x → 0.934578	x → 0.93598
	x → 0.920413	x → 0.923394	x → 0.925355	x → 0.926982	x → 0.928456
	x → 0.911134	x → 0.914393	x → 0.916503	x → 0.918229	x → 0.919781
Grid	{ x → 0.900354	x → 0.90393	x → 0.906208	x → 0.908045	x → 0.90968 }
	{ x → 0.887688	x → 0.891626	x → 0.894096	x → 0.896057	x → 0.897784 }
	x → 0.872605	x → 0.87696	x → 0.879651	x → 0.881755	x → 0.883584
	x → 0.854358	x → 0.859198	x → 0.862147	x → 0.864416	x → 0.866361
	x → 0.831862	x → 0.837266	x → 0.840521	x → 0.842984	x → 0.845064
	x → 0.803477	x → 0.809543	x → 0.813159	x → 0.815853	x → 0.818093
	x → 0.766615	x → 0.773449	x → 0.777494	x → 0.780465	x → 0.782896
	x → 0.71693	x → 0.724637	x → 0.729181	x → 0.732479	x → 0.735137
	x → 0.64657	x → 0.65519	x → 0.660274	x → 0.663933	x → 0.666842
	x → 0.539794	x → 0.549078	x → 0.554587	x → 0.558537	x → 0.561649
	x → 0.360032	x → 0.368516	x → 0.37362	x → 0.377294	x → 0.380179

This equation shows the  $x_1$  value for decreasing bulk phase molar ratio of  $\text{CO}_2$  moving down a column. Each column represents different pressures: 0.2, 0.4, 0.6, 0.8, and 1.0 bar moving left to right. From these values, selectivity can be calculated in a more efficient manner.

**Table 23.** Data Points for CO<sub>2</sub> and CH<sub>4</sub> isotherms at 273 K for BLP-10(Cl).

CO <sub>2</sub> , 273 K		CH <sub>4</sub> , 273 K	
Pressure (torr)	Uptake (cc/g)	Pressure (torr)	Uptake (cc/g)
6.0461	0.9356	5.93902	0.0416
6.84228	1.0637	8.04308	0.0563
7.79532	1.1913	22.51348	0.169
10.51992	1.5937	37.73628	0.2711
20.52684	3.0387	72.71984	0.5165
35.5148	5.0654	95.9424	0.6764
68.72224	9.2002	133.5168	0.9294
93.2368	12.0046	171.5244	1.1711
129.7168	15.8969	209.494	1.4193
167.8156	19.6332	247.5928	1.6587
206.0132	23.194	285.5776	1.8924
244.1728	26.5584	323.5624	2.1269
282.3552	29.762	362.0336	2.266
320.4616	32.8366	399.6156	2.4853
358.6136	35.7933	437.6232	2.699
396.72	38.6394	475.5548	2.9177
434.872	41.3792	513.6004	3.1379
472.9632	44.0077	551.6612	3.3382
511.1456	46.5285	589.6232	3.5494
549.2444	48.9447	627.5624	3.7613
587.3584	51.3042	665.684	3.962
625.3812	53.5877	703.57	4.165
663.48	55.8137	741.6612	4.3604
701.5788	57.9644		
739.594	60.063		

**Table 24.** Langmuir-Freundlich Fitting Coefficients for BLP-10(Cl).

Gas	a	b	c	d	e	f
CO <sub>2</sub> , 273 K	5.0698	0.4766	0.7407	1.5278	2.6425	1.0459
CH <sub>4</sub> , 273 K	3.6811	0.0570	1.0801	--	--	--

## 6.4 IAST Calculations for Halogenated Borazine-Linked Polymers

By applying the methodology detailed in Section 6.3, IAST calculations were performed for all seven BLPs. Following initial visual inspection of the isothermal graphs for all BLPs, BLP-10(Cl) was selected for individual IAST calculations to assess its capabilities in the separation of CO<sub>2</sub>/N<sub>2</sub> and CO<sub>2</sub>/CH<sub>4</sub> gas mixtures. Therefore, CO<sub>2</sub> and N<sub>2</sub> gas sorption isotherms were collected at 298 K while CO<sub>2</sub> and CH<sub>4</sub> gas sorption isotherms were collected at 273 K. The resulting graphs are displayed in Figures 139-142. The selectivity of CO<sub>2</sub> over N<sub>2</sub> for BLP-10(Cl) at 1 bar does not exceed 12 until the bulk phase molar ratio of N<sub>2</sub> is over 0.95. In fact, the selectivity does not reach any appreciable levels at even the more favorable low pressures until the bulk phase molar ratio of N<sub>2</sub> approaches 1. These values are several times lower than what has been found for a myriad of compounds including Bio-MOF-11,<sup>297, 322-323</sup> non-covalent porous materials (NPMs),<sup>324</sup> and BILPs.<sup>156</sup> However, the selectivity of BLP-10(Cl) for CO<sub>2</sub> over CH<sub>4</sub> is quite significant. At 1 bar for a 50/50 mixture of CO<sub>2</sub> and CH<sub>4</sub>, the selectivity is 28. Even at greater molar ratios of methane, as would be the case in natural gas, the CO<sub>2</sub>/CH<sub>4</sub> selectivity is still over 24 at 1 bar. Additionally, the shape of the curve suggests that this value would increase with a further increase in pressure although such an occurrence cannot be confirmed without high pressure sorption data. These selectivity values for CO<sub>2</sub>/CH<sub>4</sub> in BLP-10(Cl) exceeds the values for activated carbons<sup>325</sup> and ZIFs<sup>148-149</sup> in addition to being comparable to what has been reported previously for PIMs,<sup>326</sup> TZPIMs,<sup>327</sup> and some of the more selective MOFs.<sup>17</sup> Initial slope calculations were performed to assess the validity of IAST in BLPs, as was done for BILPs, and these results were in excellent agreement with the IAST values at low pressure.

**Figure 139.** CO<sub>2</sub>/N<sub>2</sub> Selectivity for BLP-10(Cl) at 298 K by Pressure.

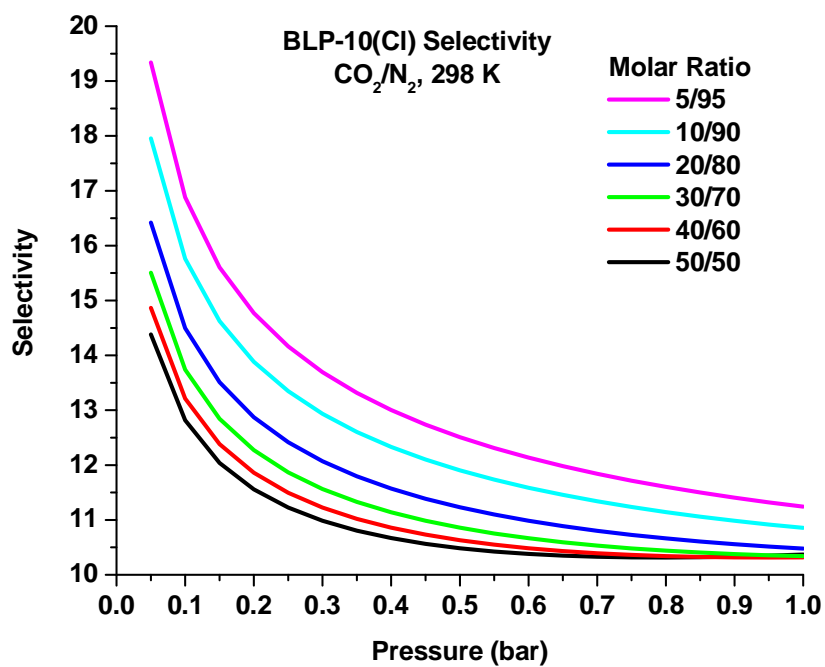


**Figure 140.** CO<sub>2</sub>/N<sub>2</sub> Selectivity for BLP-10(Cl) at 298 K by Molar Ratio.

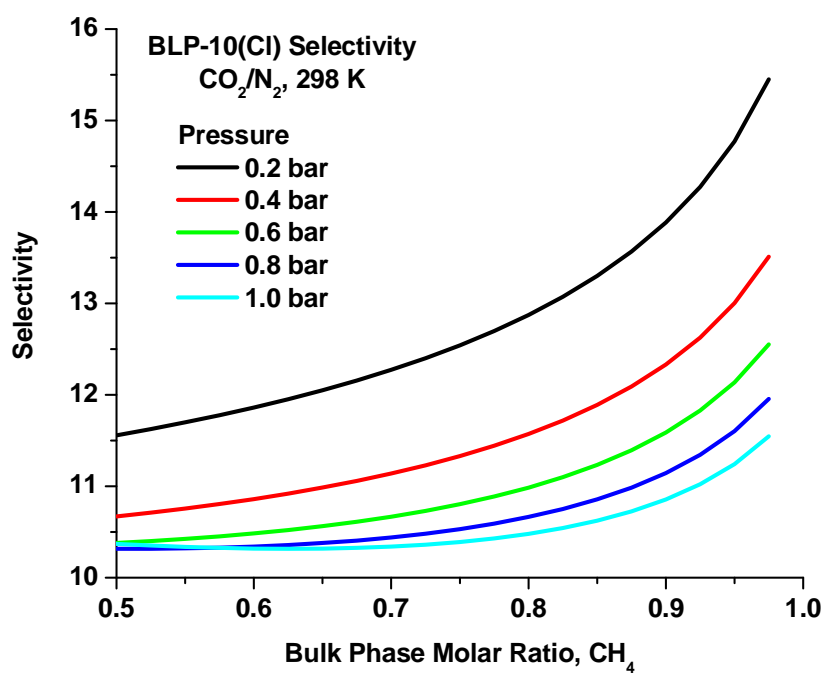


**Figure 141.** CO<sub>2</sub>/CH<sub>4</sub> Selectivity for BLP-10(Cl) at 273 K by Pressure.

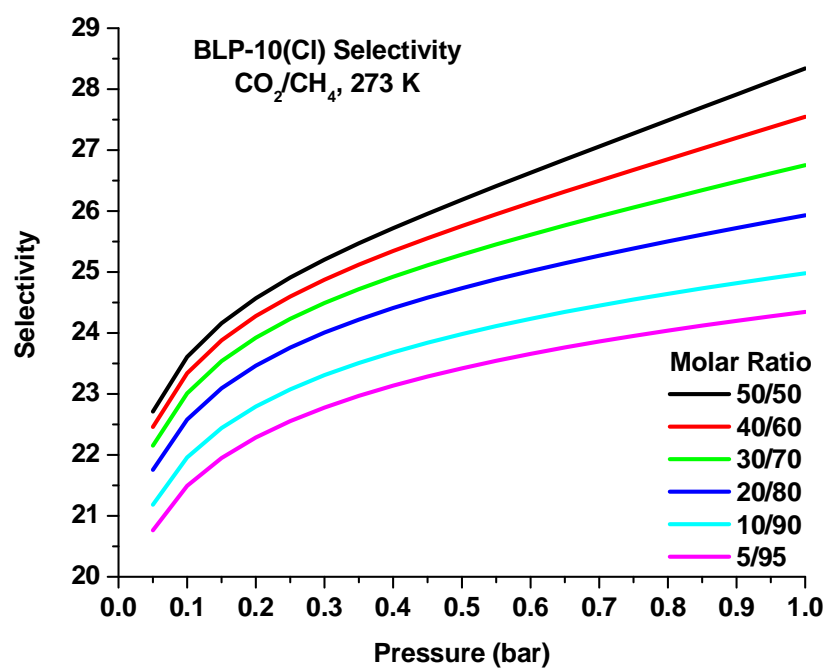
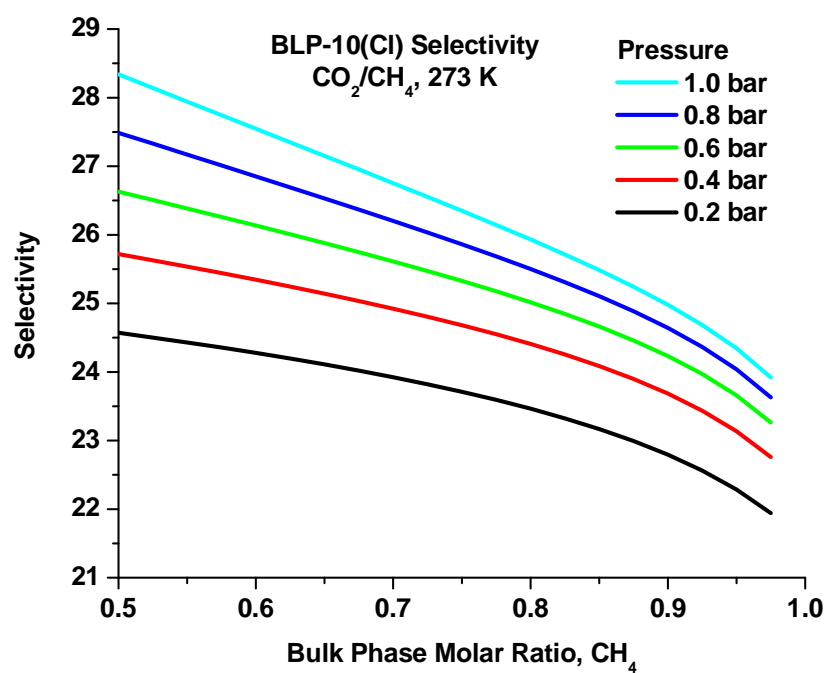


**Figure 142.** CO<sub>2</sub>/CH<sub>4</sub> Selectivity for BLP-10(Cl) at 273 K by Molar Ratio.



Following the selectivity inspection into BLP-10(Cl) as well as analysis of the carbon dioxide and nitrogen isotherms for the other six BLPs, CO<sub>2</sub>/N<sub>2</sub> selectivity was no longer pursued. However, the CO<sub>2</sub>/CH<sub>4</sub> selectivity for the other six BLPs was investigated owing to BLP-10(Cl)'s remarkable capabilities in this area. For these six BLPs, carbon dioxide and methane sorption experiments were performed at 273 K, and the IAST calculation studies were done in a similar fashion for BLP-10(Cl). The resulting graphs are displayed in Figures 143-154. Four of these polymers, BLP-1(Cl), BLP-2(Cl), BLP-10(Br), and BLP-12(Cl), do not exhibit significant levels of CO<sub>2</sub>/CH<sub>4</sub> selectivity. Their values do not exceed 13 at 1 bar for even the most favorable of molar ratios. In the cases of BLP-2(Cl) and BLP-12(Cl), for example, both polymers store good amounts of CO<sub>2</sub>; however, they both also store much higher levels of CH<sub>4</sub> than the other BLPs which contribute to their lower selectivities. Nevertheless, BLP-1(Br) and BLP-2(Br) exhibit significant CO<sub>2</sub>/CH<sub>4</sub> selectivity as was found for BLP-10(Cl). Both of these polymers exhibit selectivities between 23 and 28 at low pressure for all molar ratios. Additionally, these values increase as the pressure approaches 1 bar much like the case for BLP-10(Cl), and similarly, the shape of the curve suggests that the selectivity would increase with increasing pressure for all molar ratios. The dramatic increase in selectivity for BLP-1(Br) and BLP-2(Br) results from the methane uptake approaching saturation quicker than carbon dioxide. Interestingly, the CO<sub>2</sub> uptakes for BLP-1(Cl), BLP-2(Cl), and BLP-12(Cl) exceed that of BLP-1(Br) and BLP-2(Br); however the latter group's low methane uptakes compensate for any CO<sub>2</sub>-based disadvantage.

As a result of these calculations, both BLPs and BILPs represent exciting candidates for separation applications. For BILPs, this separation would involve the removal of



carbon dioxide from nitrogen which could have a significant impact on the environment. BLPs would be most appropriately used as a carbon dioxide separator from methane. This type of selectivity could make natural gas production more cost-effective.

**Figure 143.** CO<sub>2</sub>/CH<sub>4</sub> Selectivity for BLP-1(Br) at 273 K by Pressure.

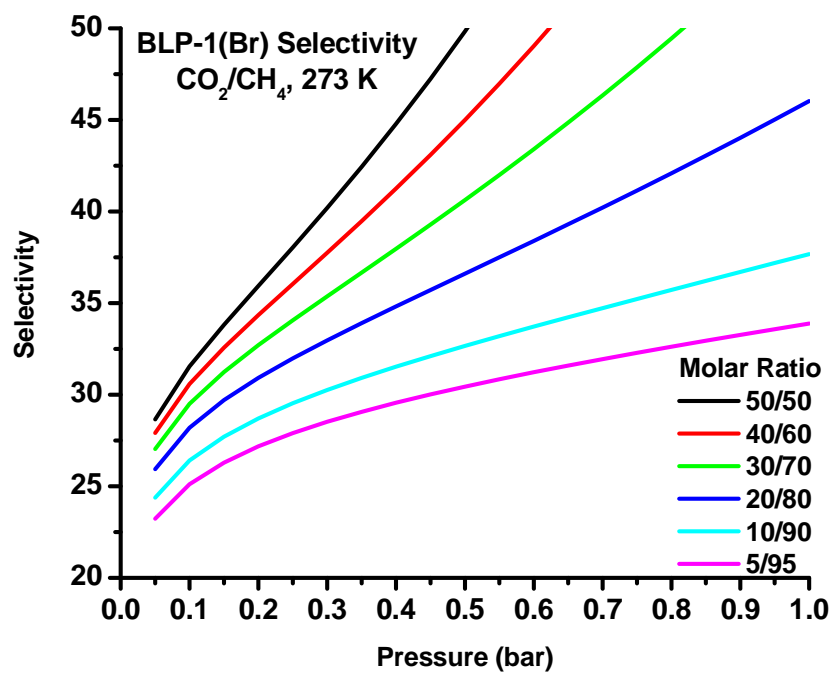


**Figure 144.** CO<sub>2</sub>/CH<sub>4</sub> Selectivity for BLP-1(Br) at 273 K by Molar Ratio.

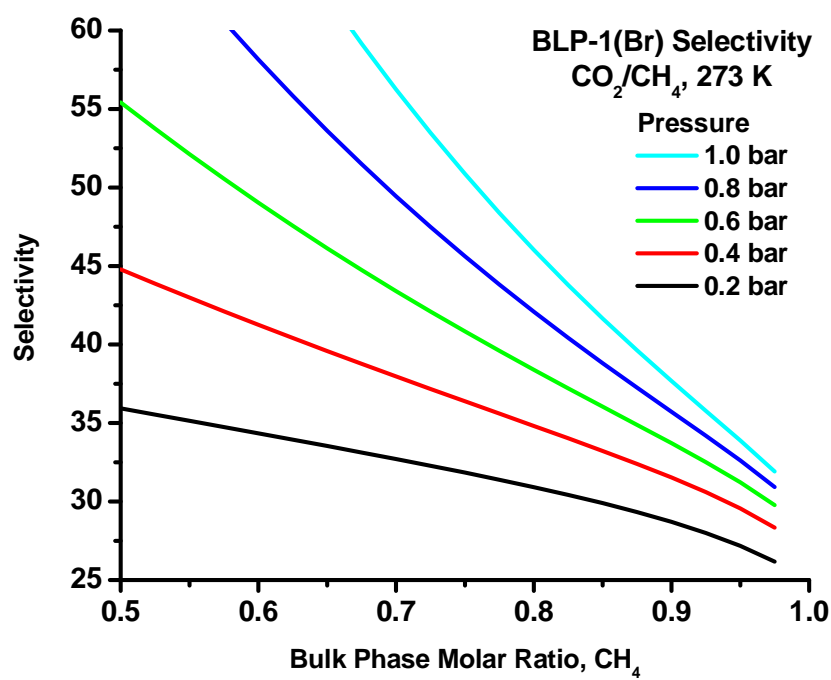


**Figure 145.** CO<sub>2</sub>/CH<sub>4</sub> Selectivity for BLP-1(Cl) at 273 K by Pressure.

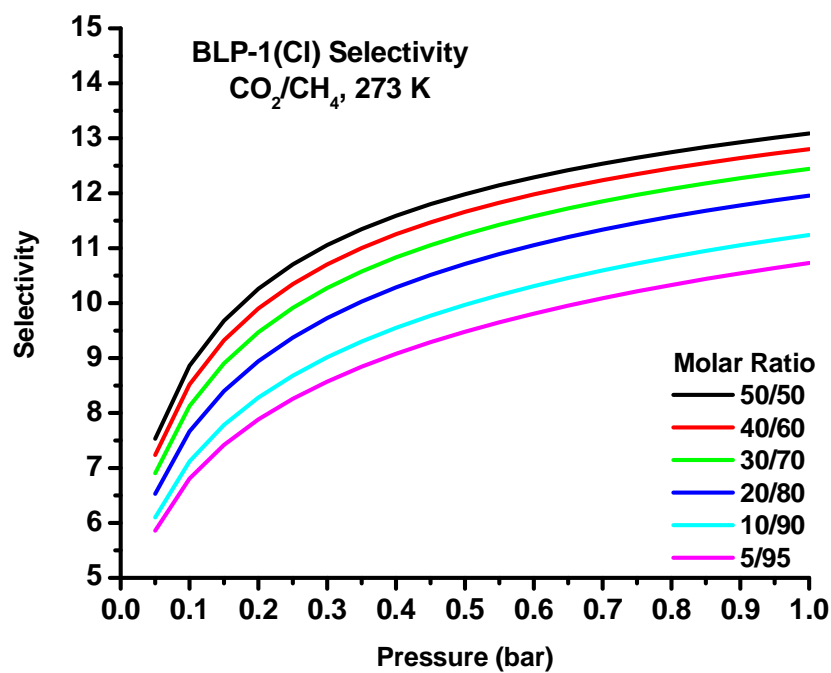


**Figure 146.** CO<sub>2</sub>/CH<sub>4</sub> Selectivity for BLP-1(Cl) at 273 K by Molar Ratio.

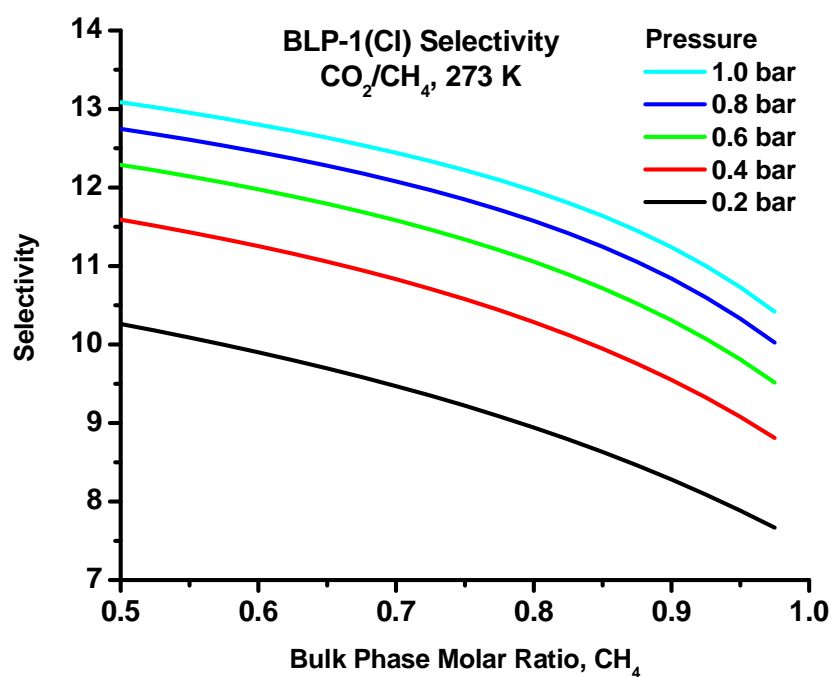


**Figure 147.** CO<sub>2</sub>/CH<sub>4</sub> Selectivity for BLP-2(Br) at 273 K by Pressure.

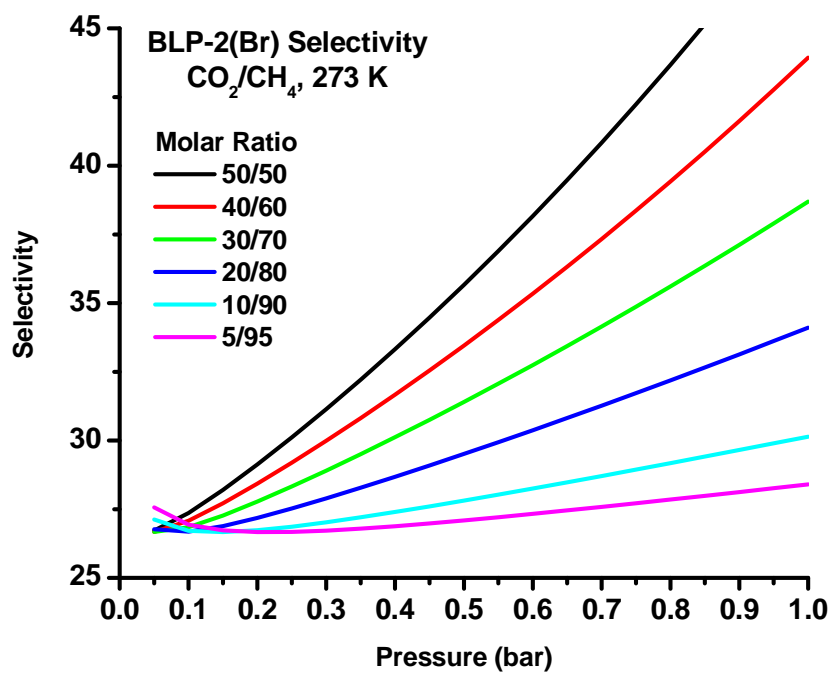


**Figure 148.** CO<sub>2</sub>/CH<sub>4</sub> Selectivity for BLP-2(Br) at 273 K by Molar Ratio.

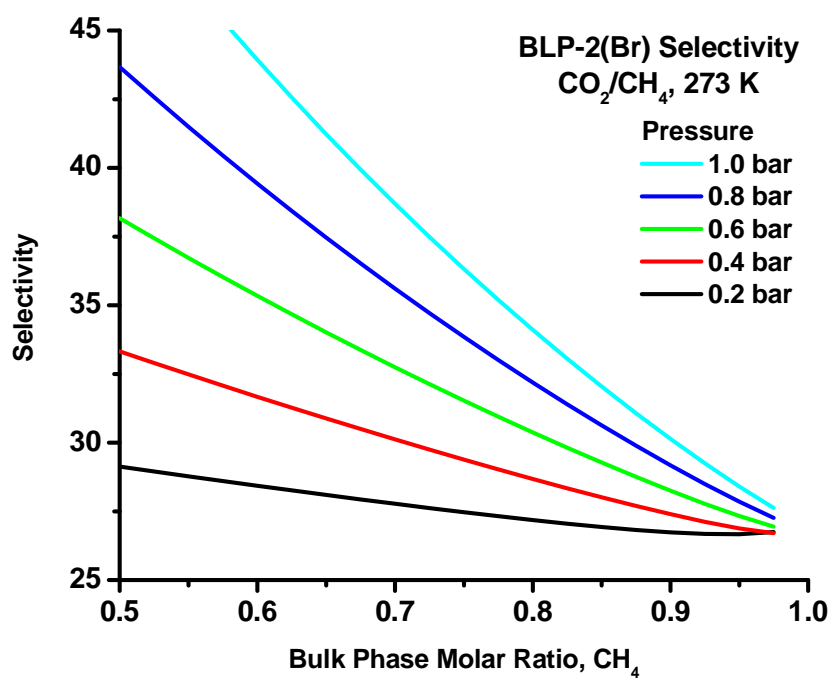


**Figure 149.**  $\text{CO}_2/\text{CH}_4$  Selectivity for BLP-2(Cl) at 273 K by Pressure.

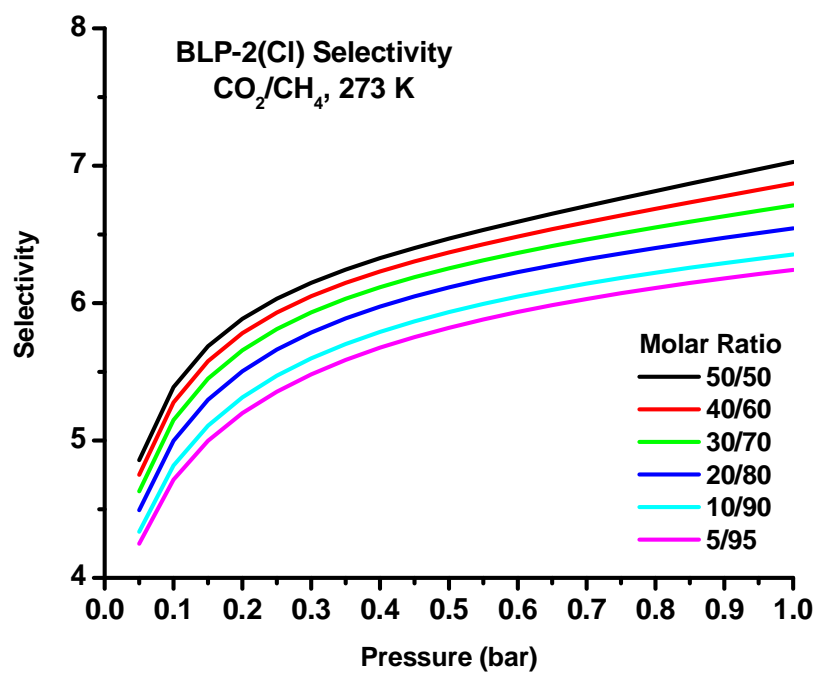


**Figure 150.**  $\text{CO}_2/\text{CH}_4$  Selectivity for BLP-2(Cl) at 273 K by Molar Ratio.

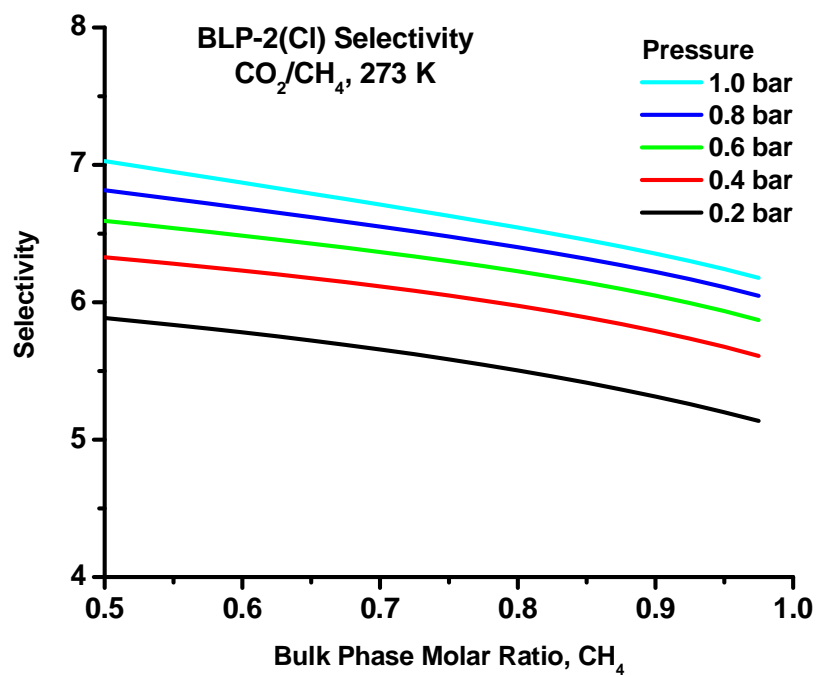


**Figure 151.** CO<sub>2</sub>/CH<sub>4</sub> Selectivity for BLP-10(Br) at 273 K by Pressure.

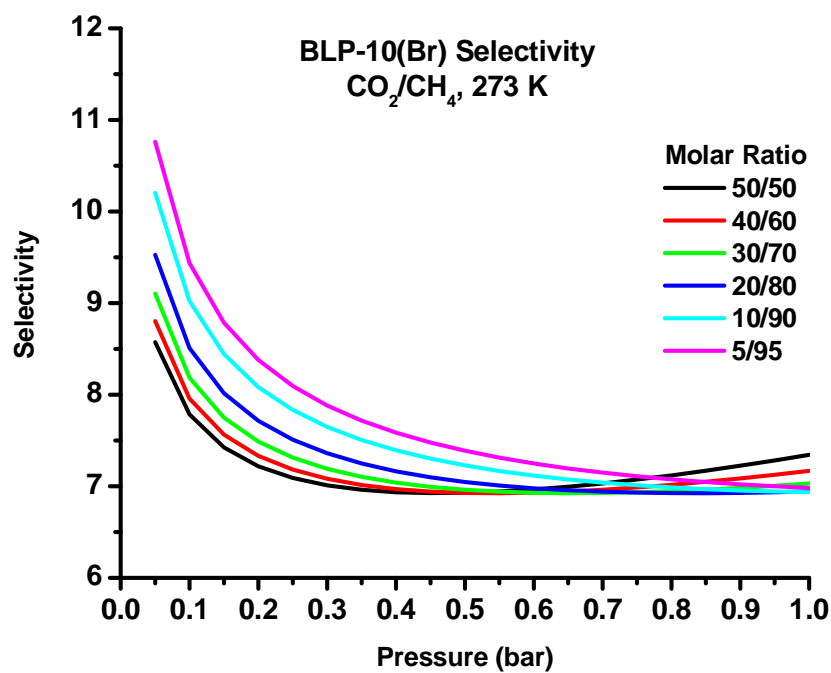


**Figure 152.** CO<sub>2</sub>/CH<sub>4</sub> Selectivity for BLP-10(Br) at 273 K by Molar Ratio.

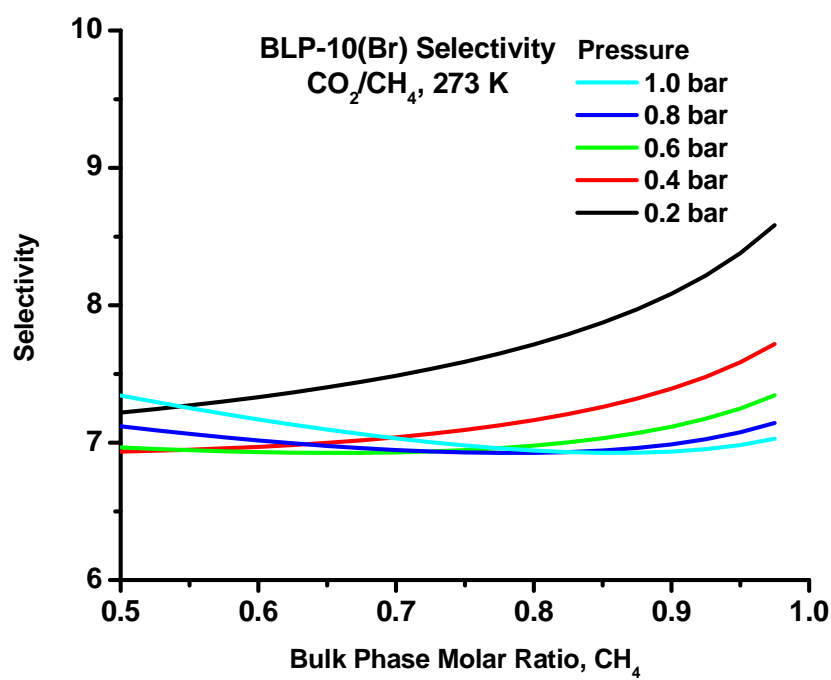


**Figure 153.** CO<sub>2</sub>/CH<sub>4</sub> Selectivity for BLP-12(Cl) at 273 K by Pressure.

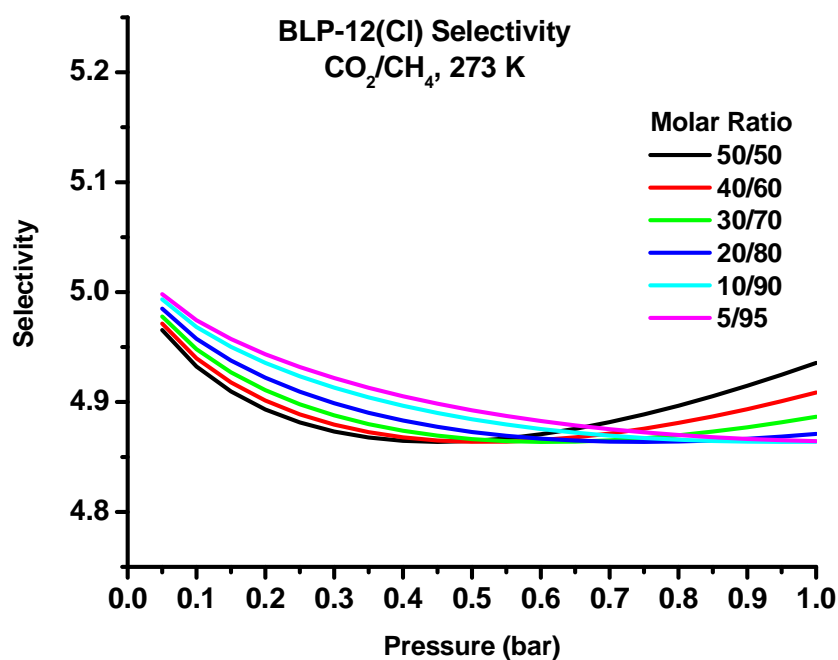
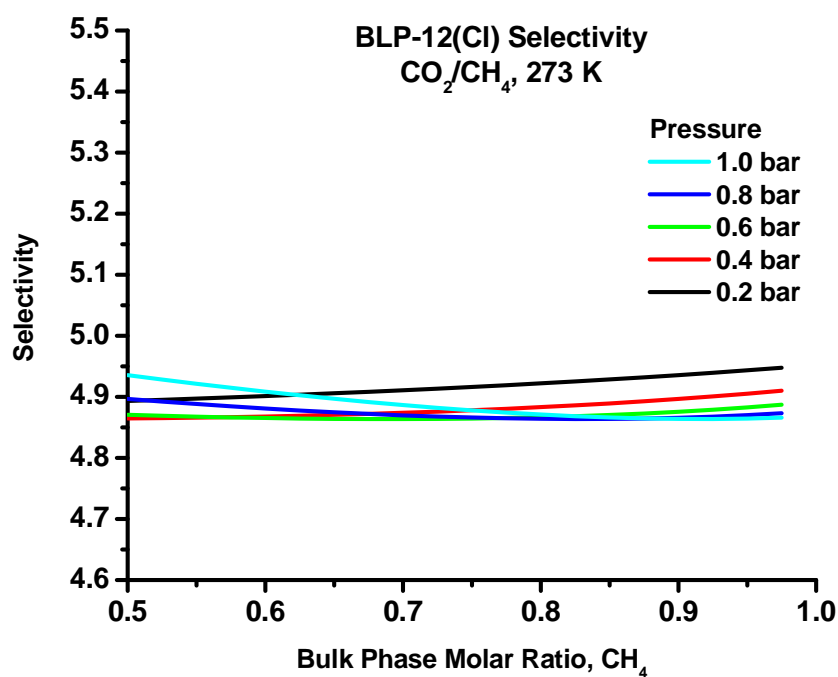


**Figure 154.** CO<sub>2</sub>/CH<sub>4</sub> Selectivity for BLP-12(Cl) at 273 K by Molar Ratio.



## Chapter 7

### Concluding Remarks

The research shown in this dissertation should exemplify why borazine-linked polymers (BLPs) are an exciting material for economical and environmental purposes. The goal of this dissertation is to gain a greater understanding of the factors that affect gas storage and separation applications through the development of polymers incorporating borazine, which has been uninvestigated for such applications. The important aspects of this dissertation are below.

First, seven unique BLPs have been synthesized by a simple one-pot synthesis. In each case, they were made through the introduction of an aryl amine (*p*-phenylenediamine, 1,3,5-tris-(4-aminophenyl)benzene, benzidine, or tetra-(4-aminophenyl)methane) with a boron trihalides (boron tribromide or boron trichloride) under reduced temperature and anhydrous conditions. Presumably, these compounds form a boron-nitrogen adduct; however, such a comment is speculative since the extremely moisture-sensitive boron-halide bond forbids investigation by standard spectroscopic methods. Regardless of whether or not an adduct is formed, the system, upon removal of DCM and replacement with toluene, was subjected to thermolysis. The precipitate was filtered and washed to produce the polymer in high yields. Successful formation of the borazine building block and the integrity of the aryl backbone were confirmed by FT-IR, solid state NMR, and elemental analysis.



Second, all BLPs were subjected to nitrogen sorption studies at 77 K. These studies showed that BLPs exhibited high surface area especially when compared to analogous crystalline systems despite the fact that all BLPs were amorphous. The pore size distributions for BLPs revealed single, reasonably sharp peaks suggesting that BLPs possess short-range order without long-range crystallinity. BLPs were also subjected to hydrogen sorption studies at 77 K and 87 K as well as carbon dioxide and methane studies each performed at 273 K and 298 K. The hydrogen uptakes at 1 bar were on par with most organic polymers illustrating that crystallinity is not a prerequisite for efficient hydrogen storage. The carbon dioxide uptakes were also decent while BLPs did not store appreciable levels of methane. Isosteric heats of adsorption were calculated for each gas based on the experimental sorption studies. The results showed that BLPs exhibit good levels of affinity between the small gas molecules and the surface of the polymers. Additionally, theoretical studies were performed by the Dr. Jena group at Virginia Commonwealth University utilizing three different methodologies, B3LYP, M06, and SVWN each with the 6-311+G\* basis sets. The results for M06 and SVWN agreed well with the experimental results while the results from B3LYP highlighted the importance of taking into account dispersive forces while dealing with weakly bound systems.

Third, BLPs were subjected to selectivity studies to determine their theoretical capabilities in gas separation applications. Both the initial slopes method and the ideal adsorbed solution theory (IAST) were used to calculate selectivity values. Selectivity calculated by the initial slopes method was in excellent agreement with the low pressure range based on the IAST helping to illustrate IAST's applicability despite any concerns

over the non-ideality of BLPs. Although the  $\text{CO}_2/\text{N}_2$  selectivities of BLPs do not approach values found for a number of other porous polymers, some BLPs exhibit exceptionally high  $\text{CO}_2/\text{CH}_4$  selectivity. Additionally, according to the IAST calculations, these values can be expected to rise with increasing pressure. As a result, BLPs could be good candidates for the purification of natural gas with typical levels of carbon dioxide impurities.

The research presented in this dissertation also conveys the potential for many directions of future investigation. One such avenue is the incorporation of different aryl amine building blocks. The facile synthetic approach to BLPs allows for a myriad of possibilities. Altering the structure and geometry as well as the degree of aromaticity within the amine could yield a number of different BLPs with potentially exciting gas storage or separation capabilities. Synthetic procedures would be expected to proceed in a similar fashion to the BLPs within this work by the introduction of the aryl amine to boron trihalide followed by thermolysis. Although current progress in this work might indicate a straightforward process, a few concerns exist. In order for successful introduction of the amine and boron source, complete solubility of the former must be achieved. Ordinarily, this obstacle is actually a simple endeavor; however, the solvent of choice must also be stable in the presence of the boron trihalide. This latter criterion has the potential to cause problems. As such, investigation into altering the solubility properties in boron trihalide-friendly solvents by substitution of the amine protons would need to be investigated. One possibility is the lithiation of the amine with subsequent addition of chlorotrimethylsilane as has been established previously in literature.<sup>328</sup> Repeating the lithiation/addition process would yield di-substituted amines; however,

substitution of both protons for each amine might introduce steric hindrance that prevents the formation of the amine-borane adduct. In addition to changing the amine, another possibility is to change the halide attached to the boron. This work discussed the inclusion of chlorine and bromine into BLPs. As an extrapolation, the inclusion of fluorine could be investigated. As a result of the impact that electronegativity has on the storage of polarizable gases, fluorine incorporation could result in BLPs of very interesting properties. However, difficulties in successfully synthesizing such polymers might arise from the difference in solvent stability for boron trifluoride as well as the strength the boron-fluorine bond. Additionally, the release of hydrofluoric acid in any successfully fluorinated-based BLP synthesis would need to be addressed over safety concerns.

The very reactive boron-halide bond in BLPs brings about the possibility for post-synthesis modification. Lithium-based or Grignard reagents would allow for many variations from just a single BLP. For instance, reacting a halogen-decorated BLP with methyl magnesium chloride, ethyl magnesium chloride, or phenyl magnesium chloride would yield three unique polymers. Depending on the nature of the functional group, the electronic and spatial characteristics of the polymer would be altered thus affecting its performance in gas storage and separation applications. Of course, choosing appropriate functional groups would need to be made with size considerations in mind so that the molecule can penetrate inside the polymer network. Otherwise, only post-synthesis modification of the outside surface of the polymer would occur.

Another natural extension of this work is the investigation of these BLPs in high pressure gas sorption experiments. Data achieved from these studies will not only be

able to be investigated for their optimum levels of gas uptake but also give a better assessment for gas separation applications. IAST, which is an excellent means of calculating theoretical selectivity, is restricted by the pressure ranges that the pure component sorption experiments use. As such, expanding the pressure range would also expand the applicable range of the IAST calculations. Additional investigations as an extension of the work presented in this material would be the determination of selectivity based on experimental observations of gas mixture systems. Since forming a BLP membrane could be difficult, a gas chromatograph could be used to make this assessment. Packing a column with the BLP of interest and passing a gas mixture through the instrument could give an experimental assessment of the selectivity capabilities. These experiments could also confirm (or deny) the applicability of IAST for a particular system such that more descriptive application-based claims can be made for gas mixture concentrations that are not as readily available.

Overall, the work presented in this dissertation has given new insight into gas storage and separation as well as extrapolating on current technological ideologies. Nevertheless, more research must be done on a number of fronts to help in the realization of alternative energy sources while limiting the environmental impact. Advancements in organic porous materials and particularly in borazine-linked polymers could be useful in these pursuits.

## References

1. United Nations, Department of Economic and Social Affairs, World Population to 2300,  
<http://www.un.org/esa/population/publications/longrange2/WorldPop2300final.pdf>  
(accessed September 21, 2011).
2. Gibson, R. C.; Greene, D. L.; Kahn, J. R., Fuel economy rebound effect for US household vehicles. *Energy Journal* **1999**, 20 (3), 1-31.
3. Greene, D. L., Fuel Choice for Multifuel Vehicles. *Contemporary Policy Issues* **1990**, 8 (4), 118-137.
4. Zuettel, A., Materials for hydrogen storage. *Mater. Today (Oxford, U. K.) FIELD Full Journal Title:Materials Today (Oxford, United Kingdom)* **2003**, 6 (9), 24-33.
5. Ritter, J. A.; Ebner, A. D.; Wang, J.; Zidan, R., Implementing a hydrogen economy. *Mater. Today (Oxford, U. K.) FIELD Full Journal Title:Materials Today (Oxford, United Kingdom)* **2003**, 6 (9), 18-23.
6. Ogden, J. M., Prospects for building a hydrogen energy infrastructure. *Annu Rev Energ Env* **1999**, 24, 227-279.

7. Schlapbach, L.; Züttel, A., Hydrogen-storage materials for mobile applications. *Nature* **2001**, 414 (6861), 353-358.
8. National Gas Supply Association, <http://www.naturalgas.org/overview/background.asp> (accessed September 21, 2011).
9. Lengeler, J. W.; Drews, G.; Schlegel, H. G., *Biology of the prokaryotes*. Thieme ; Distributed in the USA by Blackwell Science: Stuttgart ; New York Malden, MA, 1999; p xxvii, 955 p.
10. Oxtoby, D. W., *Principles of modern chemistry*. 7th Ed. ed.; Cengage Learning - Brooks/Cole: Belmont, CA, 2011.
11. Goyal, R. S.; Jain, S. C.; Shrivastav, D.; Kanchan, V. K., Impact of carbon on climate. *Journal of Applied Geochemistry* **2010**, 12 (4), 535-544.
12. Pimentel, C., Carbon metabolism of crops and the increase of atmospheric CO<sub>2</sub> and O<sub>3</sub> situation and previsions. *Bragantia* **2011**, 70 (1), 1-12.
13. Jacobson, M. Z., Short-term effects of controlling fossil-fuel soot, biofuel soot and gases, and methane on climate, Arctic ice, and air pollution health. *Journal of Geophysical Research, [Atmospheres]* **2010**, 115 (D14), D14209/1-D14209/24.
14. Shaffer, G.; Olsen, S. M.; Pedersen, J. O. P., Long-term ocean oxygen depletion in response to carbon dioxide emissions from fossil fuels. *Nature Geoscience* **2009**, 2 (2), 105-109, S105/1-S105/2.
15. D'Alessandro, D. M.; Smit, B.; Long, J. R., Carbon Dioxide Capture: Prospects for New Materials. *Angew Chem Int Edit* **2010**, 49 (35), 6058-6082.

16. Ma, S. Q.; Zhou, H. C., Gas storage in porous metal-organic frameworks for clean energy applications. *Chem Commun* **2010**, 46 (1), 44-53.
17. Keskin, S.; van Heest, T. M.; Sholl, D. S., Can Metal-Organic Framework Materials Play a Useful Role in Large-Scale Carbon Dioxide Separations? *Chemsuschem* **2010**, 3 (8), 879-891.
18. Kuroki, S.; Chokai, M.; Wu, L.; Nabaie, Y.; Kakimoto, M.-a.; Miyata, S., High-performance carbon alloy cathode catalysts for fuel cells prepared from polymer precursor. *Kobunshi Ronbunshu* **2011**, 68 (7), 417-426.
19. Yoshizaki, A.; Hirata, K.; Ishida, M., Development of hydrogen energy creation type fuel cell system and ubiquitous hydrogen energy supply system. *Nenryo Denchi* **2011**, 10 (4), 101-106.
20. Yang, Y.; Sun, G.; Xu, M., Microbial fuel cells come of age. *Journal of Chemical Technology and Biotechnology* **2011**, 86 (5), 625-632.
21. Tjong, S. C., Polymer nanocomposite bipolar plates reinforced with carbon nanotubes and graphite nanosheets. *Energy & Environmental Science* **2011**, 4 (3), 605-626.
22. Wolfschmidt, H.; Paschos, O.; Stimming, U., Hydrogen reactions on nanostructured surfaces. *Fuel Cell Science* **2010**, 1-70.
23. Alvarez, G.; Alcaide, F.; Miguel, O.; Cabot, P. L.; Martinez-Huerta, M. V.; Fierro, J. L. G., Electrochemical stability of carbon nanofibers in proton exchange membrane fuel cells. *Electrochimica Acta* **2011**, 56 (25), 9370-9377.
24. Gharibi, H.; Javaheri, M.; Kheirmand, M.; Mirzaie, R. A., Optimization of the amount of Nafion in multi-walled carbon nanotube/Nafion composites as Pt

- supports in gas diffusion electrodes for proton exchange membrane fuel cells. *Int. J. Hydrogen Energy* **2011**, 36 (20), 13325-13334.
25. Kheirmand, M.; Asnafi, A., Analytic parameter identification of proton exchange membrane fuel cell catalyst layer using electrochemical impedance spectroscopy. *Int. J. Hydrogen Energy* **2011**, 36 (20), 13266-13271.
26. Kim, S.; Meyers, J. P., The influence of hydrogen- and cation-underpotential deposition on oxide-mediated Pt dissolution in proton-exchange membrane fuel cells. *Electrochimica Acta* **2011**, 56 (24), 8387-8393.
27. Sun, Z.; Sun, H.; Tang, Y.; Zuo, J.; Wu, Y., Proton transfer in proton exchange membrane based on RDF. *Advanced Materials Research (Durnten-Zurich, Switzerland)* **2011**, 295-297 (Pt. 2, Manufacturing Science and Technology), 1742-1746.
28. Chen, Y.; Lee, C. H.; Lane, O.; McGrath, J. E., Synthesis and characterization of multiblock hydrophobic partially fluorinated (polyarylene ether ketone)-hydrophilic (disulfonated polyarylene ether sulfone) copolymers for proton exchange membranes. *Preprints of Symposia - American Chemical Society, Division of Fuel Chemistry* **2010**, 55 (2), 344-345.
29. Frutsaert, G.; David, G.; Ameduri, B.; Jones, D. J.; Roziere, J.; Glipa, X., Synthesis and characterization of novel fluorinated polymers bearing pendant imidazole groups and blend membranes: New materials for PEMFC operating at low relative humidity. *J. Membr. Sci.* **2011**, 367 (1-2), 127-133.
30. VanHouten, R. A.; Lane, O.; McGrath, J. E., Synthesis of segmented hydrophobic hydrophilic fluorinated disulfonated block copolymers for use as



- proton exchange membranes. *Preprints of Symposia - American Chemical Society, Division of Fuel Chemistry* **2008**, 53 (2), 765-766.
31. Kim, D. S.; Kim, Y. S.; Guiver, M. D.; Ding, J.; Pivovar, B. S., Highly fluorinated comb-shaped copolymer as proton exchange membranes (PEMs): Fuel cell performance. *J. Power Sources* **2008**, 182 (1), 100-105.
  32. Khalfan, A. N.; Sanchez, L. M.; Kodiweera, C.; Greenbaum, S. G.; Bai, Z.; Dang, T. D., Water and proton transport properties of hexafluorinated sulfonated poly(arylenethioethersulfone) copolymers for applications to proton exchange membrane fuel cells. *J. Power Sources* **2007**, 173 (2), 853-859.
  33. Woo, M. H.; Kwon, O.; Choi, S. H.; Hong, M. Z.; Ha, H.-W.; Kim, K., Zirconium phosphate sulfonated poly(fluorinated arylene ether)s composite membranes for PEMFCs at 100-140°C. *Electrochimica Acta* **2006**, 51 (27), 6051-6059.
  34. Maruyama, J.; Inaba, M.; Ogumi, Z., Effect of fluorinated alcohol on the kinetics of cathodic oxygen reduction at gold electrodes. *Electrochimica Acta* **1999**, 45 (3), 415-422.
  35. U. S. Department of Energy, Energy Efficiency and Renewable Energy, [http://www1.eere.energy.gov/hydrogenandfuelcells/storage/current\\_technology.html](http://www1.eere.energy.gov/hydrogenandfuelcells/storage/current_technology.html) (accessed September 19, 2011).
  36. U. S. Department of Energy, Office of Science, <http://science.energy.gov/bes/> (accessed September 19, 2011).
  37. Manners, I.; Staubitz, A.; Robertson, A. P. M.; Sloan, M. E., Amine- and Phosphine-Borane Adducts: New Interest in Old Molecules. *Chem Rev* **2010**, 110 (7), 4023-4078.

38. Staubitz, A.; Robertson, A. P. M.; Manners, I., Ammonia-Borane and Related Compounds as Dihydrogen Sources. *Chem Rev* **2010**, *110* (7), 4079-4124.
39. Staubitz, A.; Sloan, M. E.; Robertson, A. P. M.; Friedrich, A.; Schneider, S.; Gates, P. J.; Gunne, J. S. A. D.; Manners, I., Catalytic Dehydrocoupling/Dehydrogenation of N-Methylamine-Borane and Ammonia-Borane: Synthesis and Characterization of High Molecular Weight Polyaminoboranes. *J Am Chem Soc* **2010**, *132* (38), 13332-13345.
40. Stephens, F. H.; Pons, V.; Baker, R. T., Ammonia borane: the hydrogen source par excellence? *Dalton Transactions* **2007**, (25), 2613-2626.
41. Fulton, J. L.; Linehan, J. C.; Autrey, T.; Balasubramanian, M.; Chen, Y.; Szymczak, N. K., When is a nanoparticle a cluster? An operando EXAFS study of amine borane dehydrocoupling by Rh<sub>4-6</sub> clusters. *J Am Chem Soc* **2007**, *129* (39), 11936-11949.
42. Nguyen, M. T.; Nguyen, V. S.; Matus, M. H.; Grant, D. J.; Dixon, D. A., Computational study of the release of H<sub>2</sub> from ammonia borane dimer (BH<sub>3</sub>NH<sub>3</sub>)(<sub>2</sub>) and its ion pair isomers. *J Phys Chem A* **2007**, *111* (36), 8844-8856.
43. Ramachandran, P. V.; Gagare, P. D., Preparation of ammonia borane in high yield and purity, methanolysis, and regeneration. *Inorg Chem* **2007**, *46* (19), 7810-7817.
44. Manners, I.; Clark, T. J.; Jaska, C. A.; Turak, A.; Lough, A. J.; Lu, Z. H., Transition metal-catalyzed dissociation of phosphine-gallane adducts: Isolation of

- mechanistic model complexes and heterogeneous catalyst poisoning studies. *Inorg Chem* **2007**, *46* (18), 7394-7402.
45. Manners, I.; Clark, T. J.; Whittell, G. R., Highly efficient colloidal cobalt- and rhodium-catalyzed hydrolysis of H<sub>3</sub>N center dot BH<sub>3</sub> in air. *Inorg Chem* **2007**, *46* (18), 7522-7527.
46. Chirik, P. J.; Pun, D.; Lobkovsky, E., Amineborane dehydrogenation promoted by isolable zirconium sandwich, titanium sandwich and N-2 complexes. *Chem Commun* **2007**, (31), 3297-3299.
47. Mohajeri, N.; T-Raissi, A.; Adebisi, O., Hydrolytic cleavage of ammonia-borane complex for hydrogen production. *J Power Sources* **2007**, *167* (2), 482-485.
48. McGrady, G. S.; Langmi, H. W., Non-hydride systems of the main group elements as hydrogen storage materials. *Coordin Chem Rev* **2007**, *251* (7-8), 925-935.
49. Baker, R. T.; Keaton, R. J.; Blacquiere, J. M., Base metal catalyzed dehydrogenation of ammonia-borane for chemical hydrogen storage. *J Am Chem Soc* **2007**, *129* (7), 1844-+.
50. Baker, R. T.; Stephens, F. H.; Matus, M. H.; Grant, D. J.; Dixon, D. A., Acid initiation of ammonia-borane dehydrogenation for hydrogen storage. *Angew Chem Int Edit* **2007**, *46* (5), 746-749.
51. Ito, H.; Nozaki, T.; Saikubo, A.; Yamada, N.; Kanda, K.; Niibe, M.; Saitoh, H., Hydrogen-storage characteristics of hydrogenated amorphous carbon nitrides. *Thin Solid Films* **2008**, *516* (19), 6575-6579.

52. Orimo, S.-i.; Nakamori, Y.; Eliseo, J. R.; Züttel, A.; Jensen, C. M., Complex Hydrides for Hydrogen Storage. *Chemical Reviews (Washington, DC, United States)* **2007**, *107* (10), 4111-4132.
53. Zhao, D.; Yuan, D.; Zhou, H.-C., The current status of hydrogen storage in metal-organic frameworks. *Energy & Environmental Science* **2008**, *1* (2), 222-235.
54. Long, J. R.; Dinca, M., Hydrogen storage in microporous metal-organic frameworks with exposed metal sites. *Angew Chem Int Edit* **2008**, *47* (36), 6766-6779.
55. Zhou, H. C.; Collins, D. J., Hydrogen storage in metal-organic frameworks. *J Mater Chem* **2007**, *17* (30), 3154-3160.
56. Hubberstey, P.; Lin, X.; Jia, J. H.; Schroder, M.; Champness, N. R., Hydrogen storage in metal-organic frameworks. *Crystengcomm* **2007**, *9* (6), 438-448.
57. Yaghi, O. M.; Rowsell, J. L. C., Strategies for hydrogen storage in metal-organic frameworks. *Angew Chem Int Edit* **2005**, *44* (30), 4670-4679.
58. Antonelli, D. M.; Seayad, A. M., Recent advances in hydrogen storage in metal-containing inorganic nanostructures and related materials. *Adv Mater* **2004**, *16* (9-10), 765-777.
59. Sculley, J.; Yuan, D. Q.; Zhou, H. C., The current status of hydrogen storage in metal-organic frameworks-updated. *Energy & Environmental Science* **2011**, *4* (8), 2721-2735.
60. Deng, H. X.; Doonan, C. J.; Furukawa, H.; Ferreira, R. B.; Towne, J.; Knobler, C. B.; Wang, B.; Yaghi, O. M., Multiple Functional Groups of Varying Ratios in Metal-Organic Frameworks. *Science* **2010**, *327* (5967), 846-850.

61. Mokaya, R.; Xia, Y., Ordered mesoporous carbon monoliths: CVD nanocasting and hydrogen storage properties. *J Phys Chem C* **2007**, *111* (27), 10035-10039.
62. Mokaya, R.; Yang, Z. X.; Xia, Y. D., Enhanced hydrogen storage capacity of high surface area zeolite-like carbon materials. *J Am Chem Soc* **2007**, *129* (6), 1673-1679.
63. McKeown, N. B.; Budd, P. M.; Book, D., Microporous polymers as potential hydrogen storage materials. *Macromol Rapid Comm* **2007**, *28* (9), 995-1002.
64. Budd, P. M.; Butler, A.; Selbie, J.; Mahmood, K.; McKeown, N. B.; Ghanem, B.; Msayib, K.; Book, D.; Walton, A., The potential of organic polymer-based hydrogen storage materials. *Phys Chem Chem Phys* **2007**, *9* (15), 1802-1808.
65. McKeown, N. B.; Ghanem, B. S.; Msayib, K. J.; Harris, K. D. M.; Pan, Z.; Budd, P. M.; Butler, A.; Selbie, J.; Book, D.; Walton, A., A triptycene-based polymer of intrinsic microporosity that displays enhanced surface area and hydrogen adsorption. *Chem Commun* **2007**, (1), 67-69.
66. McKeown, N. B.; Budd, P. M., Polymers of intrinsic microporosity (PIMs): organic materials for membrane separations, heterogeneous catalysis and hydrogen storage. *Chem Soc Rev* **2006**, *35* (8), 675-683.
67. Budd, P. M.; Maffei, A. V.; McKeown, N. B., Adsorption studies of a microporous phthalocyanine network polymer. *Langmuir* **2006**, *22* (9), 4225-4229.
68. McKeown, N. B.; Gahnem, B.; Msayib, K. J.; Budd, P. M.; Tattershall, C. E.; Mahmood, K.; Tan, S.; Book, D.; Langmi, H. W.; Walton, A., Towards polymer-based hydrogen storage materials: Engineering ultramicroporous cavities within

- polymers of intrinsic microporosity. *Angew Chem Int Edit* **2006**, 45 (11), 1804-1807.
69. Budd, P. M.; McKeown, N. B.; Fritsch, D., Free volume and intrinsic microporosity in polymers. *J Mater Chem* **2005**, 15 (20), 1977-1986.
70. McKeown, N. B.; Budd, P. M., Exploitation of Intrinsic Microporosity in Polymer-Based Materials. *Macromolecules* **2010**, 43 (12), 5163-5176.
71. Lavigne, J. J.; Tilford, R. W.; Gemmill, W. R.; zur Loye, H. C., Facile synthesis of a highly crystalline, covalently linked porous boronate network. *Chem Mater* **2006**, 18 (22), 5296-5301.
72. Jiang, D. L.; Wan, S.; Guo, J.; Kim, J.; Ihee, H., A Belt-Shaped, Blue Luminescent, and Semiconducting Covalent Organic Framework. *Angew Chem Int Edit* **2008**, 47 (46), 8826-8830.
73. Jiang, D. L.; Wan, S.; Guo, J.; Kim, J.; Ihee, H., A Photoconductive Covalent Organic Framework: Self-Condensed Arene Cubes Composed of Eclipsed 2D Polypyrene Sheets for Photocurrent Generation. *Angew Chem Int Edit* **2009**, 48 (30), 5439-5442.
74. Dichtel, W. R.; Spitler, E. L., Lewis acid-catalysed formation of two-dimensional phthalocyanine covalent organic frameworks. *Nat Chem* **2010**, 2 (8), 672-677.
75. Thomas, A.; Weber, J.; Antonietti, M., Microporous networks of high-performance polymers: Elastic deformations and gas sorption properties. *Macromolecules* **2008**, 41 (8), 2880-2885.
76. Sabir, A. K.; Lu, W. C.; Roland, C.; Bernholc, J., Ab initio simulations of H-2 in Li-doped carbon nanotube systems. *J Phys-Condens Mat* **2007**, 19 (8).

77. Myers, A. L.; Bhatia, S. K., Optimum conditions for adsorptive storage. *Langmuir* **2006**, 22 (4), 1688-1700.
78. Zhu, Z. H.; Lu, G. Q.; Wang, F. Y., Why H atom prefers the on-top site and alkali metals favor the middle hollow site on the basal plane of graphite. *J Phys Chem B* **2005**, 109 (16), 7923-7927.
79. Nahm, K. S.; Zacharia, R.; Kim, K. Y.; Kibria, A. K. M. F., Enhancement of hydrogen storage capacity of carbon nanotubes via spill-over from vanadium and palladium nanoparticles. *Chem Phys Lett* **2005**, 412 (4-6), 369-375.
80. Froudakis, G. E., Why alkali-metal-doped carbon nanotubes possess high hydrogen uptake. *Nano Lett* **2001**, 1 (10), 531-533.
81. Lu, G. Q.; Ding, R. G.; Yan, Z. F.; Wilson, M. A., Recent advances in the preparation and utilization of carbon nanotubes for hydrogen storage. *J Nanosci Nanotechnol* **2001**, 1 (1), 7-29.
82. Lin, J.; Chen, P.; Wu, X.; Tan, K. L., High H<sub>2</sub> uptake by alkali-doped carbon nanotubes under ambient pressure and moderate temperatures. *Science* **1999**, 285 (5424), 91-93.
83. Liang, J. J.; Kung, W. C. P., Confinement of Mg-MgH<sub>2</sub> systems into carbon nanotubes changes hydrogen sorption energetics. *J Phys Chem B* **2005**, 109 (38), 17837-17841.
84. Turker, L., Hydrogen storage capacity of Be@C-115 system. *J Mol Struct-Theochem* **2005**, 723 (1-3), 105-110.
85. Turker, L.; Eroglu, I.; Yucel, M.; Gunduz, U., Hydrogen storage capability of carbon nanotube Be@C-120. *Int J Hydrogen Energ* **2004**, 29 (15), 1643-1647.

86. Rashidi, A. M.; Nouralishahi, A.; Khodadadi, A. A.; Mortazavi, Y.; Karimi, A.; Kashefi, K., Modification of single wall carbon nanotubes (SWNT) for hydrogen storage. *Int J Hydrogen Energ* **2010**, 35 (17), 9489-9495.
87. Sun, Q.; Jena, P.; Wang, Q.; Marquez, M., First-principles study of hydrogen storage on Li(12)C(60). *J Am Chem Soc* **2006**, 128 (30), 9741-9745.
88. Jena, P.; Sun, Q.; Wang, Q.; Kawazoe, Y., Clustering of Ti on a C(60) surface and its effect on hydrogen storage. *J Am Chem Soc* **2005**, 127 (42), 14582-14583.
89. Hupp, J. T.; Mulfort, K. L., Alkali metal cation effects on hydrogen uptake and binding in metal-organic frameworks. *Inorg Chem* **2008**, 47 (18), 7936-7938.
90. Long, J. R.; Dinca, M., High-enthalpy hydrogen adsorption in cation-exchanged variants of the microporous metal-organic framework Mn-3[(Mn4Cl)(3)(BTT)(8)(CH3OH)(10)](2). *J Am Chem Soc* **2007**, 129 (36), 11172-11176.
91. Hupp, J. T.; Mulfort, K. L., Chemical reduction of metal-organic framework materials as a method to enhance gas uptake and binding. *J Am Chem Soc* **2007**, 129 (31), 9604-+.
92. Goddard, W. A.; Han, S. S., Lithium-doped metal-organic frameworks for reversible H-2 storage at ambient temperature. *J Am Chem Soc* **2007**, 129 (27), 8422-+.
93. Fischer, R. A.; Muller, M.; Hermes, S.; Kaehler, K.; van den Berg, M. W. E.; Muhler, M., Loading of MOF-5 with Cu and ZnO nanoparticles by gas-phase



- infiltration with organometallic precursors: properties of Cu/ZnO@MOF-5 as catalyst for methanol synthesis. *Chem Mater* **2008**, 20 (14), 4576-4587.
94. Fischer, R. A.; Schroeder, F.; Esken, D.; Cokoja, M.; van den Berg, M. W. E.; Lebedev, O. I.; van Tendeloo, G.; Walaszek, B.; Buntkowsky, G.; Limbach, H. H.; Chaudret, B., Ruthenium nanoparticles inside porous [Zn<sub>4</sub>O(bdC)(3)] by hydrogenolysis of adsorbed [Ru(cod)(cot)]: A solid-state reference system for surfactant-stabilized ruthenium colloids. *J Am Chem Soc* **2008**, 130 (19), 6119-6130.
  95. Kaskel, S.; Sabo, M.; Henschel, A.; Froede, H.; Klemm, E., Solution infiltration of palladium into MOF-5: synthesis, physisorption and catalytic properties. *J Mater Chem* **2007**, 17 (36), 3827-3832.
  96. Fischer, R. A.; Hermes, S.; Zacher, D.; Baunemann, A.; Woll, C., Selective growth and MOCVD loading of small single crystals of MOF-5 at alumina and silica surfaces modified with organic self-assembled monolayers. *Chem Mater* **2007**, 19 (9), 2168-2173.
  97. Fischer, R. A.; Hermes, S.; Schroter, M. K.; Schmid, R.; Khodeir, L.; Muhler, M.; Tissler, A.; Fischer, R. W., Metal@MOF: Loading of highly porous coordination polymers host lattices by metal organic chemical vapor deposition. *Angew Chem Int Edit* **2005**, 44 (38), 6237-6241.
  98. Fischer, R. A.; Hermes, S.; Schroder, F.; Amirjalayer, S.; Schmid, R., Loading of porous metal-organic open frameworks with organometallic CVD precursors: inclusion compounds of the type [LnM](a)@MOF-5. *J Mater Chem* **2006**, 16 (25), 2464-2472.

99. Fischer, R. A.; Hermes, S.; Schroder, F.; Chelmowski, R.; Woll, C., Selective nucleation and growth of metal-organic open framework thin films on patterned COOH/CF<sub>3</sub>-terminated self-assembled monolayers on Au(111). *J Am Chem Soc* **2005**, *127* (40), 13744-13745.
100. Mirkin, C. A.; Farha, O. K.; Spokoyny, A. M.; Mulfort, K. L.; Hawthorne, M. F.; Hupp, J. T., Synthesis and hydrogen sorption properties of carborane based metal-organic framework materials. *J Am Chem Soc* **2007**, *129* (42), 12680-+.
101. Kang, J. K.; Choi, Y. J.; Lee, J. W.; Choi, J. H., Ideal metal-decorated three dimensional covalent organic frameworks for reversible hydrogen storage. *Appl Phys Lett* **2008**, *92* (17).
102. Froudakis, G. E.; Klontzas, E.; Tylanakis, E., Hydrogen storage in 3D covalent organic frameworks. A multiscale theoretical investigation. *J Phys Chem C* **2008**, *112* (24), 9095-9098.
103. Garberoglio, G., Computer simulation of the adsorption of light gases in covalent organic frameworks. *Langmuir* **2007**, *23* (24), 12154-12158.
104. Zhong, C. L.; Yang, Q. Y., Molecular Simulation Study of the Stepped Behaviors of Gas Adsorption in Two-Dimensional Covalent Organic Frameworks. *Langmuir* **2009**, *25* (4), 2302-2308.
105. Yaghi, O. M.; Han, S. S.; Furukawa, H.; Goddard, W. A., Covalent organic frameworks as exceptional hydrogen storage materials. *J Am Chem Soc* **2008**, *130* (35), 11580-+.
106. Yang, R. T.; Li, Y. W., Hydrogen storage in metal-organic and covalent-organic frameworks by spillover. *Aiche J* **2008**, *54* (1), 269-279.

107. Lavigne, J. J.; Tilford, R. W.; Mugavero, S. J.; Pellechia, P. J., Tailoring microporosity in covalent organic frameworks. *Adv Mater* **2008**, 20 (14), 2741-+.
108. Cooper, A. I.; Jiang, J. X.; Su, F.; Trewin, A.; Wood, C. D.; Niu, H.; Jones, J. T. A.; Khimyak, Y. Z., Synthetic control of the pore dimension and surface area in conjugated microporous polymer and copolymer networks. *J Am Chem Soc* **2008**, 130 (24), 7710-7720.
109. Cooper, A. I.; Jiang, J. X.; Su, F.; Trewin, A.; Wood, C. D.; Campbell, N. L.; Niu, H.; Dickinson, C.; Ganin, A. Y.; Rosseinsky, M. J.; Khimyak, Y. Z., Conjugated microporous poly (aryleneethynylene) networks. *Angew Chem Int Edit* **2007**, 46 (45), 8574-8578.
110. Tylianakis, E.; Klontzas, E.; Froudakis, G. E., The effect of structural and energetic parameters of MOFs and COFs towards the improvement of their hydrogen storage properties. *Nanotechnology* **2009**, 20 (20).
111. Han, S. S.; Mendoza-Cortes, J. L.; Goddard, W. A., Recent advances on simulation and theory of hydrogen storage in metal-organic frameworks and covalent organic frameworks. *Chem Soc Rev* **2009**, 38 (5), 1460-1476.
112. Babarao, R.; Jiang, J. W., Exceptionally high CO(2) storage in covalent-organic frameworks: Atomistic simulation study. *Energy & Environmental Science* **2008**, 1 (1), 139-143.
113. Choi, Y. J.; Choi, J. H.; Choi, K. M.; Kang, J. K., Covalent organic frameworks for extremely high reversible CO(2) uptake capacity: a theoretical approach. *J Mater Chem* **2011**, 21 (4), 1073-1078.

114. Tylianakis, E.; Klontzas, E.; Froudakis, G. E., Multi-scale theoretical investigation of hydrogen storage in covalent organic frameworks. *Nanoscale* **2011**, 3 (3), 856-869.
115. Suri, M.; Dornfeld, M.; Ganz, E., Calculation of hydrogen storage capacity of metal-organic and covalent-organic frameworks by spillover. *J Chem Phys* **2009**, 131 (17).
116. Assfour, B.; Seifert, G., Adsorption of hydrogen in covalent organic frameworks: Comparison of simulations and experiments. *Micropor Mesopor Mat* **2010**, 133 (1-3), 59-65.
117. Assfour, B.; Seifert, G., Hydrogen adsorption sites and energies in 2D and 3D covalent organic frameworks. *Chem Phys Lett* **2010**, 489 (1-3), 86-91.
118. Mendoza-Cortes, J. L.; Han, S. S.; Furukawa, H.; Yaghi, O. M.; Goddard, W. A., Adsorption Mechanism and Uptake of Methane in Covalent Organic Frameworks: Theory and Experiment. *J Phys Chem A* **2010**, 114 (40), 10824-10833.
119. Klontzas, E.; Tylianakis, E.; Froudakis, G. E., Designing 3D COFs with Enhanced Hydrogen Storage Capacity. *Nano Lett* **2010**, 10 (2), 452-454.
120. Cote, A. P.; El-Kaderi, H. M.; Furukawa, H.; Hunt, J. R.; Yaghi, O. M., Reticular synthesis of microporous and mesoporous 2D covalent organic frameworks. *J Am Chem Soc* **2007**, 129 (43), 12914-+.
121. Yaghi, O. M.; El-Kaderi, H. M.; Hunt, J. R.; Mendoza-Cortes, J. L.; Cote, A. P.; Taylor, R. E.; O'Keeffe, M., Designed synthesis of 3D covalent organic frameworks. *Science* **2007**, 316 (5822), 268-272.

122. Cote, A. P.; Benin, A. I.; Ockwig, N. W.; O'Keeffe, M.; Matzger, A. J.; Yaghi, O. M., Porous, crystalline, covalent organic frameworks. *Science* **2005**, *310* (5751), 1166-1170.
123. Mastalerz, M., The next generation of shape-persistent zeolite analogues: Covalent organic frameworks. *Angew Chem Int Edit* **2008**, *47* (3), 445-447.
124. Kuhn, P.; Antonietti, M.; Thomas, A., Porous, covalent triazine-based frameworks prepared by ionothermal synthesis. *Angew Chem Int Edit* **2008**, *47* (18), 3450-3453.
125. O'Keeffe, M.; Uribe-Romo, F. J.; Hunt, J. R.; Furukawa, H.; Klock, C.; Yaghi, O. M., A Crystalline Imine-Linked 3-D Porous Covalent Organic Framework. *J Am Chem Soc* **2009**, *131* (13), 4570-+.
126. Yaghi, O. M.; Hunt, J. R.; Doonan, C. J.; LeVangie, J. D.; Cote, A. P., Reticular synthesis of covalent organic borosilicate frameworks. *J Am Chem Soc* **2008**, *130* (36), 11872-11873.
127. Yaghi, O. M.; O'Keeffe, M.; Ockwig, N. W.; Chae, H. K.; Eddaoudi, M.; Kim, J., Reticular synthesis and the design of new materials. *Nature* **2003**, *423* (6941), 705-714.
128. O'Keeffe, M.; Delgado-Friedrichs, O.; Yaghi, O. M., Taxonomy of periodic nets and the design of materials. *Phys Chem Chem Phys* **2007**, *9* (9), 1035-1043.
129. O'Keeffe, M.; Delgado-Friedrichs, O.; Yaghi, O. M., Three-periodic nets and tilings: edge-transitive binodal structures. *Acta Crystallogr A* **2006**, *62*, 350-355.

130. O'Keeffe, M.; Delgado-Friedrichs, O.; Foster, M. D.; Proserpio, D. M.; Treacy, M. M. J.; Yaghi, O. M., What do we know about three-periodic nets? *J Solid State Chem* **2005**, *178* (8), 2533-2554.
131. Kuhn, P.; Forget, A.; Su, D. S.; Thomas, A.; Antonietti, M., From Microporous Regular Frameworks to Mesoporous Materials with Ultrahigh surface Area: Dynamic Reorganization of Porous Polymer Networks. *J Am Chem Soc* **2008**, *130* (40), 13333-13337.
132. Furukawa, H.; Yaghi, O. M., Storage of Hydrogen, Methane, and Carbon Dioxide in Highly Porous Covalent Organic Frameworks for Clean Energy Applications. *J Am Chem Soc* **2009**, *131* (25), 8875-8883.
133. Lan, J. H.; Cao, D. P.; Wang, W. C.; Smit, B., Doping of Alkali, Alkaline-Earth, and Transition Metals in Covalent-Organic Frameworks for Enhancing CO<sub>2</sub> Capture by First-Principles Calculations and Molecular Simulations. *Acs Nano* **2010**, *4* (7), 4225-4237.
134. Cao, D. P.; Lan, J. H.; Wang, W. C.; Smit, B., Lithium-Doped 3D Covalent Organic Frameworks: High-Capacity Hydrogen Storage Materials. *Angew Chem Int Edit* **2009**, *48* (26), 4730-4733.
135. Li, F.; Zhao, J. J.; Johansson, B.; Sun, L. X., Improving hydrogen storage properties of covalent organic frameworks by substitutional doping. *Int J Hydrogen Energ* **2010**, *35* (1), 266-271.
136. Sun, Y. Y.; Lee, K.; Kim, Y. H.; Zhang, S. B., Ab initio design of Ca-decorated organic frameworks for high capacity molecular hydrogen storage with enhanced binding. *Appl Phys Lett* **2009**, *95* (3).

137. Wu, M. M.; Wang, Q.; Sun, Q.; Jena, P.; Kawazoe, Y., First-principles study of hydrogen adsorption in metal-doped COF-10. *J Chem Phys* **2010**, *133* (15).
138. Klontzas, E.; Tylanakis, E.; Froudakis, G. E., Hydrogen Storage in Lithium-Functionalized 3-D Covalent-Organic Framework Materials. *J Phys Chem C* **2009**, *113* (50), 21253-21257.
139. Lan, J. H.; Cao, D. P.; Wang, W. C., Li-Doped and Nondoped Covalent Organic Borosilicate Framework for Hydrogen Storage. *J Phys Chem C* **2010**, *114* (7), 3108-3114.
140. Lan, J. H.; Cao, D. P.; Wang, W. C., High Uptakes of Methane in Li-Doped 3D Covalent Organic Frameworks. *Langmuir* **2010**, *26* (1), 220-226.
141. Furukawa, H.; Miller, M. A.; Yaghi, O. M., Independent verification of the saturation hydrogen uptake in MOF-177 and establishment of a benchmark for hydrogen adsorption in metal-organic frameworks. *J Mater Chem* **2007**, *17* (30), 3197-3204.
142. Matzger, A. J.; Wong-Foy, A. G.; Yaghi, O. M., Exceptional H<sub>2</sub> saturation uptake in microporous metal-organic frameworks. *J Am Chem Soc* **2006**, *128* (11), 3494-3495.
143. Texier-Mandoki, N.; Dentzer, J.; Piquero, T.; Saadallah, S.; David, P.; Vix-Guterl, C., Hydrogen storage in activated carbon materials: Role of the nanoporous texture. *Carbon* **2004**, *42* (12-13), 2744-2747.
144. Guiver, M. D.; Du, N. Y.; Robertson, G. P.; Pinnau, I., Polymers of Intrinsic Microporosity with Dinaphthyl and Thianthrene Segments. *Macromolecules* **2010**, *43* (20), 8580-8587.

145. Cooper, A. I.; Dawson, R.; Laybourn, A.; Khimyak, Y. Z.; Adams, D. J., High Surface Area Conjugated Microporous Polymers: The Importance of Reaction Solvent Choice. *Macromolecules* **2010**, *43* (20), 8524-8530.
146. Kanatzidis, M. G.; Pandey, P.; Katsoulidis, A. P.; Eryazici, I.; Wu, Y. Y.; Nguyen, S. T., Imine-Linked Microporous Polymer Organic Frameworks. *Chem Mater* **2010**, *22* (17), 4974-4979.
147. Kanatzidis, M. G.; Katsoulidis, A. P., Phloroglucinol Based Microporous Polymeric Organic Frameworks with -OH Functional Groups and High CO<sub>2</sub> Capture Capacity. *Chem Mater* **2011**, *23* (7), 1818-1824.
148. Yaghi, O. M.; Phan, A.; Doonan, C. J.; Uribe-Romo, F. J.; Knobler, C. B.; O'Keeffe, M., Synthesis, Structure, and Carbon Dioxide Capture Properties of Zeolitic Imidazolate Frameworks. *Accounts Chem Res* **2010**, *43* (1), 58-67.
149. Yaghi, O. M.; Wang, B.; Cote, A. P.; Furukawa, H.; O'Keeffe, M., Colossal cages in zeolitic imidazolate frameworks as selective carbon dioxide reservoirs. *Nature* **2008**, *453* (7192), 207-U6.
150. Banerjee, R.; Panda, T.; Pachfule, P.; Chen, Y. F.; Jiang, J. W., Amino functionalized zeolitic tetrazolate framework (ZTF) with high capacity for storage of carbon dioxide. *Chem Commun* **2011**, *47* (7), 2011-2013.
151. Rosi, N. L.; An, J.; Geib, S. J., High and Selective CO<sub>2</sub> Uptake in a Cobalt Adeninate Metal-Organic Framework Exhibiting Pyrimidine- and Amino-Decorated Pores. *J Am Chem Soc* **2010**, *132* (1), 38-+.



152. Long, J. R.; Demessence, A.; D'Alessandro, D. M.; Foo, M. L., Strong CO(2) Binding in a Water-Stable, Triazolate-Bridged Metal-Organic Framework Functionalized with Ethylenediamine. *J Am Chem Soc* **2009**, *131* (25), 8784-+.
153. Blom, R.; Arstad, B.; Fjellvag, H.; Kongshaug, K. O.; Swang, O., Amine functionalised metal organic frameworks (MOFs) as adsorbents for carbon dioxide. *Adsorption* **2008**, *14* (6), 755-762.
154. Shimizu, G. K. H.; Vaidhyanathan, R.; Iremonger, S. S.; Dawson, K. W., An amine-functionalized metal organic framework for preferential CO(2) adsorption at low pressures. *Chem Commun* **2009**, (35), 5230-5232.
155. Vaidhyanathan, R.; Iremonger, S. S.; Shimizu, G. K. H.; Boyd, P. G.; Alavi, S.; Woo, T. K., Direct Observation and Quantification of CO(2) Binding Within an Amine-Functionalized Nanoporous Solid. *Science* **2010**, *330* (6004), 650-653.
156. El-Kaderi, H. M.; Rabbani, M. G., Template-Free Synthesis of a Highly Porous Benzimidazole-Linked Polymer for CO(2) Capture and H(2) Storage. *Chem Mater* **2011**, *23* (7), 1650-1653.
157. Cui, Y.; Liu, Y.; Xu, X.; Zheng, F. K., Chiral octupolar metal-organoboron NLO frameworks with (14,3) topology. *Angew Chem Int Edit* **2008**, *47* (24), 4538-4541.
158. Lambert, J. B.; Liu, Z. Q.; Liu, C. Q., Metal-organic frameworks from silicon- and germanium-centered tetrahedral ligands. *Organometallics* **2008**, *27* (7), 1464-1469.
159. Yamaguchi, S.; Shirasaka, T.; Tamao, K., Tridurylboranes extended by three arylethynyl groups as a new family of boron-based pi-electron systems. *Org Lett* **2000**, *2* (26), 4129-4132.

160. Ong, C. W.; Liao, S. C.; Chang, T. H.; Hsu, H. F., Rapid synthesis of new discotic liquid crystals based on diquinoxalino[2,3-a : 2',3'-c]phenazine containing hexakis(alkoxy) side arms. *Tetrahedron Lett* **2003**, 44 (7), 1477-1480.
161. Perepichkat, D. F.; Brusso, J. L.; Hirst, O. D.; Dadvand, A.; Ganesan, S.; Cicoira, F.; Robertson, C. M.; Oakley, R. T.; Rosei, F., Two-dimensional structural motif in thienoacene semiconductors: Synthesis, structure, and properties of tetrathienoanthracene isomers. *Chem Mater* **2008**, 20 (7), 2484-2494.
162. Yamaguchi, S.; Akiyama, S.; Tamao, K., Tri-9-anthrylborane and its derivatives: New boron-containing pi-electron systems with divergently extended pi-conjugation through boron. *J Am Chem Soc* **2000**, 122 (26), 6335-6336.
163. Space, B.; Belof, J. L.; Stern, A. C.; Eddaoudi, M., On the mechanism of hydrogen storage in a metal-organic framework material. *J Am Chem Soc* **2007**, 129 (49), 15202-15210.
164. Mellon, E. K., Jr.; Lagowski, J. J., Interaction of methyl-substituted borazines with various acceptor molecules. *Nature (London, United Kingdom)* **1963**, 199 (4897), 997-8.
165. Nayar, V. S. V.; Peacock, R. D., Reaction of Pentafluoroaniline with Boron Tribromide. *Nature* **1965**, 207 (4997), 630-&.
166. Manners, I.; Jaska, C. A.; Clark, T. J.; Clendenning, S. B.; Grozea, D.; Turak, A.; Lu, Z. H., Poisoning of heterogeneous, late transition metal dehydrocoupling catalysts by boranes and other group 13 hydrides. *J Am Chem Soc* **2005**, 127 (14), 5116-5124.

167. Manners, I.; Jaska, C. A., Heterogeneous or homogeneous catalysis? Mechanistic studies of the rhodium-catalyzed dehydrocoupling of amine-borane and phosphine-borane adducts. *J Am Chem Soc* **2004**, *126* (31), 9776-9785.
168. Jaska, C. A.; Temple, K.; Lough, A. J.; Manners, I., Catalytic dehydrocoupling of amine-borane adducts to form aminoboranes and borazines. *Phosphorus Sulfur* **2004**, *179* (4-5), 733-736.
169. Manners, I.; Jaska, C. A., Catalytic dehydrocoupling of amine-borane and phosphine-borane adducts: The mechanism is heterogeneous in one case and homogeneous in the other. *J Am Chem Soc* **2004**, *126* (5), 1334-1335.
170. Manners, I.; Jaska, C. A.; Temple, K.; Lough, A. J., Transition metal-catalyzed formation of boron-nitrogen bonds: Catalytic dehydrocoupling of amine-borane adducts to form aminoboranes and borazines. *J Am Chem Soc* **2003**, *125* (31), 9424-9434.
171. Manners, I.; Jaska, C. A.; Temple, K.; Lough, A. J., Rhodium-catalyzed formation of boron-nitrogen bonds: a mild route to cyclic aminoboranes and borazines. *Chem Commun* **2001**, (11), 962-963.
172. Manners, I.; Clark, T. J.; Lee, K., Transition-metal-catalyzed dehydrocoupling: A convenient route to bonds between main-group elements. *Chem-Eur J* **2006**, *12* (34), 8634-8648.
173. Manners, I.; Clark, T. J.; Russell, C. A., Homogeneous, titanocene-catalyzed dehydrocoupling of amine-borane adducts. *J Am Chem Soc* **2006**, *128* (30), 9582-9583.

174. Manners, I.; Staubitz, A.; Soto, A. P., Iridium-catalyzed dehydrocoupling of primary amine-borane adducts: A route to high molecular weight polyaminoboranes, boron-nitrogen analogues of polyolefins. *Angew Chem Int Edit* **2008**, *47* (33), 6212-6215.
175. Manners, I.; Sloan, M. E.; Clark, T. J., Homogeneous Catalytic Dehydrogenation/Dehydrocoupling of Amine-Borane Adducts by the Rh(I) Wilkinson's Complex Analogue RhCl(PHCy(2))(3) (Cy = cyclohexyl). *Inorg Chem* **2009**, *48* (6), 2429-2435.
176. Noth, H.; Anand, B.; Schwenk-Kircher, H.; Troll, A., Contribution to the chemistry of boron, part 260. Structural chemistry of borazines. *Eur J Inorg Chem* **2008**, (20), 3186-3199.
177. Kaupp, G.; Naimi-Jamal, M. R.; Stepanenko, V., Waste-free and facile solid-state protection of diamines, anthranilic acid, diols, and polyols with phenylboronic acid. *Chem-Eur J* **2003**, *9* (17), 4156-4160.
178. Maruyama, S.; Kawanishi, Y., Syntheses and emission properties of novel violet-blue emissive aromatic bis(diazaborole)s. *J Mater Chem* **2002**, *12* (8), 2245-2249.
179. Suginome, M.; Noguchi, H.; Hojo, K., Boron-masking strategy for the selective synthesis of oligoarenes via iterative Suzuki-Miyaura coupling. *J Am Chem Soc* **2007**, *129* (4), 758-759.
180. Yamaguchi, S.; Wakamiya, A.; Ide, T., Toward pi-conjugated molecule bundles: Synthesis of a series of B,B',B''-trianthryl-N,N',N''-triarylborazines and the bundle effects on their properties. *J Am Chem Soc* **2005**, *127* (42), 14859-14866.

181. Wagner, M.; Haberecht, M. C.; Heilmann, J. B.; Haghiri, A.; Bolte, M.; Bats, J. W.; Lerner, H. W.; Holthausen, M. C., Multiply borylated arenes: X-ray crystal structure analyses and quantum chemical calculations. *Z Anorg Allg Chem* **2004**, 630 (6), 904-913.
182. Diemer, S.; Noth, H.; Storch, W., Synthesis of boron-halogenated diborylamines and diborylhydrazines by cleavage of stannazanes. *Eur J Inorg Chem* **1999**, (10), 1765-1779.
183. Roesler, R.; Forster, T. D.; Krahulic, K. E.; Tuononen, H. M.; McDonald, R.; Parvez, M., A sigma-donor with a planar six-pi-electron B(2)N(2)C(2) framework: Anionic N-heterocyclic carbene or heterocyclic terphenyl anion? *Angew Chem Int Edit* **2006**, 45 (38), 6356-6359.
184. Yamamoto, T.; Yamaguchi, I.; Choi, B. J.; Koizumi, T. A.; Kubota, K., pi-Conjugated polyphenylenes with diazaborole side chains synthesized via 1,2-phenylenediamine polymer. *Macromolecules* **2007**, 40 (3), 438-443.
185. Yamamoto, Y.; Miyamoto, K.; Umeda, J.; Nakatani, Y.; Yamamoto, T.; Miyaura, N., Synthesis of B-trisubstituted borazines via the rhodium-catalyzed hydroboration of alkenes with N,N',N''-trimethyl or N,N',N''-triethylborazine. *J Organomet Chem* **2006**, 691 (23), 4909-4917.
186. Paine, R. T.; Koestle, W.; Borek, T. T.; Wood, G. L.; Pruss, E. A.; Duesler, E. N.; Hiskey, M. A., Synthesis, characterization, and explosive properties of the nitrogen-rich borazine [H<sub>3</sub>N<sub>3</sub>B<sub>3</sub>(N-3)(3)]. (vol 38, pg 3741, 1999). *Inorg Chem* **1999**, 38 (21), 4920-4920.

187. Noth, H.; Troll, A., The N-lithiation of 2,4,6-triphenylborazine. *Eur J Inorg Chem* **2005**, (17), 3524-3535.
188. Bernard, S.; Salles, V.; Li, J. P.; Brioude, A.; Chehaidi, S.; Foucaud, S.; Miele, P., Design of Highly Dense Boron Nitride by the Combination of Spray-Pyrolysis of Borazine and Additive-Free Sintering of Derived Ultrafine Powders. *Chem Mater* **2009**, 21 (13), 2920-2929.
189. Bernard, S.; Duperrier, S.; Calin, A.; Sigala, C.; Chiriac, R.; Miele, P.; Balan, C., Design of a series of preceramic B-tri(methylamino)borazine-based polymers as fiber precursors: Shear rheology investigations. *Macromolecules* **2007**, 40 (4), 1028-1034.
190. Che, C. M.; Sham, I. H. T.; Kwok, C. C.; Zhu, N. Y., Borazine materials for organic optoelectronic applications. *Chem Commun* **2005**, (28), 3547-3549.
191. Yamaguchi, S.; Wakamiya, A., Boron as a key component for new pi-electron materials. *Pure Appl Chem* **2006**, 78 (7), 1413-1424.
192. Tomko, T.; Rajagopalan, R.; Aksoy, P.; Foley, H. C., Synthesis of boron/nitrogen substituted carbons for aqueous asymmetric capacitors. *Electrochimica Acta* **2011**, 56 (15), 5369-5375.
193. Li, J.; Bernard, S.; Salles, V.; Gervais, C.; Miele, P., Preparation of Polyborazylene-Derived Bulk Boron Nitride with Tunable Properties by Warm-Pressing and Pressureless Pyrolysis. *Chem. Mater.* **2010**, 22 (6), 2010-2019.
194. Termoss, H.; Toury, B.; Pavan, S.; Brioude, A.; Bernard, S.; Cornu, D.; Valette, S.; Benayoun, S.; Miele, P., Preparation of boron nitride-based coatings on

- metallic substrates via infrared irradiation of dip-coated polyborazylene. *J. Mater. Chem.* **2009**, 19 (18), 2671-2674.
195. Metin, O.; Duman, S.; Dinc, M.; Ozkar, S., Oleylamine-Stabilized Palladium(0) Nanoclusters As Highly Active Heterogeneous Catalyst for the Dehydrogenation of Ammonia Borane. *J. Phys. Chem. C* **2011**, 115 (21), 10736-10743.
196. Sutton, A. D.; Burrell, A. K.; Dixon, D. A.; Garner, E. B., III; Gordon, J. C.; Nakagawa, T.; Ott, K. C.; Robinson, J. P.; Vasiliu, M., Regeneration of Ammonia Borane Spent Fuel by Direct Reaction with Hydrazine and Liquid Ammonia. *Science (Washington, DC, United States)* **2011**, 331 (6023), 1426-1429.
197. Mal, S. S.; Stephens, F. H.; Baker, R. T., Transition metal catalyzed dehydrogenation of amine-borane fuel blends. *Chemical Communications (Cambridge, United Kingdom)* **2011**, 47 (10), 2922-2924.
198. Himmelberger, D. W.; Alden, L. R.; Bluhm, M. E.; Sneddon, L. G., Ammonia Borane Hydrogen Release in Ionic Liquids. *Inorganic Chemistry (Washington, DC, United States)* **2009**, 48 (20), 9883-9889.
199. Himmelberger, D. W.; Yoon, C. W.; Bluhm, M. E.; Carroll, P. J.; Sneddon, L. G., Base-Promoted Ammonia Borane Hydrogen-Release. *J. Am. Chem. Soc.* **2009**, 131 (39), 14101-14110.
200. Davis, B. L.; Dixon, D. A.; Garner, E. B.; Gordon, J. C.; Matus, M. H.; Scott, B.; Stephens, F. H., Efficient Regeneration of Partially Spent Ammonia Borane Fuel. *Angewandte Chemie, International Edition* **2009**, 48 (37), 6812-6816, S6812/1-S6812/18.

201. Delgado-Friedrichs, O.; O'Keeffe, M.; Yaghi, O. M., Three-periodic nets and tilings: edge-transitive binodal structures. *Acta Crystallogr A* **2006**, 62, 350-355.
202. Ockwig, N. W.; Delgado-Friedrichs, O.; O'Keeffe, M.; Yaghi, O. M., Reticular chemistry: Occurrence and taxonomy of nets and grammar for the design of frameworks. *Accounts Chem Res* **2005**, 38 (3), 176-182.
203. Bonneau, C.; Delgado-Friedrichs, O.; O'Keeffe, M.; Yaghi, O. M., Three-periodic nets and tilings: minimal nets. *Acta Crystallogr A* **2004**, 60, 517-520.
204. Friedrichs, O. D.; O'Keeffe, M. O.; Yaghi, O. M., Three-periodic nets and tilings: semiregular nets. *Acta Crystallogr A* **2003**, 59, 515-525.
205. Friedrichs, O. D.; O'Keeffe, M.; Yaghi, O. M., Three-periodic nets and tilings: regular and quasiregular nets. *Acta Crystallogr A* **2003**, 59, 22-27.
206. O'Keeffe, M.; Peskov, M. A.; Ramsden, S. J.; Yaghi, O. M., The Reticular Chemistry Structure Resource (RCSR) Database of, and Symbols for, Crystal Nets. *Accounts Chem Res* **2008**, 41 (12), 1782-1789.
207. Lukose, B.; Kuc, A.; Heine, T., The Structure of Layered Covalent-Organic Frameworks. *Chem-Eur J* **2011**, 17 (8), 2388-2392.
208. Accelrys, I., Materials Studio 4.3 V. **2003**.
209. Ltd., C. S., CrystalMaker Version 1.4.5.
210. Jackson, K. T. R., M. G.; Reich, T. E.; El-Kaderi, H. M., Synthesis of highly porous borazine-linked polymers and their application to H(2), CO(2), and CH(4) storage. *Polym Chem* **2011**, 2, 2775-2777.
211. Allaoud, S.; Zair, T.; Karim, A.; Frange, B., Atropisomerism in Ortho-Aryl-Substituted Borazines. *Inorg Chem* **1990**, 29 (7), 1447-1449.



212. Blackbor.Jr; Blackmor.Je; Lockhart, J. C., Thermal Elimination of Hydrogen Chloride from Adducts of Aromatic Amines with Boron Trichloride with Reference to Borazole Formation. *J Chem Soc A* **1971**, (1), 49-&.
213. Groszos, S. J.; Stafiej, S. F., Organoboron compounds. I. A new synthesis of B,B',B''-trialkyl and triaryl-N,N',N''-triphenylborazoles. *J. Am. Chem. Soc.* **1958**, 80, 1357-60.
214. Reich, T. E.; Jackson, K. T.; Li, S.; Jena, P.; El-Kaderi, H. M., Synthesis and characterization of highly porous borazine-linked polymers and their performance in hydrogen storage application. *J Mater Chem* **2011**, 21 (29), 10629-10632.
215. Bao, C. Y.; Lu, R.; Jin, M.; Xue, P. C.; Tan, C. H.; Xu, T. H.; Liu, G. F.; Zhao, Y. Y., Helical stacking tuned by alkoxy side chains in pi-conjugated triphenylbenzene discotic derivatives. *Chem-Eur J* **2006**, 12 (12), 3287-3294.
216. Plietzsch, O.; Schilling, C. I.; Tolev, M.; Nieger, M.; Richert, C.; Muller, T.; Brase, S., Four-fold click reactions: Generation of tetrahedral methane- and adamantane-based building blocks for higher-order molecular assemblies. *Org Biomol Chem* **2009**, 7 (22), 4734-4743.
217. Laliberte, D.; Maris, T.; Wuest, J. D., Molecular tectonics - Use of urethanes and ureas derived from tetraphenylmethane and tetraphenylsilane to build porous chiral hydrogen-bonded networks. *Can J Chem* **2004**, 82 (2), 386-398.
218. Jaschke, T.; Jansen, M., A new borazine-type single source precursor for Si/B/N/C ceramics. *J Mater Chem* **2006**, 16 (27), 2792-2799.
219. Bechelany, M.; Bernard, S.; Brioude, A.; Cornu, D.; Stadelmann, P.; Charcosset, C.; Fiaty, K.; Miele, P., Synthesis of boron nitride nanotubes by a template-

- assisted polymer thermolysis process. *J Phys Chem C* **2007**, 111 (36), 13378-13384.
220. Lory, E. R.; Porter, R. F., Infrared Studies of Matrix-Isolated Species in Hydrogen-Boron-Nitrogen System. *J Am Chem Soc* **1973**, 95 (6), 1766-1770.
221. Noeth, H.; Wrackmeyer, B., *NMR Basic Principles and Progress, Vol. 14: Nuclear Magnetic Resonance Spectroscopy of Boron Compounds*. 1978; p 461 pp.
222. Framery, E.; Vaultier, M., Efficient synthesis and NMR data of N- or B-substituted borazines. *Heteroatom Chem* **2000**, 11 (3), 218-225.
223. Gervais, C.; Babonneau, F.; Maquet, J.; Bonhomme, C.; Massiot, D.; Framery, E.; Vaultier, M., N-15 cross-polarization using the inversion-recovery cross-polarization technique and B-11 magic angle spinning NMR studies of reference compounds containing B-N bonds. *Magn Reson Chem* **1998**, 36 (6), 407-414.
224. Gervais, C.; Framery, E.; Duriez, C.; Maquet, J.; Vaultier, M.; Babonneau, F., B-11 and N-15 solid state NMR investigation of a boron nitride preceramic polymer prepared by ammonolysis of borazine. *J Eur Ceram Soc* **2005**, 25 (2-3), 129-135.
225. Macomber, R. S., *A Complete Introduction to Modern NMR Spectroscopy*. 1998; p 382 pp.
226. Moon, K.-T.; Min, D.-S.; Kim, D.-P., Synthesis of borazine and its polymer-derived boron nitride. *Journal of Industrial and Engineering Chemistry (Seoul)* **1997**, 3 (4), 288-292.
227. Brunauer, S.; Deming, L. S.; Deming, W. E.; Teller, E., A theory of the van der Waals adsorption of gases. *J. Am. Chem. Soc.* **1940**, 62, 1723-32.

228. Brunauer, S.; Emmett, P. H.; Teller, E., Adsorption of gases in multimolecular layers. *J. Am. Chem. Soc.* **1938**, *60*, 309-19.
229. Schumacher, K.; Ravikovitch, P. I.; Du Chesne, A.; Neimark, A. V.; Unger, K. K., Characterization of MCM-48 materials. *Langmuir* **2000**, *16* (10), 4648-4654.
230. Ravikovitch, P. I.; Vishnyakov, A.; Russo, R.; Neimark, A. V., Unified approach to pore size characterization of microporous carbonaceous materials from N(2), Ar, and CO(2) adsorption isotherms. *Langmuir* **2000**, *16* (5), 2311-2320.
231. Murray, L. J.; Dinca, M.; Long, J. R., Hydrogen storage in metal-organic frameworks. *Chem Soc Rev* **2009**, *38* (5), 1294-1314.
232. Svec, F.; Germain, J.; Frechet, J. M. J., Nanoporous Polymers for Hydrogen Storage. *Small* **2009**, *5* (10), 1098-1111.
233. Wood, C. D.; Tan, B.; Trewin, A.; Niu, H. J.; Bradshaw, D.; Rosseinsky, M. J.; Khimyak, Y. Z.; Campbell, N. L.; Kirk, R.; Stockel, E.; Cooper, A. I., Hydrogen storage in microporous hypercrosslinked organic polymer networks. *Chem Mater* **2007**, *19* (8), 2034-2048.
234. Germain, J.; Svec, F.; Frechet, J. M. J., Preparation of Size-Selective Nanoporous Polymer Networks of Aromatic Rings: Potential Adsorbents for Hydrogen Storage. *Chem Mater* **2008**, *20* (22), 7069-7076.
235. Ghanem, B. S.; Hashem, M.; Harris, K. D. M.; Msayib, K. J.; Xu, M. C.; Budd, P. M.; Chaukura, N.; Book, D.; Tedds, S.; Walton, A.; McKeown, N. B., Triptycene-Based Polymers of Intrinsic Microporosity: Organic Materials That Can Be Tailored for Gas Adsorption. *Macromolecules* **2010**, *43* (12), 5287-5294.

236. Ben, T.; Ren, H.; Ma, S. Q.; Cao, D. P.; Lan, J. H.; Jing, X. F.; Wang, W. C.; Xu, J.; Deng, F.; Simmons, J. M.; Qiu, S. L.; Zhu, G. S., Targeted Synthesis of a Porous Aromatic Framework with High Stability and Exceptionally High Surface Area. *Angew Chem Int Edit* **2009**, *48* (50), 9457-9460.
237. Tozawa, T.; Jones, J. T. A.; Swamy, S. I.; Jiang, S.; Adams, D. J.; Shakespeare, S.; Clowes, R.; Bradshaw, D.; Hasell, T.; Chong, S. Y.; Tang, C.; Thompson, S.; Parker, J.; Trewin, A.; Bacsá, J.; Slawin, A. M. Z.; Steiner, A.; Cooper, A. I., Porous organic cages. *Nat Mater* **2009**, *8* (12), 973-978.
238. Morris, W.; Leung, B.; Furukawa, H.; Yaghi, O. K.; He, N.; Hayashi, H.; Houndonougbo, Y.; Asta, M.; Laird, B. B.; Yaghi, O. M., A Combined Experimental-Computational Investigation of Carbon Dioxide Capture in a Series of Isorecticular Zeolitic Imidazolate Frameworks. *J Am Chem Soc* **2010**, *132* (32), 11006-11008.
239. Banerjee, R.; Phan, A.; Wang, B.; Knobler, C.; Furukawa, H.; O'Keeffe, M.; Yaghi, O. M., High-throughput synthesis of zeolitic imidazolate frameworks and application to CO<sub>2</sub> capture. *Science* **2008**, *319* (5865), 939-943.
240. Banerjee, R.; Furukawa, H.; Britt, D.; Knobler, C.; O'Keeffe, M.; Yaghi, O. M., Control of Pore Size and Functionality in Isorecticular Zeolitic Imidazolate Frameworks and their Carbon Dioxide Selective Capture Properties. *J Am Chem Soc* **2009**, *131* (11), 3875-+.
241. Yang, W. B.; Greenaway, A.; Lin, X. A.; Matsuda, R.; Blake, A. J.; Wilson, C.; Lewis, W.; Hubberstey, P.; Kitagawa, S.; Champness, N. R.; Schroder, M.,

- Exceptional Thermal Stability in a Supramolecular Organic Framework: Porosity and Gas Storage. *J Am Chem Soc* **2010**, 132 (41), 14457-14469.
242. Farha, O. K.; Spokoyny, A. M.; Hauser, B. G.; Bae, Y. S.; Brown, S. E.; Snurr, R. Q.; Mirkin, C. A.; Hupp, J. T., Synthesis, Properties, and Gas Separation Studies of a Robust Diimide-Based Microporous Organic Polymer. *Chem Mater* **2009**, 21 (14), 3033-3035.
243. Millward, A. R.; Yaghi, O. M., Metal-organic frameworks with exceptionally high capacity for storage of carbon dioxide at room temperature. *J Am Chem Soc* **2005**, 127 (51), 17998-17999.
244. Eddaoudi, M.; Kim, J.; Rosi, N.; Vodak, D.; Wachter, J.; O'Keeffe, M.; Yaghi, O. M., Systematic design of pore size and functionality in isorecticular MOFs and their application in methane storage. *Science* **2002**, 295 (5554), 469-472.
245. Seki, K.; Mori, W., Syntheses and characterization of microporous coordination polymers with open frameworks. *J Phys Chem B* **2002**, 106 (6), 1380-1385.
246. Zhou, W.; Wu, H.; Hartman, M. R.; Yildirim, T., Hydrogen and methane adsorption in metal-organic frameworks: A high-pressure volumetric study. *J Phys Chem C* **2007**, 111 (44), 16131-16137.
247. Ma, S. Q.; Sun, D. F.; Simmons, J. M.; Collier, C. D.; Yuan, D. Q.; Zhou, H. C., Metal-organic framework from an anthracene derivative containing nanoscopic cages exhibiting high methane uptake. *J Am Chem Soc* **2008**, 130 (3), 1012-1016.
248. Menon, V. C.; Komarneni, S., Porous adsorbents for vehicular natural gas storage: A review. *J Porous Mat* **1998**, 5 (1), 43-58.

249. Bhatia, S. K.; Myers, A. L., Optimum conditions for adsorptive storage. *Langmuir* **2006**, 22 (4), 1688-1700.
250. Tedds, S.; Walton, A.; Broom, D. P.; Book, D., Characterisation of porous hydrogen storage materials: carbons, zeolites, MOFs and PIMs. *Faraday Discuss* **2011**, 151, 75-94.
251. Yanik, R., Calculations of isosteric heats of adsorption of neon and hydrogen adsorbed on charcoal in the temperature range 22-90 K. *Vacuum* **1996**, 47 (2), 205-207.
252. Mason, J. A.; Sumida, K.; Herm, Z. R.; Krishna, R.; Long, J. R., Evaluating metal-organic frameworks for post-combustion carbon dioxide capture via temperature swing adsorption. *Energy & Environmental Science* **2011**, 4 (8), 3030-3040.
253. McDonald, T. M.; D'Alessandro, D. M.; Krishna, R.; Long, J. R., Enhanced carbon dioxide capture upon incorporation of N,N'-dimethylethylenediamine in the metal-organic framework CuBTTri. *Chem Sci* **2011**, 2 (10), 2022-2028.
254. Barcia, P. S.; Silva, J. A. C.; Rodrigues, A. E., Adsorption equilibrium and kinetics of branched hexane isomers in pellets of BETA zeolite. *Micropor Mesopor Mat* **2005**, 79 (1-3), 145-163.
255. Rowsell, J. L. C.; Yaghi, O. M., Effects of functionalization, catenation, and variation of the metal oxide and organic linking units on the low-pressure hydrogen adsorption properties of metal-organic frameworks. *J Am Chem Soc* **2006**, 128 (4), 1304-1315.

256. Britt, D.; Furukawa, H.; Wang, B.; Glover, T. G.; Yaghi, O. M., Highly efficient separation of carbon dioxide by a metal-organic framework replete with open metal sites. *P Natl Acad Sci USA* **2009**, *106* (49), 20637-20640.
257. Jagiello, J.; Bandosz, T. J.; Putyera, K.; Schwarz, J. A., Adsorption near-Ambient Temperatures of Methane, Carbon Tetrafluoride, and Sulfur-Hexafluoride on Commercial Activated Carbons. *J Chem Eng Data* **1995**, *40* (6), 1288-1292.
258. Czepirski, L.; Jagiello, J., Virial-Type Thermal Equation of Gas Solid Adsorption. *Chem Eng Sci* **1989**, *44* (4), 797-801.
259. Wang, Z. G.; Zhang, B. F.; Yu, H.; Sun, L. X.; Jiao, C. L.; Liu, W. S., Microporous polyimide networks with large surface areas and their hydrogen storage properties. *Chem Commun* **2010**, *46* (41), 7730-7732.
260. Lu, W. G.; Yuan, D. Q.; Zhao, D.; Schilling, C. I.; Plietzsch, O.; Muller, T.; Brase, S.; Guenther, J.; Blumel, J.; Krishna, R.; Li, Z.; Zhou, H. C., Porous Polymer Networks: Synthesis, Porosity, and Applications in Gas Storage/Separation. *Chem Mater* **2010**, *22* (21), 5964-5972.
261. Becke, A. D., Density-Functional Thermochemistry .3. The Role of Exact Exchange. *J Chem Phys* **1993**, *98* (7), 5648-5652.
262. Vosko, S. H.; Wilk, L.; Nusair, M., Accurate Spin-Dependent Electron Liquid Correlation Energies for Local Spin-Density Calculations - a Critical Analysis. *Can J Phys* **1980**, *58* (8), 1200-1211.
263. Zhao, Y.; Truhlar, D. G., The M06 suite of density functionals for main group thermochemistry, thermochemical kinetics, noncovalent interactions, excited states, and transition elements: two new functionals and systematic testing of

- four M06-class functionals and 12 other functionals. *Theor Chem Acc* **2008**, 120 (1-3), 215-241.
264. Frisch, M. J. T., G. N.; Schlegel, H. B. et al, **2009**.
  265. Krishnan, R.; Binkley, J. S.; Seeger, R.; Pople, J. A., Self-Consistent Molecular-Orbital Methods .20. Basis Set for Correlated Wave-Functions. *J Chem Phys* **1980**, 72 (1), 650-654.
  266. Mclean, A. D.; Chandler, G. S., Contracted Gaussian-Basis Sets for Molecular Calculations .1. 2nd Row Atoms, Z=11-18. *J Chem Phys* **1980**, 72 (10), 5639-5648.
  267. Reed, A. E.; Weinstock, R. B.; Weinhold, F., Natural-Population Analysis. *J Chem Phys* **1985**, 83 (2), 735-746.
  268. Keith, D. W.; Minh, H.-D.; Stolaroff, J. K., Climate Strategy with Co<sub>2</sub> Capture from the Air. *Climatic Change* **2006**, 74 (1-3), 17-45.
  269. Lee, K. B.; Beaver, M. G.; Caram, H. S.; Sircar, S., Reversible Chemisorbents for Carbon Dioxide and Their Potential Applications. *Ind Eng Chem Res* **2008**, 47 (21), 8048-8062.
  270. Cheon, Y. E.; Suh, M. P., Multifunctional fourfold interpenetrating diamondoid network: Gas separation and fabrication of palladium nanoparticles. *Chem-Eur J* **2008**, 14 (13), 3961-3967.
  271. Xue, M.; Liu, Y.; Schaffino, R. M.; Xiang, S. C.; Zhao, X. J.; Zhu, G. S.; Qiu, S. L.; Chen, B. L., New Prototype Isorecticular Metal-Organic Framework Zn<sub>4</sub>O(FMA)<sub>3</sub> for Gas Storage. *Inorg Chem* **2009**, 48 (11), 4649-4651.



272. Miller, S. R.; Wright, P. A.; Devic, T.; Serre, C.; Ferey, G.; Llewellyn, P. L.; Denoyel, R.; Gaberova, L.; Filinchuk, Y., Single Crystal X-ray Diffraction Studies of Carbon Dioxide and Fuel-Related Gases Adsorbed on the Small Pore Scandium Terephthalate Metal Organic Framework,  $\text{Sc}_2(\text{O}_2\text{CC}(\text{C}_6\text{H}_4)\text{CO}_2)_3$ . *Langmuir* **2009**, 25 (6), 3618-3626.
273. Comotti, A.; Bracco, S.; Sozzani, P.; Horike, S.; Matsuda, R.; Chen, J.; Takata, M.; Kubota, Y.; Kitagawa, S., Nanochannels of two distinct cross-sections in a porous Al-based coordination polymer. *J Am Chem Soc* **2008**, 130 (41), 13664-13672.
274. Ma, B. Q.; Mulfort, K. L.; Hupp, J. T., Microporous pillared paddle-wheel frameworks based on mixed-ligand coordination of zinc ions. *Inorg Chem* **2005**, 44 (14), 4912-4914.
275. Bae, Y. S.; Mulfort, K. L.; Frost, H.; Ryan, P.; Punnnathanam, S.; Broadbelt, L. J.; Hupp, J. T.; Snurr, R. Q., Separation of  $\text{CO}_2$  from  $\text{CH}_4$  using mixed-ligand metal-organic frameworks. *Langmuir* **2008**, 24 (16), 8592-8598.
276. Wang, Q. M.; Shen, D. M.; Bulow, M.; Lau, M. L.; Deng, S. G.; Fitch, F. R.; Lemcoff, N. O.; Semanscin, J., Metallo-organic molecular sieve for gas separation and purification. *Micropor Mesopor Mat* **2002**, 55 (2), 217-230.
277. Chowdhury, P.; Bikkina, C.; Meister, D.; Dreisbach, F.; Gumma, S., Comparison of adsorption isotherms on Cu-BTC metal organic frameworks synthesized from different routes. *Micropor Mesopor Mat* **2009**, 117 (1-2), 406-413.

278. Liang, Z. J.; Marshall, M.; Chaffee, A. L., CO(2) Adsorption-Based Separation by Metal Organic Framework (Cu-BTC) versus Zeolite (13X). *Energ Fuel* **2009**, 23, 2785-2789.
279. Llewellyn, P. L.; Bourrelly, S.; Serre, C.; Vimont, A.; Daturi, M.; Hamon, L.; De Weireld, G.; Chang, J. S.; Hong, D. Y.; Hwang, Y. K.; Jhung, S. H.; Ferey, G., High uptakes of CO(2) and CH(4) in mesoporous metal-organic frameworks MIL-100 and MIL-101. *Langmuir* **2008**, 24 (14), 7245-7250.
280. Miller, S. R.; Pearce, G. M.; Wright, P. A.; Bonino, F.; Chavan, S.; Bordiga, S.; Margiolaki, I.; Guillou, N.; Feerey, G.; Bourrelly, S.; Llewellyn, P. L., Structural Transformations and Adsorption of Fuel-Related Gases of a Structurally Responsive Nickel Phosphonate Metal-Organic Framework, Ni-STA-12. *J Am Chem Soc* **2008**, 130 (47), 15967-15981.
281. Dietzel, P. D. C.; Besikiotis, V.; Blom, R., Application of metal-organic frameworks with coordinatively unsaturated metal sites in storage and separation of methane and carbon dioxide. *J Mater Chem* **2009**, 19 (39), 7362-7370.
282. Caskey, S. R.; Wong-Foy, A. G.; Matzger, A. J., Dramatic tuning of carbon dioxide uptake via metal substitution in a coordination polymer with cylindrical pores. *J Am Chem Soc* **2008**, 130 (33), 10870-+.
283. Bae, Y. S.; Farha, O. K.; Spokoyny, A. M.; Mirkin, C. A.; Hupp, J. T.; Snurr, R. Q., Carborane-based metal-organic frameworks as highly selective sorbents for CO(2) over methane. *Chem Commun* **2008**, (35), 4135-4137.

284. Cheon, Y. E.; Suh, M. P., Selective gas adsorption in a microporous metal-organic framework constructed of Co(4)(II) clusters. *Chem Commun* **2009**, (17), 2296-2298.
285. Chen, B. L.; Ma, S. Q.; Hurtado, E. J.; Lobkovsky, E. B.; Zhou, H. C., A triply interpenetrated microporous metal-organic framework for selective sorption of gas molecules. *Inorg Chem* **2007**, 46 (21), 8490-8492.
286. Bastin, L.; Barcia, P. S.; Hurtado, E. J.; Silva, J. A. C.; Rodrigues, A. E.; Chen, B., A microporous metal-organic framework for separation of CO<sub>2</sub>/N<sub>2</sub> and CO<sub>2</sub>/CH<sub>4</sub> by fixed-bed adsorption. *J Phys Chem C* **2008**, 112 (5), 1575-1581.
287. Cheon, Y. E.; Park, J.; Suh, M. P., Selective gas adsorption in a magnesium-based metal-organic framework. *Chem Commun* **2009**, (36), 5436-5438.
288. Bourrelly, S.; Llewellyn, P. L.; Serre, C.; Millange, F.; Loiseau, T.; Ferey, G., Different adsorption behaviors of methane and carbon dioxide in the isotypic nanoporous metal terephthalates MIL-53 and MIL-47. *J Am Chem Soc* **2005**, 127 (39), 13519-13521.
289. Llewellyn, P. L.; Bourrelly, S.; Serre, C.; Filinchuk, Y.; Ferey, G., How hydration drastically improves adsorption selectivity for CO<sub>2</sub> over CH<sub>4</sub> in the flexible chromium terephthalate MIL-53. *Angew Chem Int Edit* **2006**, 45 (46), 7751-7754.
290. Galli, S.; Masciocchi, N.; Tagliabue, G.; Sironi, A.; Navarro, J. A. R.; Salas, J. M.; Mendez-Linan, L.; Domingo, M.; Perez-Mendoza, M.; Barea, E., Polymorphic Coordination Networks Responsive to CO(2), Moisture, and Thermal Stimuli: Porous Cobalt(II) and Zinc(II) Fluoropyrimidinolates. *Chem-Eur J* **2008**, 14 (32), 9890-9901.

291. Choi, H. S.; Suh, M. P., Highly Selective CO(2) Capture in Flexible 3D Coordination Polymer Networks. *Angew Chem Int Edit* **2009**, *48* (37), 6865-6869.
292. Bae, Y. S.; Farha, O. K.; Hupp, J. T.; Snurr, R. Q., Enhancement of CO(2)/N(2) selectivity in a metal-organic framework by cavity modification. *J Mater Chem* **2009**, *19* (15), 2131-2134.
293. Neofotistou, E.; Malliakas, C. D.; Trikalitis, P. N., Unprecedented Sulfone-Functionalized Metal-Organic Frameworks and Gas-Sorption Properties. *Chem-Eur J* **2009**, *15* (18), 4523-4527.
294. Couck, S.; Denayer, J. F. M.; Baron, G. V.; Remy, T.; Gascon, J.; Kapteijn, F., An Amine-Functionalized MIL-53 Metal-Organic Framework with Large Separation Power for CO(2) and CH(4). *J Am Chem Soc* **2009**, *131* (18), 6326-+.
295. Dreisbach, F.; Staudt, R.; Keller, J. U., High pressure adsorption data of methane, nitrogen, carbon dioxide and their binary and ternary mixtures on activated carbon. *Adsorption* **1999**, *5* (3), 215-227.
296. Babarao, R.; Dai, S.; Jiang, D. E., Functionalizing Porous Aromatic Frameworks with Polar Organic Groups for High-Capacity and Selective CO(2) Separation: A Molecular Simulation Study. *Langmuir* **2011**, *27* (7), 3451-3460.
297. An, J.; Geib, S. J.; Rosi, N. L., High and Selective CO(2) Uptake in a Cobalt Adeninate Metal-Organic Framework Exhibiting Pyrimidine- and Amino-Decorated Pores. *J Am Chem Soc* **2010**, *132* (1), 38-+.
298. Das, M. C.; Xu, H.; Xiang, S. C.; Zhang, Z. J.; Arman, H. D.; Qian, G. D.; Chen, B. L., A New Approach to Construct a Doubly Interpenetrated Microporous Metal-

- Organic Framework of Primitive Cubic Net for Highly Selective Sorption of Small Hydrocarbon Molecules. *Chem-Eur J* **2011**, 17 (28), 7817-7822.
299. Myers, A. L.; Prausnitz, J. M., Thermodynamics of Mixed-Gas Adsorption. *Aiche J* **1965**, 11 (1), 121-+.
300. Herm, Z. R.; Swisher, J. A.; Smit, B.; Krishna, R.; Long, J. R., Metal-Organic Frameworks as Adsorbents for Hydrogen Purification and Precombustion Carbon Dioxide Capture. *J Am Chem Soc* **2011**, 133 (15), 5664-5667.
301. Krishna, R.; Calero, S.; Smit, B., Investigation of entropy effects during sorption of mixtures of alkanes in MFI zeolite. *Chem Eng J* **2002**, 88 (1-3), 81-94.
302. Krishna, R.; van Baten, J. M., Using molecular simulations for screening of zeolites for separation Of CO<sub>2</sub>/CH<sub>4</sub> mixtures. *Chem Eng J* **2007**, 133 (1-3), 121-131.
303. Belmabkhout, Y.; Pirngruber, G.; Jolimaître, E.; Methivier, A., A complete experimental approach for synthesis gas separation studies using static gravimetric and column breakthrough experiments. *Adsorption* **2007**, 13 (3-4), 341-349.
304. Belmabkhout, Y.; Serna-Guerrero, R.; Sayari, A., Adsorption of CO(2) from dry gases on MCM-41 silica at ambient temperature and high pressure. 1: Pure CO(2) adsorption. *Chem Eng Sci* **2009**, 64 (17), 3721-3728.
305. Belmabkhout, Y.; Sayari, A., Adsorption of CO(2) from dry gases on MCM-41 silica at ambient temperature and high pressure. 2: Adsorption of CO(2)/N(2), CO(2)/CH(4) and CO(2)/H(2) binary mixtures. *Chem Eng Sci* **2009**, 64 (17), 3729-3735.

306. Akten, E. D.; Siriwardane, R.; Sholl, D. S., Monte Carlo simulation of single- and binary-component adsorption of CO<sub>2</sub>, N<sub>2</sub>, and H<sub>2</sub> in zeolite Na-4A. *Energ Fuel* **2003**, 17 (4), 977-983.
307. Hwang, K. S.; Gong, S. Y.; Lee, W. K., Adsorption Equilibria for Hydrogen and Carbon-Dioxide on Activated Carbon at High-Pressure up to 30 Atm. *Korean J Chem Eng* **1991**, 8 (3), 148-155.
308. Jaschik, J.; Tanczyk, M.; Warmuzinski, K.; Jaschik, M., The Modelling of Multicomponent Adsorption Equilibria in Hydrogen Recovery by Pressure Swing Adsorption. *Chem Process Eng-Inz* **2009**, 30 (4), 511-521.
309. Liu, Y. H.; Liu, D. H.; Yang, Q. Y.; Zhong, C. L.; Mi, J. G., Comparative Study of Separation Performance of COFs and MOFs for CH<sub>4</sub>/CO<sub>2</sub>/H<sub>2</sub> Mixtures. *Ind Eng Chem Res* **2010**, 49 (6), 2902-2906.
310. Yang, Q. Y.; Zhong, C. L., Molecular simulation of carbon dioxide/methane/hydrogen mixture adsorption in metal-organic frameworks. *J Phys Chem B* **2006**, 110 (36), 17776-17783.
311. Benjamin, M. M., New Conceptualization and Solution Approach for the Ideal Adsorbed Solution Theory (IAST). *Environ Sci Technol* **2009**, 43 (7), 2530-2536.
312. Wu, J. Q.; Zhou, L.; Sun, Y.; Su, W.; Zhou, Y. P., Measurement and prediction of adsorption equilibrium for a H<sub>2</sub>/N<sub>2</sub>/CH<sub>4</sub>/CO<sub>2</sub> mixture. *Aiche J* **2007**, 53 (5), 1178-1191.
313. Anderson, M. R.; Mattes, B. R.; Reiss, H.; Kaner, R. B., Conjugated Polymer-Films for Gas Separations. *Science* **1991**, 252 (5011), 1412-1415.

314. Teplyakov, V. V.; Paul, D. R.; Bespalova, N. B.; Finkelshtein, E. S., Gas Permeation in a Fluorine-Containing Polynorbornene. *Macromolecules* **1992**, *25* (16), 4218-4219.
315. Yampolskii, Y. P.; Bespalova, N. B.; Finkelshtein, E. S.; Bondar, V. I.; Popov, A. V., Synthesis, Gas-Permeability, and Gas Sorption Properties of Fluorine-Containing Norbornene Polymers. *Macromolecules* **1994**, *27* (10), 2872-2878.
316. Challa, S. R.; Sholl, D. S.; Johnson, J. K., Adsorption and separation of hydrogen isotopes in carbon nanotubes: Multicomponent grand canonical Monte Carlo simulations. *J Chem Phys* **2002**, *116* (2), 814-824.
317. Babarao, R.; Hu, Z. Q.; Jiang, J. W.; Chempath, S.; Sandler, S. I., Storage and separation of CO<sub>2</sub> and CH<sub>4</sub> in silicalite, C-168 schwarzite, and IRMOF-1: A comparative study from monte carlo simulation. *Langmuir* **2007**, *23* (2), 659-666.
318. Bae, Y. S.; Hauser, B. G.; Farha, O. K.; Hupp, J. T.; Snurr, R. Q., Enhancement of CO(2)/CH(4) selectivity in metal-organic frameworks containing lithium cations. *Micropor Mesopor Mat* **2011**, *141* (1-3), 231-235.
319. Farha, O. K.; Bae, Y. S.; Hauser, B. G.; Spokoyny, A. M.; Snurr, R. Q.; Mirkin, C. A.; Hupp, J. T., Chemical reduction of a diimide based porous polymer for selective uptake of carbon dioxide versus methane. *Chem Commun* **2010**, *46* (7), 1056-1058.
320. Murthi, M.; Snurr, R. Q., Effects of molecular siting and adsorbent heterogeneity on the ideality of adsorption equilibria. *Langmuir* **2004**, *20* (6), 2489-2497.
321. (32-bit), W. M. V. N. f. W.

322. Atci, E.; Erucar, I.; Keskin, S., Adsorption and Transport of CH<sub>4</sub>, CO<sub>2</sub>, H<sub>2</sub> Mixtures in a Bio-MOF Material from Molecular Simulations. *J Phys Chem C* **2011**, *115* (14), 6833-6840.
323. Chen, Y. F.; Jiang, J. W., A Bio-Metal-Organic Framework for Highly Selective CO<sub>2</sub> Capture: A Molecular Simulation Study. *Chemsuschem* **2010**, *3* (8), 982-988.
324. Lewinski, J.; Kaczorowski, T.; Prochowicz, D.; Lipinska, T.; Justyniak, I.; Kaszukur, Z.; Lipkowski, J., Cinchona Alkaloid-Metal Complexes: Noncovalent Porous Materials with Unique Gas Separation Properties. *Angew Chem Int Edit* **2010**, *49* (39), 7035-7039.
325. Cavenati, S.; Grande, C. A.; Rodrigues, A. E., Adsorption equilibrium of methane, carbon dioxide, and nitrogen on zeolite 13X at high pressures. *J Chem Eng Data* **2004**, *49* (4), 1095-1101.
326. Budd, P. M.; Msayib, K. J.; Tattershall, C. E.; Ghanem, B. S.; Reynolds, K. J.; McKeown, N. B.; Fritsch, D., Gas separation membranes from polymers of intrinsic microporosity. *J Membrane Sci* **2005**, *251* (1-2), 263-269.
327. Du, N. Y.; Park, H. B.; Robertson, G. P.; Dal-Cin, M. M.; Visser, T.; Scoles, L.; Guiver, M. D., Polymer nanosieve membranes for CO<sub>2</sub>-capture applications. *Nat Mater* **2011**, *10* (5), 372-375.
328. Pennington, D. A.; Horton, P. N.; Hursthouse, M. B.; Bochmann, M.; Lancaster, S. J., Synthesis and catalytic activity of dinuclear imido titanium complexes: the molecular structure of [Ti(NPh)Cl( $\mu$ -Cl)(THF)(2)](2). *Polyhedron* **2005**, *24* (1), 151-156.



## **Vita**

Thomas Eugene Reich

2500 East Cary St. Apt. 306  
Richmond, VA 23223

reiche@mymail.vcu.edu, reichte11@hotmail.com

### **Date and Place of Birth:**

November 26, 1980; Hoffman Estates, Illinois

### **Academic Preparation:**

James Madison University, Harrisonburg, VA USA	Chemistry	B.Sc., 2003
Virginia Commonwealth University, Richmond, VA USA	Chemistry	Ph.D., 2011

### **Professional Appointments:**

2007-Current	Researcher, Department of Chemistry, Virginia Commonwealth University: Design, synthesis, and characterization of functionalized organic porous polymers for gas storage and separation applications utilizing organic, inorganic, and air-sensitive techniques in conjunction with a variety of analytical instrumentation. Finished coursework curriculum resulted in a 4.0 GPA.
2003-07	Head Chemist of the Wet Chemistry Department, Air, Water, & Soil Laboratories: Oversaw and performed within the department by high throughput analytical testing of environmental samples by a wide range of methods conforming to EPA and DEQ standards and regulations
2002-03	Researcher, Department of Chemistry, James Madison University: Analysis of fish otoliths (ear bones) as an assessment of the impact of environmental pollutants on aquatic animals

## Publications

1. **Reich, T. E.**; Jackson, K. J.; Li, S.; Jena, P.; El-Kaderi, H. M. "Synthesis and characterization of highly porous borazine-linked polymers and their performance in hydrogen storage application" *Journal of Materials Chemistry*, **2011**, 21, 10629-10632.
2. **Reich, T. E.**; Jackson, K. T.; El-Kaderi, H. M. "High CO<sub>2</sub>/CH<sub>4</sub> Selectivity in Borazine-Linked Polymers" *Langmuir* (submitted).
3. **Reich, T. E.**; Jackson, K. T.; El-Kaderi, H. M. "Gas Storage and Separation Potential of Borazine-Linked Polymers" (in preparation).
4. Rabbani, M. G.; **Reich, T. E.**; Kassab, R.; Jackson, K. T.; El-Kaderi, H. M. "High Gas Uptake and Selectivity by Triptycene-Derived Benzimidazole-Linked Polymers" *Chem. Commun.* DOI:10.1039/C2CC16986J.
5. Jackson, K. T.; **Reich, T. E.**; El-Kaderi, H. M. "Synthesis and Characterization of Porous Microcrystalline Polymers Linked by Borazine Rings" (in preparation).
6. Jackson, K. T.; Rabbani, M. G.; **Reich, T. E.**; El-Kaderi, H. M. "Synthesis of Highly Porous Borazine-Linked Polymers and Their Application to H<sub>2</sub>, CO<sub>2</sub>, and CH<sub>4</sub> Storage" *Polym. Chem.*, **2011**, 2, 2775-2777.
7. El-Shall, M. S.; Abdelsayed, V.; Khder, A. S.; Hassan, H. M.A.; El-Kaderi, H. M.; **Reich, T.E.** "Metallic and Bimetallic Nanocatalysts Incorporated into Highly Porous Coordination Polymer MIL-101" *Journal of Materials Chemistry* **2009**, 19(41), 7625-7631.
8. **Reich, T. E.**; Downey, D. M. "Elemental Analysis of Brook Trout Otoliths and Relationship to Habitat Water Chemistry" *Proceedings of the National Conference on Undergraduate Research* **2003**, 1-4.

## Oral Presentations

1. **Reich, T. E.**; Jackson, K. J.; Rabbani, M. G.; El-Kaderi, H. M. "Design, Synthesis, and Characterization of Multifunctional Nanoporous Organic Architectures", First United Arab Emirates Conference on Pure and Applied Chemistry (ECPAC11), American University of Sharjah (Sharjah, UAE), March 1-3, **2011**.
2. **Reich, T. E.**; El-Kaderi, H. M. "Nanoporous Borazine-Linked Polymers and Their Potential Use in Gas Storage and Separation Applications", Sixth Annual Virginia Graduate Student Research Forum (Richmond, VA), February 3, **2011**.

3. **Reich, T. E.** “The Effects of Scholarship on Graduate Students’ Lives”, 2010 Scholarship Donors Dinner, Virginia Commonwealth University (Richmond, VA), November 18, **2010**.
4. **Reich, T. E.;** El-Kaderi, H. M. “Designed Synthesis of Halogen-Decorated Nanoporous Organic Polymers and Their Performance in Gas Storage Applications”, Virginia Commonwealth University (Richmond, VA), January 27, **2010**.
5. **Reich, T. E.** “Molybdenum-Based Alkylidene Catalysts for the Synthesis of Quebrachamine”, Virginia Commonwealth University (Richmond, VA), April 14, **2009**.
6. **Reich, T. E.;** Downey, D. M. “Elemental Analysis of Brook Trout Otoliths and Relationship to Habitat Water Chemistry”, 2003 National Conference on Undergraduate Research (Salt Lake City, UT) March 13-15, **2003**.

### **Awards, Scholarships, and Honors**

2002	National Science Foundation Scholarship—Research Experiences for Undergraduates
2003	James Madison University Scholarship Award to attend the National Conference of Undergraduate Research in Salt Lake City, Utah
2008	Philip Morris Summer Research Scholarship Award
2009	James V. Quagliano Fellowship Award for outstanding work as a graduate student
2009	Lidia M. Vallarino Scholarship Award
2010	U.S. Department of Energy Scholarship Award to attend the 2010 Lindau Nobel Laureate Meeting in Lindau, Germany
2010	Gerald and Susan Bass Scholarship Award
2010	Altria Fellowship Award